Universitat Autònoma de Barcelona

Growth, Structure, and Optical Properties of Highly Ordered Organic Thin Films of Phthalocyanine and Diindenoperylene

Josep Oriol Ossó Torné

Institut de Ciència de Materials de Barcelona
Max-Planck-Institut für Metallforschung

Departament de Física
Sota la direcció del
Dr. Miquel Garriga i Bacardí
Bellaterra, novembre 2004

Prefaci

En els darrers anys, materials orgànics amb propietats semiconductores han despertat molt interès. Aquests nous materials ofereixen molts avantatges davant els seus equivalents inorgànics com ara baix cost, flexibilitat i la possibilitat d'escollir d'entre un nombre quasi infinit de compostos diferents aquell que conté les propietats que ens interessen. A més, les anomenades molècules lleugeres, presenten propietats òptiques i electròniques molt interessants, que les fan ideals per a diverses aplicacions com ara dispositius transparents, guies d'ona i pantalles planes de grans dimensions. Actualment ja es comercialitzen diversos dispositius fabricats a partir de materials orgànics com ara pantalles de telèfons mòbils o de càmeres digitals. Similarment al cas dels semiconductors inorgànics convencionals, per a obtenir dispositius amb bones propietats electròniques es requereix l'obtenció del material en forma de capes primes amb un elevat ordre estructural i lliure d'impureses. Aquest aspecte és un problema en materials orgànics relacionat amb el caràcter feble de les forces d'interacció entre molècules (de tipus van der Waals). A més, la baixa simetria que presenten tan les molècules com les cel·les unitat dels cristalls que formen fan encara més difícil l'obtenció de capes primes ben ordenades. A tot això sovint s'ha d'afegir el problema de polimorfisme, comú en molts d'aquests compostos. Les propietats òptiques i electròniques que les capes presenten depenen en gran mesura de l'estructura cristal·lina que aquestes adopten, determinada en part per les condicions en què la capa ha estat dipositada. Així, tot i que diversos dispositius basats en capes primes de molècules orgàniques ja han estat construïts (com díodes emissors de llum o OLEDs i transistors d'efecte camp o OFETs), s'ha fet evident que, com en el cas dels semiconductors tradicionals inorgànics, l'ordre cristal·lí del material que forma el dispositiu és clau per a obtenir el màxim rendiment de la capa activa orgànica.

En aquest treball, capes primes de materials orgànics han estat evaporades mitjançant la tècnica d'*epitàxia de feixos moleculars orgànics*. Les capes han estat dipositades sobre tipus diferents de substrats i sota condicions de creixement diverses, per a estudiar en quines condicions s'obté un grau d'ordre estructural elevat. Els compostos orgànics utilitzats són coure-hexadecafluoroftalocianina ($F_{16}CuPc$), semiconductor orgànic de tipus n, i diindenoperylene (DIP), de tipus p. Com a substrats s'han utilitzat tres òxids diferents, SiO_2, MgO i Al_2O_3. S'ha realitzat un estudi sistemàtic de la influència de les condicions durant l'evaporació i dels substrats utilitzats en l'estructura cristal·lina que les capes adopten. S'ha estudiat també la influència del grau d'ordre en les propietats optoelectròniques que les capes presenten.

Per a estudiar les propietats estructurals de les capes s'han utilitzat principalment dues tècniques d'anàlisi, el microscopi de forces atòmiques (AFM) i la difracció de raigs-x. L'AFM és una tècnica que permet l'estudi de la morfologia del substrat i de la capa, i aporta informació sobre l'estructura en el pla de la capa. També resulta útil per a determinar la forma i les dimensions que els cristallets adopten i, a diferència de les tècniques de difracció, ens dona informació en l'espai real. La difracció de raigs-x ens ofereix informació no només sobre la superfície sinó també sobre tot el volum de la capa i ens ajuda a caracteritzar l'estructura tan en la direcció normal (reflectivitat de raigs-x) a la superfície com en el pla (difracció en incidència rasant). Les propietats òptiques es determinen utilitzant l'el·lipsometria espectral. Aquesta tècnica ha resultat particularment útil en l'anàlisi de l'anisotropia que algunes capes presenten. Tot i que l'estudi de materials amb propietats anisòtropes és complicat, l'el·lipsometria ens permet localitzar l'orientació del tensor dielèctric amb facilitat i quantificar el grau d'anisotropia de les capes orgàniques. Finalment, la tècnica d'espectroscòpia Raman s'ha utilitzat per a determinar el grau d'ordre i l'orientació de les molècules en la capa.

Aquesta memòria està estructurada de la següent forma. Després d'una breu introducció dels conceptes més generals d'aquest treball en el capítol 1, en el capítol 2 s'introdueixen les propietats dels semiconductors orgànics, fent un breu resum dels progressos que han tingut lloc durant els darrers anys. En aquest capítol s'introdueixen també els compostos orgànics utilitzats en aquest estudi i en particular les propietats de les ftalocianines, que es poden considerar un cas model per a il·lustrar els avantatges i inconvenients que els semiconductors

moleculars ofereixen davant els seus equivalents inorgànics. En els capítols 3 i 4 s'introdueixen els aspectes teòrics i experimentals de les tècniques utilitzades. En el capítol 3 es mostren alguns aspectes teòrics de creixement cristal·lí, així com la tècnica d'epitàxia de feixos moleculars i es descriu el sistema de buit utilitzat en el creixement de les capes primes. Els fonaments teòrics de les diferents tècniques experimentals utilitzades en aquest estudi (microscopi de forces atòmiques, difracció de raigs-x i el·lispometria espectral i espectroscòpia Raman) es descriuen breument en el capítol 4. Finalment, en els capítols 5–7 es presenten els resultats obtinguts.

Contents

Chapter 1

Introduction

Semiconducting organic materials have attracted interest during the last decades due to their interesting optoelectronic properties. Their application in new flexible and transparent devices [1, 2], their tuning possibilities, and a potential low cost in the manufacturing lead to an increase of the academic activity in this field. The advances in the last decade attracted also the interest of the industry, and many companies have nowadays their own development division working on the field of organic electronics. At present, many applications of organic semiconductors have been demonstrated [3], and several devices that use organic semiconducting materials can already be found in the market. Although those materials cannot compete in performance with the traditional inorganic semiconductors (with charge carrier mobilities several orders of magnitude higher), they can be used in innovative applications such as large-area light emitting devices, on flexible substrates [2] or when low cost is required.

Organic materials with semiconducting properties can be classified into two big groups, *polymers* and *low-weight organic molecules* [4]. In particular, low-weight organic molecules show very interesting optoelectronic properties for the development of new applications as transparent devices, waveguides, large-area flat displays [5, 6], or organic solar cells [7, 8]. In contrast to polymers, small organic molecules form ordered crystalline structures. The close packing of the molecules in the solid enhances the π-*orbital* overlap in the material, origin of its semiconducting and transport properties [9, 10]. Hence, similarly to the conventional inorganic semiconductors, in order to improve the electronic properties of the material highly ordered structures are required [1, 11, 12]. Moreover, the

combination of different type of organic molecules is needed in the development of some devices such as organic solar cells, or organic light-emitting diodes, where at least two organic layers are combined. Therefore, a comprehensive survey of the organic-organic interface is crucial for technological applications.

The use of *molecular beam epitaxy* for the deposition of organic layers has been an important advance in the study of those systems [11, 13, 14]. The application of molecular beam epitaxy in the growth of organic materials has been denoted with the term *organic molecular beam epitaxy* or more generally *organic molecular beam deposition* where no epitaxial relation between the substrate and the overgrown layer is required. The ultra-high-vacuum environment and the well controlled growth conditions this technique offers allow the production of high-quality layers with an exceptional purity.

However, the growth of organic thin films presents several problems inherently related to the nature of these relatively large molecules. First of all, the unit cells of these materials are large compared to those of the typical inorganic substrates, and they exhibit a very low symmetry [15, 16]. This frequently leads to the epitaxial growth of films presenting multiple rotational and translational domains, since several energetically equivalent orientations of the organic lattice on the inorganic substrate exist. Secondly, the chemical nature of the substrate is crucial. Strongly interacting substrates usually limit the surface mobility of the molecules during film formation, thus leading to a high density of grains. Moreover, polymorphism is favored by the weak intermolecular interactions responsible of the crystal packing. Thus, it is often found that the first few monolayers deposited on the substrate crystallize in a modified structure due to the interaction with the substrate. Related to this, the morphology of the layer may exhibit different scenarios depending on the growth mode adopted by the layer (Frank–van der Merwe, Stranski–Krastanov, or Volmer–Weber) [17, 18].

In conclusion, situations where the presence of several azimuthal domains, small grain size, and coexistence of different polymorphic forms appear are common in the growth of organic thin layers. Due to these deviations from ideal growth, the physical properties of the organic layers do not hold compare to their single-crystal counterparts, which can be considered as the upper limit for some technologically relevant properties such as the charge carrier mobility [1, 19].

Most of the studies on organic semiconducting materials deal only with $p-$type

semiconductors (good hole conducting materials) since n-type and stable organic semiconductors are rare [20, 21]. However, $n-$type materials are also needed in the construction of $pn-$junctions, as in solar cells [7], and also to implement the well-established complementary logic in organic circuits [22–24]. In this work we study two organic materials, an n-type compound of the family of the phthalocyanines and a p-type compound, diindenoperylene. Both of them are planar low-weight molecules.

In this thesis organic films have been grown by organic molecular beam deposition under different growth conditions and on different substrates to study the influence of those parameters on the properties of the layers. We determine under which deposition conditions the structure of the layers is optimized and which is the influence that the different substrates have on the final structure. The optoelectronic properties of the films are strongly linked to their degree of structural definition. Therefore, prior to the study of their optoelectronic properties a full structural characterization is needed. Thus, a multi-technique study of the properties of the films is required. In this work, several techniques allow the independent characterization of the structural and optical properties of layers of phthalocyanines and diindenoperylene.

The structure of this thesis is as follows. In Chapter 2 the properties of organic semiconductors are reviewed and the motivation of this work is presented. The organic compounds studied in this work are also introduced in Chapter 2, where a brief summary of the published work on these materials is made. The organic molecular beam deposition technique is described in in Chapter 3, where also the ultra-high-vacuum system used in the growth of the organic layers is introduced. The properties of the substrates used and their preparation are also described in Chapter 3. In Chapter 4 the experimental techniques are discussed together with a short introduction to the theoretical background of each of them. Chapters 5 to 7 present and discuss the results obtained in this study. In Chapters 5 and 6 the properties of phthalocyanine and diindenoperylene layers on the different substrates used are presented. It is shown that different degrees of structural ordering in the layers are obtained depending on the substrate used and on the deposition conditions. It is shown that the final optoelectronic properties of the layers are strongly influenced by the degree of order they present. In Chapter 7

heterostructures combining both compounds (phthalocyanine and diindenoperylene) are shortly discussed, and some of the problems that may arise from the complexity of these interfaces are emphasized. Finally, in Chapter 8 we summarize the main results obtained. Special emphasis is made on the relationship between the results obtained from all the techniques used in the study.

Chapter 2

Organic semiconductors

The present chapter is devoted to organic compounds which present semiconducting properties. As *organic compounds* we consider those materials containing basically carbon, in association with hydrogen, oxygen, and nitrogen. The unique chemistry of carbon allows the construction of very complex molecular structures, and the possibility to combine them with many other different atoms or atomic groups. This rich variety of structure and electronic properties that organic compounds offer is probably the most attractive advantage of these materials. Their physical properties can be tailored by modifying their molecular structure. The desired optoelectronic properties for a given device can thus be obtained simply by choosing the appropriate material or by synthesizing a new molecule which meets the requirements needed for a certain application. Furthermore, molecular materials present several other advantages against their inorganic counterparts which make them suitable for the development of new applications [25, 26]. They show very interesting mechanical properties and are suitable for the fabrication of low-cost electronic circuits.

This chapter is organized as follows. In Section 2.1 a short review of the first studies as well as the last developments on organic semiconductors is made. Also in this section, the basic properties of organic semiconductors are introduced. Section 2.2 summarizes the usual problems found in the growth and characterization of thin films of those materials. Section 2.3 introduces one of the molecular compounds used in this work, the *phthalocyanines*. This compound is used as an example to illustrate the main advantages organic semiconductors offer but also to present some of the problems that need to be solved for the development of

organic devices. Finally, in Section 2.4 the second organic molecule used, *diindenoperylene*, is presented, and a review of the available work on this molecule is made. We should point out that these two materials were already combined to construct an organic solar cell in 1981 [27].

2.1 Basic properties of organic semiconductors

The semiconducting properties of organic compounds are known for nearly one century. Photoconduction in anthracene crystals was discovered in 1906 by Pochettino [28] while its dark conductivity was studied simultaneously with that of silicon in 1910. In spite of these early work, only few papers appeared in the period from 1940 to 1960 [29–31]. In the 1960s the first books and reviews exclusively dedicated to organic semiconductors appeared [32–34]. But it has been during the last three decades when an important increment of the work on this field occurred in many research laboratories followed by an increase of the interest from industry.

Nowadays, several organic-based devices can already be found in the market, and many major electronics firms as Kodak, Hewlett-Packard, IBM, Philips, Pioneer, Siemens, or Sony have their own development division working on this field. Many other new companies appeared (spin-off companies in many cases) dedicated exclusively to the production and development of new organic semiconducting materials (Covion, Dupont Olight, Universal Display Corporation). Organic electronic devices as multicolor automobile stereo displays (Pioneer MEH-P9000) or single OLEDs (Philips shaver 8894XL) appeared in the market during the last decade. Nowadays, organic materials are being used as full-color displays in devices such as digital cameras (Kodak EasyShare LS633) or mobile phones to achieve sharp images that are visible from any angle.

Apart from the enormous tuning possibilities of organic compounds, these materials present many other advantages against their inorganic counterparts. Organic materials, due to the weak intermolecular interactions (van der Waals type) that held the molecules together, are tough, and can be used to construct new flexible electronic devices. They are also excellent candidates for the production of large-area full-color displays at low-cost using organic light-emitting devices (OLEDs), which may eventually replace liquid crystal displays and even the standard cathode ray tube of our traditional home televisions. Organic circuits fabricated by printing techniques have been proposed for smart cards which carry product or

personal information, applications in which low-cost rather than high-performance is required [35, 36].

The semiconducting properties of molecular materials can be explained from the covalent bonding between carbon atoms [4]. The electronic configuration of carbon is $1s^2\ 2s^2\ 2p^2$. In an organic molecule simple, double, and triple bonds can be formed between adjacent carbon atoms. Thus, in the benzene (C_6H_6) molecule shown in Figure 2.1 each carbon atom forms sp^2 *σ-bonds* with its neighboring carbon atoms and with one hydrogen atom. It also forms a *π-orbital* perpendicular to the molecular plane.

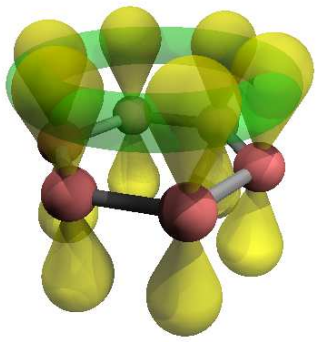

Figure 2.1: Schematic representation of the π-orbitals in the benzene (C_6H_6) molecule, responsible of its semiconducting properties. In the solid, the overlap between π-orbitals of adjacent molecules will allow the charge transport through the solid.

The interactions in a double bond split the energy levels into a bonding and an anti-bonding molecular π-orbital (see Figure 2.2). The two electrons occupy the former larger binding energy orbital or highest occupied molecular orbital (HOMO), while the latter remains empty and is called the lowest unoccupied molecular orbital (LUMO). Optical or thermal excitation can promote an electron to an unoccupied level. For larger molecules further splitting occurs, and finally electronic bands are formed. Intermolecular interactions in the solid lead also to additional splitting. However, band formation is not sufficient for the organic materials to behave as semiconductors, there must be a mechanism of charge carrier transport between molecules. This is achieved due to the overlap of the

π-orbitals from one molecule with those of its neighboring molecules. Therefore a close packing of the molecules and a crystalline structure free of defects is essential to maximize the π-orbitals overlap and thus improve the conduction properties of the material. The low molecular symmetry leads to highly anisotropic conduction parameters since the effective path for charge carrier transport is perpendicular to the molecular plane, direction of maximum π-overlap [33]. Thus, parameters as the charge carrier mobility must be described by a *mobility tensor* μ_{ij} [37]. In general, all the physical properties of these materials may present anisotropic behavior due to the low symmetry of the molecular constituents and the low-symmetric crystalline structures they form.

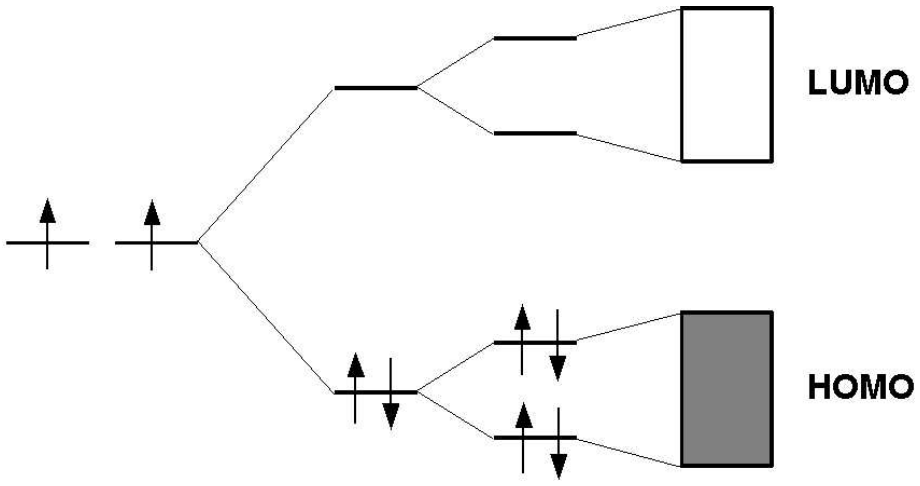

Figure 2.2: Schematic view of the splitting of the energy levels due to the interactions in the π-orbitals of a molecule leads to the formation of the HOMO and LUMO energy bands. Molecular interactions in the solid lead to further splitting of the molecular orbitals.

2.2 Organic semiconducting thin films

The complexity and anisotropy of the structure of those materials, involving many atoms covalently bonded forming the molecular unit, and van der Waals type forces holding the molecules together in the crystal, complicates their processing as well as the study of their properties [4, 38]. For the fabrication of electronic devices such as OLEDs [39, 40], organic field effect transistors (OFETs) [41] or solar cells [7, 8, 42], organic materials deposited as thin films need to be produced.

However, the growth of ordered structures in organic thin films has shown many difficulties related to the nature of these materials [11, 12]. In contrast to conventional inorganic semiconductors thin film growth, where the ad-molecules are usually single atoms with spherical symmetry, for organics each ad-molecule can involve more than 50 atoms, covalently bonded forming a unit with very low symmetry. The dimensions of these molecular units are in the nanometer scale, and thus, deposition on inorganic substrates presents lattice mismatches of one order of magnitude [13]. This situation may lead to the appearance of several energetically equivalent translational domains of the overgrown film. In addition, the complex crystalline structures formed as the molecules crystallize also contribute to the formation of equivalent translational and rotational domains [17]. The interaction with the substrate plays an important role in the final structure of the organic layer. In particular, the balance between the molecule-molecule and molecule-substrate interactions may lead to completely different growth scenarios. Low-interacting substrates promote molecular diffusion and thus in some cases well-ordered films can be formed. On the other side, strong-interacting substrates usually limit the surface mobility during film formation, leading to a high density of grains. In general, the interactions between the organic layer and the substrate are van der Waals type, and therefore *physisorption* occurs. However, in the extreme case of a highly reactive surface *chemisorption* may take place, and the adsorbed molecules may even dissociate. The interaction with the substrate is crucial also in the final morphology of the layer. Finally, the formation of films with several coexisting polymorphic forms is frequently found in organic thin film growth.

Thus, many structural imperfections as azimuthal disorder, formation of multiple domains, grain boundaries, dewetted morphologies, and also the tendency to polymorphism have to be overcome by appropriately selecting all the parameters that influence the growth of the layers [43]. Those concern not only the growth conditions (as substrate temperature, thickness, and growth rate), but also the reactiveness, morphology, and symmetry of the substrate surface. In addition, in organic heterostructures, needed in many applications as OLEDs or organic solar cells, other issues related with the complex organic-organic interface may appear. These can involve interdiffusion at the interface, or organic on organic epitaxy.

2.3 Phthalocyanines

The word *phthalocyanine* comes from the combination of two Greek terms which perfectly define the colorful properties of this material, these are na*phtha* (rockoil) and *cyanide* (dark blue). This material is a blue dye known for many years. The first phthalocyanine was produced accidentally in 1907, when Braun and Tcherniac observed the precipitation of a highly insoluble product on heating an alcoholic solution of a benzamide [44]. Linstead and coworkers determined in the 1930s the molecular structure of the phthalocyanines [45], and showed that the different phthalocyanine derivatives known fitted in the molecular scheme shown in Figure 2.3. The parent compound, hydrogenated phthalocyanine, with chemical formula $C_{32}H_{18}N_8$, has 2 hydrogen atoms in the center of the ring, and 16 surrounding the molecule. Later on, Robertson determined the crystal structure of several phthalocyanines by x-ray diffraction measurements [46–48].

Phthalocyanines were also involved in the origin of the interest on the semiconducting properties of organic solids in 1948, when Eley and Vartanyan studied their conductivity. Nowadays, they are one of the best studied systems in organic chemistry, and several text books devoted exclusively to their chemistry and physical properties have been published [49, 50].

Phthalocyanines and particularly metallo-phthalocyanines [42] (where the two central hydrogen atoms have been substituted by a metallic atom) present very interesting properties which make them an excellent example to illustrate the advantages organic materials offer. Phthalocyanines are easily sublimed and can be crystallized with an exceptional purity. They are highly stable and do not show degradation up to temperatures above 400°C. They are not affected by strong acids or bases [50]. Phthalocyanines show very interesting optical properties. The conjugated π-system, containing 18 electrons in the macrocyclic ring, leads to very intense absorption bands in the visible [49]. Their bluish colorful appearance arises from the presence of a strong absorption band at the red end of the visible spectrum, near 670 nm.

Several thousands of tons of phthalocyanine are produced every year. Due to their intense coloring properties, they are used as pigments in many industrial paints (as car paintings) or in inks for color laser printers, they are also used as the data storage layer of many CD's we use every day [51]. Their sensitivity to ambient gases has been used in the construction of gas detectors, which are based on the

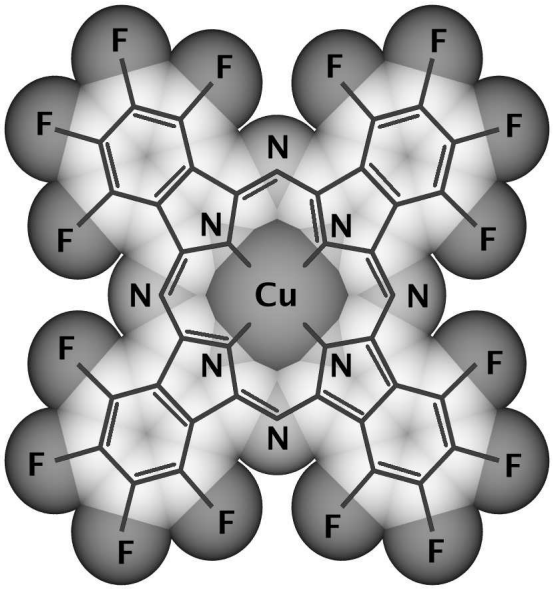

Figure 2.3: Schematic representation of the molecular structure of $F_{16}CuPc$ with chemical formula $C_{32}F_{16}N_8Cu$. Other phthalocyanine derivatives have similar structures. The parent compound has 16 hydrogen surrounding the molecule and two hydrogen atoms in the center.

change of conductivity of the material upon gas absorption [52]. They are a very versatile system, more than 70 different phthalocyanines have been synthesized only by changing the central atom. Phthalocyanines containing in the center of the ring the different atom species highlighted in the periodic table of Figure 2.4 have been produced [49]. The replacement of the central atom slightly modifies the electronic properties of the material [50, 53], while its molecular structure is, in most cases, unchanged.

Among all phthalocyanine derivatives, copper-phthalocyanine (CuPc) is one of the most studied derivatives, and was one of the first metallo-phthalocyanines to be synthesized in 1927. The compound used in this work is *copper hexadecafluorophthalocyanine* ($F_{16}CuPc$), in which the 16 hydrogen atoms surrounding the molecule have been substituted by fluorine, having thus a molecular weight of $M = 863.9$ g/mol. While CuPc is a *p*-type organic semiconductor, $F_{16}CuPc$

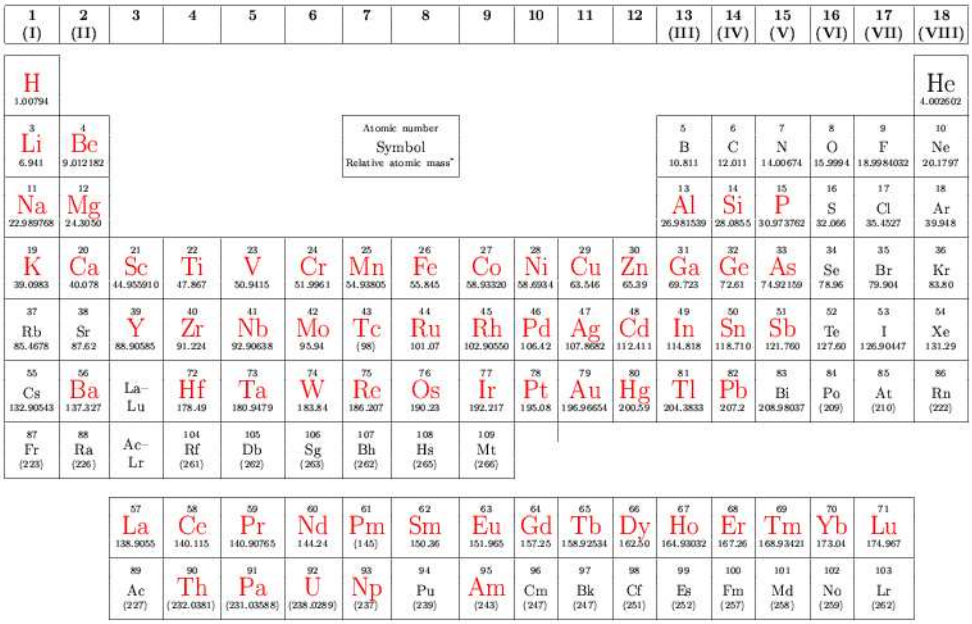

Figure 2.4: More than 70 different phthalocyanines have been synthesized only by changing the central atom. Apart from the parent compound ($C_{32}H_{18}N_8$), having two hydrogen atoms in the center, phthalocyanines having in the center of the ring the highlighted atoms in the periodic table (more than 70) have been synthesized.

becomes *n*-type upon fluorination. This is an excellent example of how the modification of the molecular structure can change the properties of the material. In fact, F_{16}CuPc is one of the most stable *n*-type organic semiconductors known at present, and it has been used to construct the first *n*-channel organic transistor [54], in complementary logic organic circuits [35, 55, 56], and also in paper-like electronic displays [36].

The first study of the structure of several phthalocyanines was reported by Robertson in 1935 [46]. Monoclinic structures with the space group $P2_1/a$ (C_{2h}^5 or 14:*b*3) were reported for the metal-free, nickel-, copper- and platinum derivatives, with two molecules per unit cell in all cases. The results on the metal-free compound were confirmed recently by Matsumoto [57]. A more detailed study was

published on the copper derivative by Brown [58], who obtained similar results for the cell parameters. The values reported are shown in Table 2.1. CuPc and other phthalocyanines crystallize forming long and narrow needles (up to 1 cm length but only 0.1 cm × 0.01 cm wide). The long axis of the needle coincides with the *b*-axis of the monoclinic structure [46, 58]. In Figure 2.5 the packing of the molecules in the unit cell of β-CuPc is shown. Figure 2.5(a) shows the packing on the *ac*-plane of the crystal, while Figure 2.5(b) shows the *ab*-plane.

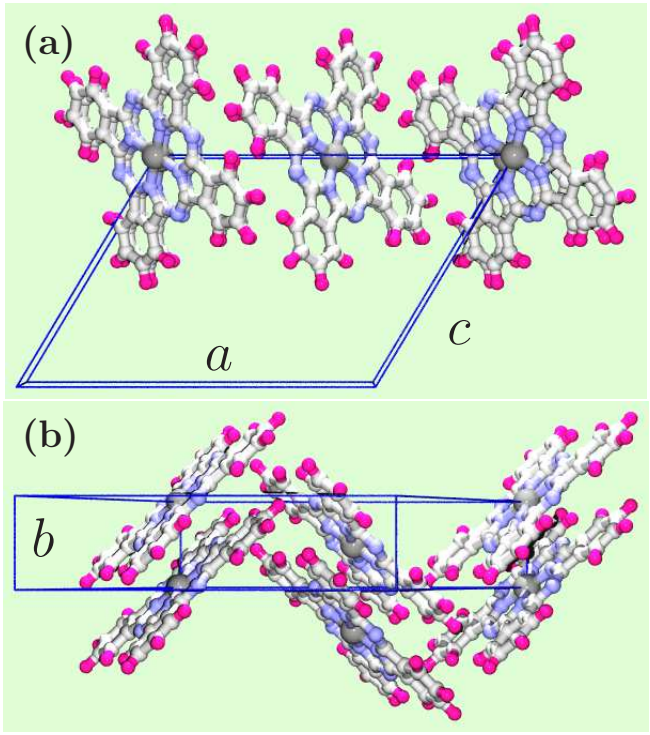

Figure 2.5: Packing of the molecules in the β-CuPc structure reported by Robertson [46]. (a) Projection on the *ac*-plane and (b) projection on the *ab*-plane, where the unique monoclinic *b*-axis points in the viewing direction in (a) and is aligned vertically in (b).

In thin films of various phthalocyanines, two structural phases have been reported, a metastable α and a stable β forms [59]. The growth of the α-form is obtained in thin films when the substrate temperature is maintained below a phase

	H_2Pc [46]	H_2 Pc [57]	β-CuPc [46]	β-CuPc [58]	F_{16}CuPc [62]
M	514.55	514.55	575.67	575.67	863.9
Space group	$P2_1/a$	$P2_1/a$	$P2_1/a$	$P2_1/a$	$P2_1/a$
a (Å)	19.85	19.870	19.6	19.407	20.018
b (Å)	4.72	4.731	4.79	4.79	5.106
c (Å)	14.8	14.813	14.6	14.628	15.326
β	122.25°	121.98°	120.60°	120.56°	111.83°
U (Å^3)	1173	1181	1180	1166	1454
Z	2	2	2	2	2

Table 2.1: Cell parameters reported for metal-free and copper-phthalocyanine by Robertson [46], Brown [58], and Matsumoto [57]. In the last column we show also the unit cell parameters of the compound F_{16}CuPc, derived from powder diffraction measurements (Appendix B).

transition temperature during growth [60]. Irreversible phase transformations can be induced by a thermal treatment [61]. Other polymorphic structures of CuPc as γ-, δ-, and χ-modifications have been also reported [42].

The crystal structure of F_{16}CuPc does not appear in the literature. However, its powder spectrum shows similar lines to that of the CuPc. From the powder spectra the unit cell constants shown in the last column of Table 2.1 can be derived [62], details on this study can be found in Appendix B. A similar crystal structure to that of the CuPc with an expanded unit cell is obtained. The larger values of the unit cell parameters can be related to the substitution of the hydrogen atoms surrounding the molecule by fluorine.

2.4 Diindenoperylene

The second organic molecule studied in this work is *diindenoperylene* (DIP), also referred as periflanthene. The molecular structure of DIP is shown in Figure 2.6. It is also a planar molecule, formed by a perylene core with two indeno groups, with chemical formula $C_{32}H_{16}$. Its molecular weight is 400.48 g/mol and has a sublimation point above 350°C in vacuum. Its molecular dimensions are 18.4 Å along the long axis and 7 Å along the short axis calculated according to the *Cambridge crystallographic database* [63]. It is a red dye first synthesized in 1934 by Braun [64]. Its molecular structure is a bit simpler than that of F_{16}CuPc since

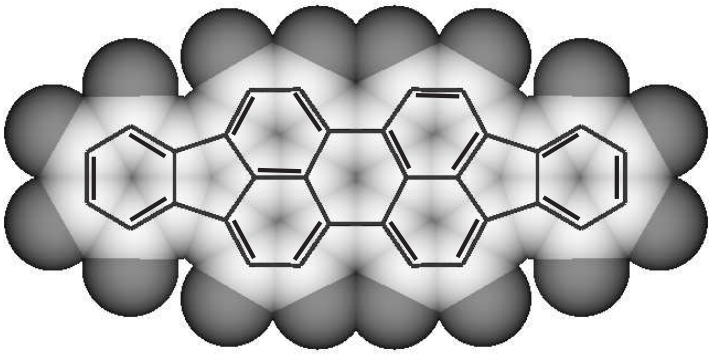

Figure 2.6: Schematic view of the molecular structure of a DIP molecule with chemical formula $C_{32}H_{16}$.

it only contains carbon and hydrogen, and a total of 48 atoms, against the 57 atoms that conform the F_{16}CuPc molecule. However, the molecular symmetry is lower in DIP, which has D_{2h} symmetry.

In contrast to the huge amount of published work on phthalocyanines, there are very few studies on DIP available. Besides the published reports on its synthesis [64, 65], it was not until 1951 that several studies reporting powder diffraction measurements on DIP appeared [66–68]. However, the bulk crystal structure of DIP was not known until recently when Pflaum *et al.* determined a triclinic structure by x-ray diffraction measurements on DIP single crystals [69]. Nevertheless, other crystalline structures have been reported from studies of thin films of DIP on several substrates, which differ from its bulk structure [70]. The reported unit cell parameters are summarized in Table 2.2. Thus, the DIP crystal structure of DIP thin films is not yet well-established. From the reported studies it is apparent that it differs from the bulk phase. Recently, detailed studies on the structure [71] and the conduction properties [63] of DIP thin films on SiO_2 appeared. It was shown that three different structural phases can be observed in thin films. A first structure is obtained when the films are evaporated in UHV at a substrate temperature of $\leq 160°C$. The two other phases can be induced by annealing the layers at temperatures above 160 and 200°C [71]. In both cases the structural

	Pflaum,Frey & Karl Single crystal	Hoshino *et al.* DIP/NaCl	Hoshino *et al.* DIP/Perylene
	Triclinic	Monoclinic	Monoclinic
a (Å)	11.59	8.67	11.0
b (Å)	12.97	6.96	10.6
c (Å)	14.88	18.55	17.5
α	98.11°	90.0°	90.0°
β	98.10°	93.5°	106.0°
γ	114.53°	90.0°	90.0°
Z	4	2	2

Table 2.2: Several DIP crystal structures determined on single crystals and thin films. The triclinic structure has been determined in DIP single crystals by Pflaum *et al.*, with four molecules per unit cell and $P\bar{1}$ symmetry [69]. Different crystalline structures in thin films with monoclinic symmetry have been reported by Hoshino [70].

modifications are irreversible, and thus the changes are maintained when the temperature is lowered again. At temperatures above 160°C desorption of the DIP layers starts [71].

DIP thin films have shown very interesting conduction properties, which have been related to the high structural definition (particularly to the low mosaicity measured by x-ray diffraction) of the layers [63]. Very interesting structural results have been recently reported [71] for DIP layers on oxidized silicon wafers. It has been shown that highly ordered films can be obtained, with mosaicities narrower than 0.01° as probed by x-ray diffraction. The high degree of order of those organic layers was also observed by cross-sectional TEM (transmission electron microscopy) measurements, which allowed the resolution of individual molecular monolayers [72]. Despite the good structural quality of the layers, it has been shown that their roughness increases rapidly with thickness [73]. DIP has been also used in studies of the metal-organic interfaces. Particularly in the study of the thermal stability of Au contacts on DIP layers [74], and DIP thin films on polycrystalline Au [75]. DIP has been also used to determine the effects induced in the organic films by the deposition of insulating layers of aluminum oxide on the organic layer [76].

The exceptional degree of order found in DIP thin films on oxidized silicon has been one of the main reasons to choose this material in the present work. Moreover, DIP is a *p-type* organic semiconductor, and thus complementary to the other organic compound studied here, F_{16}CuPc. As we already mentioned, phthalocyanines and DIP have been already combined in the construction of organic solar cells [27].

Chapter 3

Organic Molecular Beam Epitaxy

In this chapter we introduce the deposition technique of *molecular beam epitaxy* (MBE) used for the growth of the organic thin films studied in this work. MBE is a technique used for the production of high-purity layers based on the evaporation of material in a ultra-high vacuum (UHV) environment. Heated sources produce the molecular or atomic beams that react with the substrate surface, which is maintained at a desired temperature. Compared to other evaporation techniques, MBE offers a higher level of control on the growth conditions, especially on the beam fluxes. Growth rates below 1 ML/min can be easily achieved by control of the temperature of the evaporation sources. The use of beam blocking shutters allows the deposition of complex heterostructures with sharp interfaces. In addition, the UHV conditions provide an environment free of contaminants.

The contents of this chapter are organized as follows. In Section 3.1 the general concepts of the MBE technique are introduced and the advantages it offers against other evaporation techniques are discussed. Specific issues related with the application of MBE in the growth of organic layers are also emphasized in Section 3.1. In Section 3.2 some general aspects of thin film growth relevant in this study are addressed. In Section 3.3 the different parts of the UHV equipment used in this work are described. Finally, in Section 3.4 the main characteristics of the substrates used, as well as their preparation procedure are explained.

3.1 MBE and OMBE

MBE is a technique used for the epitaxial growth of materials. It is based on the reaction between a molecular or atomic beam and a substrate maintained at the desired temperature (T_g) under UHV conditions [77]. The molecular beams are usually generated at sources as *Knudsen cells* or electron beam evaporators, where the constituent materials are evaporated.

MBE was first used in the late 1960s in the growth of GaAs layers and it has been successfully applied in the epitaxial growth of many inorganic semiconductors as well as in the growth of metal or insulating layers. MBE presents several advantages against other epitaxial growth techniques. Due to the UHV environment in which the growth is realized, epitaxial layers with an extremely high purity can be obtained. In addition, this technique offers a high degree of control on the growth parameters. The beam fluxes can be precisely controlled by the temperature of the source. The molecular beams can be individually blocked by beam shutters, and therefore complex heterostructures with atomically sharp interfaces can be produced [78]. Very low rates can be achieved by controlling the temperature of the source. The high control over the beam flux allows the reproducible deposition of layers at the submonolayer regime and the "in-situ" study of the growth process at a processable time-scale. Moreover, the UHV environment admit the use of characterization techniques as electron diffraction (LEED and RHEED) or Auger electron spectroscopy, techniques which are useful not only for the characterization of the overgrown films, but also for the control of the substrate surface before deposition, and for growth-monitoring.

The application of MBE in the growth of organic materials has been an important advance for the controlled growth of high-purity organic layers [14]. The first reported study of the MBE growth of an organic compound was by Hara *et al.* in 1989 [79]. They reported the growth of CuPc layers on MoS_2. After this early work many reports and reviews on the application of MBE in organic thin film growth appeared [13, 15, 80], and the technique was referred to as *organic molecular beam epitaxy* (OMBE). The term *organic molecular beam deposition* (OMBD) became more frequently used since epitaxy of organic thin films on inorganic substrates, with an epitaxial relation between the lattices of the deposited layer and the substrate, does not always occur. OMBD can be applied to "small molecules" which can be sublimated under UHV conditions. The evaporation sources used for

organic materials are normally Knudsen cells. The low sublimation temperatures of organic materials (usually between 100 and 500°C) simplifies the design of the sources.

The main differences between inorganic and organic MBE originate from the distinct nature of the molecular constituents. While in inorganic MBE the units are frequently single atoms, in OMBD complex molecules are used. These molecules are extended objects with very low symmetry [11, 16]. As we briefly addressed in Chapter 2, the dimensions of the molecules and the unit cells in which they crystallize are larger than the inorganic substrates, and their symmetry is lower. This large lattice mismatch between substrate and organic layer leads to several possible translational and orientational domains of the organic lattice on the substrate.

A second important difference between inorganic and organic MBE is the weaker interactions involved in the growth process of organic materials. The molecule-molecule as well as molecule-substrate interactions are usually van der Waals type. The term *van der Waals epitaxy* has been used to refer to epitaxial organic thin films [80] on low-interacting surfaces. Also, the usual temperatures involved in OMBE are lower than in inorganic MBE due to the weaker character of these van der Waals forces [11].

Despite the last developments in the growth of ordered organic layers [81], there are still many problems which have to be solved before we can profit of all the interesting properties of organic semiconductors [12]. Probably one of the most attracting properties of these materials is their intrinsic anisotropy [82, 83]. However, due to structural disorder, thin films of those materials present commonly isotropic properties [84]. OMBD offers the path for the optimum control of the growth conditions in a clean environment free of contaminants [11, 81]. The understanding of the influence of the substrate surface, and in particular its reactiveness and morphology, on the growth of the organic layer is crucial to achieve control on the growth process.

3.2 Thin Film growth

The process of thin film growth takes place at the substrate surface, where the incident molecular beam interacts with the atoms on the surface and crystallization

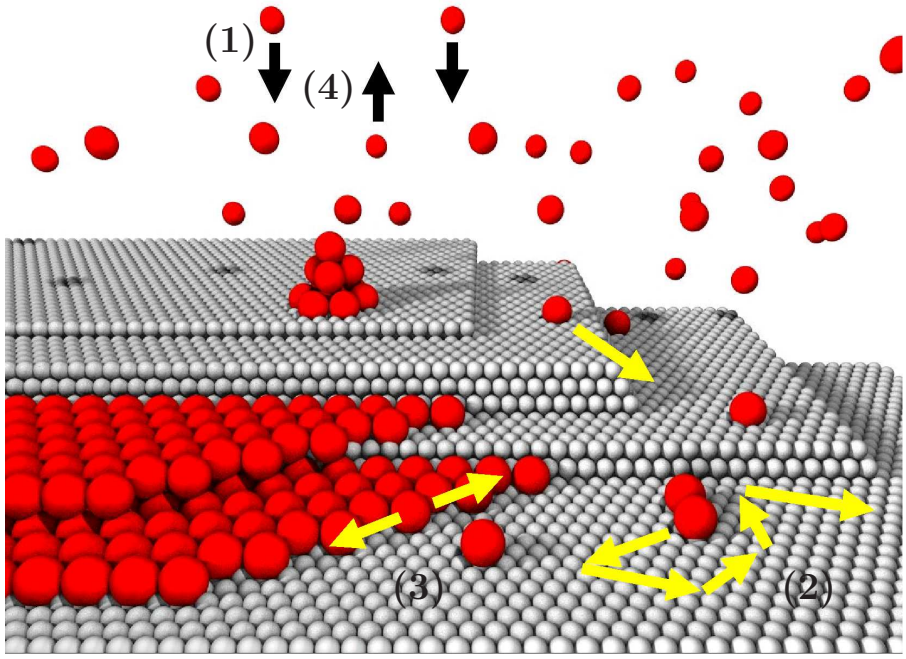

Figure 3.1: Surface processes occurring during film formation in MBE. (1) adsorption, (2) surface migration, (3) incorporation,and (4) desorption. Figure taken from reference [18].

of the impinging molecules occur. This situation is illustrated in Figure 3.1. Several surface processes are involved in the growth, the most important, exemplified in Figure 3.1 are

- *adsorption* of the impinging molecules on the surface,
- *migration* and *dissociation* of the molecules along the surface,
- *incorporation* of the molecules in crystal sites of the substrate or of the overgrowing layer,
- *desorption*.

Thus, when a molecule hits the surface, it can migrate before it finds an incorporation site or it can meet a second molecule to form a dimmer. This dimmer can dissociate or can increase its size by the incorporation of other molecules. Finally, non-incorporated molecules will desorb thermally.

All these kinetic processes are quantitatively described by several growth parameters. First of all, the *molecular flux* F_i describes the number of molecules of the constituent i impinging on the substrate surface. This flux is determined by the source temperature T_i. T_i also determines the energy of the molecules arriving on the surface, which is maintained at a temperature T_g ($T_g < T_i$). The fraction of molecules which are incorporated, will interact with the substrate until thermodynamic equilibrium is reached at the temperature T_g. The molecules which are not incorporated, and therefore are desorbed, will leave the surface with an energy corresponding to the temperature T_e. We can now define an *accommodation coefficient* as

$$a = \frac{T_i - T_e}{T_i - T_g} \tag{3.1}$$

which is a measure of the level of thermal equilibrium reached by the arriving atoms with the substrate. Thus, $a = 1$ when $T_e = T_g$. A second parameter frequently used is the *sticking coefficient* (also referred as condensation coefficient) of the molecules as

$$s = \frac{N_{ad}}{N_{tot}} \tag{3.2}$$

where N_{ad} is the number of adsorbed molecules and N_{tot} is the number of molecules arriving on the surface. Thus, s is the probability that one atom or molecule impinging on the surface sticks. For high substrate temperatures, the sticking coefficient may have very low values, and even $s = 0$ for sufficiently high T_g. However, all the arriving atoms can be accommodated on the surface, and therefore $a = 1$, and then gain sufficient energy to leave the substrate.

The adsorption of a molecule on a surface is usually described by a two step process. First, *physisorption* takes place, where the involved attracting forces are van der Waals type. The second step is *chemisorption*, in which electron transfer occurs. Usually two sticking coefficients are defined, one for each type of adsorption. For the molecules and substrates used in this study, only physisorption of the adsorbates takes place. However, due to the distinct nature of the inorganic substrate and the organic layer, different sticking coefficients have to be defined for the first deposited organic monolayer (organic on inorganic sticking coefficient, s_{o-i}) and for the subsequent deposited material (organic on organic sticking coefficient, s_{o-o}).

The interaction of the film with the substrate may also lead to different morphologies of the overgrown layer. There are three possible *growth modes* of a crystal on a surface [85] depicted in Figure 3.2. In Frank-van der Merwe growth or layer-by-layer growth (Figure 3.2(a)), the first atoms or molecules on the surface form a closed monolayer on the substrate before the second monolayer starts to nucleate. The subsequent layers continue with the same behavior. The growth mode illustrated in Figure 3.2(b) is called Stranski-Krastanov or layer plus island. In this case the early stages of the growth are similar to the layer-by-layer, since the first monolayers are closed. However, once a certain *critical thickness* is reached, islands are formed on top of these first closed layers. Finally, in the third growth mode (Figure 3.2(b)), called Volmer-Weber or island growth, small clusters nucleate on the substrate surface and grow forming islands.

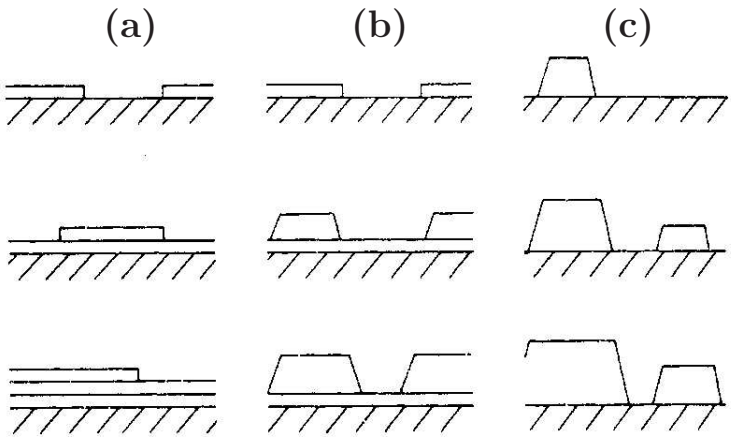

Figure 3.2: Schematic representation of the growth of a layer in (a) Frank-van der Merwe (layer-by-layer), (b) Stranski-Krastanov (layer plus islands), and (c) Volmer-Weber (island) the different growth modes. Extracted from reference [85].

In general, layer-by-layer growth takes place when the interaction of the ad-molecules with the substrate is stronger than the interaction between ad-molecules. Island growth is found in the opposite case, that is, when the interaction between ad-molecules predominates. Finally, the intermediate case, layer plus island growth, can be originated by several reasons. For instance, in situations where the lattice parameter or molecular orientation of the first monolayers can not be continued into the bulk crystal, and favors subsequent island formation [85].

3.3 UHV system

The UHV system used in this study for the deposition of the organic layers is a commercial Omicron system composed of three chambers. An schematic view of the system is shown in Figure 3.3. A small fast entry load-lock chamber allows the introduction and extraction of samples without breaking the vacuum of the main chambers. This chamber is provided with a sample storage stage, which is equipped with a heating station. This station has a ceramic heater for temperatures up to 500°C, and four additional positions for sample storage. This heating station is specially useful for the outgassing of the substrates before introduction to the MBE system, thus unnecessary contamination of the growth chamber is avoided. A transfer rod allows the transportation of samples from this chamber into the MBE deposition section.

The MBE chamber is equipped with four Knudsen cells for the evaporation of

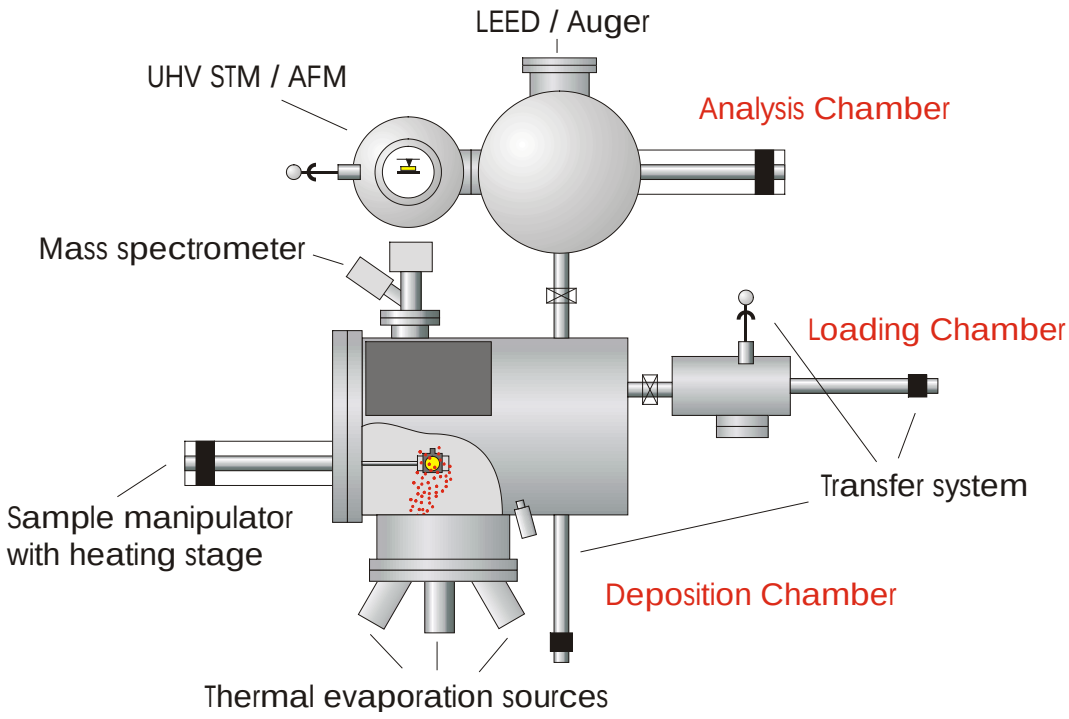

Figure 3.3: Schematic top view of the UHV system used for the evaporation of the organic layers. The system is composed by a growth chamber, an analysis chamber and a fast entry load-lock chamber. A transfer system allows the transportation of samples between the different chambers without breaking the vacuum (from reference [18]).

materials and a quadrupole mass spectrometer (QMS) which can measure up to 1000 a.u. and thus detect the presence not only of the residual gases but also of the molecular materials evaporated from the Knudsen cells. The base pressure of this section of the system is about 5×10^{-10} mbar. During growth the deposition rate and thickness are monitored using a quartz crystal microbalance (QCM). On the sample manipulator of this chamber the sample can be heated up to 800°C, or cooled down by using liquid-nitrogen. The pressure during growth can be further reduced by using a liquid-nitrogen cooled cryo-shroud.

In the analysis chamber, an AFM system (AFM/STM Omicron system) allows the *in-situ* surface characterization of the films. The samples can be transferred from the growth stage to the AFM without breaking the vacuum. Also in the analysis chamber LEED and Auger spectroscopy can be performed. The sample can also be heated up to 800°C in this chamber. The base pressure of this section is 5×10^{-11} mbar.

The system is pumped by a turbo-molecular pump which can be used to pump separately the three chambers, two ion-pumps (one in the MBE and one in the analysis chamber) and two titanium sublimation pumps complete the vacuum generation system.

3.4 Substrates used

As substrates for the deposition of the organic layers, three different oxides have been used, i.e., oxidized silicon wafers, single-crystalline Al_2O_3 (sapphire), and MgO. Since all three substrates are oxides, their interaction with the molecules is van der Waals type and therefore no chemical reaction is expected. However, as described below, their surface is very different due to their different crystalline structure, with considerably different morphologies.

Oxidized silicon substrates were chosen as substrates since they are well-known and widely used in the growth of thin films, they can be easily cleaned and present an atomically flat surface. Si(100) with native oxide ($\sim$ 3 nm) was used. In contrast to the highly reacting clean silicon surface, where diffusion of the ad-molecules is blocked, the oxide layer allows the migration of molecules thus favoring the formation of well-ordered films. Moreover, oxidized silicon is technologically interesting since the oxide layer serves as the insulating layer between the Si substrate and the organic film, thus, the substrate can be used as the gate for the

construction of an organic transistor.

Al_2O_3 single crystalline substrates are obtained in a highly pure form (*corundum* and *sapphire*) and its crystalline structure [86] and surface [87] are well-characterized. Although Al_2O_3 is rhombohedral, it is commonly described in terms of hexagonal Miller-Bravais indices [88]. For details on the crystal structure and morphology of the Al_2O_3 substrates we refer to Appendix A.

The sapphire substrates used in this study are A-plane oriented, or Al_2O_3 $(11\bar{2}0)$. In this orientation, the *c-axis* of the substrate is in the surface plane, and thus is a two-fold symmetry surface having a rectangular unit cell on the plane. The surface of the as obtained substrates has been mechanically polished. After this polishment procedure it is disordered and presents roughnesses around 2-5 nm. An annealing treatment can be used to reorganize the surface and obtain an atomically flat substrate. Thus, before introduction in the UHV chamber, the substrates are annealed in air at temperatures above 1000°C. After this annealing treatment the surface is characterized by the formation of atomically flat terraces that correspond to the $(11\bar{2}0)$ low-index plane. The terraces appear to account for the small misalignment between the physical surface and the crystallographic A-plane. The magnitude and orientation angles between these two surfaces, the so called *miscut angle*, can be easily determined with high accuracy by x-ray diffraction measurements. The magnitude and orientation of the miscut, together with the temperature and duration of the annealing process, will determine the morphology of the substrate. In Appendix A we give further details and examples of the morphologies obtained under different conditions.

In Figure 3.4 an AFM image of the surface of the substrate before growth is shown. In this case, the substrate has a miscut of 0.26° and an orientation of 49° from the *c*-axis. The annealing treatment was performed at 1400°C during 15 hours. This lead to terraces of 130 nm wide and 1.8 nm step height. The surface of the terraces is atomically flat, and is the plane $(11\bar{2}0)$ or A-plane of the Al_2O_3.

Finally, MgO (100) substrates have also been used in this study. MgO has a cubic bulk structure with $a = 4.203$ Å. The morphology of the substrates used is shown in Figure 3.5. As can be seen in this AFM image, the surface exhibits crystallites with cubic shape. The root mean square roughness derived from this

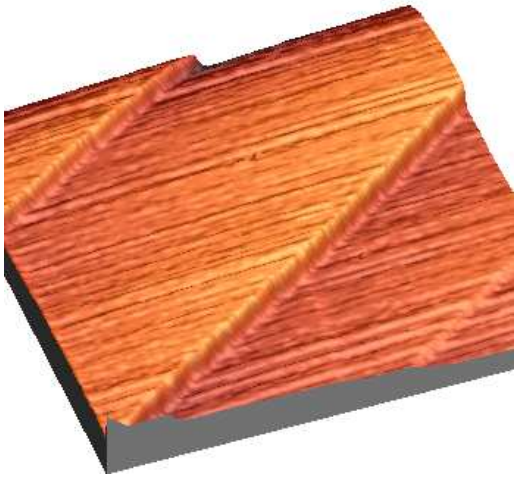

Figure 3.4: AFM image (1×1 μm) of the surface of the Al_2O_3 substrates before growth. The terrace surface corresponds to the $(11\bar{2}0)$ planes of the substrate. The step height is around 18 Å. The substrate has been annealed at 1500°C during 18 hours.

image is $\sigma_{rms} = 3$ nm and therefore relatively high compared to the other substrates used.

The cleaning procedure used to obtain a contamination-free surface of the different substrates used is as follows. SiO_2 substrates have been cleaned in ethanol and dried with a stream on nitrogen. Al_2O_3 and MgO have been cleaned by successive ultrasonic baths with organic solvents (acetone and ethanol). Prior to film growth, all the substrates have been kept at 750°C for at least 12 hours in UHV for outgassing. After these procedures the surface of all substrates is free of any contaminant as probed by AFM measurements performed just before deposition of the organic films.

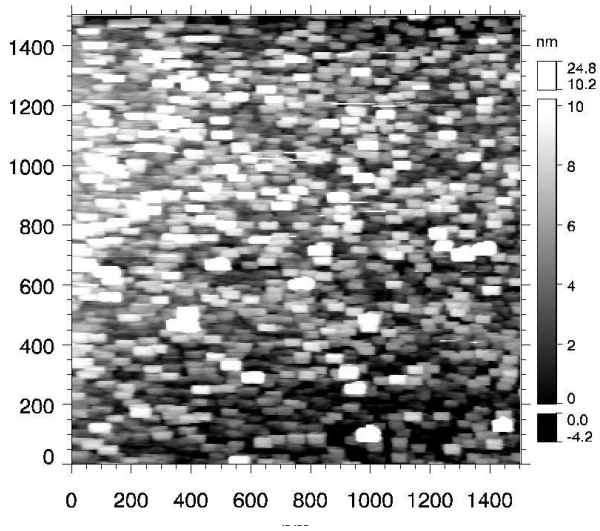

Figure 3.5: AFM image (1.5 × 1.5 μm) of the morphology of MgO(100) before growth.

Chapter 4

Experimental techniques

In the present chapter we describe the different techniques utilized to characterize structurally and optically the organic layers. The goal of this work is to determine the influence of the growth conditions in the structural properties of the layers and to establish their influence in the final optoelectronic properties of the organic films. This is only possible by the combination of techniques of different areas, which independently characterize the structural and optical properties of the films. Thus, this is a multitechnique study using several techniques which provide information on the morphology, the crystalline structure, and the optical response of the layers. The techniques used are atomic force microscopy, x-ray diffraction, spectroscopic ellipsometry and Raman scattering. The combination of all those different techniques allows a better understanding of the properties of the organic layers. While atomic force microscopy bears information on the morphology of the layers and on their in-plane structure at the nanometer to micrometer scale, x-ray diffraction probe the crystalline structure of the layers in a macroscopic scale. The comparison of the structural results obtained with these techniques with the Raman scattering data, permits a better understanding of the molecular packing and ordering in the layers. Furthermore, ellipsometric measurements allow the location of electronic transitions and the quantification of the anisotropy of the layers, which is related with the degree of structural order present. With the interdisciplinary nature of this work we aim to a better understanding of the interrelation between the structural and optical properties of the organic layers.

In Section 4.1 we present the details on the atomic force microscope used to characterize the morphology of the substrate used and also of the overgrown layer. In Section 4.2 the basic principles of x-ray scattering are presented together with the different geometries used for the structural characterization of the layers, and also the theoretical methods used to interpret the results. In Section 4.3, spectroscopic ellipsometry is introduced. In this section the experimental aspects of the measurement are presented. Finally, Section 4.4 introduces the Raman scattering technique.

4.1 Atomic force microscopy

4.1.1 Scanning Probe Microscopes

The invention of the scanning tunneling microscope (STM) in 1985 [89] and the *atomic force microscopy* (AFM) in 1986 [90] by Binnig *et al.*[1] redefined the concept of microscopy and gave rise to the new family of instruments known as scanned probe microscopes (SPMs). SPMs are instruments used in the study of the surface properties of materials at the atomic to micron level. Although all SPMs contain some common components, they can work in a still growing list of different modes which probe different properties of the surface. Thus, STM, the first instrument to atomically resolve real-space images of surfaces [89], is based on the measurement of a current that "tunnels" from a sharp conducting tip which probe the surface of a conducting sample. AFM has become one of the most popular SPMs. In an AFM, a very sharp tip of few microns long and often less than 10 nm in diameter is located at the free end of a cantilever. The cantilever deflection is measured as the tip is scanned over the sample (or the sample is scanned under the tip, as is the usual case). The measured deflection allows to generate a map of the surface topography. AFM measurements can be performed on conducting samples as well as on semiconductors and insulators. Other SPMs, as magnetic force microscope (MFM), scanning near-field optical microscopy (SNOM) are some examples of the many SPMs which use different interactions to probe different properties of the surface. AFM and STM are also used to modify the surface properties of the sample in nanolithography. These techniques can change the surface by modifying it atom by atom.

[1] Gerd Binnig and Heinrich Rohrer were awarded the Nobel prize in physics for the invention of the scanning tunneling microscope in 1986.

4.1.2 Design and operation of an AFM

Most of the SPMs use the same elements to control the sample and the tip, however we concentrate on the usual components of an AFM. Usually the sample is scanned under the tip driven by a piezoelectric material that changes its dimensions in response to an applied voltage. A segmented tube design allows movement in the xy-plane (surface plane) as well as in the z-axis (perpendicular to the surface). The deflection of the cantilever as the sample is scanned is usually detected by optical techniques. A laser beam reflected on the free end of the cantilever is focused on a position-sensitive photodetector (PSPD) by using one or more mirrors. This setup allows the precise detection of small vertical displacements of the cantilever (in the sub-ångström scale), as well as lateral deflection of the cantilever (using a four quadrant PSPD). All these components are shown in Figure 4.1. In addition, the associated electronics allow the control and alignment of the different parts of the instrument, while the measured data is acquired by a computer.

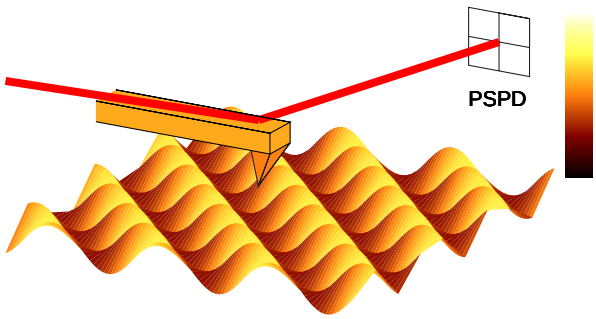

Figure 4.1: Schematic of a tip scanning a surface in an AFM. A laser beam reflected on the free end of the cantilever is focused on a four-quadrant PSPD. This allows the precise detection of small cantilever deflections.

AFM measurements can be performed in two different modes which differ on the distance between the tip and the surface of the sample. The cantilever deflection is due to the forces between the tip and the surface of the sample as their relative distance is changed. This interaction is described by the *van der Waals forces*

between tip and surface. The dependence of these forces on the distance tip-surface is shown qualitatively in Figure 4.2. As can be seen in this plot, as the tip approaches the surface, an attractive force is exerted on it while there is no "physical contact" between surfaces. This attraction between the atoms of both surfaces increases as their distance becomes smaller until their electron clouds are so close that begin to repel each other electrostatically. As the distance decreases the repulsion increases until the attractive and repulsive forces balance and the resulting van der Waals force is zero. At this point starts the "physical contact" between the tip and the surface of the sample. The two regions highlighted in the curve of Figure 4.2 define the regimes of the two modes commonly used in AFM, *contact* and *non-contact* modes.

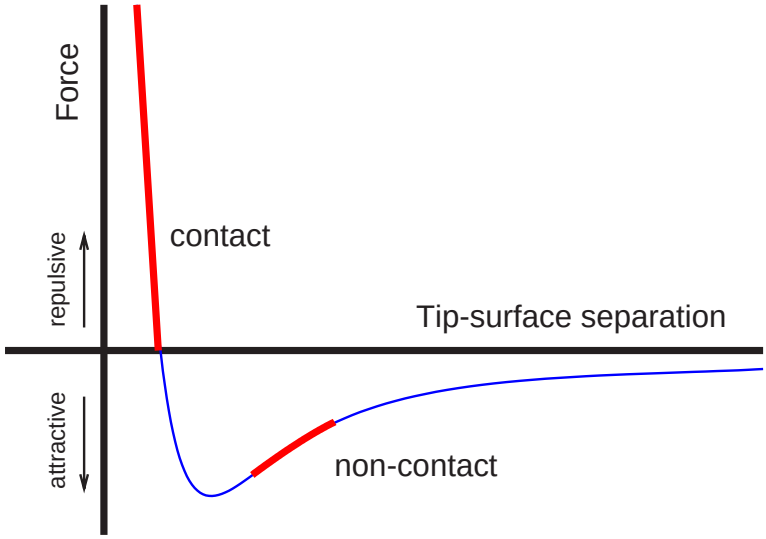

Figure 4.2: Interaction (van der Waals force) between the tip and the surface as a function of the distance between both surfaces. The highlighted regions are the regimes at which the contact and non-contact AFM work.

In contact-mode AFM, the topographical image of the surface can be derived from the deflection of the cantilever, in which case the measurement is performed at a constant height (z) of the sample (constant-height mode). It can also be derived, as is more frequent, from the variation of the height of the surface (controlled by the component z of the piezoelectric) needed to maintain a constant deflection of the cantilever. This is achieved by using the deflection of the cantilever as the input to a feedback circuit which moves the scanner back or forward until

the desired deflection is achieved. In this case the topographical image is derived from the motion of the scanner and the applied force on the sample surface is kept constant independently of the changes in height of the topography (constant-force mode). This mode is especially useful in tough samples where damage has to be avoided. The lateral deflection of the cantilever as the sample is scanned can be used to image changes of surface friction (which can arise from different materials on the surface) or from changes in the slope of the sample. Thus, the lateral deflection can be used to image different materials on the surface and also to obtain edge-enhanced effects on stepped surfaces.

In non-contact mode AFM the attractive force between the sample and the tip is probed. This attractive force is weaker than the forces involved in contact-AFM and less sensitive to height changes as can be seen from its smoother dependence on the distance in Figure 4.2. Therefore, a different detection mechanism must be employed. In this case, the cantilever is oscillated at a frequency close to its resonant frequency at a given amplitude. As the tip approaches the sample, differences in the frequency or the amplitude are detected. The feedback circuit restores then the original values by moving the sample forwards or backwards. From this feedback the topographical image of the surface is derived. Either the amplitude or the frequency can be used as the feedback parameter. Usually, amplitude modulation (AM) is used in measurements in ambient conditions while frequency modulation (FM) can be used in systems which work under UHV conditions.

AFM in non-contact mode is especially useful in tough samples where surface damage can be caused by the tip. It is also useful to detect the presence of condensed water on the surface. While in contact-AFM the tip penetrates the water layer, in non-contact measurements the tip detects the presence of the additional layer. However, non-contact measurements depend critically on the tip and cantilever used in the measurement, they are also very sensitive to building vibrations.

A slight modification of the non-contact AFM mode exists, in which the cantilever oscillates at its resonant frequency with a high amplitude. The tip enters in physical contact with the surface at each oscillation. Consequently, this mode of operation is known as *tapping mode*. The potential damage contact mode may cause is minimized in tapping mode, since it eliminates friction forces. On the

other hand, the involved forces are higher than in non-contact mode, and therefore the measurement is not so sensitive to the quality of the tip or external vibrations.

4.1.3 Experimental details

The AFM used in this work is a commercial room-temperature Omicron AFM/STM system. The AFM/STM stage is located in a UHV environment attached to the OMBE system (see Chapter 3 and Figure 3.3). The samples can be transferred from the different parts of the OMBE system into the AFM keeping it under UHV conditions during the transfer. This allows the surface characterization of the as-grown films immediately after deposition, avoiding thus, water condensation on the surface. The AFM can be operated in contact as well as in FM non-contact mode. The maximum scanning area is 5×5 μm.

In non-contact AFM measurements single-crystalline Si cantilevers were used, with frequencies from 269 to 311 kHz. The tip radii were typically around 10 nm. In contact mode measurements, rectangular cantilevers with normal spring constant of 0.1 or 0.01 N/m were used. In this case, the measurements were performed at very low load to avoid damage on the surface, while force vs. distance curves were taken at short intervals to correct tip shifts due to temperature oscillations.

4.2 X-ray diffraction

In contrast to AFM, x-ray diffraction experiments provide information in the reciprocal space. Moreover, the information obtained is not limited to the surface of the films but can probe the entire thickness of the layer. The illuminated area of the films is usually larger than few microns, and therefore the obtained information is an statistical average of a macroscopic volume. After more than 100 years of the discovery of x-rays by W.C. Röntgen in 1895 [2], x-ray diffraction is nowadays a well-established technique that, under different scattering geometries, allows the study of the structural properties of materials [91–93].

[2] W.C. Röntgen was awarded the first Nobel prize in physics in 1901 for the discovery of x-rays.

4.2.1 Optical constants for x-rays

Refraction and reflection of electromagnetic waves at interfaces are described by the *refractive index* n. In vacuum $n = 1$ and for visible light $n > 1$. X-rays are electromagnetic waves with wavelengths of the order of an ångström, and refraction at interfaces can be described by the refractive index, which for x-rays can be written as

$$n = 1 - \delta + i\beta \tag{4.1}$$

where δ and β are the *dispersive* and *dissipative* parts, which are related with the electron density of the medium, ρ_e, and the lineal absorption coefficient, μ, through

$$\begin{aligned} \delta &= \frac{\lambda^2}{2\pi} r_e \rho_e \\ \beta &= \frac{\lambda}{4\pi} \mu \end{aligned} \tag{4.2}$$

where λ is the wavelength of the radiation and r_e is the classical radius of the electron ($r_e = 2.8 \cdot 10^{-15}$ m). For solid materials δ is of the order of $10^{-5} - 10^{-6}$ and β takes even smaller values ($10^{-6} - 10^{-8}$).

From Equation (4.1) it is seen that n is smaller than unity for x-rays. This has several consequences in the propagation of x-rays, which differ from the behavior of visible light. First of all, the phase velocity of x-rays inside a medium with refractive index n is c/n and thus larger than the velocity of light c. A second effect is the phenomenon of *total external reflection*, which has important implications in x-ray experiments. The incident (α_i) and refracted (α_t) grazing angles at the interface of a medium with the vacuum (see Figure 4.3) are related through *Snell's law*

$$\cos \alpha_i = n \cos \alpha_t \tag{4.3}$$

since $n < 1$, below a certain value of the incident grazing angle total external reflection occurs. This incident angle is called the *critical angle* α_c, and is related with the refractive index through

$$\alpha_c = \sqrt{2\delta} \tag{4.4}$$

since δ takes values around 10^{-5}, the critical angle is of the order of few fractions of a degree. By using Equation (4.2) in this last expression it can be seen that the critical angle depends on the wavelength of the radiation and on the electron

density of the material ρ_e. In Figure 4.3 the *scattering vector* $\vec{q} = \vec{k}_i - \vec{k}_f$ of the process is plotted, where $\vec{k}_i$ and $\vec{k}_f$ are the incident and diffracted wave vectors respectively.

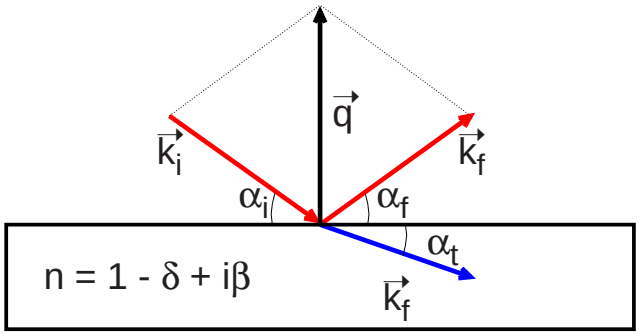

Figure 4.3: Refraction and reflection of x-rays at an interface between a medium with refractive index n and the vacuum. Since $n < 1$ for x-rays from Snell's law (Equation (4.3)) it follows that $\alpha_i > \alpha_t$, and therefore below the critical angle α_c total external reflection takes place.

4.2.2 X-ray reflectivity

From x-ray reflectivity studies information on the interface structure can be derived. In this case the specular condition $\alpha_i = \alpha_f$ is satisfied, and therefore $\vec{q} = q_z$ with $q_x = q_y = 0$. Here we have taken the z-axis perpendicularly to the interface, while x and y lie in its plane. The fact that the scattering vector has only z-component different from zero, implies that only structural information along this direction is derived from measurements performed in this geometry. In particular, the electron density profile along z, laterally averaged, is measured. This situation is depicted in Figure 4.4.

In an ideal flat and sharp interface, the reflectivity is described by the *Fresnel coefficients* r and t [94, 95]. It can be shown [93] that for $\alpha_i < \alpha_c$, and in absence of absorption, $|r|^2 = 1$ and therefore the reflected intensity is constant while total external reflection takes place. For $\alpha_i >> \alpha_c$ it is found that the intensity falls off according to $|r|^2 \simeq 1/\alpha_i^4$.

However, in real interfaces there is always a certain roughness, and therefore

the ideal Fresnel reflectivity has to be modified. The surface roughness is introduced in the modified Fresnel coefficients as

$$r_{real} = r_{ideal} \cdot e^{-2k_{iz}k_{fz}\sigma^2} \tag{4.5}$$

$$t_{real} = t_{ideal} \cdot e^{\frac{1}{2}(k_{fz}-k_{iz})^2\sigma^2} \tag{4.6}$$

therefore, the reflected intensity is lower in rough surfaces while transmission into the less dense medium is enhanced by roughness. Nevertheless, as it follows from Equation (4.5), $|r|^2 = 1$ for $\alpha_i < \alpha_c$ independently of the roughness of the surface.

4.2.3 Parrat formalism

In 1954 Parrat developed a recursive algorithm to calculate the x-ray reflectivity intensity of N layers on a substrate [96]. In this model, each layer j is described by a constant thickness D_j and refractive index n_j (or, equivalently, electron density ρ_j). The Fresnel coefficients of each interface, $r_{j,j+1}$ and $t_{j,j+1}$ are then individually calculated. The ratio between reflected and transmitted wave-amplitudes can be then calculated as

$$X_j = \frac{|r_j|^2}{|t_j|^2} = e^{-2ik_{z,j}z_j} \frac{r_{j,j+1} + X_{j+1}e^{2ik_{z,j+1}z_j}}{1 + r_{j,j+1} + X_{j+1}e^{2ik_{z,j+1}z_j}} \tag{4.7}$$

with the Fresnel coefficients

$$r_{j,j+1} = \frac{k_{z,j} - k_{z,j+1}}{k_{z,j} + k_{z,j+1}}. \tag{4.8}$$

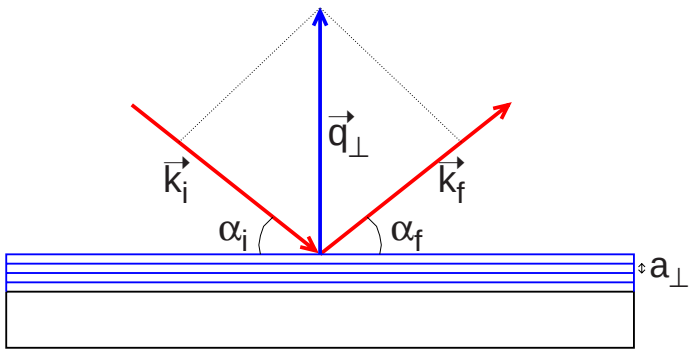

Figure 4.4: Reflection of an x-ray beam on a surface under specular conditions ($\alpha_i = \alpha_f$). In this case $\vec{q}$ is perpendicular to the surface, and therefore $\vec{q} = q_z$ with $q_x = q_y = 0$.

For a system of N layers on a substrate we will have $X_{N+1} = 0$ as a boundary condition, since there is no reflection from the bottom surface of the substrate. Then all other Xj are calculated recursively. It should be emphasized that the Parrat formalism is intrinsically dynamic since it considers multiple scattering effects.

Equation (4.7) is derived for the ideal interface case. However, surface roughness can be easily introduced in the algorithm by using r_{real} described by Equation (4.5).

4.2.4 Grazing incidence diffraction

As we have seen in Section 4.2.2, x-rays impinging on a material surface at grazing angles $\alpha_i < \alpha_c$ undergo total external reflection. Within this range, the transmitted wave is exponentially damped into the medium

$$E_t \sim e^{i\vec{k}_\parallel \vec{r}_\parallel} e^{-z/\Lambda} \tag{4.9}$$

where Λ is the penetration depth, and presents a minimum for $\alpha_i \to 0$, in which case $\Lambda = \lambda/2\pi\alpha_c$ and takes values of few nanometers [92]. It is called *evanescent wave*, and travels parallel to the surface.

X-ray measurements at small incident (α_i) angles or *grazing incidence x-ray diffraction* (GIXD) can therefore make use of these conditions. First of all the surface scattering is enhanced and the probed depth of the material can be controlled by the incident angle. In Figure 4.5 the geometry used in GIXD is shown, the incident and final angle are exaggerated for clarity. As can be observed in this figure, the scattering vector ($\vec{q} = \vec{k}_i - \vec{k}_f$) will be nearly parallel to the plane of the film, and therefore $\vec{q} = \vec{q}_\parallel$ will only contain components q_x and q_y, while $q_z \simeq 0$ (in the case that $\alpha_i < \alpha_c$, $q_z = 0$). Thus, measurements performed in this geometry will provide information on the structure in the plane of the film.

4.2.5 Experimental details

Different x-ray sources have been used in this study. In-house stations were used to characterize the substrates before growth as well as for rapid sample characterization just after deposition. Additional measurements with synchrotron radiation provided more information and more accurate data. The in-house stations were basically two sources, both using HOPG-monochromators. A standard x-ray tube with Co-K_α ($\lambda = 1.7921$ Å) radiation with a four-circle diffractometer, especially

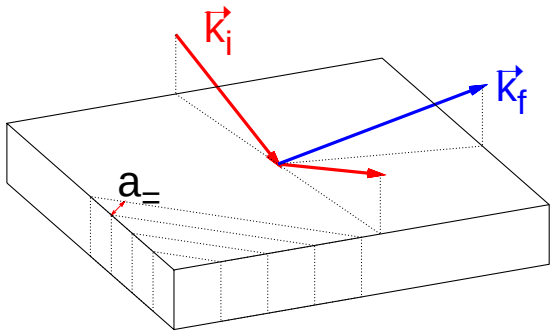

Figure 4.5: Schematic representation of the geometry used in GIXD. The scattering vector, $\vec{q} = \vec{k}_i - \vec{k}_f$, is nearly parallel to the plane of the film, and therefore $q_z \simeq 0$.

useful for the determination of misorientation angles in the Al_2O_3 substrates (see Section A); and a Mo-K_α rotating anode ($\lambda = 0.7107$ Å) with a six-circle diffractometer, which was used for reflectivity measurements on the organic layers as well as for GIXD measurements. Measurements with synchrotron radiation were performed at sources of European Synchrotron Radiation Facility (ESRF) in Grenoble, France; Ångströmquelle Karlsruhe (ANKA) in Karlsruhe, Germany; and at the Hamburger Synchrotronstrahlungslabor (HASYLAB) in Hamburg, Germany.

The ESRF is a 3rd generation synchrotron facility, the experiments have been carried out at the high-brilliance multi-purpose Troïka beamline (ID10B) [97, 98]. At this beamline the structure of the DIP layers has been studied using a beam energy of 12.9 keV. A six-circle diffractometer was used to perform x-ray reflectivity studies in vertical geometry. GIXD measurements were also performed to study the in-plane structure of the layers. HASYLAB is a 2nd generation synchrotron source with a 4.4 GeV electron storage ring. The measurements on $F_{16}CuPc$ layers have been performed at the W1 beamline at the energy of 8.9 keV [99, 100]. Finally, in experiments performed at the MPI-MF surface diffraction beamline in ANKA [101] at the energy of 15 keV bilayer structures were studied by x-ray reflectivity.

4.3 Spectroscopic ellipsometry

Spectroscopic ellipsometry (SE) has become a widely used technique for the optical characterization of materials. It is based on the measurement of changes in the polarization state of light upon interaction through reflection or transmission with a sample. The basic setup of an ellipsometer is shown in Figure 4.6. The sample is mounted at the axis of a goniometer stage to allow changes in the angle of incidence φ, i.e., the angle between the normal to the surface of the sample and the incoming light beam direction. These two axis, together with the reflected (or transmitted) light beam define the *plane of incidence* (POI). On the illuminating arm, light from a broad band source (high-pressure Xe arc lamp) is collimated and passed through the polarizer to define a well known and adjustable incident polarization state (χ_i). On the detection arm, a second polarizer (called analyzer) followed by a detector are used to accurately determine the reflected (or transmitted) polarization state (χ_r). A monochromator placed before the detector allows to perform spectroscopic measurements. In some instruments, compensators are placed at one or both arms of the goniometer to increase accuracy of the set and measured polarization states. Also, modern ellipsometers use a computer controlled modulation of the incident polarization state, either by mechanical rotation of the polarizer or by using an electro-optic modulated polarizer. Signal detection and processing is also performed by the computer. With this setup a very low noise measurement of the reflection properties of the sample is obtained. Often, the measured spectra can be numerically derived up to second or third order with respect to energy, thus enhancing the spectral features and allowing a better analysis of its relationship to the electronic structure.

Ellipsometry is a *non-destructive* technique based *only* in the measurement of the changes in the polarization state of the light. This fact makes the technique not sensitive to the absolute measurement of light intensity. This is why ellipsometry is usually called a self-normalizing technique. Consequently, light sources with a non-monotonous spectrum or with low intensity can be used. Due to the vectorial character of the polarization, two parameters of our sample are obtained from each ellipsometric measurement. Experimentally these parameters are the *ellipsometric parameters*, namely $\tan\Psi$ and $\cos\Delta$. From these parameters, two unknowns from the sample can be derived. These can be the real and imaginary terms of the refractive index of a bulk, or the thickness and the real part of the refractive index

of a layer on a substrate.

4.3.1 Complex reflectance ratio

As we pointed out, ellipsometry measures the change in the polarization state of light reflected on the sample. The quantity used to describe this change is the *complex reflectance ratio*, which is defined as

$$\rho \equiv \frac{\chi_i}{\chi_r} = \tan\Psi e^{i\Delta}, \tag{4.10}$$

where χ_i and χ_r are, respectively, the incident and reflected polarization states. The *ellipsometric angles* Ψ and Δ describe respectively the change in amplitude and phase of the polarization state.

There are two different formalisms to describe the polarization of light [95]. The Stokes vectors formalism is suitable for partially and unpolarized light beams, and the Jones vector formalism only applies to totally polarized light. For ellipsometric measurements were there is no, or only negligible depolarization of light, the latter is much simpler to use and to analyze the spectra.

In the *Jones vector* formalism the electric field associated to an electromagnetic

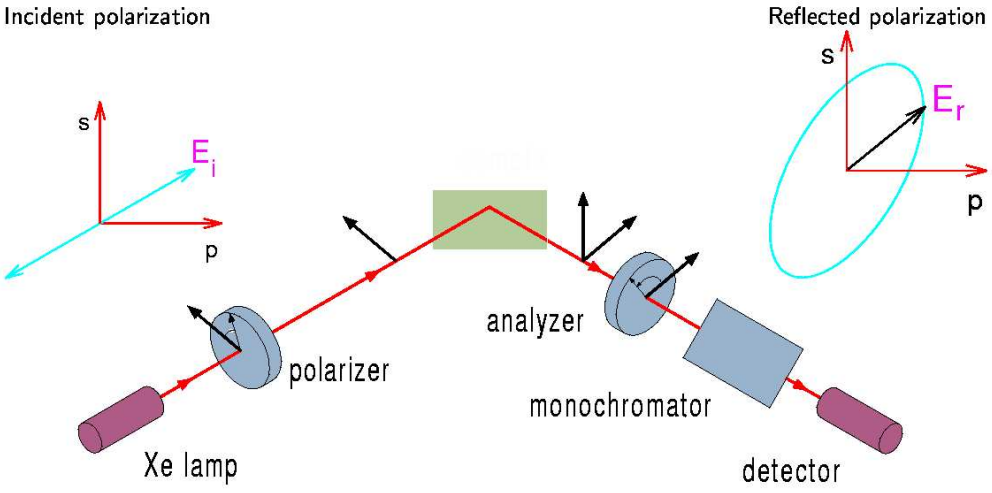

Figure 4.6: Illustration of the basic components of an ellipsometer. A known polarization state is changed after reflection on the surface of the sample. The final polarization state is measured by a polarizer and a detector.

wave is described through the vector:

$$\vec{E} = \begin{pmatrix} E_p \\ E_s \end{pmatrix}, \tag{4.11}$$

where E_p, E_s are the electric field components in a coordinate system perpendicular to the wave propagation direction. Usually, the directions parallel (p) and perpendicular (s) to the plane of incidence are used as coordinate system. The polarization state χ of a Jones vector is given by

$$\chi = \frac{E_s}{E_p}$$

The action of optical components (mirrors, polarizers, retarders) on the polarization state is described through a *Jones matrix* that relates the electric field components before and after the particular optical component. In this formalism the sample itself can be considered an optical component, and therefore the Jones matrix relating the incident E_i and reflected E_r Jones vectors is called *reflection matrix*

$$\vec{E^r} = \begin{pmatrix} R_{pp} & R_{ps} \\ R_{sp} & R_{ss} \end{pmatrix} \vec{E^i}. \tag{4.12}$$

The reflection matrix components R_{pp}, R_{ss}, R_{ps}, and R_{sp}, depend only on the optical properties of the sample and on the angle of incidence φ. For homogeneous isotropic materials and multilayer structures, the p and s polarizations are eigenstates of the reflection process. In other words, the reflection matrix is diagonal. Its components are the *Fresnel reflection coefficients* [94] for p and s polarized light. Then, the complex reflectance ratio is

$$\rho = \frac{r_p}{r_s}. \tag{4.13}$$

There are different types of ellipsometers each optimized for different types of measurements. In our measurements, we have used a rotating polarizer ellipsometer (RPE), where the incident polarization state is periodically modulated at around 80 Hz by mounting the polarizer on a motor axis. The analyzer is held fixed at an adjustable azimuth. Thus, the intensity at the detector can be written as

$$I = I_0[1 + \alpha\cos(2\omega t) + \beta\sin(2\omega t)], \tag{4.14}$$

where I_0 is the average intensity, and α and β are the *Fourier coefficients*, and ω is the angular frequency of the rotating element. The Fourier coefficients carry

information on the optical properties of the sample, but also depend on the angle of incidence and the analyzer angle A, i.e., they are a function of the reflection matrix coefficients and A [95, 102]. Inverting this relation we obtain the measured ellipsometric parameters

$$\begin{aligned} \tan\Psi &= \sqrt{\frac{1+\alpha}{1-\alpha}} \cdot |\tan A| \\ \cos\Delta &= \frac{\beta}{\sqrt{1-\alpha^2}} \cdot \frac{\tan A}{|\tan A|} \end{aligned} \tag{4.15}$$

4.3.2 Complex dielectric tensor

The response of a medium to an external electric field is described by the *dielectric tensor*, a second rank tensor that relates the applied field $\vec{E}$ to the induced electric displacement $\vec{D}$ through

$$\vec{D} = \varepsilon \cdot \vec{E}, \qquad \varepsilon = \varepsilon_1 + i\varepsilon_2 \tag{4.16}$$

The real ε_1 and imaginary ε_2 parts are two symmetric 3×3 matrices. The two components of the dielectric tensor can be represented by two ellipsoids, whose principal axis correspond to the space directions where $\vec{D}$ and $\vec{E}$ are parallel. For high symmetry crystals, the principal axes coincide with the lattice symmetry axes, and ε_1 and ε_2 have the same orientation, which is independent of light frequency. For monoclinic and triclinic crystals, the lower symmetry allows for different orientations of real and imaginary parts of the dielectric tensor, which can also show a spectral variation of its orientation. Due to the causality principle, the real and imaginary parts of the dielectric tensor are related to each other through the *Kramers-Kronig relations* (KKR), which are sometimes used to obtain the dielectric tensor from reflectivity or transmission measurements. In SE, the use of KKR is not necessary because at each wavelength two quantities are obtained from which both components of the dielectric tensor can be derived.

For isotropic homogeneous bulk materials the dielectric tensor is a scalar and can be analytically derived from the complex reflectance ratio with the expression

$$\tilde{\varepsilon} = \left(\frac{1-\rho}{1+\rho}\right)^2 \tan^2\varphi \cdot \sin^2\varphi + \sin^2\varphi. \tag{4.17}$$

For multilayer samples or anisotropic materials there is no direct analytical

relation between the measured ellipsometric parameters and the optical and structural properties of the sample. To determine these parameters, a numerical inversion procedure is used, where the parameters are obtained from a fit of the measured ellipsometric spectra to a model simulation of the reflection process.

Equation (4.17), called the *two phase model*, is often used to present the ellipsometric data in a more suitable form. This is especially helpful to emphasize changes in spectral features in a series samples or as a function of composition, temperature, or growth conditions. For multilayered samples, or even for bulk samples with a very thin oxide or roughness overlayer, ε as obtained from Equation (4.17) does not correspond to the real dielectric function of the material. For such cases the expression *pseudodielectric function* is used to refer to the ellipsometric spectra evaluated with the two phase model.

4.3.3 Anisotropic materials: The $\beta-$scan method

In general, to completely determine the dielectric tensor of a low symmetry crystal we need the three principal values of the real and imaginary parts plus their orientations, that is 12 real magnitudes. Two different approaches have been used to address this problem with spectroscopic ellipsometry.

The *generalized ellipsometry method* [103] consists in the measurement of three normalized elements of the Jones matrix of the sample, which are then related to its properties. Usually, several measurements at different orientations of the sample, polarizer, and analyzer, and at different angles of incidence have to be measured to be able to determine the normalized Jones matrix elements. Since the reflection matrix components depend also on the angle of incidence and the analyzer and polarizer angles, special care has to be taken in this method to relate the different measurements done at different experimental setups. The *β-scan method* [104] directly connects the measured ellipsometric parameters with the properties of the sample. Both methods have been successfully applied to determine the optical properties of uniaxial and biaxial orthorhombic media.

In the β-scan method the analysis of the ellipsometric parameters follows a very similar process to the standard (as opposed to generalized) ellipsometry for isotropic samples. A complex *pseudoreflectance ratio* is defined as the ratio between incident and reflected polarization states [104, 105].

$$< \rho > \quad = \quad \frac{\chi_i}{\chi_r} = \frac{(R_{pp}/R_{ss}) + (R_{sp}/R_{ss}) \tan A}{1 + (R_{ps}/R_{ss})(\tan A)^{-1}} \tag{4.18}$$

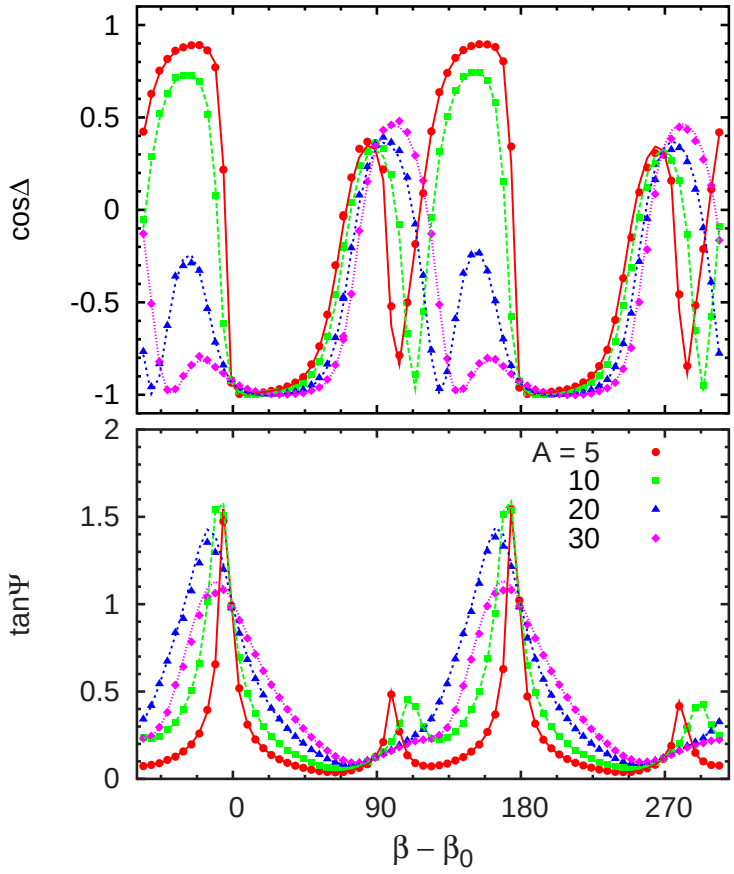

Figure 4.7: Example of beta scan of a $F_{16}CuPc$ film on Al_2O_3 at different values of the analyzer and at the fixed energy of 1.5 eV.

$$< \rho > \quad = \quad \tan\Psi e^{i\Delta} \tag{4.19}$$

where $\tan\Psi$ and $\cos\Delta$ are defined by Equations (4.15). We have introduced that the detected reflected polarization state is determined by the analyzer azimuth A, and α and β are the first Fourier coefficients of the intensity measured at the detector. Usually a series of measurements are performed at several sample and analyzer azimuths.[3] When plotted against the sample azimuth β the $\tan\Psi$ and $\cos\Delta$ ellipsometric parameters at different analyzer azimuths describe (see Figure 4.7) periodic curves with two or four crossing points. At these points the reflection matrix is diagonal and the complex pseudoreflectance ratio is independent of the analyzer azimuth. The crossing points correspond to sample positions

[3] A β-scan corresponds to sweeping the β Euler angle that describes the sample orientation in the reference system defined by the plane of incidence.

where one of the principal axes of the dielectric tensor lies in the plane defined by the axes normal to the surface of the sample and normal to the POI. By fitting the measured β-scans to an anisotropic model for the reflection process [105–107] is it possible to obtain the real and imaginary parts of the three dielectric tensor components and, simultaneously, the direction of its three principal axis.

4.4 Raman scattering

Raman scattering is an inelastic light scattering process discovered by C. V. Raman.[4] In this process there is an exchange of energy between an incident light beam and the elementary excitations of the sample, usually lattice vibrations, i.e. phonons or molecular vibrations. The frequency of the incident light is shifted and the system is left in an altered state. In the *Stokes scattering* (see Figure 4.9) the scattered light has lower frequency while an elementary excitation (phonon or vibration) is created. For the *anti-Stokes scattering* the scattered light has a higher frequency and needs to absorb an elementary excitation. In the Raman scattering process several quantities have to be conserved, namely the energy and wavevector:

$$\omega = \omega' \pm \Omega \tag{4.20}$$

$$\vec{k} = \vec{k}' \pm \vec{Q} \tag{4.21}$$

Also, the polarization states of the incident and scattered light are important to determine the intensity of the scattered light. Depending on the symmetry properties of the molecule or crystal, the tensor describing the Raman scattering can have one or more non-zero independent components. These are the selection rules for the scattering process. Only incoming and scattered polarizations that are connected through a non-zero tensor component will be observed. In Appendix C a summary is presented with the selection rules tables that apply to the samples measured in this thesis.

The usual experimental setup needed to acquire Raman spectra is composed of a very intense and monochromatic light source (a suitable laser beam) to excite

[4] C. V. Raman as awarded the Nobel prize in physics in 1930 for the discovery of the Raman scattering process.

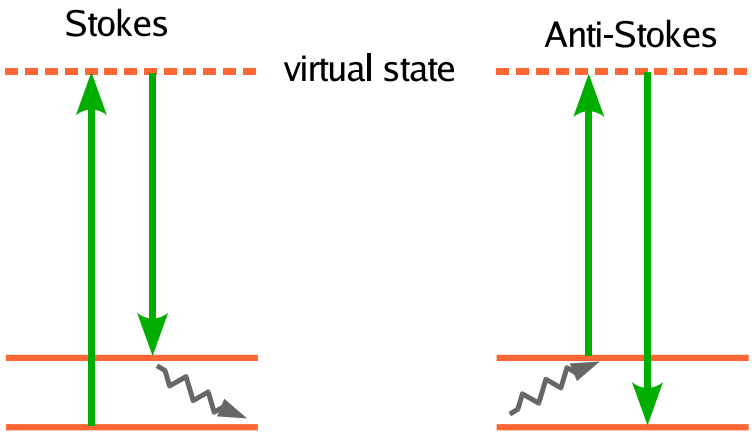

Figure 4.8: Raman scattering process. The phonon can be emitted as shown in the figure (Stokes scattering) or absorbed (anti-Stokes scattering).

the sample, the optics needed to focus the scattered light, and a spectrometer with a charge-coupled device detector (CCD), or a photomultiplier.

In the measurements performed in the present study, room temperature measurements were made using $\sim 1.5\times10^4$ W/cm^2 of the 514.5 nm line of an argon-ion

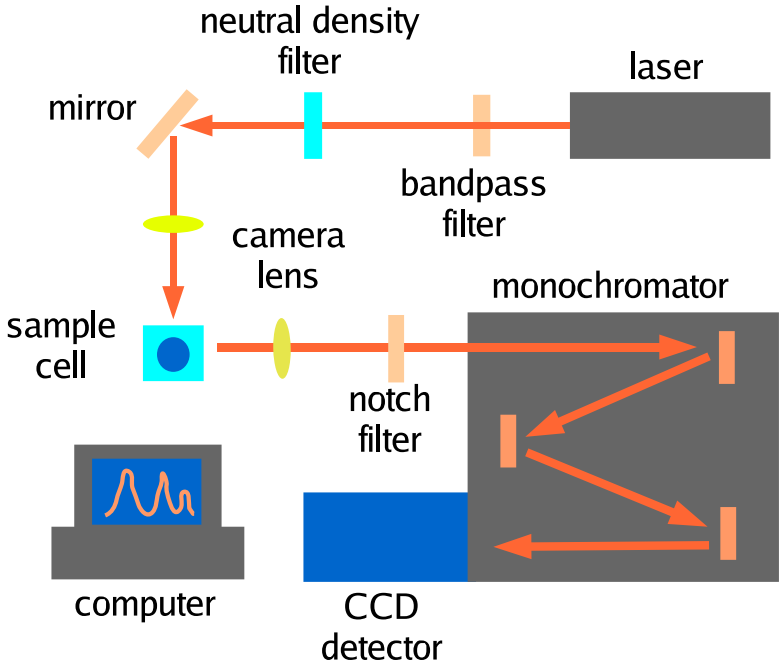

Figure 4.9: Typical experimental setup used in Raman scattering.

laser as exciting radiation. Scattered light was analyzed with a Jobin Yvon T-4000 XY triple spectrometer equipped with a multichannel. An optical microscope with a $\times 50$ objective was used to focus the laser beam on the sample and collect the scattered light. The laser light spot on the sample was between 1 and 2 μm in diameter. The spectral resolution was $\sim$2 cm^{-1}.

Chapter 5

F_{16}CuPc thin films

In the present chapter we discuss the properties of thin films of the compound F_{16}CuPc evaporated on the various substrates used, i.e., oxidized silicon, MgO, and Al_2O_3. We compare the properties of the films, relating them to the crystalline structure and morphology of each substrate used, and in particular to the balance between the molecule-molecule and molecule-substrate interactions in each case. We study the influence of the growth conditions in the final structure of the layers to determine the optimum conditions.

In this chapter we show that, while the packing of the molecules is similar in the layers deposited on the different substrates, the degree of order they present is highly influenced by the morphology and crystalline structure of each substrate. The substrate used and the deposition conditions play an important role in the final properties of the layers. The use of different techniques, which provide complementary information on the properties of the layers, allows to characterize independently their structure and their optoelectronic properties.

In Sections 5.1, 5.2, and 5.3 we discuss the structural and optical properties of films of F_{16}CuPc deposited on SiO_2, MgO, and Al_2O_3 respectively. In Section 5.4 we present a Raman scattering study of the layers and relate the results to the data obtained with the other characterization techniques used. In these sections, we focus in the properties of the films that show the best structural definition, and let for Section 5.5 the discussion about the dependence of the properties of the films as the growth conditions (growth temperature T_g and thickness of the layers D) are varied. Finally, we summarize the main results of this chapter in Section 5.6.

5.1 Isotropic $F_{16}CuPc$ thin films on SiO_2

As we already mentioned, the study of the properties of the $F_{16}CuPc$ films has been performed as a function of the growth conditions to determine the parameters for which the best structural definition of the organic layer is obtained. The degree of order is measured in terms of the surface smoothness (measured by AFM and x-ray diffraction) and the mosaicity of the layer (rocking width of the Bragg reflections along the specular). We postpone the study of the influence of the growth conditions in the films to Section 5.5 and start presenting the main structural and optical properties of the layers that present a higher degree of crystalline order, since it allows to draw a clearer picture of the main characteristics of those layers. The best structural properties are obtained for a substrate temperature of $T_g = 230°C$, and thicknesses between 10 and 20 nm.

5.1.1 Morphology and structure

Although the morphology of the grown layers strongly depends on the growth conditions at which the layer has been deposited, in all films grown at $T_g > 100°C$ it is characterized by elongated terraces, as shown in the AFM images of Figure 5.1. All images shown in this figure belong to a 20 nm film deposited at $T_g = 230°C$ and have been acquired in contact mode just after deposition. As can be seen in Figure 5.1(a), the elongated terraces are randomly oriented in the film plane, with a length of up to several 100 nm and an aspect ratio (length:width) around 10:1. As shown in images (b) and (c), those terraces are formed by long and narrow needles, which are approximately oriented perpendicularly to the terraces. In Figure 5.1(d) we have plotted the z-profile depicted in image (c). In this profile we can see that the plateau is atomically flat and that the step height is around 1.5 nm in all cases. This height is approximately the size of a molecule. Thus, this regular step pattern is suggestive of essentially *upright-standing molecules*. As we show in the next section, x-ray diffraction measurements confirm this interesting stacking of the molecules, already observed in similar systems [60, 108, 109] and also for different compounds [72, 110]. The line scan shown in Figure 5.1(d) has been deliberately performed over an area where the deepest depression of the surface has been found. In this particular point there are five opened layers. However, in general only the three or four top layers are not completely closed in this film. The root mean square roughness (σ_{rms}) of this layer is only 1.1 nm, as

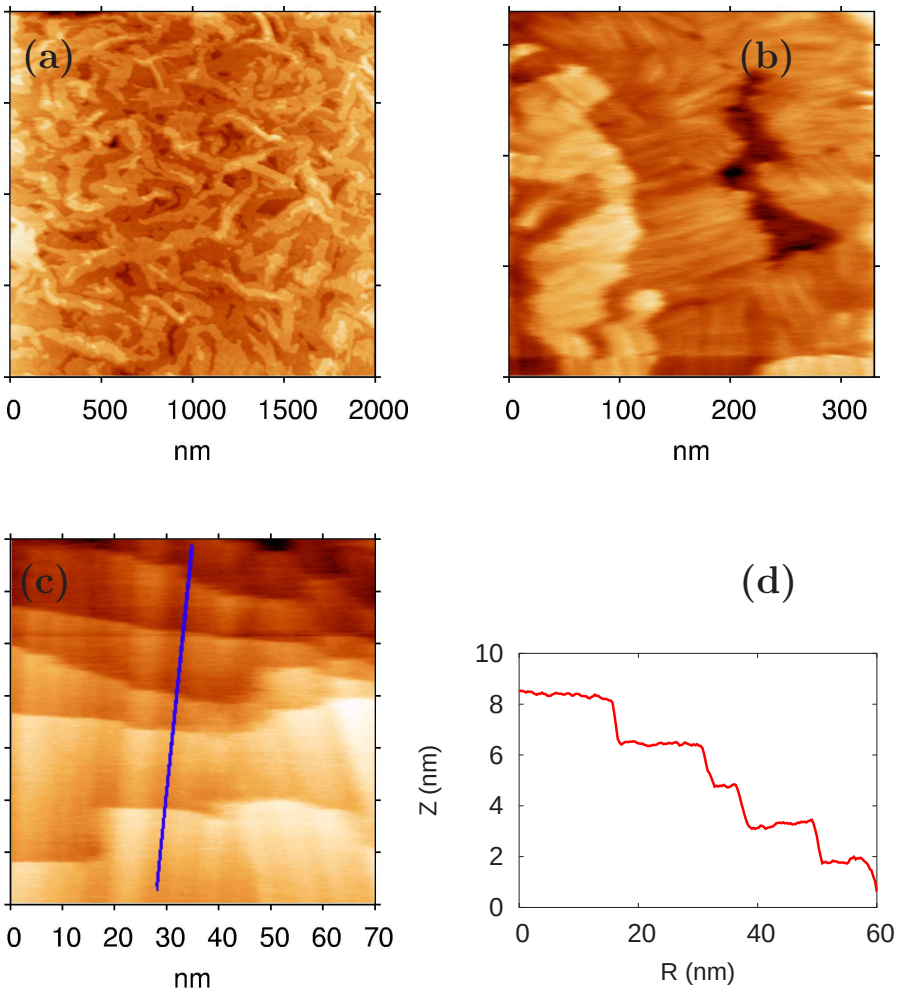

Figure 5.1: Morphology of a 20 nm thick $F_{16}CuPc$ film on SiO_2 deposited at $T_g = 230°C$. Image (a) shows an area of 2000×2000 nm^2, where we can observe that long, randomly oriented terraces are formed on the surface. It is found that only the last few monolayers are not closed and a very smooth film is obtained with $\sigma_{rms} = 1.1$ nm. Scanning a smaller area of the surface (320×320 nm in image (b) and 70×70 nm in image (c)) it is found that the terraces are formed by small needles. In (d) a z-profile plot of the line of image (c) has been plotted. We should point out that this line scan has been deliberately performed over an area where the deepest depression of the surface has been found.

we discuss in Section 5.5, the surface roughness depends on T_g and also on D. Nevertheless, in all films grown at $T_g = 230°C$ the surface is very smooth with a roughness below 10% of the total layer thickness.

The crystalline structure of the layers in the direction perpendicular to the film plane has been studied by x-ray diffraction under specular conditions (see Section 4.2). Figure 5.2(a) shows a typical specular scan of a 20 nm thick film deposited at $T_g = 230°C$ with a fitted curve following the Parrat formalism. As we discussed, from these scans we can obtain information about the structure along the z-direction, perpendicular to the film plane, more precisely we obtain the electron density profile in this direction. We can distinguish three separate regions in the spectrum of Figure 5.2(a). A first region at momentum transfer q_z below 0.03 $Å^{-1}$ where a constant intensity is measured at the detector (after the correction for illuminated area has been performed). This is the region below the critical angle α_c, where *total external reflection* takes place (see Section 4.2.1). The critical angle α_c indicates the electron density average value of the layer through Equations (4.2) and (4.4). At momentum transfer $0.03 < q_z < 0.25$ $Å^{-1}$ well-defined *Kiessig interferences* corresponding to the total film thickness are visible, in this region the intensity decays following the *Fresnel reflectivity* approximately as $1/\theta^4$ superimposed by intensity oscillations. From the width of the Kiessig fringes the average film thickness D can be estimated by using

$$D = \frac{\lambda}{2\sin(\Delta(2\theta)/2)} = \frac{2\pi}{\Delta q} \tag{5.1}$$

where λ is the wavelength of the radiation, and $\Delta(2\theta)$ the variation (of the scattering angle) between two minima of the intensity. Equation (5.1) is a kinematic approximation, the determination of the exact thickness has to take into account multiple scattering effects (Parrat formalism), which shifts the position of the minima (and their distance in q_z) slightly.

Finally, at $q_z = 0.42$ $Å^{-1}$ the first order out-of-plane Bragg reflection is seen with its associated *Laue satellites*. The position of the Bragg peak corresponds approximately to a lattice spacing, $a_\perp$, of 15 Å. The presence of the Laue oscillations is due to the finite thickness of the film, or, in other words, due to the fact that the number of repetitions of the lattice constant n_c in this direction is small ($n_c \simeq 14$ for $D = 20$ nm). When $n_c \to \infty$ the Laue oscillations disappear and a Delta function is obtained in kinematic approximation. It should be mentioned

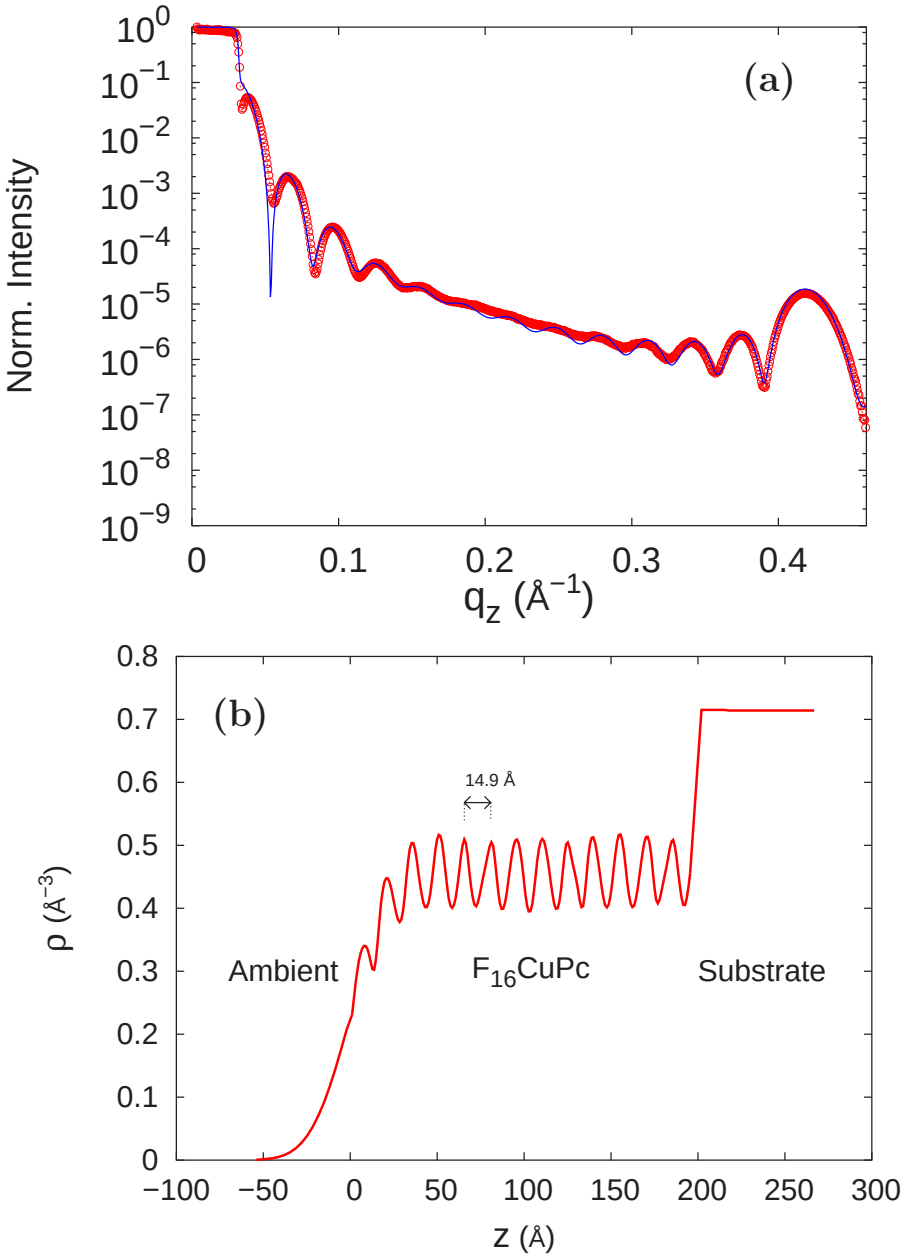

Figure 5.2: (a) X-ray diffraction scan along the specular rod with a fitted curve following the Parrat formalism of a $F_{16}CuPc$ film with a thickness of 20 nm deposited at a substrate temperature of 230°C. (b) First order approximation of the electron density profile along the surface normal ρ_z. The variations of the electron density in the organic layer are modeled with a 14.9 Å periodic sine function. The parameters derived from the fit are shown in Table 5.1.

that the thickness deduced from the Laue oscillations is, in these films, identical to that deduced from the Kiessig interferences, implying that the out-of-plane order is high and coherent over the entire film thickness.

In Figure 5.2(a) we have plotted a fit of the scan (solid line) together with the experimental data. This fit has been performed using the Parrat formalism discussed in Section 4.2.3. The electron density profile obtained from the fit is shown in Figure 5.2(b). Note that if the data to fit are limited to the first order Bragg reflection, then a sinusoidal electron density profile is fully sufficient. Further refinement (on a shorter real-space length scale) would require the analysis of higher-order Bragg reflections. Thus, the function describing the electron density in the organic layer can be written as

$$\rho_e(z) = \widehat{\rho}_e + A\cos(2\pi z/a_\perp + \phi) \tag{5.2}$$

where $\widehat{\rho}_e$ is the average electron density of the organic layer, A is the amplitude of the oscillations of the electronic density, and ϕ is the phase of the sinusoidal wave. While the first term of Equation (5.2) is sufficient to describe the two first regions of the scan in Figure 5.2(a) (i.e., $q_z < 0.25$ Å^{-1}), the sinusoidal variation is needed to account for the first order Bragg reflection. The fit parameters describing the system are shown in Table 5.1 and are δ and β (see Section 4.2) of each material (i.e., Si-substrate, SiO_2, organic layer, and vacuum), the roughness of each interface, and the thickness of the organic layer. Since δ and β depend on the wavelength used, we find it more convenient to give the corresponding values of the electron density ρ and the lineal absorption coefficient μ. The relation between those magnitudes is given by Equation (4.2). We should also point out that small variations in the value of μ of the organic layer do not influence the fit, since μ accounts for absorption at the organic layer which is rather low.

As we already mentioned, the position of the Bragg reflection stands for a lattice parameter in the z-direction, $a_\perp$, of about 15 Å. This value is in full agreement with the step height measured by AFM of the terraces observed on the surface of the film (see Figure 5.1). This value is also approximately the height of an $F_{16}CuPc$ molecule, from what we can infer that the molecules adopt an essentially up-right configuration in the film, standing more or less perpendicular to the substrate surface. Small variations of $a_\perp$ are found as a function of the growth parameters as we discuss in Section 5.5.1. However, in all the cases $a_\perp$ is close to 15 Å. Growth of

	D (nm)	ρ (Å^{-3})	μ(Å^{-2})	σ_{rms} (nm)
ambient (vacuum)	N/A	0	0	N/A
organic layer	20	$\rho_e(z)^*$	$3.062 \cdot 10^{-7}$	1.8
SiO_2	2.5	$2.015 \cdot 10^{-5}$	$4.575 \cdot 10^{-7}$	0.4
Si substrate	N/A	$2.012 \cdot 10^{-5}$	$4.574 \cdot 10^{-7}$	0.2
*electron density	$\rho_e(z) = \widehat{\rho}_e + A\cos(2\pi z/a_\perp + \phi)$ [Å^{-3}]			
of organic layer	$\widehat{\rho}_e = 1.286 \cdot 10^{-5}$	$A = 1.7 \cdot 10^{-6}$	$a_\perp = 14.9$	$\phi = 2\pi$

Table 5.1: Parameters derived from the fit of Figure 5.2 following the Parrat formalism. The electron density profile of the organic layer is described by Equation (5.2).

phthalocyanines on more strongly interacting substrates showed that the molecules lie flat on the surface at submonolayer coverages. In fact, phthalocyanines were among the first organic molecules on metals studied by STM with submolecular resolution [80, 111, 112]. It has been shown that phthalocyanines on different types of substrates exhibit different molecular orientations, depending on the substrate-molecule interaction [113]. In order to study more precisely the orientation of the molecules in the present films we have used Raman scattering measurements to determine the angle $\alpha_\circ$ between the molecule plane and the substrate plane. The precise orientation of the molecules in the film is discussed in detail in Section 5.4.

The degree of alignment of the orientation of the crystallographic planes along the z-direction is determined by performing rocking scans over the Bragg reflections in this direction. In Figure 5.3 a scan over the Bragg peak plotted in Figure 5.2(a) is shown. The *full width at half maximum* (FWHM) of the peak is 0.017°, an extremely low value for organic materials. The value of 0.017° is approximately the resolution of the diffractometer in the configuration used, therefore the actual mosaicity of the layer is $\leq$ 0.017°. This quantity indicates the good crystallinity of the film, and has been shown to influence the conduction properties of the organic layers [19, 63]. As we discuss later, the mosaicity of those films depends on the growth conditions, especially on the substrate temperature during growth.

To investigate the in-plane structure of the layers, GIXD has been used to locate in-plane Bragg reflections of the film. The analysis of the in-plane structure is

somewhat limited due to the limited number of in-plane reflections found and by the azimuthal averaging on this isotropic substrate. However, this in-plane powder facilitates the location in the reciprocal space of Bragg reflections, since they are distributed in all in-plane directions. This information is later used to easily locate the same reflections on the in-plane oriented films on sapphire (see Section 5.3). Although a broad range of $q_{||}$ has been scanned (from 0.32 up to 3 $Å^{-1}$), only one reflection has been found at $q_{||} = 1.982$ $Å^{-1}$, this is shown in Figure 5.4. In accordance with the random orientation of the crystallites observed by AFM, this Bragg reflection is found in all azimuthal orientations of the sample with the same intensity, implying that there is no preferred orientation of the organic crystallites in the plane of the film. From the radial width of the in-plane diffraction spot we can deduce that the in-plane crystallite dimensions are in excess of 12 nm in the measured 13 nm thick film. This data is in agreement with the AFM data, where needles longer than that value are obtained. However, we must point out here that the obtained crystallite size is found to depend on the thickness of the layer as shown in Section 5.5.2. The 12 nm value is a lower limit for the needle size in the direction defined by the Bragg reflection, which does not necessarily coincide

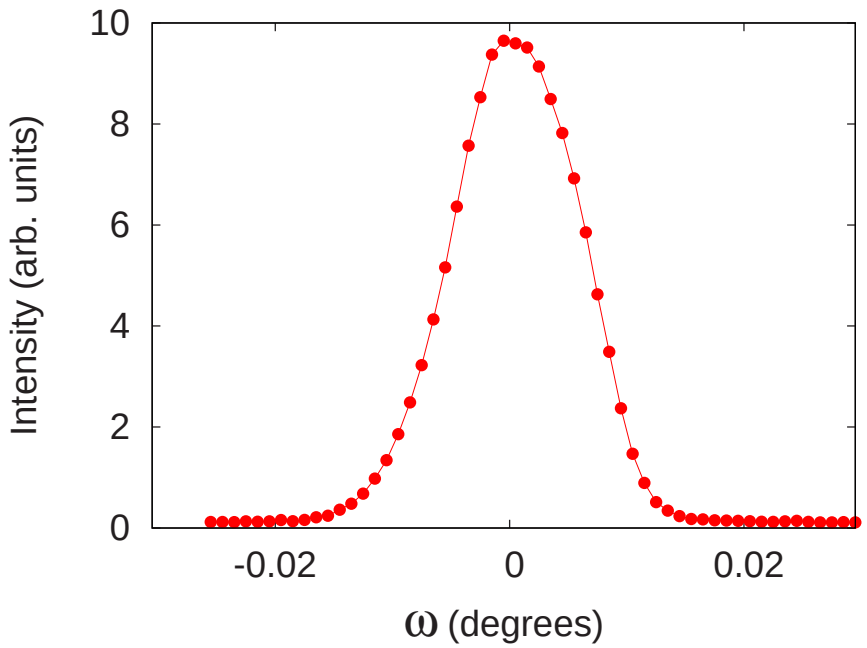

Figure 5.3: Rocking scan over the first order Bragg reflection of Figure 5.2. The full width half maximum (FWHM) of the peak is 0.017°, value on the order of the resolution of the measurement. The solid line is a guide to the eye.

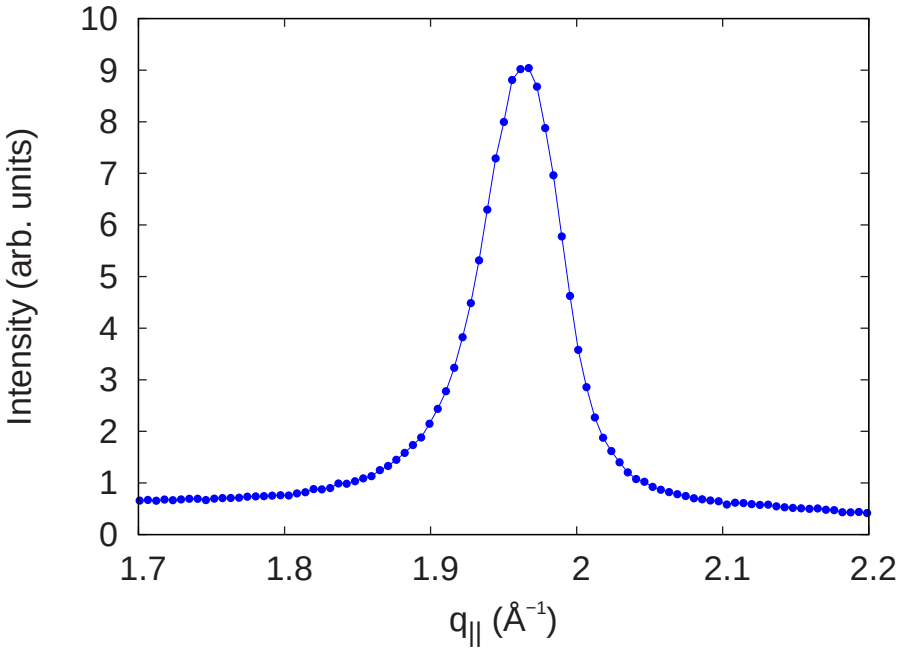

Figure 5.4: In-plane reflection at $q_{||} = 1.982$ Å^{-1}. The FWHM of the peak is 0.052 Å^{-1}, which implies a domain size of ∼12 nm for this 13 nm thick film of F_{16}CuPc on SiO_2. The solid line is a guide to the eye.

with the observed long axis of the needles.

5.1.2 Optical Properties

Spectroscopic ellipsometry has been used to determine the complex refractive index of the layers. The values of n and k in the energy range from 1.4 to 3.7 eV of a 13 nm layer are shown in Figure 5.5(a). The model used to numerically fit the spectra is a four phase model, i.e., ambient/F_{16}CuPc/SiO_2/Si-substrate. The SiO_2 thickness was fixed to 3 nm as determined on a bare substrate. Since the spot of the light reflected on the sample surface in the ellipsometric measurements is much larger than the crystallite dimensions, the anisotropies that the organic material may locally present are averaged out, and measurements at different azimuthal orientations of the sample are completely equivalent. Thus the in-plane components of the dielectric tensor reflect an effective medium with a random distribution of azimuthal orientations of the crystallites [102]. Thus, those films are at most uniaxial, with $\varepsilon_Z \simeq \varepsilon_X = \varepsilon_Y$. The out-of-plane component ε_Z has a lower contribution to the measured data [102, 114], and therefore is difficult to

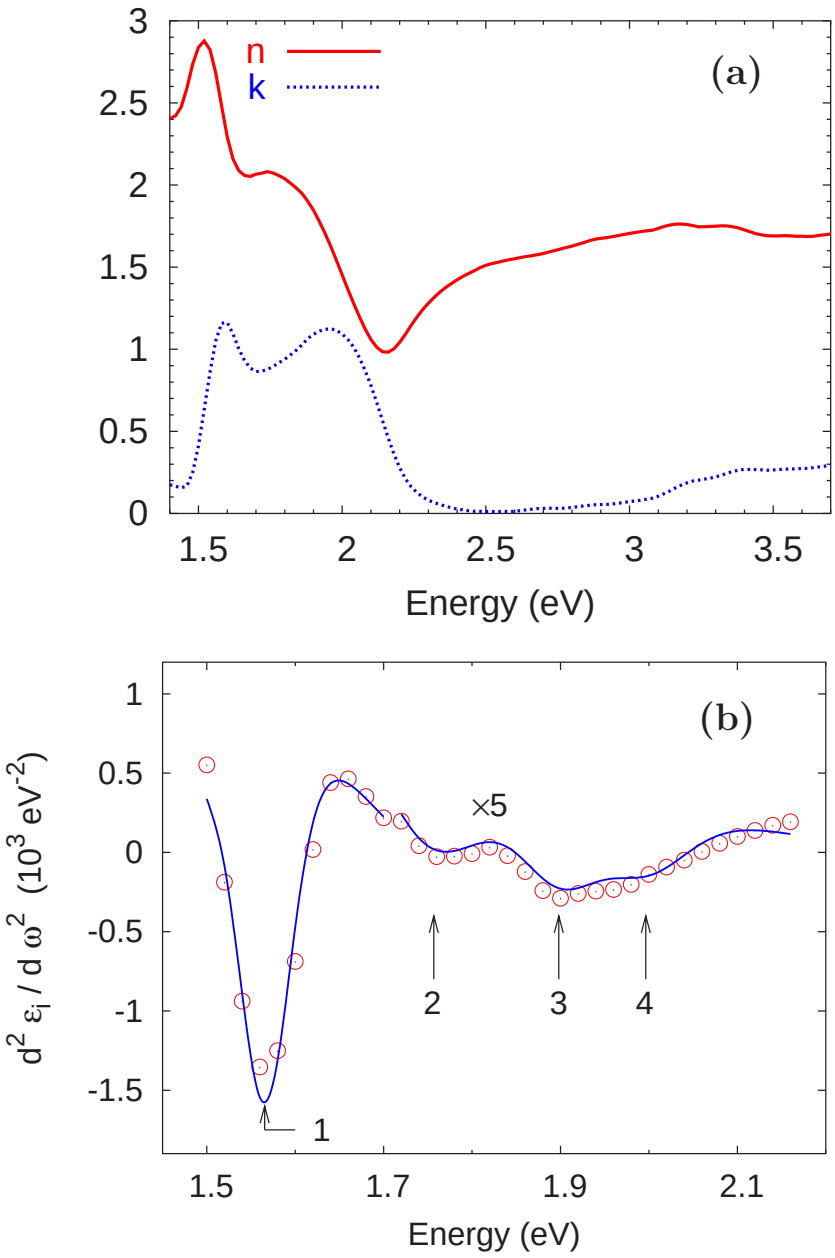

Figure 5.5: (a) Ellipsometrically determined complex refractive index $N = n + \mathrm{i}k$ from a numerical fit using an isotropic four-phase model (ambient/F_{16}CuPc /SiO_2/Si-substrate). The SiO_2 thickness was fixed to 3 nm (determined prior to growth) and the fitted film thickness is 13 ± 1 nm. The deposition temperature is 230°C. (b) Second derivative of the imaginary part of the dielectric function in the Q-band region. The experimental data is plotted as circles and the fit is shown by the solid line. The arrows show the observed transition energies. Note that for clarity reasons the data above 1.7 eV have been magnified by a factor of 5.

determine from the measurement. However, measurements performed at different angles of incidence have no other dependence than what is given by the change in the light path length (geometry factor), from what we can infer that this component must be similar to the in-plane components. The molecular symmetry of the phthalocyanines would also favor the similarity of the out-of-plane component with one of the in-plane components. In Section 5.3.2 this argument is discussed in more detail.

In Figure 5.5(b), the second derivative of the imaginary part of the dielectric function of the same F_{16}CuPc layer is plotted (circles) together with a fit (solid line). Please note that, for clarity reasons, the values above 1.7 eV have been magnified by a factor of 5 and that the plot shows only the data on the lower energy range, since this is the most interesting range that comprises several electronic transitions of the organic material. Electronic transitions (marked with arrows) at the energies 1.57 (1), 1.76 (2), 1.90 (3), and 2.00 eV (4) ($\pm$0.01 eV) are observed. These positions are similar to those observed in films on Al_2O_3 (see Section 5.3.2), and are $\pi \rightarrow \pi^*$ excitonic transitions characteristic of the phthalocyanine rings. These four transitions form the Q-band of F_{16}CuPc [50]. The position of these excitons is linked to the stacking of the molecules inside the unit cell. A more detailed discussion on the relationship between the structural properties of phthalocyanines and their optical properties is postponed to Section 5.3.2 since the anisotropy of the films on Al_2O_3 give more insight into the understanding of the optical properties of F_{16}CuPc [82].

5.2 Films of F_{16}CuPc on MgO

The films deposited on MgO substrates present a lower structural definition than those deposited on SiO_2 under the same deposition conditions. As we discussed in Section 3.4, the surface of the MgO substrates presents a rough morphology (see Figure 3.5), and consequently the deposited film has also a rough morphology. The molecules stand, as on SiO_2, perpendicular to the substrate surface, but the crystalline structure has a lower quality, with x-ray rocking widths of 0.15°. The films are also optically isotropic. The dielectric function is plotted as the curve labeled ε_{ISO} in Figure 5.13 (page 72), showing spectral features very similar to the films on SiO_2.

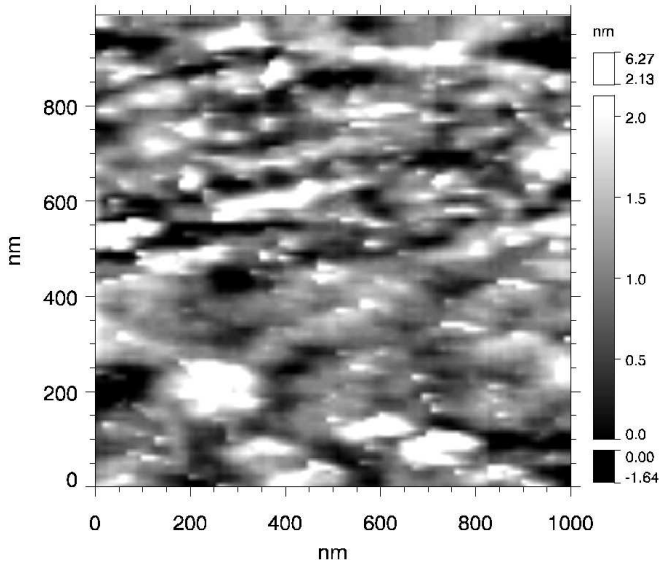

Figure 5.6: AFM image of an $F_{16}CuPc$ thin film on MgO.

5.3 $F_{16}CuPc$ thin films on Al_2O_3

In this section we discuss the properties of $F_{16}CuPc$ thin films on Al_2O_3 $(11\bar{2}0)$ substrates. As we show, some properties of these films are very similar to those of the films on SiO_2 or MgO, grown at exactly the same growth conditions. All three substrates are oxides, and thus the substrate-molecule interaction is similar, what leads to a locally similar packing of the molecules. However, the symmetry and morphology of the surface will influence the structural and therefore the optical properties of the layers. Details on the crystalline structure and morphology of the Al_2O_3 substrates used can be found in Section 3.4 and Appendix A.

Films on Al_2O_3 are found to be especially interesting since they differ from films on the other substrates in that they present, under certain growth conditions, an in-plane alignment of the organic crystallites, while the high out-of-plane order is still preserved. This preferred orientation of the organic layer is observed by all the characterization techniques used in the present study. Thus, in contrast to the films on SiO_2 or MgO, highly anisotropic properties are derived from all the different measurements revealing an anisotropic growth of the layers. Particularly, the upright stacking of the molecules is found in all three substrates. This orientation promotes transfer of charge carriers through the film plane, since this is the direction of maximum π-orbital overlap. This kind of molecule orientation is

especially suitable for devices that need charge carrier transport in the film plane, as OFETs, in which case the transport through the channel can be improved by choosing the orientation in which the transport properties are higher. However, the fact that the crystallites are randomly oriented in the plane, as is the case in the isotropic films, will reduce the transport properties of the layers. In addition, small crystallite sizes reduce further the conduction properties, since grain boundaries act as traps in the transport process [37]. Thus, not only azimuthal orientation, but also larger domain sizes are needed for device applications. As we show here, these requirements are met by the organic layers evaporated on Al_2O_3 under adequate growth conditions.

Furthermore, the growth of single crystals of those organic compounds has been shown to be often a difficult task due to their low sublimation pressure and the difficulty to find suitable solvents [115]. Even when these crystals can be produced, their dimensions are frequently too small to characterize them with standard techniques. Hence, the possibility to fabricate organic thin films with only one azimuthal domain can be used for the investigation of the intrinsic properties of those materials, using them as substitutes of their single crystalline solid, and thus allow the study of some properties of those materials that could not be accessed otherwise.

5.3.1 Structure and morphology

The structural properties of the $F_{16}CuPc$ layers on Al_2O_3 studied by x-ray diffraction show some similarities to the films on SiO_2. X-ray diffraction measurements along the specular path are shown in Figure 5.7. As can be seen, well-defined interfaces are evidenced by the Kiessig fringes that appear after the critical angle (Figure 5.7), while a Bragg reflection appears at $q_z = 0.42$ Å^{-1} (shown in the inset of Figure 5.7) as in the films on SiO_2, corresponding to a lattice parameter $a_\perp = 14.9$ Å. Thus, the molecules stand equally upright on the substrate, and small mosaicites have been also measured in those films. We should mention that the stepped morphology of the interface substrate-organic layer is reflected in the measured x-ray data. Thus, the degree of definition of the Kiessig fringes depends on the azimuthal orientation of the sample relative to the x-ray beam projection. The width of the rocking scans over the Bragg reflection (or the mosaicity) also

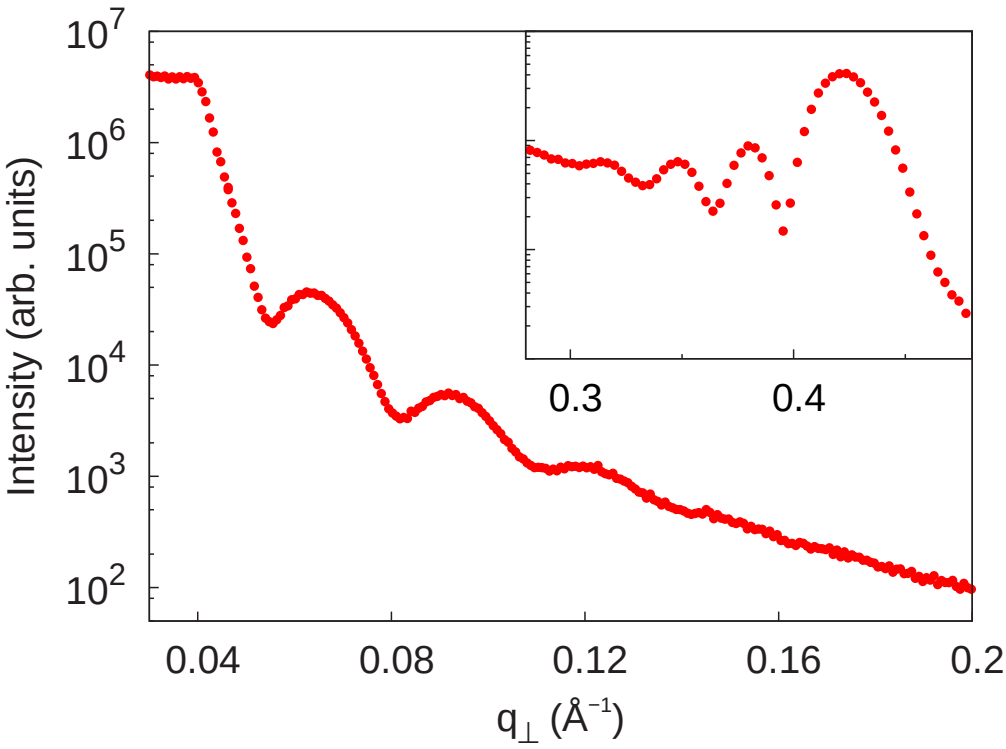

Figure 5.7: X-ray scan along the specular path of a 20 nm thin film on Al_2O_3 deposited at $T_g = 230°C$ showing well-defined Kiessig fringes. The inset shows the first order Bragg reflection at $q_z = 0.42$ Å^{-1} revealing a stacking of the molecules perpendicular to the substrate.

depends on the sample orientation, achieving its maximum value when the x-ray beam is perpendicular to the step edges. Furthermore, the organic film will present a miscut of the same magnitude as the substrate and thus, the organic crystallographic planes will not be perfectly aligned with the physical surface of the film. We discuss this issue in further detail in Section 6.2.2 for the films of DIP on Al_2O_3 in which case an analogous situation has been found.

The morphology of the layers on Al_2O_3 differs substantially from the films on SiO_2. AFM images taken in non-contact mode showed a wetting morphology that reproduced the steps of the substrate as can be observed in Figure 5.8(a). The parallel stripes with a typical separation of about 100 nm observed on the film follow the pattern of the stepped substrate, measured before deposition, thus propagating the terraces through the film [116]. Later AFM measurements in

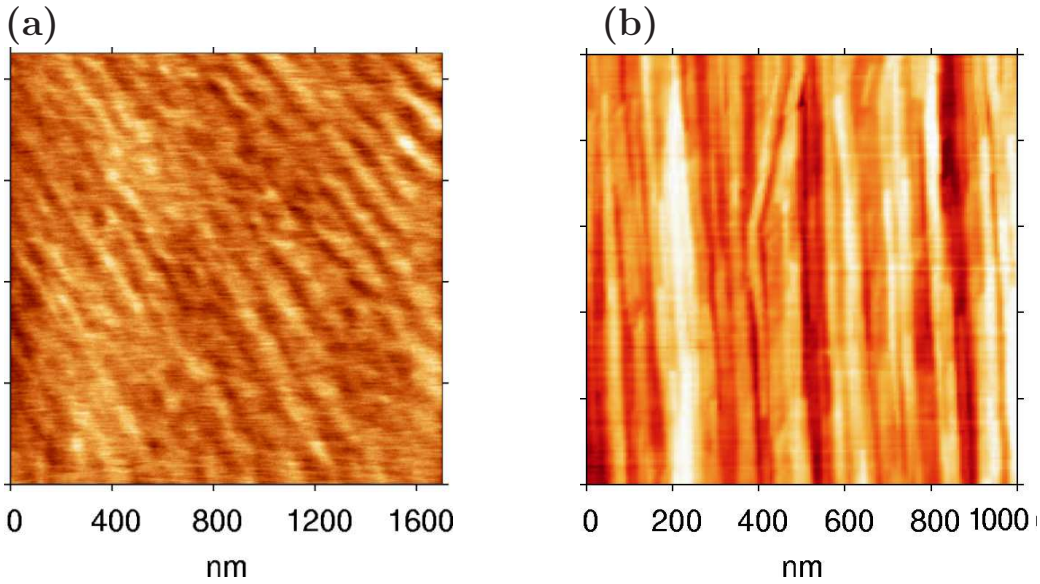

Figure 5.8: AFM images of $F_{16}CuPc$ films on Al_2O_3. (a) Non-contact AFM image of a 12 nm thick film deposited at $T_g = 230°C$. The observed parallel stripes are due to the stepped substrate surface propagated through the wetted film. (b) Contact mode AFM image of a 34 nm thick film where elongated needles can be observed [117].

contact mode allowed to resolve parallel elongated needles. Those needles can be up to several microns long, extending over several terraces of the substrate. Their width varies between 20 and 100 nm [117]. The in-plane stacking of the molecules could also be observed by AFM. In Figure 5.9 high resolution images are shown. The stripes seen in those images are parallel to the long edges of the observed needles. The average distance between the stripes is 9.5 ± 0.6 Å. Along the stripes a second periodicity of 4.4 ± 0.6 Å can be observed [117]. The direction of the observed stripes can be assigned to the *b*-axis of the monoclinic structure, and thus the stripes are columnar stacks of molecules. The *c*-axis of the substrate is approximately along the perpendicular to the direction defined by the needles shown in Figure 5.8(b). However, the AFM measurements do not allow to determine a relationship between the unit cells of the layer and the substrate.

As we show in Section 5.1, the formation of needle-like crystallites has been also observed for the films on SiO_2, in which case the crystallites were randomly oriented in the plane. In addition the dimensions of the needle can be several orders of magnitude larger in films on Al_2O_3 than in films on SiO_2. Thus, the

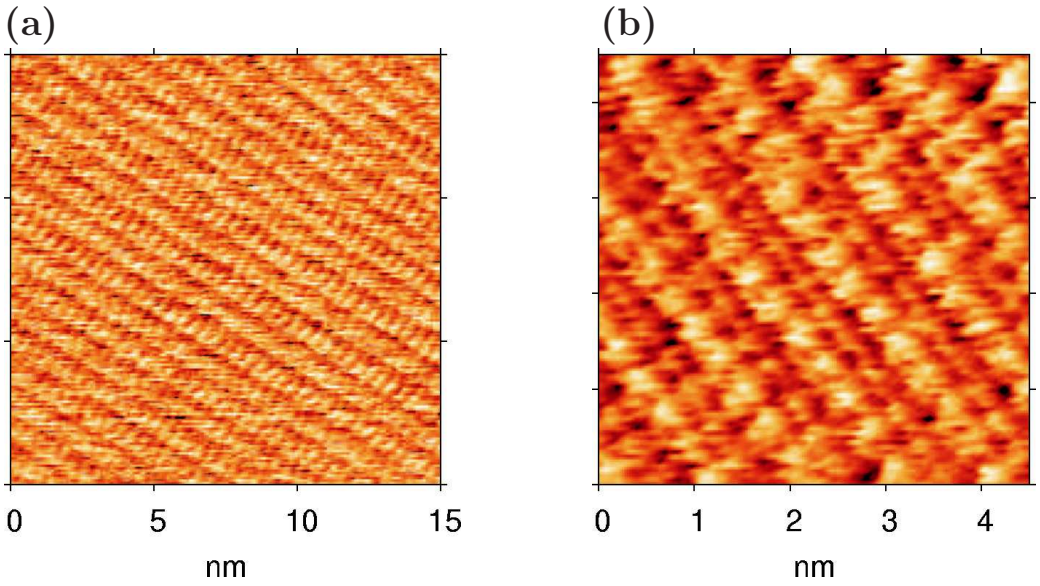

Figure 5.9: High resolution AFM topographical images showing two in-plane periodicities of 9.5 Å and 4.4 Å. The direction of the stripes is assigned to the b-axis of the layer, in which direction the molecules stack in molecular columns parallel to the needles observed in Figure 5.8 [117].

formation of the needle-like shaped crystallites is a characteristic property of this material, which has been observed in thin films of other derivatives [60, 61] and also in single crystal growth of many phthalocyanines [115]. As we have shown, the deposition on Al_2O_3 leads to unidirectionally aligned needles with enhanced dimensions.

The in-plane structure of the layers has been also studied by GIXD. The reflection at $q_{\|} = 1.982$ Å^{-1} found in the films on SiO_2 has been also observed in the films on Al_2O_3. This Bragg reflection is shown in the radial x-ray scan shown in Figure 5.10(a) for two films of different thicknesses deposited at $T_g = 230°C$. However, films on Al_2O_3 show a preferred in-plane orientation of the crystallites revealed by the azimuthal distribution of this reflection. An in-plane "rocking" scan (performed by rotating the sample around its azimuth while the scattering vector is kept constant) is shown in Figure 5.10(b), the modulation of this Bragg reflection as the sample is rotated reveals the azimuthal distribution of the organic crystallites in the film. Thus, the width of this peak is a measure of the degree of in-plane alignment or "in-plane mosaicity". As we discuss in Section 5.5 the

characteristics of this peak vary with the growth conditions.

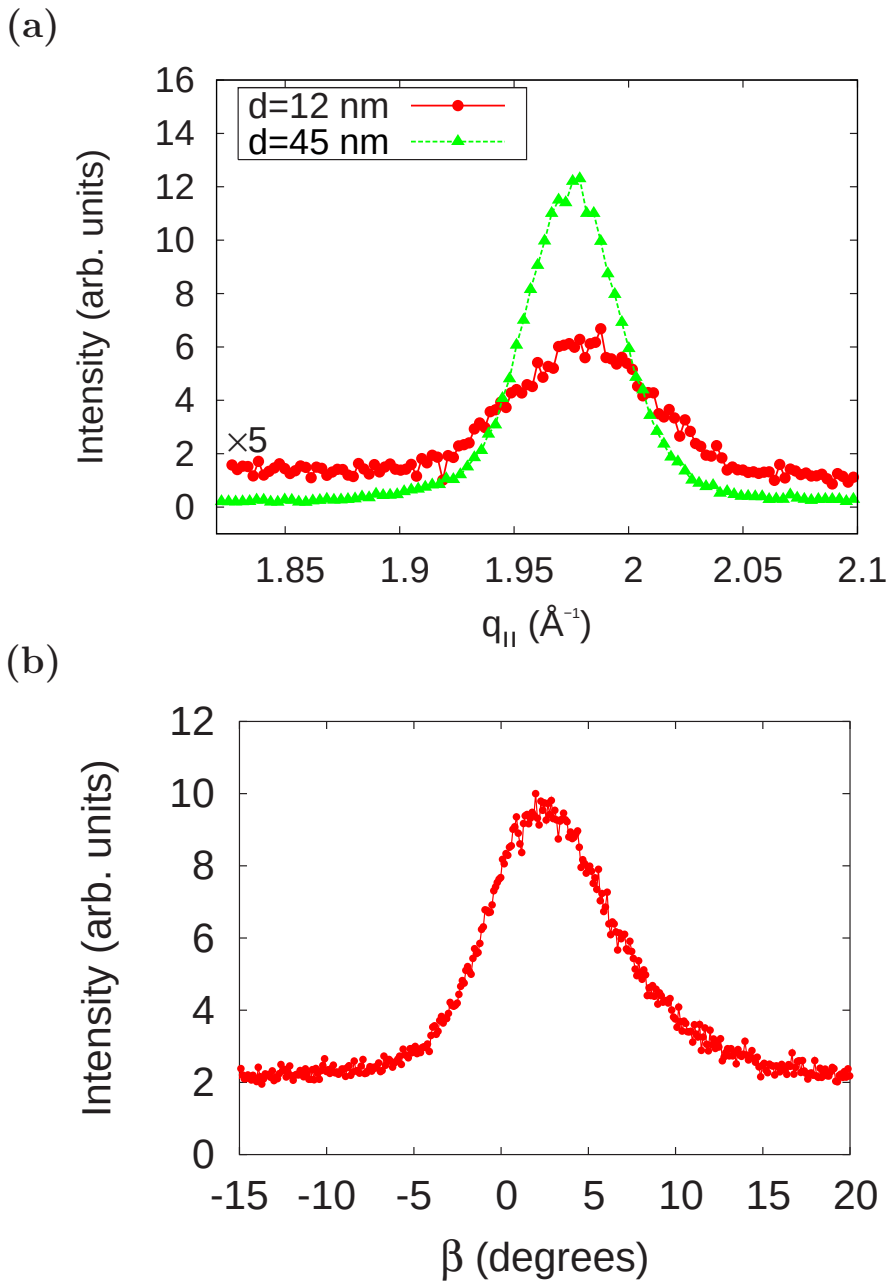

Figure 5.10: (a) In-plane Bragg reflection at $q_z = 1.982$ Å^{-1} measured in two samples grown at $T_g = 230°C$ with thicknesses of 12 and 45 nm. The curve representing the data of the thinner film has been magnified by a factor of 5 for clarity reasons. (b) Azimuthal dependence of the in-plane reflection of the 12 nm film shown in (a). The x-axis is the azimuthal orientation of the sample, where $\beta = 0$ is the direction defined by the c-axis of the Al_2O_3 substrate.

5.3.2 Optical properties

The in-plane orientation of the films is reflected in the optical properties of the layers. As we have seen in Section 5.1, the layers grown on SiO_2 are optically isotropic due to the randomly oriented crystallites that conform the organic film. In the present case, ellipsometric measurements at different azimuthal orientations of the sample differ substantially. This is due to the intrinsic strong anisotropic properties of $F_{16}CuPc$ and to the fact that the crystallites are also oriented in the plane of the layer. As we have seen in Section 4.3, spectroscopic ellipsometry is a very useful technique to deal with anisotropic materials. The β-scan method (see Section 4.3 and reference [104]) allows to determine the orientation of the dielectric tensor of the samples, and therefore simplifies the interpretation of the ellipsometric data acquired at high symmetry orientations of the anisotropic sample.

A typical monoclinic crystalline structure of a phthalocyanine layer on a substrate is indicated schematically in Figure 5.11. The definitions of the principal axes of the dielectric tensor of the organic layer (X, Y, Z), the laboratory axes (x, y, z), and the angles β (azimuthal orientation of the sample) and $\beta_\circ$ (angle between the c-axis of the substrate and the Y axis) are also given in Figure 5.11. The optical response of the individual crystallites is highly anisotropic. However, the ellipsometric measurements contain averaged information of their dielectric tensor, and the films behave as an effective dielectric medium. The dielectric tensor derived from the measurements bears information about the nature of the crystallites and their distribution.

The orientation of the principal axes of the dielectric tensor can be obtained from β-scan measurements. A set of β-scan curves of a 45 nm thick $F_{16}CuPc$ film on Al_2O_3 is shown in Figure 5.12. The values of the ellipsometric parameters $\tan\Psi$ and $\cos\Delta$ are plotted as a function of the azimuthal orientation of the sample $\beta - \beta_\circ$, and their exact values depend on each sample, on the measurement energy, and on the incident angle. The curves are measured for different analyzer angles $A = 5$, 10, 20, and 30° and at a fixed energy of $E = 1.5$ eV. We can see that the curves exhibit strong variations as a function of the angle β. This is due to the strong optical anisotropies of the layer. Interestingly, they present a 180° symmetry and the curves for different analyzer positions cross every 90°. Such an

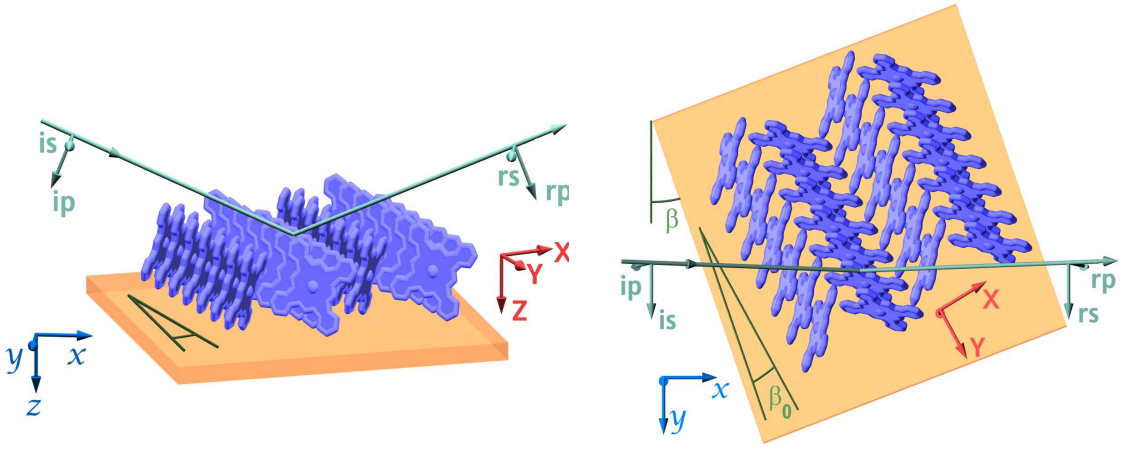

Figure 5.11: Schematic representations of a typical phthalocyanine crystalline structure indicating the measurement configuration and the definitions of the principal axes of the dielectric tensor of the organic layer (X, Y, Z), the laboratory axes (x, y, z), and the angles β and β_o.

azimuthal dependence is characteristic of a sample with two principal axes in the surface plane [104]. The direction of those axes is given by the points where the curves cross. At these positions the non-diagonal terms of the reflection matrix vanish, $R_{sp} = R_{ps} = 0$ (see Section 4.3 and Equation (4.12)) and thus the values of the ellipsometric parameters are independent of the analyzer angle. Moreover, these orientations show no dispersion as a function of energy, as a monoclinic symmetry would allow. Thus, β-scans at different energies show the same behavior, i.e., the crossings are at the same sample orientations. In a bare Al_2O_3 substrate the highest anisotropy of the measured $\tan\Psi$ is lower than the 1% of the total observed in most of the $F_{16}CuPc$ layers. Furthermore, there are no electronic transitions of the substrate in the measured spectral range, and therefore, the observed structures and their large anisotropies stem from the organic films, whose optical spectra can be numerically obtained by simplifying the general anisotropic case to a biaxial layer on an isotropic substrate in an isotropic ambient.

We have performed numerical fits of groups of spectra measured at different angles of incidence at the four symmetric azimuths with x either along X or Y [82]. The seven fitted parameters are the unknown three complex components of N_1 and the layer thickness d_1. The layer thickness can be best determined in the region of transparency of the phthalocyanine layer [118] (below 1.4 eV and

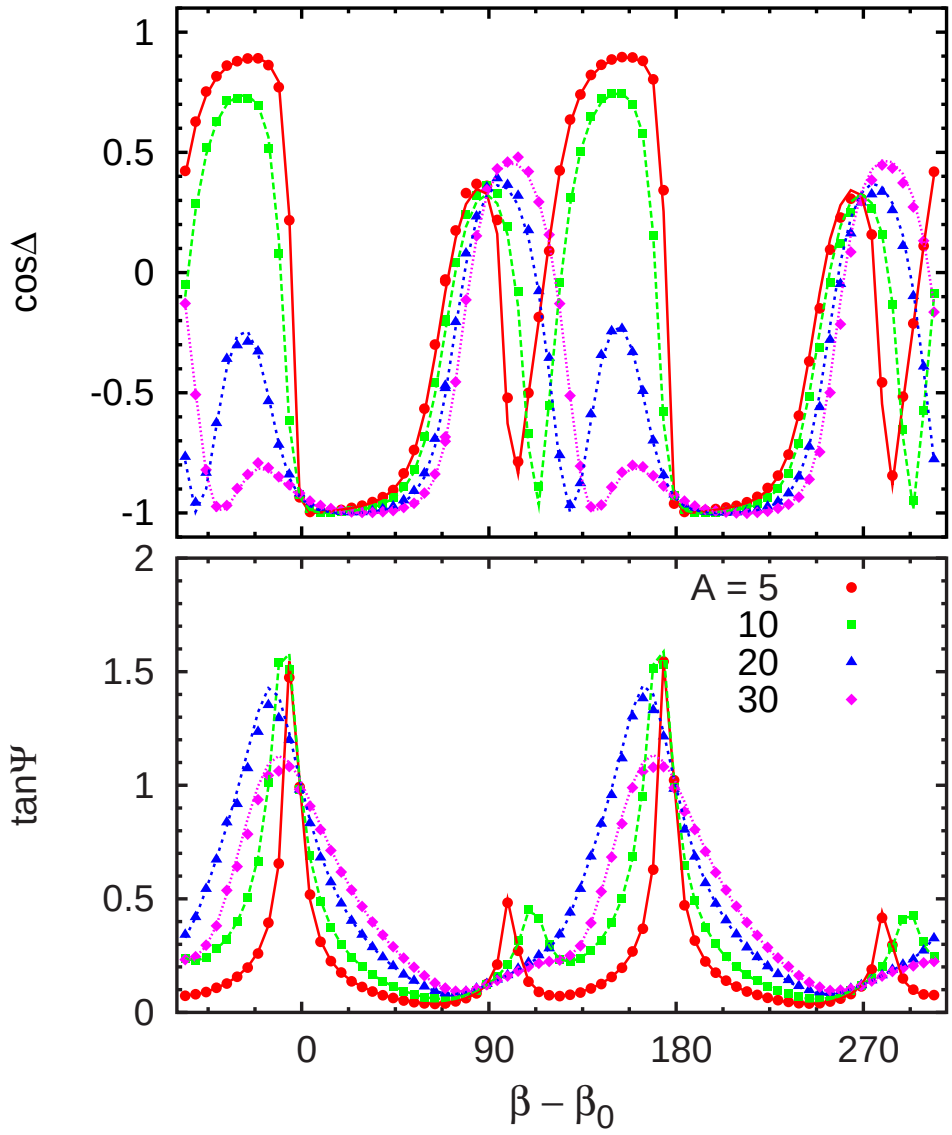

Figure 5.12: β-scans of a $F_{16}CuPc$ film on Al_2O_3 with $D = 45$ nm and $T_g = 230°C$. The curves have been taken at different values of the analyzer and at the fixed energy of 1.5 eV.

around 2.5 eV). To fit the dielectric tensor we have typically eight independent measurements (two orientations at two angles of incidence).

Thus, performing spectroscopic measurements at the azimuthal orientations given by the crossing points of the β-scans, we can obtain the components of the dielectric tensor shown in Figure 5.13 (i.e. ε_X and ε_Y). These components are obtained by considering the observed biaxial (orthorhombic-like) behavior. The particular orientation of the tensor is rather unfavorable to allow a precise measurement of the perpendicular component, specially because its value results very similar to the largest component of the in-plane functions (ε_X). In addition, measurements at different incident angles have been performed to detect possible differences between the spectra due to the different weight of this z-component as the incidence angle is changed. No significant difference has been found between these spectra, supporting the fact that $\varepsilon_Z \simeq \varepsilon_X$. Therefore we have considered a uniaxial behavior with ordinary components $\varepsilon_Z = \varepsilon_X$ and an extraordinary component ε_Y. The lower values of ε_Y, which imply a lower polarizability, are associated with the b-axis orientation in the phthalocyanine crystals in which the molecules stack. Thus, the Y component is identified with the in-plane orientation defined by the needles measured by AFM (see Figures 5.8 and 5.9), and the measurements are in agreement with the molecular needles being almost aligned along the substrate c-axis, with a difference of $\beta_\circ \simeq 4^\circ$ derived from the comparison of the layers with the bare substrate.

In Figure 5.13 we have also plotted the isotropic effective dielectric tensor of a layer deposited on MgO (ε_{ISO}). As expected, the values of the isotropic layer lie between the two in-plane components of the anisotropic films, since it is a certain average of those curves. As we already mentioned in Section 5.1.2, the observed transitions in this spectral range are $\pi - \pi^*$ transitions characteristic of the phthalocyanine ring [119]. The structured band centered at 1.8 eV is identified as the Q-band, and that at 3.4 eV as the B-band or Soret band. The Q-band has been studied for many phthalocyanine complexes [120] and is related to the formation of singlet excitons ($S_0 \rightarrow S_1$ transitions) in the phthalocyanine ring. Information about the relative orientation of the molecules in the crystalline structure may be extracted from the details observed in this Q-band, where three different components can be found. Two of them have been reported for CuPc at about 1.75 and 1.95 eV [120–122]. The third component is a sharp peak at 1.55 eV usually not present for other phthalocyanines complexes. After a second

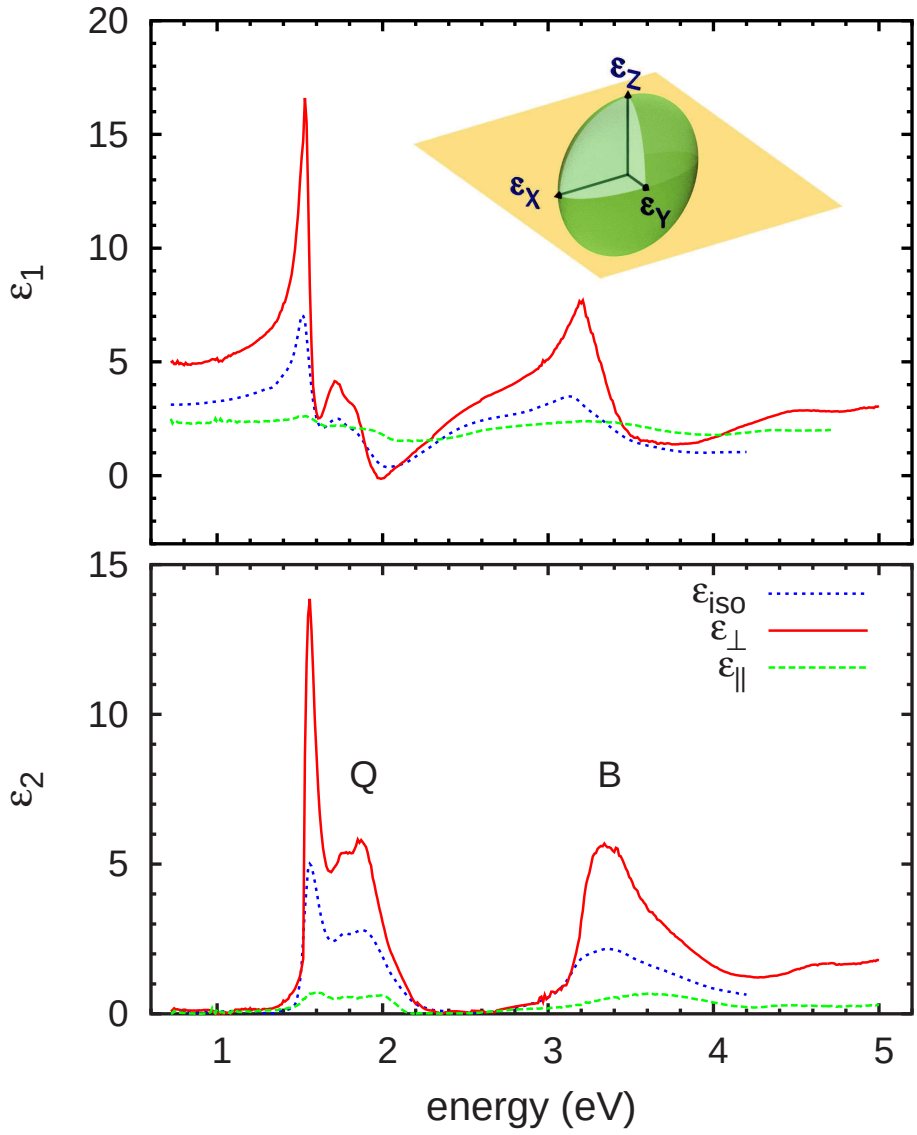

Figure 5.13: Complex dielectric tensor $\varepsilon_1 + i\varepsilon_2$ of two $F_{16}CuPc$ layers deposited at the same growth conditions on Al_2O_3 and MgO. The in-plane components of the layer on Al_2O_3 are ε_X and ε_Y, those measurements have been performed at the azimuthal orientations given by the crossing points of Figure 5.12. As expected, ε_{iso} takes values between the two components ε_X and ε_Y, being thus a certain average of these components.

derivative of the spectra is performed, it can be observed that the broad structure at 1.95 eV is composed of two bands close to 1.9 and 2.0 eV. It is interesting to note that these features are mainly associated with the ε_X component of the fitted dielectric tensor (see Figure 5.13) while the ε_Y component is less structured. These observations are consistent with a monoclinic structure as represented in Figure 5.11 where the monoclinic b-axis is almost parallel to the substrate c-axis, with an angle between them of $\beta_\circ \simeq 4°$. Thus, the stacking direction of molecules is nearly parallel to the c-axis, with the molecules in a stand-up configuration, as observed also by x-ray diffraction, AFM, and also Raman scattering (see Section 5.4). Such a molecular orientation would also justify the similarity between ε_X and ε_Z, both associated with dipoles of the molecular planes.

5.4 Raman scattering on F_{16}CuPc thin films

Raman scattering measurements are very sensitive to the degree of order of the molecular films. As we show in this section, this technique allows the quantification of molecular order of the films, as well as the determination of the orientation of the molecules. The results are consistent with a type of ordering in which the molecular planes form a finite angle $\alpha_\circ$ with the substrate surface, in accordance with the previously discussed results obtained from x-ray diffraction, AFM, and ellipsometry. The in-plane orientation of the films on Al_2O_3 can be well characterized by Raman scattering. Measurements at different azimuthal angles of the sample allow the direct determination of the orientation of the layer relative to the substrate structure, as well as the quantification of the degree of order present in the layers.

All measurements were performed in the backscattering configuration and in the 150 to 1600 cm^{-1} frequency shift interval. Spectra with parallel (P) and crossed (C) polarizations were recorded. These are designated, respectively, by: $\bar{z}'(x',x')z'$ and $\bar{z}'(x',y')z$', where z' is the laboratory axis perpendicular to the film surface (the $x'y'$-plane) (see Figure 5.14). The scattered intensity depends on the relation of these laboratory axes and the symmetry axes of either the molecule or the crystal, which are designated by X, Y, and Z, the latter being parallel to the C_4 symmetry axis of the F_{16}CuPc molecule or to the C_2 axis of the corresponding monoclinic crystal. The choice of X and Y axes in the plane of the molecule, among the two possibilities for a molecule of tetragonal symmetry,

is indicated in Figure 5.14(a). While for the isotropic films on SiO_2 and MgO the azimuthal orientation of the sample does not have an influence on the measured spectra, the in-plane oriented layers on Al_2O_3 show different spectra at different azimuthal orientations. Thus, for those films, Raman measurements were taken at several azimuthal angles by rotating the sample around the axis perpendicular to its surface. With this technique we can use the Raman lines arising from the substrate in the same spectra to determine the relative orientation of the organic layer. The orientation of the sapphire substrate will be denoted by the coordinate system axes X', Y' and Z', where the crystallographic sapphire c-axis coincides with Y' while Z' is perpendicular to the substrate surface. The axes definitions are illustrated in Figure 5.14(b) and (c). In all experiments, the incident polarization was kept constant along the x' axis. For measurements of the angular dependence of the intensity of the Raman peaks, the sample was mounted on a goniometer, which was manually rotated in different angular increments (mostly of 5° or 10°), around the z' axis. Care was taken in centering the sample so that upon rotation the beam remained within a narrow region around the initial spot. We estimate that all our angular measurements were performed within a circle with a diameter not larger than ten times the size of the laser spot (i.e., about 15 μm). For these experiments, the rotation angle, β, is defined as that between the laboratory x'-axis and the X'-axis of the sapphire A-plane substrates (see Figure 5.14). The value of β is determined by monitoring the intensity of the A_{1g} peak of sapphire, located at 644 cm^{-1}, in both parallel and crossed polarizations. Because this is an A_{1g} vibration with only $Z'Z'$ component ($a_s \simeq 0$) its intensity depends on β through [123]

$$I(x', x') = b_s^2 \sin^4 \beta, \qquad I(x', y') = \frac{b_s^2}{4} \sin^2 2\beta \tag{5.3}$$

where b_s is an amplitude parameter, obtained in arbitrary units by fitting the Raman intensity of this peak as a function of β with Equations (5.3). This expression was tested by measuring the Raman response of a bare substrate and found to describe the observed angular dependence of the intensities within a 1% accuracy. These spectra were also used to identify and subtract from the spectra of the films those peaks arising from the substrate. The orientation of the molecules (or crystallites where applicable) on the substrate is defined by two angles: $\alpha_\circ$, the angle between the Z and z' axes, and $\delta_\circ$ defining the angle between the molecular planes in the monoclinic unit cell. Finally, $\beta_\circ$ is the angle between the X and

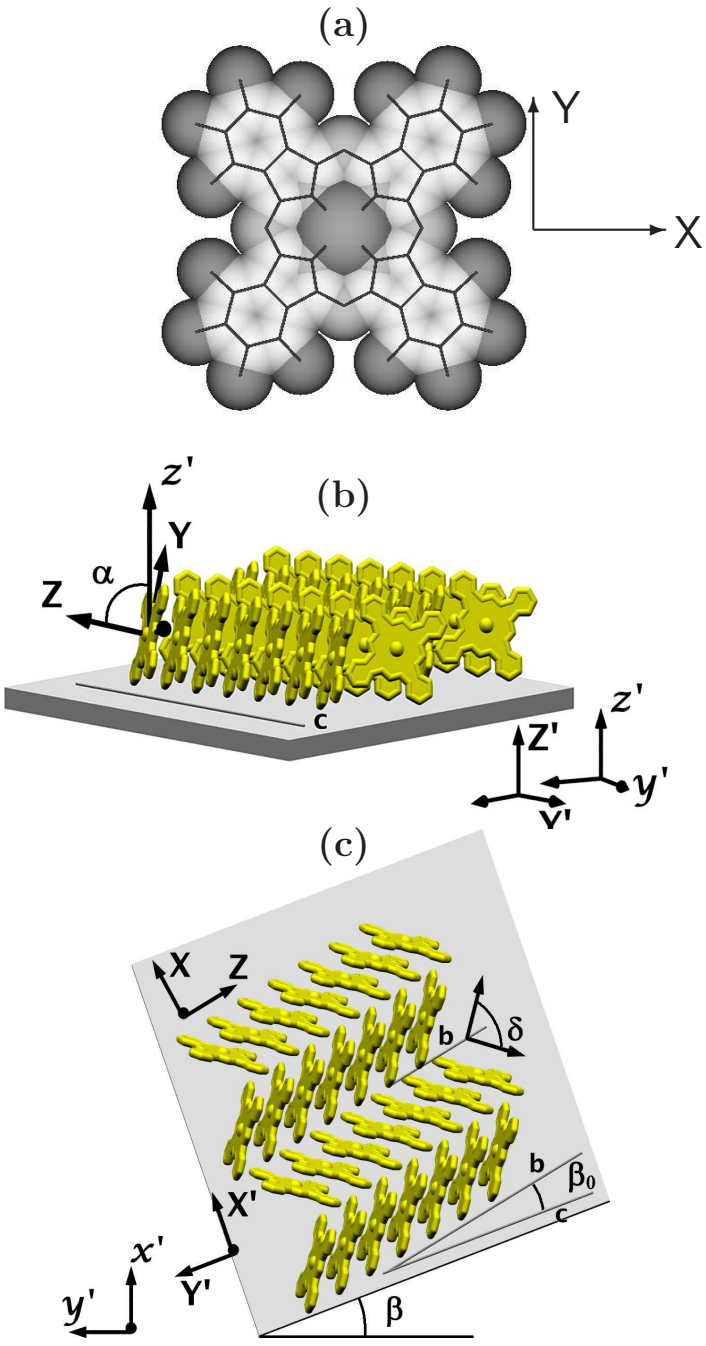

Figure 5.14: (a) Definition of the X and Y axis used for the normal mode calculations. (b) Side view and (c) top view of the definition of the coordinate systems used. XYZ define the principal axes of the crystal with monoclinic symmetry, $x'y'z'$ are the laboratory axes, and $X'Y'Z'$ define the substrate orientation, with Y' parallel to the Al_2O_3 c-axis. Also shown are the definitions of the angles α and δ that define the molecular orientation and $\beta_\circ$ accounting for the orientation of the film relative to the substrate (angle between the X and X' axes).

X' axes (assumed to be on the $x'y'$-plane) that accounts for small alignment differences between those axes, this angle has been independently observed also by ellipsometry (Section 5.3.2).

5.4.1 Differences in the spectra of films on different substrates

Raman scattering measurements on samples on the different substrates used are plotted in Figure 5.15. Both polarizations show similar spectral features in all samples. However, while the spectra at parallel (P) and crossed (C) polarizations of the films on SiO_2 and MgO are very similar, significant differences appear between both polarizations in the spectra of the film on Al_2O_3. This is due to the in-plane ordering of those films, as is reflected in the strong changes between spectra taken at different azimuthal orientations. As we discuss later, from this dependence we can obtain information on the degree of order, as well as on the molecular orientation. Films grown on Al_2O_3 substrates show more spectral features, with higher intensities and narrower lines. This is shown in Figure 5.16 where the P-polarized spectra for two films grown at the same conditions ($T_g = 230°C$, $D = 20$ nm) on Al_2O_3 and SiO_2 are shown. Both spectra show the same lines and are qualitatively similar, however their intensities are different. The higher intensity of the spectrum of the sample on Al_2O_3 is clearly reflected in the higher signal to noise ratio of the spectra. This is an important difference between these films, since evidences a higher crystallinity of the layers on Al_2O_3. The higher "quality" of the spectra of the films on Al_2O_3, and the fact that these films are in-plane ordered facilitate the assignment of the Raman modes. Thus, in what follows we shall center our discussion on films on Al_2O_3 substrates.

5.4.2 Symmetry considerations

As we already stated, $F_{16}CuPc$, as most of the metallo-phthalocyanines, is a planar molecule with D_{4h} symmetry. The normal vibrations of this type of molecule are distributed among the representations of the D_{4h} point group according to [124, 125]:

$$\begin{aligned}\Gamma(\text{vib}) &= 14\,A_{1g} + 13\,A_{2g} + 14\,B_{1g} + 14\,B_{2g} + 13\,E_g + \\ &+ 6\,A_{1u} + 8\,A_{2u} + 7\,B_{1u} + 7\,B_{2u} + 28\,E_u \end{aligned} \quad (5.4)$$

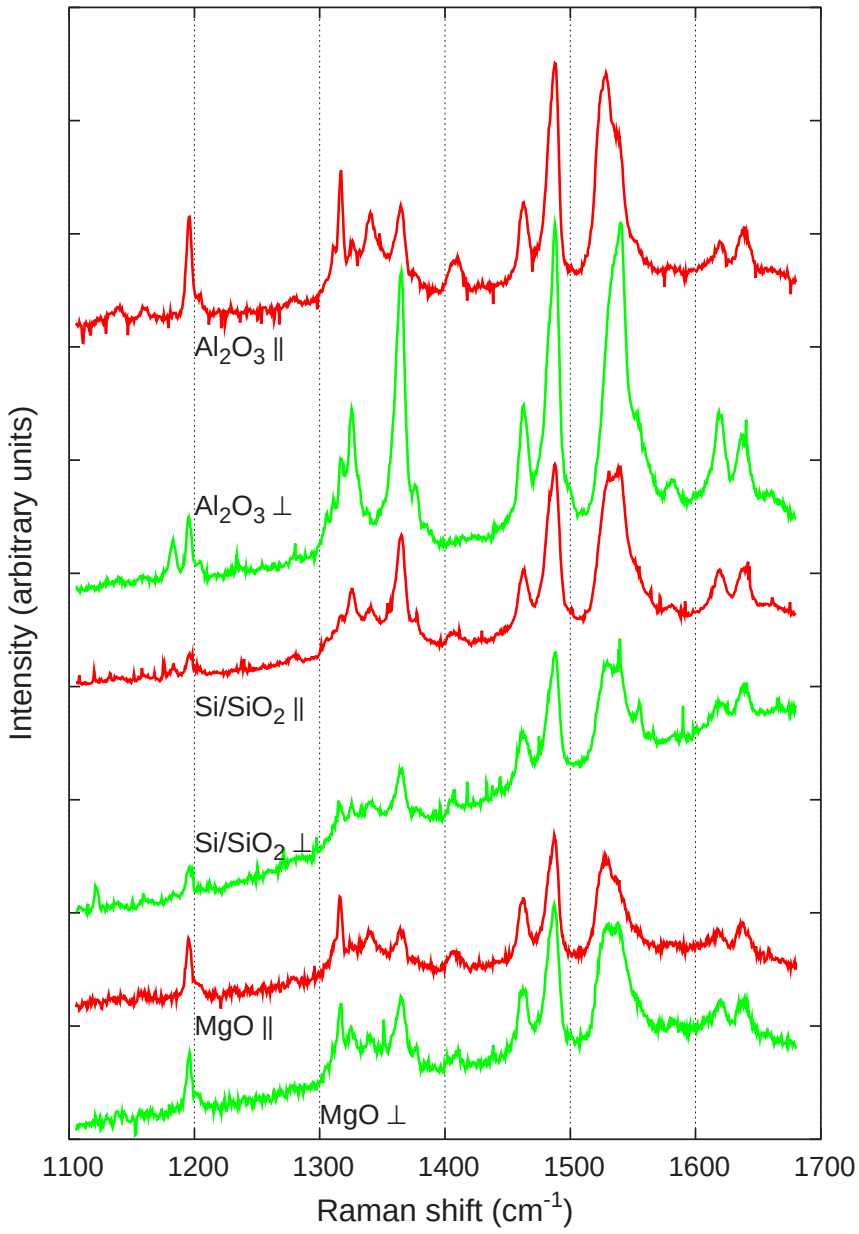

Figure 5.15: Parallel and crossed polarization spectra of an F_{16}CuPc film on the various substrates. Significant differences between both polarizations are only observed in the film on Al_2O_3.

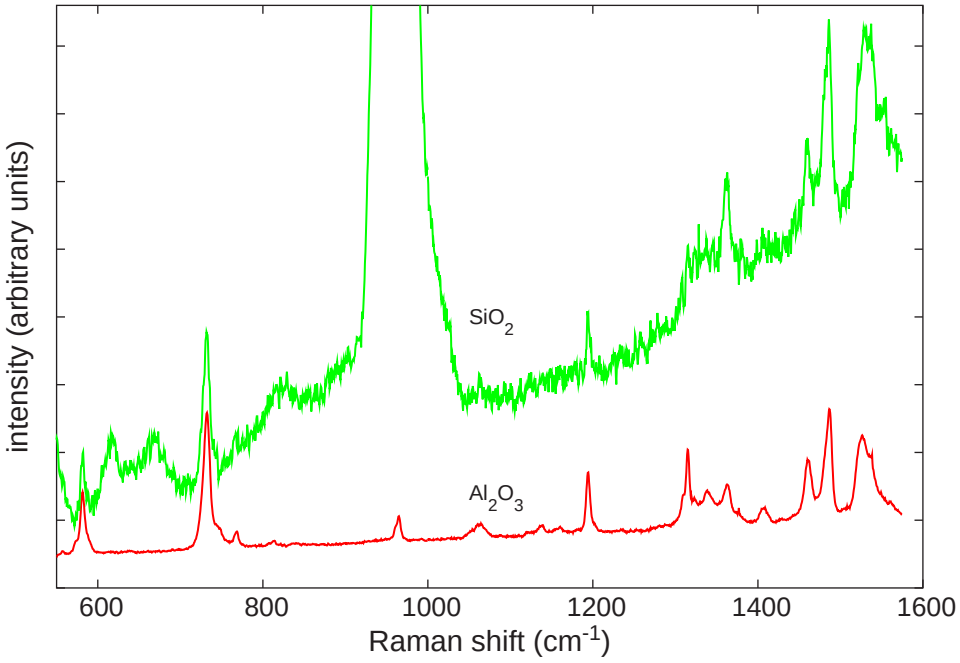

Figure 5.16: Comparison between the spectra in parallel polarizations of two layers with $D = 20$ nm and $T_g = 230°C$ deposited on SiO_2 and Al_2O_3. Although both spectra show the same lines, the quality of the film on Al_2O_3 is higher as evidenced by sharper peaks and higher intensity. The large peak around 950 cm^{-1} is a second order peak from the Si substrate.

of which only the A_{1g}, B_{1g}, B_{2g} and E_g modes are Raman active. The Raman tensors of these modes have the form [125]:

$$A_{1g}: \begin{pmatrix} a_o & 0 & 0 \\ 0 & a_o & 0 \\ 0 & 0 & b_o \end{pmatrix}, \quad B_{1g}: \begin{pmatrix} c_o & 0 & 0 \\ 0 & -c_o & 0 \\ 0 & 0 & 0 \end{pmatrix}, \quad B_{2g}: \begin{pmatrix} 0 & d_o & 0 \\ d_o & 0 & 0 \\ 0 & 0 & 0 \end{pmatrix}$$
$$E_g: \begin{pmatrix} 0 & 0 & 0 \\ 0 & 0 & e_o \\ 0 & e_o & 0 \end{pmatrix}, \text{ and } \begin{pmatrix} 0 & 0 & e_o \\ 0 & 0 & 0 \\ e_o & 0 & 0 \end{pmatrix}. \tag{5.5}$$

These tensors refer to the molecular symmetry axes (see Figure 5.14), with Z being the C_4 axis and XY defining the molecular plane.

In the crystal, molecular vibrations undergo two types of changes. First, mode frequencies of all modes may be shifted while the reduced symmetry of the unit cell may produce splittings in degenerate molecular modes (E_g). Raman selection

rules are changed, in order to obey those of the Raman tensors corresponding to the point group of the crystal (C_{2h}), rather than that of the free molecule (D_{4h}). The second effect may appear when there is more than one molecule per unit cell, splitting non-degenerate molecular modes into multiplets. This effect, called correlation field effect or *Davydov splitting*, is due to the coupling between the internal vibrations of the symmetry equivalent molecules in one unit cell. In addition to the internal molecular modes, modified to a greater or lesser extent by the crystal structure, there are also external modes originating in rigid vibrations or rotations of the molecules within a unit cell. Since the inter-molecular forces are usually much weaker than the covalent intra-molecular ones and since the masses involved are higher, the corresponding modes normally appear at low frequencies and their observation usually requires the use of a vacuum chamber where the sample is kept to exclude low frequency spectral features originated in air and atmospheric water. Since our samples were not kept in such a chamber during the measurements we limit our discussion to spectral features above 150 cm^{-1} which correspond to internal molecular vibrations.

In a monoclinic centrosymmetric F_{16}CuPc crystal with two molecules per unit cell, the vibrational modes are distributed among the irreducible representations of the factor group C_{2h} according to [126, 127]:

$$\begin{aligned} \Gamma(\text{external}) &= 3A_g + 3B_g + 2A_u + B_u \\ \Gamma(\text{internal}) &= 81A_g + 81B_g + 84A_u + 84B_u \end{aligned} \tag{5.6}$$

Of these, only the A_g and B_g modes are Raman active, with Raman tensors of the general form:

$$A_g : \begin{pmatrix} a & d & 0 \\ d & b & 0 \\ 0 & 0 & c \end{pmatrix}, \qquad B_g : \begin{pmatrix} 0 & 0 & e \\ 0 & 0 & f \\ e & f & 0 \end{pmatrix}. \tag{5.7}$$

In the above expressions, a set of axes (X, Y, and Z) is chosen so that the crystallographic (C_2 or b-axis) is along the Z direction and the XY-plane is perpendicular to it as shown in Figure 5.14.

The analysis and interpretation of the behavior of the Raman lines observed can be performed by considering either the molecule or the crystal, as we show in the following section.

5.4.3 Mode assignment

Several Raman studies of hydrogenated CuPc and related materials are available in the literature [60, 125–130]. However, the criteria for mode assignment used in many of them are not entirely reliable. In references [125, 127] measurements on single crystals are used for mode assignment, and in reference [128] powdered samples were used and mode assignment was performed by comparison with porphyrines. However, no agreement is found between both studies. Other authors make mode assignments by attributing spectral features to vibrations of the smaller molecular groups (benzene, pyrrol, etc.) which build up the larger phthalocyanine molecule. In Table 5.2 we compare the frequency and relative intensities of the Raman peaks observed in our experiments and those of references [126, 130], when available. As can be seen there is a good agreement between observed lines, specially considering that the data correspond to spectra of different compounds of the same family.

Raman shift (cm^{-1})				Normalized intensity $I(x'x')$	unpolarized CuPc	
PtPc	CuPc	$F_{16}CuPc$	Ω	$F_{16}CuPc$	514.5 nm	603.2 nm
	169	175	173	220	40	90
225	236	202		94	40	90
275		280	272	40		
		465	468	200		
482	486	471		115	40	280
		512	514	76		
		559	547	40		
607	588	583	588*	737	180	130
679	678	732	722*	1620	280	520
755	743	767	766	143	40	430
	778	814		58	40	70
	831	836	828	283	90	120
955	947	930	948	670	340	34
		962		120		
		966.5		182		

(continued)

PtPc	CuPc	F_{16}CuPc	Ω	F_{16}CuPc	514.5 nm	603.2 nm
	1037	1062	1057	295	60	—
1114	1106				50	200
		1124	1116	36		
1145	1140	1137.5	1153*	460	210	220
		1140		98		
		1151		444		
		1154		Shoulder		
		1161		68		
1196		1182		Shoulder		
1219	1217	1194	1158	736	—	220
		1311		114		
1312	1305	1316	1316*	865		
		1325		38		
		1332		Shoulder	—	260
1343	1341	1340	1339	130 double?	430	340
		1364		230 double?		
		1377	1383	Shoulder		
		1408		174		
1436	1431				50	—
1458	1452	1462	1428	627	260	370
	1470				50	—
	1484	1487		1216	200	—
1530	1528	1523	1525	1000 doublet?	1000	1000
		1538		523 shoulder		
	1590	1561	1559	22 double?	50	—
	1612				30	—
		1620		182		
		1637	1680	374		

Table 5.2: Comparison between Raman lines available in the literature for PtPc [130] and CuPc [126] and the lines observed for the compound F_{16}CuPc. Also listed are the results for A_{1g} vibrational modes of the free molecule from our model calculations (Ω). Shadings indicate doublets arising from a single molecular mode. The vibrational modes associated with the lines labelled with "*" are shown in Figure 5.17.

A more reliable basis for mode assignment is obtained by comparing the experimental data with the results of a model calculation for the normal modes of the free molecule. We have used the B3LYP/6-31G approximation in Gaussian98 [131]. Approximate atom coordinates were obtained from the existing crystal structure data [58, 132] of other phthalocyanines and optimized with Gaussian98 before calculating the normal modes. A comparison between calculated molecular modes and structures in the measured Raman spectra is also shown in Table 5.2, where we list the calculated frequencies Ω. All strong features in the observed Raman spectra can be attributed to A_{1g} molecular modes, although in some cases two experimental peaks must be assigned to the same molecular vibration. This can be explained by the appearance of Davydov doublets, and the corresponding structures are highlighted by shading in Table 5.2. The discussion about the splitting of some lines is discussed in Section 5.4.5. Some vibrational modes are shown in Figure 5.17, where the atomic displacements are indicated by the arrows the length of which is proportional to the amplitude of the atomic movement.

The above discussion assigns all strong spectral features to molecular vibrations of A_{1g} symmetry. This seems to be the case in most of the crystals of planar molecules, as the assignments of other authors show. In the work of references [133, 134] on PTCDA, the spectral features are also derived from A_g (fully symmetric) molecular modes. They attribute this to the proximity between the laser lines used and the HOMO-LUMO optical transitions. The latter produce symmetric charge displacements which only couple to fully symmetric vibrations. This means that only the totally symmetric molecular modes are resonantly enhanced. Since we work under similar circumstances, we expect also that most of the strong peaks in our spectra arise from molecular vibrations belonging to the A_{1g} symmetry. These might still be modified by interactions within the crystal and split into A_g and B_g crystal modes (Davydov splittings) if the unit cell contains more than one molecule and the A_{1g} Raman tensor components a and b are different enough (see Equation (5.4)).

5.4.4 Angular dependence of the intensities

As we discussed earlier, Raman spectra acquired at different azimuthal orientations of the layers allow the study of the degree of in-plane orientation of the crystallites. In the case of measuring at parallel polarization configuration, the intensities of all the strong lines of in-plane oriented films follow a periodicity of 180° as the sample

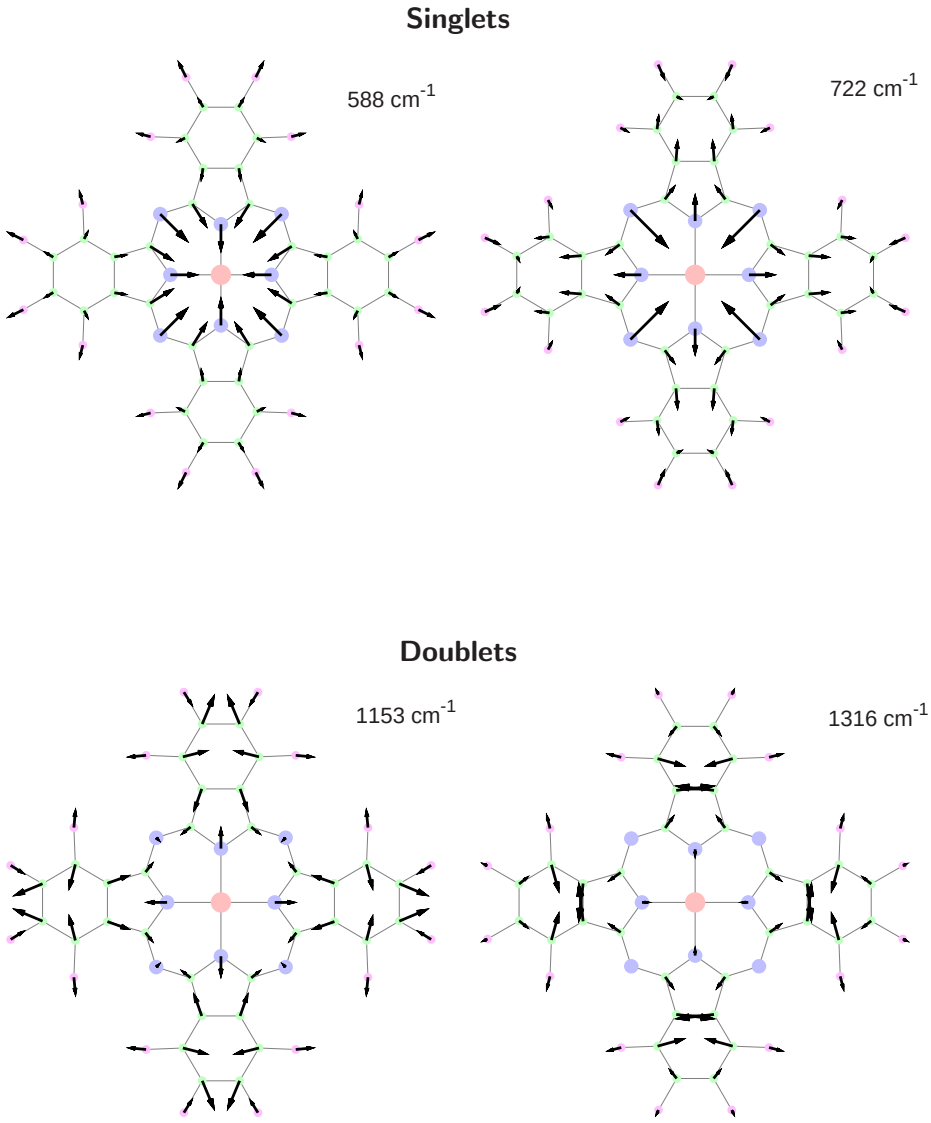

Figure 5.17: Selected A_{1g} vibrational modes of the free F_{16}CuPc molecule for two singlets (588 cm^{-1} and 722 cm^{-1}) and two doublets (1153 cm^{-1} and 1316 cm^{-1}) that present Davydov splitting.

is rotated. The maximum peak intensity is reached when the incoming light is approximately polarized perpendicularly to the Al_2O_3 c-axis, that is $\beta \simeq 0°$, while the minimum is $\beta \simeq 90°$. This is shown in Figure 5.18(b) where the parallel spectra of two layers with thicknesses $D = 5$ and 45 nm are shown for $\beta = 0$, 45, and 90°. The dependence of the peak intensities measured at crossed polarization show two kinds of behavior. For isolated peaks at frequencies below 1250 cm^{-1} there is a 90° symmetry of the spectra, and the maximum intensity is achieved for $\beta \simeq 45°$, as can be observed in Figure 5.18(d). This angular dependence is not found in the case of doublets above 1250 cm^{-1}, as can be observed in Figure 5.18(d). We discuss in detail the observed dependence of such doublets in Section 5.4.5.

The behavior of the parallel and crossed intensities at the lower frequency range can be described by

$$\begin{aligned} I(x',x') &= \left(A\cos^2(\beta-\beta_\circ)+B\right)^2+C \\ I(x',y') &= A'\sin^2(\beta-\beta_\circ)+C' \end{aligned} \tag{5.8}$$

where A, A', C, C', and $\beta_\circ$ are the adjustable parameters, of which $\beta_\circ$ accounts for the possible misalignments between the layer and the substrate, as already stated. The parameters C and C' are a constant background introduced to account for scattering arising from possible disordered parts of the layer, that results in an average intensity for all angular orientations. The angular dependence described by Equation (5.8) is characteristic of fully symmetric modes of either molecular (A_{1g}) or crystalline (A_g) origin. In the latter case, the crystallographic b-axis must be in the plane of the film to display this modulation behavior. The angular dependence of peak intensities can be used to obtain information about the amount of order present in each sample. In-plane disordered layers show no variation in peak intensity with azimuthal angle, while in-plane oriented layers follow intensity modulations as that shown in Figure 5.19 for the Raman line at 733 cm^{-1} (circles). By using Equation (5.8) this angular dependence can be fitted as is shown by the solid line in Figure 5.19, where a ratio of $A/B = 4.87$ is derived from the fit. Structural information can also be extracted from the fit of this azimuthal dependence by using Equation (5.8). The ratio A/B contains information on the orientation of the molecules in the film. If the two molecules in the unit cell were contained in the same plane, then this ratio would be defined by the angle between the normal to the molecular plane and the normal to the plane of the film, defined

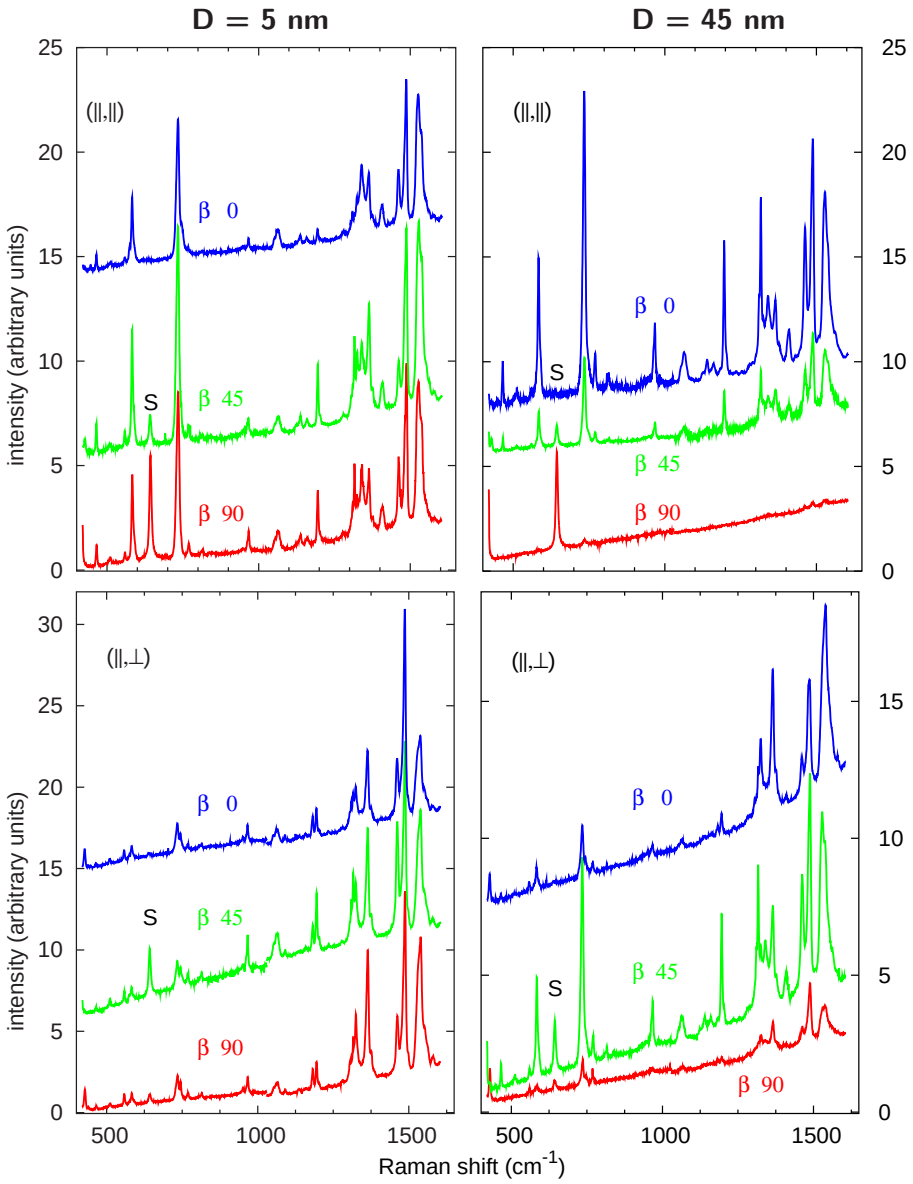

Figure 5.18: Raman spectra in P and C polarization of two layers at different azimuthal orientations (β = 0, 45, 90°). The line at 644 cm^{-1} labelled with "S" arises from the Al_2O_3 substrate.

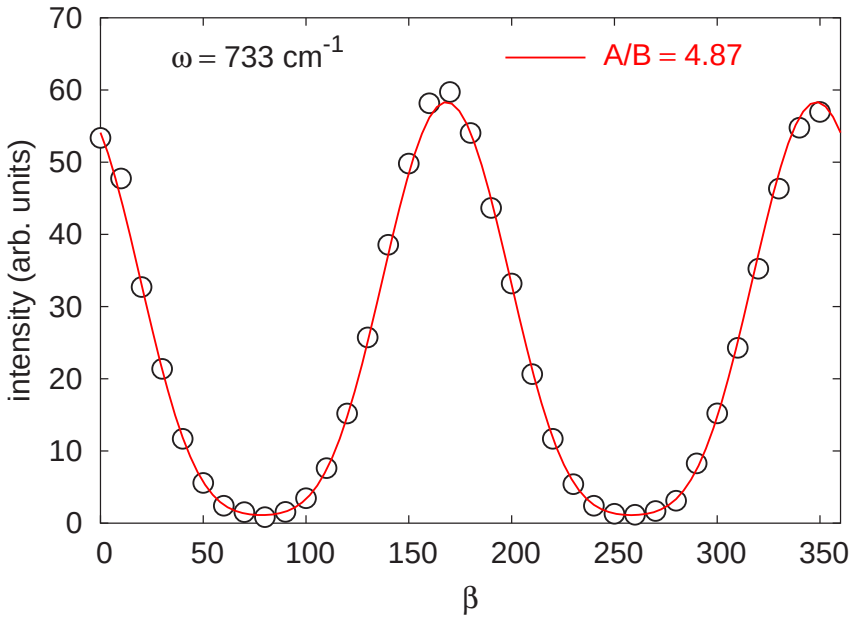

Figure 5.19: Angular dependence of the intensity of the Raman mode observed at 733 cm^{-1} in P polarization of a $F_{16}CuPc$ layer on Al_2O_3 with $D = 20$ nm and $T_g = 230°C$. The experimental points (circles) are fitted (solid line) by using Equation (5.8) from where a value of $A/B = 4.87$ is derived.

in Figure 5.14(b), through the relationship

$$\tan^2 \alpha = \frac{A/B}{1 - \varepsilon(A/B)} \simeq A/B \tag{5.9}$$

where ε is the ratio between the out-of-plane and in-plane components of the molecular Raman tensor for an A_{1g} mode, and for planar molecules $\varepsilon \simeq 0$ [125].[1] However, if the planes of the two molecules form an angle δ (as shown in Figure 5.14), as is usual in phthalocyanine crystals, this ratio would also depend on this angle. Assuming weak intermolecular interaction, as is the case of isolated Raman lines, and having the monoclinic b-axis in the plane of the film, the Raman tensor of some crystal modes of A_g (B_g) symmetry can be derived from those of the molecular modes by making symmetric (antisymmetric) linear combinations of the molecular tensors rotated in relation to one another by an angle of $\pm\delta/2$ about the molecular Y-axis. This produces the required herringbone structure with its backbone (crystalline b-axis) contained in the film plane, and leads to the

[1] Although this is not necessarily true for all Raman modes, this approximation can be assumed for strong isolated lines.

relationship

$$\sin^2(\delta/2) = (A/B + 2)^{-1}[1 - \left(\frac{\varepsilon}{1-\varepsilon}\right)(A/B)] \simeq (A/B + 2)^{-1} \tag{5.10}$$

where, again, we have considered $\varepsilon \simeq 0$ to simplify the equation.

Thus we have seen that the ratio A/B can provide information on the molecular stacking in the film. Although the exact interpretation of this modulation may be difficult, variations of the ratio A/B for different layers imply modifications of their structure, as we show in the next section. The degree of order in the layers can also be quantified through the background constant C (Equation (5.8)), as we show in Section 5.5. Moreover, the phase shift between the angular modulation of the peak originated in the substrate and the peaks from the organic layer determines the relative orientation of the layer relative to the substrate (the angle $\beta_\circ$). We have found that in all layers $\beta_0 = 2.3 \pm 0.7°$. As we discussed in Section 5.3.2, ellipsometric measurements also revealed a small misalignment of the organic layer relative to the substrate c-axis.

5.4.5 Davydov splittings

The mode assignment discussed in Section 5.4.3 attributes two experimental peaks to several molecular modes. This is explained by the appearance of Davydov splittings. In general, the spectral region above 1200 cm^{-1} shows closely spaced structures which are good candidates for assignment to Davydov doublets, while the region below 900 cm^{-1} is composed mainly of isolated structures. Examples of such splittings are found in the phonon frequency regions between 900 cm^{-1} and 980 cm^{-1} and between 1300 cm^{-1} and 1340 cm^{-1} (Figure 5.20). The calculated normal mode amplitudes corresponding to different strong spectral features are shown in Figure 5.17, together with our assignment to singlets and doublets. Comparing both types of structures it is apparent that the singlets involve distortions of the internal macrocycle while the doublets predominantly contain motions of the more peripheral atoms. This is to be expected since the strength of the interaction responsible of the splitting is higher for the modes that involve peripheral atoms.

Clusters of peaks occur in the high frequency range ($\omega > 900$ cm^{-1}) of the spectrum. While the angular dependence of some of these peaks at P polarization

spectra is qualitatively similar to those of the isolated peaks at lower frequencies, the dependence in C polarization is clearly different, this can be seen in the selected doublets shown in Figure 5.20, where the maxima and minima peak intensities are located at different angular values. This behavior is consistent with the existence of Davydov doublets in which the A_g members have intensities described by Equations (5.8), while the B_g members would have intensities depending on the rotation angle according to

$$\begin{aligned} I(x', x') &= e^2 \sin^2 2(\beta - \beta_0) + C \\ I(x', y') &= e^2 \cos^2 2(\beta - \beta_0) + C' \end{aligned} \tag{5.11}$$

where we have assumed that the b-axis of the crystal lies in the plane of the film. Figures 5.20(a) and (c) show structures that do not follow Equations (5.8) but are in qualitative agreement with the dependence described by Equations (5.11). This suggests that these structures behave according to the B_g symmetry of the crystal.

A quantitative comparison between the predictions of these equations and experimental data can be performed on the doublet indicated by vertical lines in Figure 5.20(a) at 1316 and 1324 cm^{-1}, assigned to A_g and B_g symmetry, respectively. The measured splitting of 8 cm^{-1} is comparable to those observed in other organic molecules as PTCDA[133]. The determination of the azimuthal modulation of the two peaks is not straightforward since the lines are very close together and have very different intensities, especially for the B_g member of the doublet. This azimuthal dependence is displayed in Figure 5.21(a) for P-polarization and 5.21(b) for C-polarization, respectively. In these figures, circles and triangles denote experimental intensities for the A_g and B_g members of the doublet, while solid and dashed lines represent fits with Equations (5.8) and 5.11, respectively. In the upper part of the figure, the intensity of the B_g member of the doublet has been multiplied by a scaling factor of 10 for clarity reasons. Since this peak is very weak and overlaps on its much more intense A_g partner, this data is affected by very large uncertainties. In view of this, it is not surprising that the agreement between the data and the predictions of Equations (5.11) for this peak is only qualitative. In spite of these difficulties, the angular dependence of the intensities of both peaks is well described by the equations corresponding to either A_g or B_g crystal symmetry. Quantitative agreement is best for the parallel polarization line of the A_g member of the doublet (Figure 5.21(a), circles and solid line).

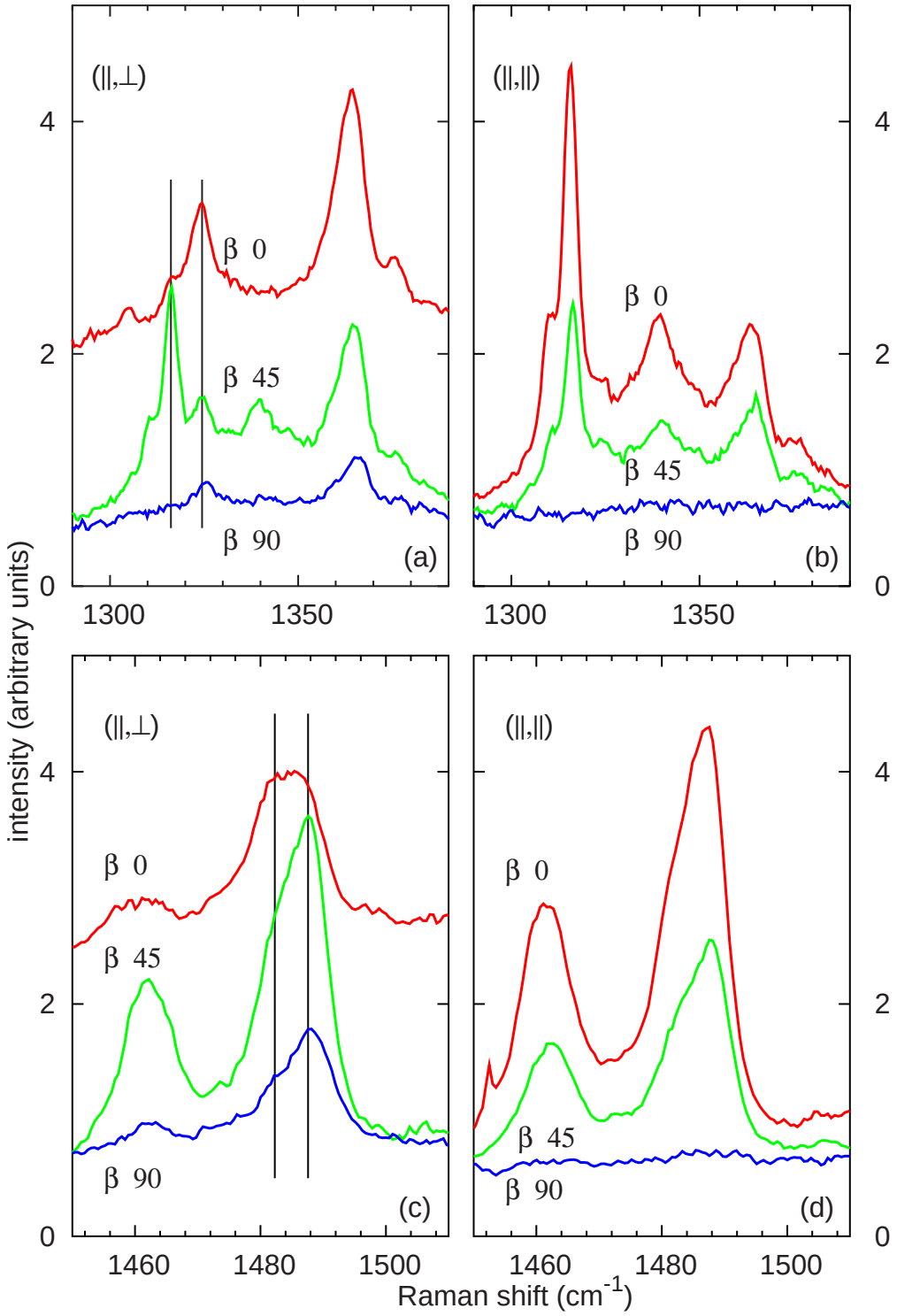

Figure 5.20: Angular dependence of two Davydov pairs in selected parts of the Raman spectra.

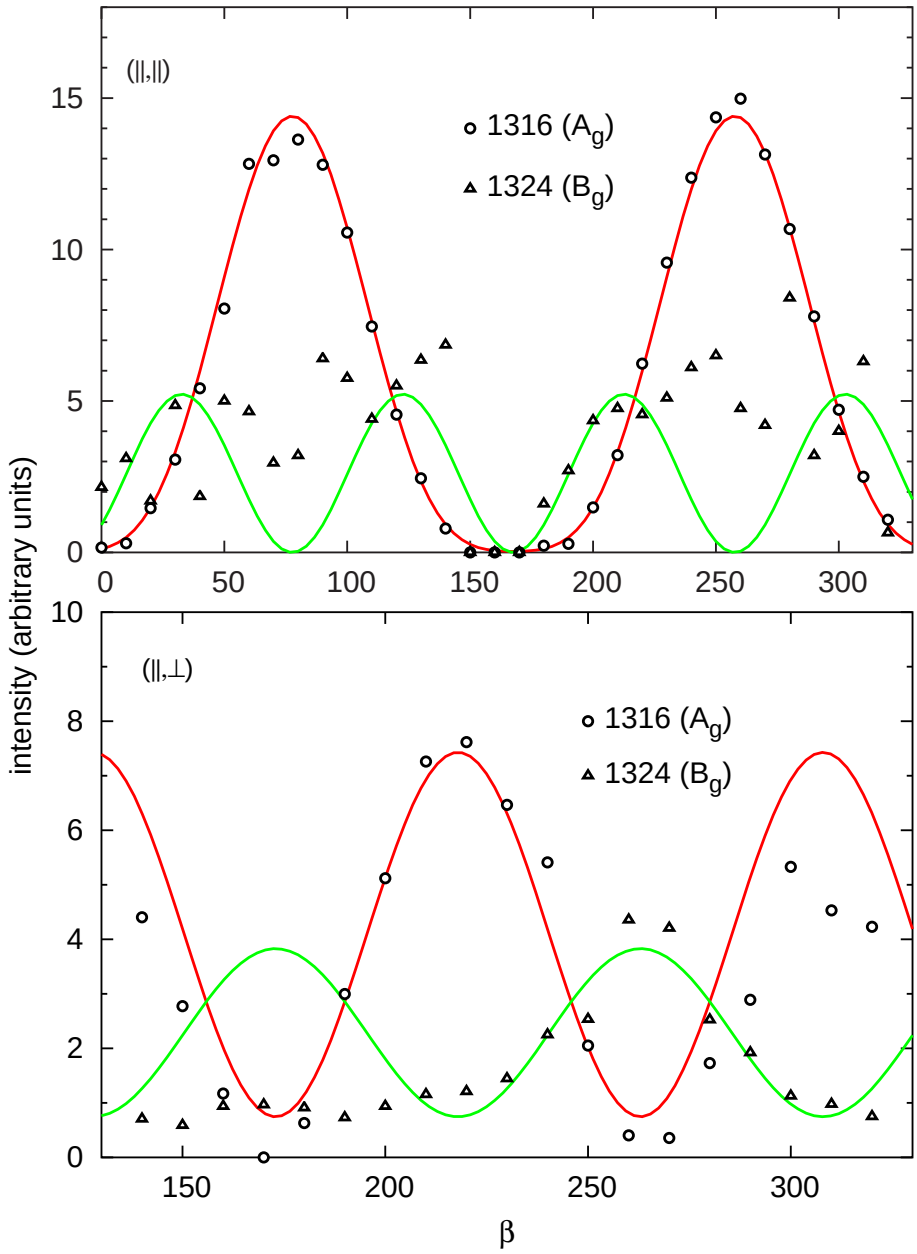

Figure 5.21: Angular dependence of the intensities of an A_g (circles) - B_g (triangles) Davydov pair together with fitted lines according to Equations (5.11). The intensity of the B_g member of the doublet has been multiplied by a scaling factor of 10 for clarity reasons.

5.5 Influence of the growth conditions

With the aim of determining the optimum growth conditions for the film growth, layers with different thicknesses, D, and at different substrate temperatures, T_g, were investigated. We can classify the studied films into two series: i) films with constant D deposited at different substrate temperatures; and ii) samples with different thicknesses but at fixed T_g. These two set of samples are discussed in Sections 5.5.1 and 5.5.2, respectively. The first group of samples was used to determine the optimum value of T_g. Thus, 20 nm films at substrate temperatures between -150°C and 310°C were evaporated. As we present in the following sections, while a good crystalline structure is obtained for $T_g > 150$°C, the optimum value is found to be at 230°C. Therefore, we fixed $T_g = 230$°C and deposited films for $D = 5$, 12, 20, 25, 30, and 45 nm to investigate the properties of the films as a function of D. All samples were prepared with an impingement rate of 0.4 nm/min monitored by the QCM and calibrated by x-ray diffraction.

5.5.1 Growth at different deposition temperatures

The substrate temperature during deposition is one of the growth parameters that have a stronger influence on the film properties, especially on the achieved degree of order, since the energy of the molecules on the surface depends on this parameter. Furthermore, it has been observed for many organic compounds, that different structural phases appear when the evaporation is performed at different temperatures. In particular, for phthalocyanines two polymorphic forms are usually observed, a metastable α-form and an energetically more stable β-form. For CuPc, several studies concluded that the α-polymorph is obtained when thin films are grown below 210°C, while above 210°C the β-CuPc form is obtained. An α to β phase transition can be induced by annealing the thin films above 250°C [61]. The α-form films usually show very rough surfaces, while for the β-form closed films presenting needle-like features have been observed. For the metal-free phthalocyanine the transition temperature is around 330°C [60]. However, there is no study of the dependence of the properties of F_{16}CuPc on the deposition temperature in the literature.

We have deposited thin films from -150°C, cooling the sample stage with liquid nitrogen, and up to 310°C. At 310°C no film on the substrate was found after growth, indicating that above this temperature there is no adsorption of

molecules. We can define the *normalized effective sticking coefficient* as

$$s_e = \frac{D}{D_{ev}} \tag{5.12}$$

where D, as usual, is the thickness of the layer and D_{ev} is the thickness expected from the evaporated material when the substrate is maintained at room temperature. In Figure 5.22 the variation of s_e with the substrate temperature is plotted. These values have been calculated from obtained thicknesses of films on SiO_2. Generally, the sticking coefficient of the first deposited monolayer (i.e., molecule-substrate) has different values than the sticking coefficient of the organic molecules on the already formed organic layer (molecule-molecule), from where differences between films on different substrates can arise. However, only small thickness differences have been observed between layers on the different substrates used in this work. Thus, our discussion refers mostly to the molecule-molecule sticking coefficient. As we can see in Figure 5.22, while s_e is constant up to $T_g = 150°C$, above this temperature it decreases until $s_e = 0$ at 310°C, indicating that the obtained thickness is below the expected thickness within this range.

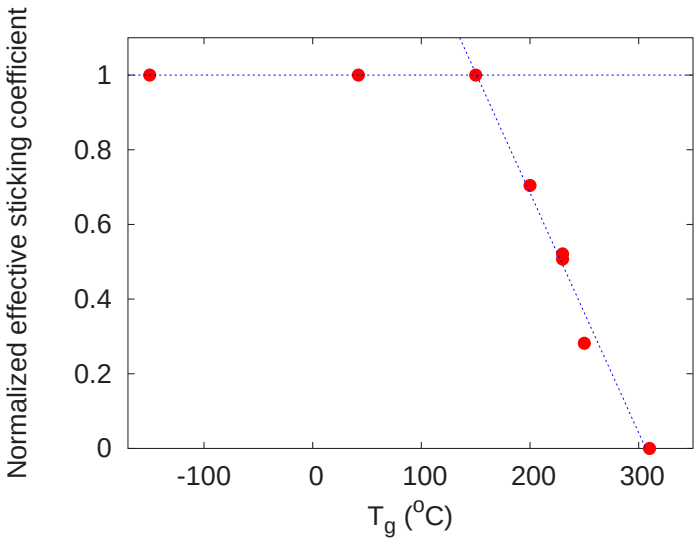

Figure 5.22: Normalized effective sticking coefficient plotted against the deposition substrate temperature T_g. For temperatures higher than 150°C there is a decrease of the sticking coefficient until at temperatures above 310°C no film is obtained on the SiO_2 substrate after growth.

The films deposited at temperatures equal or above room temperature present a morphology very similar to the AFM images shown in Sections 5.1 and 5.8 with elongated terraces in the case of films on SiO_2 (see Figure 5.1) and very

smooth films on Al_2O_3 (Figure 5.8). It is observed that the roughness decreases as T_g increases showing values from 1.6 nm at room temperature, 0.97 nm at T_g = 150°C, 0.80 nm at 230 °C, and 0.65 nm at 250°C measured on the 20 nm thick films on Al_2O_3. The films on SiO_2 present a slightly higher roughness but the same behavior with temperature. In Figure 5.23 two x-ray scans at the reflectivity

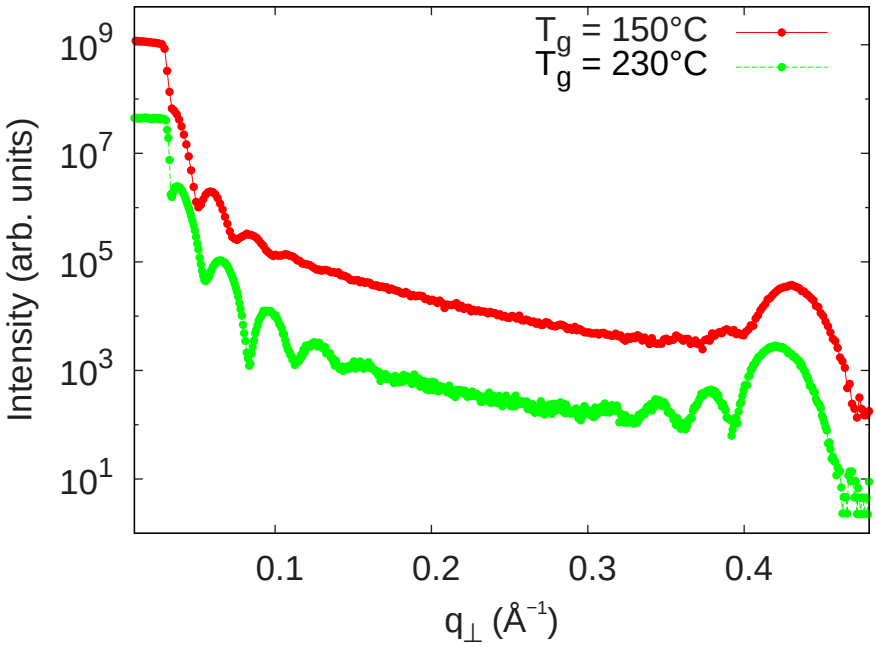

Figure 5.23: X-ray spectra for two films with equal thickness (D = 20 nm) deposited at T_g = 150 and 230°C. As we can see, the Kiessig fringes are more defined for the high-temperature film. Moreover, the position of the Bragg reflection is also modified by the growth temperature, indicating a change in the out-of-plane lattice parameter $a_\perp$ of the layer.

regime for samples grown at T_g = 150 and 230°C are compared. It can be observed that the Kiessig oscillations present a higher degree of definition for the film grown at 230°C than for the film grown at 150°C, which implies that the definition of the interfaces is higher in this film. Also, the out-of-plane lattice parameter $a_\perp$ (measured in each case at room temperature), which in this system can be related to the molecular tilt, depends on the growth temperature. This can be observed also in Figure 5.23, where a small shift of the Bragg peak position is observed. As T_g increases, the Bragg peak position shifts to lower values of the scattering vector, which means a higher value of $a_\perp$. In Figure 5.24 the values of the out-of-plane lattice parameter $a_\perp$ determined from the second order Bragg peak position are

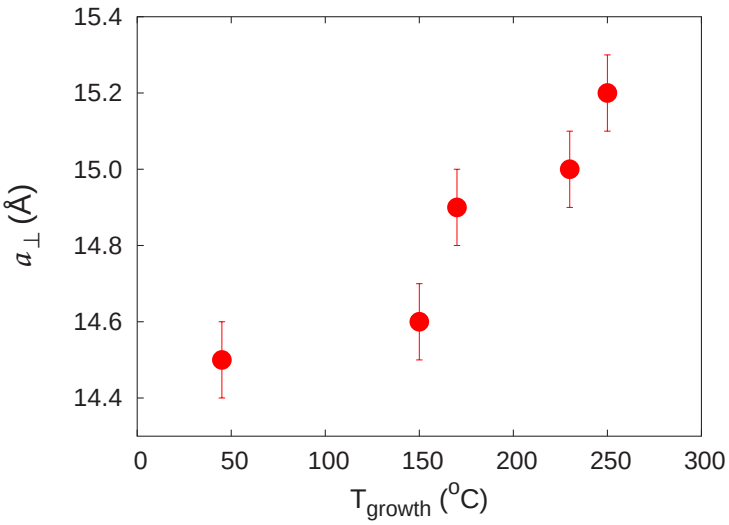

T_g (°C)	$a_\perp$ (Å)
-150	15.2
45	14.5
150	14.6
170	14.9
230	15.0
250	15.2

Figure 5.24: Out-of-plane lattice constant of the $F_{16}CuPc$ layers, $a_\perp$, as a function of the growth temperature T_g and at fixed thickness $D = 20$ nm. In the temperature range of 40°C $< T_g <$ 250°C there is an increase of $a_\perp$ as T_g increases.

plotted against the growth temperature T_g used in each case. As can be observed there is an increase of $a_\perp$ from 14.54 Å for $T_g = 45$°C until 15.2 Å for $T_g = 250$°C. However, when the substrate is maintained at $T_g = -150$°C the value of $a_\perp$ takes again the maximum measured value of 15.2 Å.

Furthermore, the films deposited at $T_g = -150$°C present a different morphology with very high roughness. As can be observed in the AFM images shown in Figure 5.25, the film crystallizes forming spherical grains and high islands, with high roughnesses, $\sigma_{rms} = 2.8$ nm for the film on SiO_2 and $\sigma_{rms} = 3.9$ nm for the film on Al_2O_3. Figures 5.25(a) and (b) show, respectively, a 20 nm thick film on SiO_2 and on Al_2O_3. As we can observe by comparing these two images, their morphology is very similar on both substrates, and thus the remarkable differences between films on both substrates observed at higher deposition temperatures are not present here. Moreover, there is no in-plane preferred orientation for the film on Al_2O_3 as is obtained at higher substrate temperatures, but only a 2D polycrystalline film with domains spread in all in-plane directions. The molecules are also standing upright, as evidences a Bragg reflection giving a 15.2 Å lattice spacing. The out-of-plane degree of order is also considerably lower at this low substrate temperature, presenting a rocking width of 0.1°. The morphology change and the different lattice constant that the films exhibit under this growth conditions may

suggest that a crystallization in a different phase takes place at these low temperatures. It is common that different crystalline phases show different morphological properties that can be used to easily distinguish them. As has been observed in CuPc thin films, where the α and β phases obtained by depositing the films at different growth temperatures, both phases show very different morphologies [61].

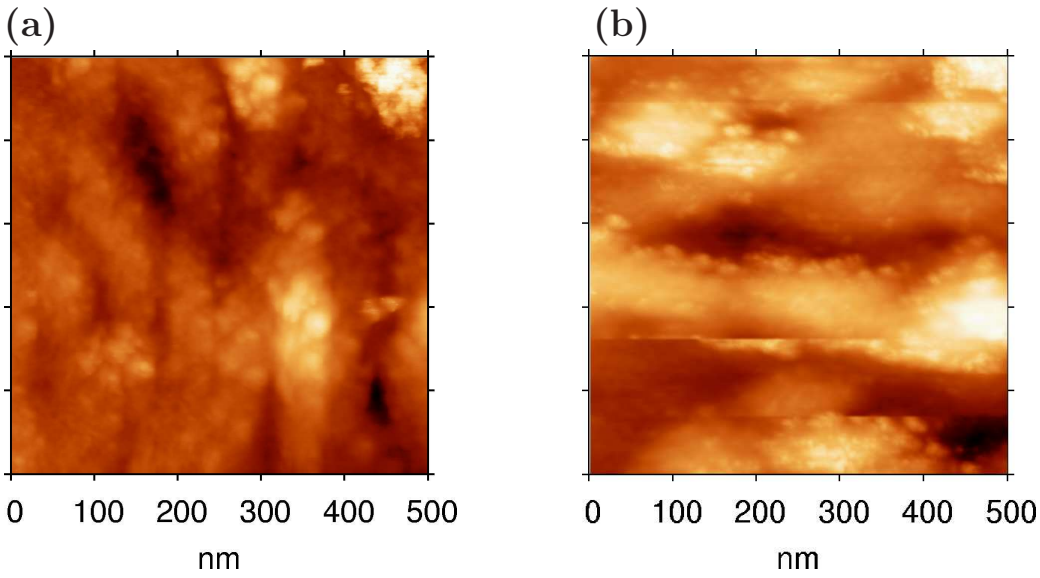

Figure 5.25: AFM images of a 20 nm thick F_{16}CuPc film grown at $T_g = -150°C$. Under this growth conditions the layers present a completely different morphology compared to the layers grown at higher temperatures (compare to Figures 5.1 and 5.8) with a much higher roughness. Furthermore, the morphology of the film on SiO_2 (image (a)) is very similar to that of the film on Al_2O_3 (image (b)).

In conclusion, the structure of the layers, and particularly the ordering level, are strongly determined by the substrate temperature during growth. The degree of order in the films, as reflected in their properties, increases as the temperature increases. However, for temperatures above 150°C, the effectiveness of incorporation of molecules in the organic layer decreases until at 310°C the desorption rate exceeds the adhesion rate, and no film is formed on the substrate. Thus, as optimum value we have chosen the intermediate temperature of 230°C, where highly ordered films are obtained, and is sufficiently far from the upper limit of 310°C.

5.5.2 Growth at different layer thicknesses

Layers with thicknesses between 5 and 45 nm deposited at $T_g = 230°C$ have been studied. The crystalline structure of the different layers do not show significant differences. The roughness of the films increases with thickness in an approximately linear dependence within this thickness range as is shown in Figure 5.26. In this figure the root mean square roughness σ_{rms} is plotted for films on SiO_2 and on Al_2O_3 against the film thickness. Interestingly, films on SiO_2 present a higher roughness, and as the thickness increases, σ_{rms} increases more rapidly than for the films on Al_2O_3. The root mean square roughness increases from $\sigma_{rms} = 0.8$ nm at a thickness of 12 nm to 2.8 nm at a thickness of 45 nm, while the films on Al_2O_3 have $\sigma_{rms} = 0.3$ nm at $D = 12$ nm and $\sigma_{rms} = 1.2$ nm at $D = 45$ nm. Given that the roughness is still moderate even for thicker films grown at this relatively high temperature (i.e., for growth not too far from equilibrium), this is suggestive of the films displaying wetting as opposed to dewetting behavior on these substrates.

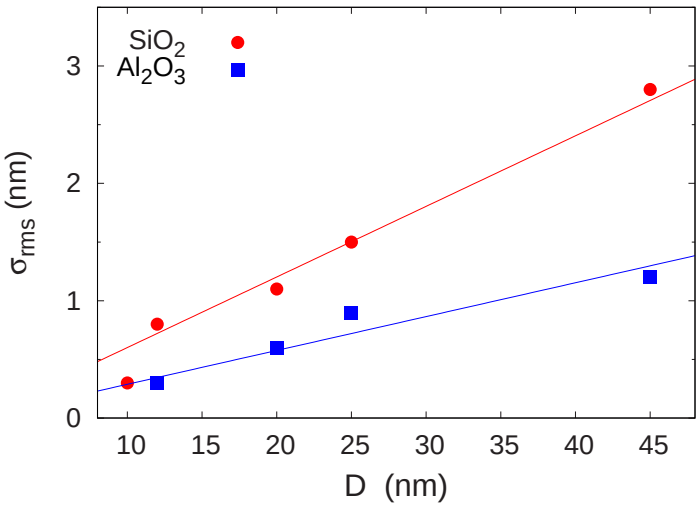

Figure 5.26: Evolution of the root mean square roughness of the organic layer as the thickness D increases. Higher values are obtained for the film on SiO_2 (circles) than for the films on Al_2O_3 (squares).

The degree of in-plane alignment of the layers on Al_2O_3 is found to depend also on the layer thickness. We can quantify the degree of in-plane order from the different techniques defining several quantities that evidence the degree of alignment

with the measured physical properties in each case. Thus, from x-ray diffraction the quantity that determines the in-plane orientation of the film is the FWHM value of the in-plane rocking scans over the Bragg reflection at $q_{||} = 1.982$ Å^{-1}, namely $\Delta\beta_\circ$. For isotropic films $\Delta\beta_\circ \rightarrow 360^\circ$ since the crystallites are randomly oriented, whereas its value decreases as the in-plane alignment of the crystallites is higher. For spectroscopic ellipsometry measurements we can define a *dichroic ratio* $\mathcal{R}$ as

$$\mathcal{R} = \frac{\varepsilon_{2X} - \varepsilon_{2Y}}{\varepsilon_{2X} + \varepsilon_{2Y}} \tag{5.13}$$

where ε_{2X} and ε_{2Y} are the imaginary part of the two in-plane components (X and Y) of the dielectric function of the organic layer. Although $\mathcal{R}$ can not be taken as an absolute measure of the degree of order, it is useful to quantify the degree of anisotropy of the layer. Thus, $\mathcal{R} = 0$ for isotropic samples whereas in a very anisotropic case we have $\mathcal{R} \rightarrow 1$. Obviously, the $\mathcal{R}$ ratio depends on the particular energy where the values of ε_2 are read. We have chosen energies close to strongly polarized transitions, where the differences between the two components are higher. In Figure 5.27 we have plotted ε_{2X} and ε_{2Y} for samples at different thicknesses, we can see that the peak around 1.55 eV is strongly polarized. We have chosen the energies $E = 1.55,\ 1.75,\ 1.95$ eV to calculate several values of $\mathcal{R}$ for the different layers. These energies are shown with dashed lines.

Another estimation of ordering can be obtained from the Raman scattering measurements by using the azimuthal variation of the peaks intensities to quantify the degree of order of each film. Thus, an order parameter can be defined from the Raman spectra by comparing the values of the fitted constant background with the amplitude of modulation A (see Equation (5.8)) as the sample is rotated for a given mode as

$$\nu = \frac{A^2}{A^2 + C} \tag{5.14}$$

thus, ν approaches 1 in highly ordered layers.

The values of these parameters ($\Delta\beta_\circ$, $\mathcal{R}$, and ν) are shown in Table 5.3, where we can see that the degree of order increases with film thickness as observed from the different techniques.

5.6 Conclusions

As we have shown in this chapter, F_{16}CuPc thin films on the various substrates used present some similar properties, as the molecular packing in the direction

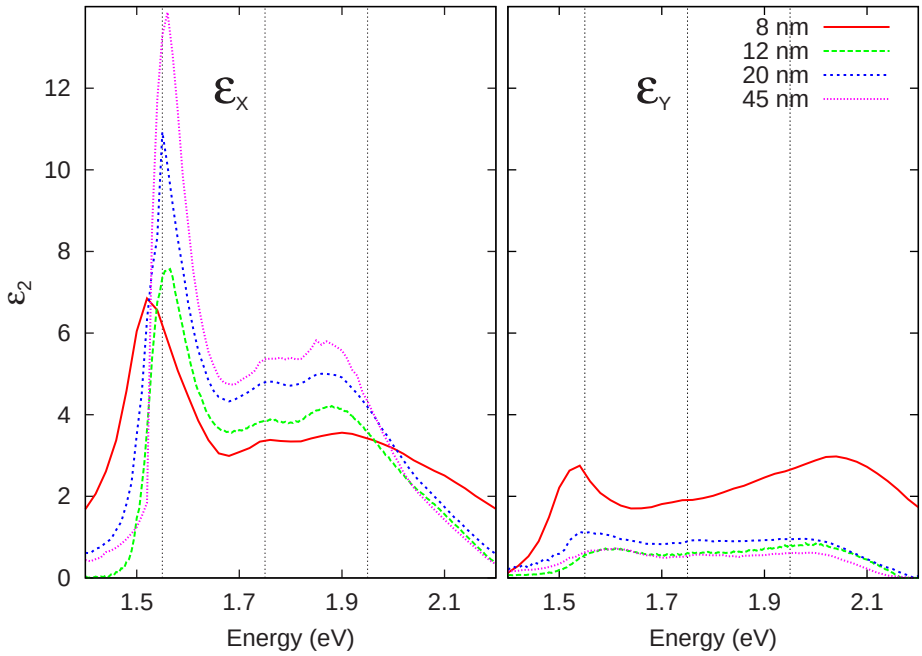

Figure 5.27: Imaginary part of the two in-plane components ε_X and ε_Y of the dielectric tensor of $F_{16}CuPc$ thin films on Al_2O_3 for several layer thicknesses. The dashed lines show the energies from which the values of the dichroic ratio $\mathcal{R}$ shown in Table 5.3 have been derived.

perpendicular to the film plane. The molecules crystallize in an upright configuration. This packing of the layers enhances the overlap of the π-orbitals in the plane of the film, end therefore promotes charge transfer in this direction. The degree of ordering depends critically on the deposition conditions and also on the substrate used.

The growth of $F_{16}CuPc$ on oxidized silicon substrates leads to very well ordered layers in the direction perpendicular to the film plane. In-plane crystallinity could be observed by GIXD with a domain size of the order of 20 nm. However, due to the amorphous nature of the oxide layer, no in-plane long-range order can be expected. Usually a polycrystalline film is obtained, where the in-plane anisotropy that the organic crystallites may locally display is averaged out due to their random azimuthal orientation. Thus, a situation that we could refer to as an "in-plane 2D powder" is obtained. Although this situation can be considered as an element of disorder of the layers which can somewhat limit their properties (as the ability to transport charge carriers), it may be used in the investigation of the properties of the material. This is due to the fact that it facilitates the

D (nm)	$\Delta\beta_\circ$ (°)	$\mathcal{R}$ at	1.55 eV	1.75 eV	1.95 eV	ν
5	-		0.33	0.19	0.05	∼0.3
12	10		0.81	0.73	0.68	0.93
20	9		0.82	0.68	0.63	0.96
45	4		0.90	0.81	0.81	1.00

Table 5.3: Values of the different parameters used to quantify the degree of order or anisotropy of the layers at different layer thicknesses.

study of some aspects that otherwise would be difficult or even not possible to perform, as the location of in-plane Bragg reflections by GIXD. Moreover, the degree of crystalline order in the direction perpendicular to the film plane is extremely high for films deposited at substrate temperatures above 100°C, having very narrow mosaicities. This degree of order can be attributed to the smoothness of the substrate surface and the low interaction substrate-adsorbates that lead to a high mobility of the molecules, enhancing thus a closely packed film. The morphology of these layers is characterized by the presence of elongated features. At higher resolution, a needle-like substructure of the terraces becomes apparent. Obviously, these features are related to the inherently strong anisotropy of the F_{16}CuPc crystallites in structure and shape (see Appendix A). However, the optical properties determined by spectroscopic ellipsometry are isotropic, due to the in-plane random orientation of the crystallites. Several electronic transitions in the Q-band could be identified by this method.

Films deposited on MgO show also isotropic properties, however, the structural definition is lower, and they present a rougher morphology. This is attributed to the rough surface of the substrates.

The organic films deposited on Al_2O_3 show the most interesting properties. These films, having an out-of-plane structure comparable to the films on SiO_2, present in addition an in-plane orientation of the crystallites under certain growth conditions. This situation reveals strong anisotropies in the organic layer. Generally, it can be concluded that in terms of their crystalline structure and quality the F_{16}CuPc films grown on silicondioxide are similar to the ones grown on sapphire, at least in terms of the out-of-plane structure. Nevertheless, since the in-plane alignment found on stepped sapphire is not present on silicondioxide, the morphology has a very different appearance, and of course also the strong in-plane anisotropy found in the optical spectra is averaged out. Both silicondioxide and

sapphire are rather inert substrates for F_{16}CuPc, which is probably the reason for the similar growth scenario in terms of the evolution of the out-of-plane lattice parameter and the related tilt angle as a function of growth temperature. In addition to the high structural definition of the films on SiO_2 and Al_2O_3, we show that very smooth surfaces (needed in device fabrication) can also be obtained in the overgrown layer when suitable growth conditions are met.

The use of complementary techniques in the study of the layers allows to interrelate the optoelectronic properties of the layers with the structure they present.

Chapter 6

DIP thin films

In this chapter we discuss the properties of the layers of the organic semiconductor DIP grown on SiO_2 and Al_2O_3. As we show, many characteristics of the DIP thin films are conceptually similar to those of the $F_{16}CuPc$ films shown in the previous chapter. As in the case of $F_{16}CuPc$, we show that highly ordered films of DIP can be obtained for suitable deposition conditions. Similarly as for $F_{16}CuPc$, the molecules are found in an up-right position, with their long axis nearly perpendicular to the substrate surface. As we show, the films on Al_2O_3 also present a certain degree of in-plane orientation as observed for phthalocyanines, demonstrating thus that the azimuthally oriented films on sapphire can be obtained not only in $F_{16}CuPc$ but also for other compounds. Furthermore, films on Al_2O_3 show a crystallite size much larger than films on SiO_2, what may improve substantially the conduction properties of those films. Interestingly, screw dislocations in the organic layer are observed, which are induced by the particular morphology of the stepped Al_2O_3 substrate. Besides the good structural properties shown by DIP thin films, this molecule is particularly interesting since it is complementary to the studied $F_{16}CuPc$ compound in that it is a *p*-type organic semiconductor. Thus after the characterization of each of the single layers, they can be combined to form organic *pn*-junctions or other technologically relevant, more complex heterostructures. DIP is of particular interest due to its molecular symmetry. In contrast to $F_{16}CuPc$ with D_{4h} symmetry, DIP has only two mirror axis and therefore its symmetry is D_{2h}. This is reflected in interesting properties of the layers, as we will show in this chapter.

We shall start presenting the results obtained for DIP thin films on SiO_2 (Section 6.1), where we also summarize the previous work performed on the study of the structure of this interesting molecule. We will also discuss the optical properties of these layers relating the observed anisotropies to their structure. In Section 6.2 we present the study of the layers on Al_2O_3, showing that the in-plane alignment of the organic crystallites observed in the preceding chapter for $F_{16}CuPc$ films on Al_2O_3 takes place also in the DIP films. We show in this section that, in addition to the good crystalline properties of the films, crystallites with very large dimensions can be obtained on Al_2O_3. In Section 6.2 we also present a study of the evolution of the properties of the film as the evaporated thickness increases, and we find an interesting spiral growth, which takes place at well determined locations on the substrate. Finally, we summarize the results of the growth and characterization of DIP in Section 6.3.

6.1 DIP thin films on SiO_2

In this section we summarize some reported details about the structure of DIP that are relevant in this work, especially those that help to understand later on the properties of the in-plane ordered layers. The structure of thin films of DIP on Si/SiO_2 has been extensively studied in reference [71]. It has been shown that the best structural properties of the layers are obtained when the growth is performed at $T_g = 150°C$. Thus, this parameter has been kept fixed in the present study, and films at other substrate temperatures have been grown only when needed for purposes of comparison.

We will first show that the DIP molecules crystallize on the SiO_2 substrate with their long axis nearly perpendicular to the surface. The degree of crystalline order in the direction perpendicular to the surface is exceptionally high with mosaicities of the order of 0.01°, while in the plane of the film a polycrystalline layer, with no in-plane preferred orientation is formed. The in-plane structure of the films is studied by GIXD, providing additional information to the already reported [71]. The fact that the symmetry of the DIP molecule is lower than that of the $F_{16}CuPc$ molecule (D_{2h} vs. D_{4h}) is reflected in the properties of the layers. The determination of the optical response by spectroscopic ellipsometry presents a higher complexity than in the $F_{16}CuPc$ case, since the component perpendicular to the film plane is considerably different from the in-plane components, and this

anisotropy has to be taken into account in the analysis and interpretation of the experimental data.

6.1.1 Structure of DIP films on SiO_2

The crystalline structure of the layers along the normal to the surface has been determined by x-ray diffraction under specular conditions. In Figure 6.1 we present an x-ray scan in the reflectivity regime (circles) of a DIP layer deposited at $T_g = 150°C$. The diffuse intensity (taken at $\Delta\omega = 0.015°$) has been already subtracted and the illuminated area correction is already taken into account (see Section 4.2.3). This reflectivity curve presents the total external reflection region followed by the Fresnel intensity decay with many Kiessig interferences, characteristic of a situation with well-defined interfaces and smooth surfaces. A fit following the Parrat formalism is also plotted (solid line) with the experimental data. The values obtained from the fit are the mean electron density of the organic layer

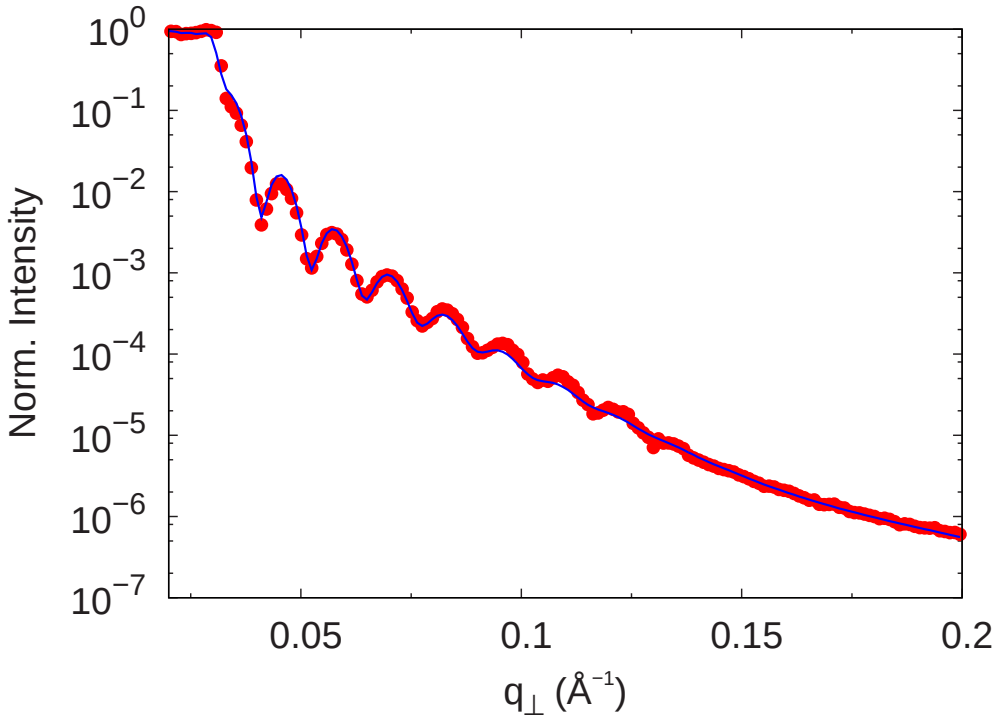

Figure 6.1: X-ray scan at the reflectivity regime (circles) together with a fit (solid line) following the Parrat formalism of a 48 nm DIP thin film on SiO_2 deposited at $T_g = 150°C$. Data taken at ID10B in the ESRF with a wavelength of $\lambda = 0.8$ Å^{-1}.

	D (nm)	ρ (Å^{-3})	μ(Å^{-2})	σ_{rms} (nm)
ambient (vacuum)	N/A	0	0	N/A
organic layer	48	$1.064 \cdot 10^{-5}$	$2.646 \cdot 10^{-8}$	2.5
SiO_2	3	$2.015 \cdot 10^{-5}$	$4.575 \cdot 10^{-7}$	1
Si substrate	N/A	$2.012 \cdot 10^{-5}$	$4.574 \cdot 10^{-7}$	0.2

Table 6.1: Parameters derived from the fit shown in Figure 6.1 following the Parrat formalism. The electron density and absorption coefficient of the SiO_2 layer and the Si-substrate have been kept fixed in the fit, all other parameters are fitted from the experimental data.

$\rho = 1.064 \cdot 10^{-5}$ Å^{-3}, its absorption coefficient $\mu = 2.646 \cdot 10^{-8}$, root mean square roughness $\sigma_{rms} = 2.5$ nm, and thickness $D = 48$ nm. All parameters included in the fit are shown in Table 6.1.

The first order Bragg reflection of the organic layer appears at higher values of the scattering vector, as is shown in Figure 6.2(a). The Bragg peak is surrounded by several Laue oscillations and is centered at $q_z = 0.3785$ Å^{-1} what corresponds to a lattice parameter $a_{\perp,DIP} = 16.6$ Å. This lattice spacing in the direction normal to the surface indicates that the molecules stand with their long axis nearly perpendicular to the substrate surface, since the dimensions of the molecule are around 7 Å $\times$ 18 Å. The thickness derived from the periodicity of Laue satellites (46 nm) is very similar to the thickness derived from the periodicity of Kiessig fringes (48 nm), implying that the DIP film is coherently ordered across the entire film thickness. A rocking scan over the Bragg reflection is shown in Figure 6.2(b), as can be observed in this curve, the rocking peak is very narrow, having a FWHM = 0.009°. Thus, the organic layer presents an extremely low mosaicity comparable to the single-crystalline Si-substrate and not very common in organic thin films. It has been shown for this particular organic compound [63] that the mosaicity of the layers is related with their conducting properties, which improve substantially as the mosaicity decreases.

The stacking of the molecules perpendicular to the substrate was also observed in previous studies [71, 72] supported by AFM and TEM (transmission electron microscopy) measurements. In Figure 6.3, an AFM image extracted from reference [72] is shown, where we can see how the morphology presents flat and rounded terraces that extend several hundreds of nanometers. Those terraces are

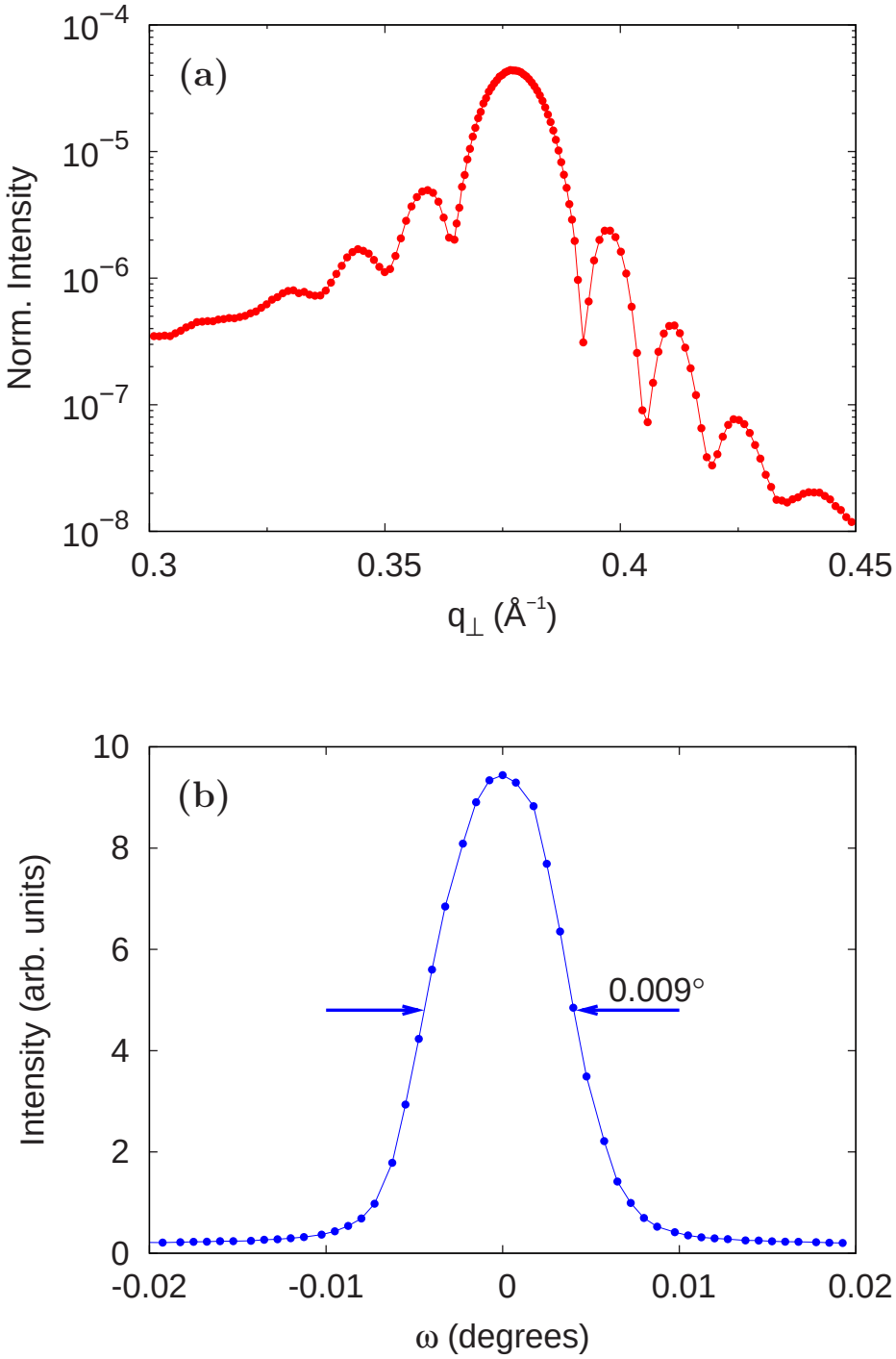

Figure 6.2: (a) First order Bragg reflection of the organic layer at $q_z = 0.3785$ Å^{-1}, what implies a lattice parameter $a_\perp = 16.67$ Å. (b) Extremely narrow rocking scan over the Bragg reflection of (a). The solid lines in both curves are plotted to serve as a visual guide.

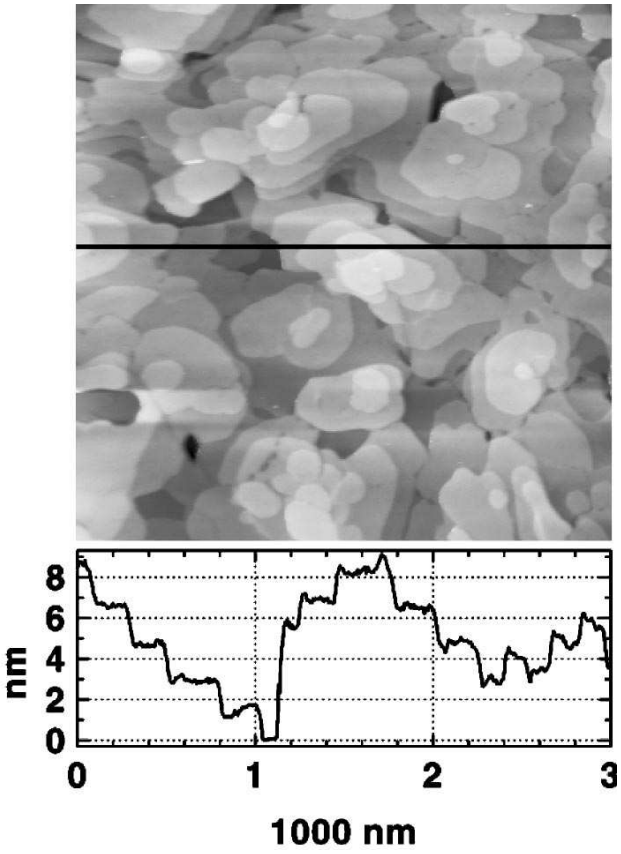

Figure 6.3: AFM image taken in non-contact mode of a 39.6 nm thick film on SiO_2. Extracted from reference [72].

separated by monomolecular steps of around 2 ± 0.5 nm step height, what is in accordance with the x-ray diffraction data, and with the up-right arrangement of the molecules. Reported cross-sectional TEM measurements allowed to resolve the upright configuration of the molecules, individual DIP monolayers are visible due to the high structural quality of those films [72]. Although the roughness of those layers is higher than that of the $F_{16}CuPc$ films, closed films are obtained, with roughnesses below the 20% of the total layer thickness.

GIXD has been used to determine the in-plane structure of the DIP thin films. Measurements performed at the synchrotron beamline ID10B at the ESRF in Grenoble allowed to locate up to 5 in-plane reflections. The measurements were performed using a radiation wavelength of $\lambda = 0.958$ Å. A six-circle diffractometer allowed to fix the initial and final angles of incidence at 0.13°, while the momentum transfer was scanned. An in-plane scan showing the Bragg reflections found is

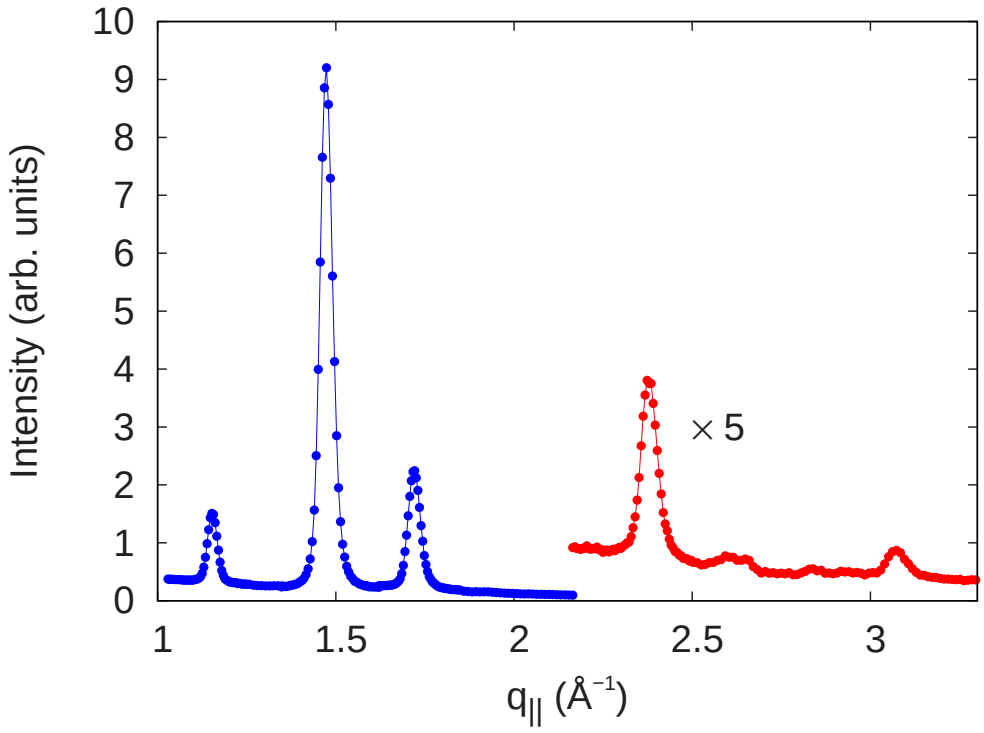

Figure 6.4: Radial scan in GIXD geometry of a 48 nm DIP film on SiO_2. Several in-plane reflections are found whose d-spacings are shown in Table 6.2. The curve above $q_{\|} = 2.2$ Å^{-1} has been magnified by a factor of 5 with the aim of clarity.

shown in Figure 6.4, where the curve above $q_{\|} = 2.2$ Å^{-1} has been magnified by a factor of 5 for reasons of clarity. The high intensity of the source allowed a more precise location of the Bragg reflections than the previously reported [71] and the location of two additional peaks (at $q_{\|} = 2.3793$ and 3.0741 Å^{-1}). The $q_{\|}$ values of all the peaks, together with their corresponding periodicities ($d_{\|}$) and their relative intensities (I_n) are listed in Table 6.2. A measure of the dimensions of the crystallites in the plane of the film can be obtained from the width of these Bragg peaks $\Delta q_{\|}$. The in-plane dimensions of the DIP grains can be estimated to be $\Delta D_{\|} \geq 2\pi/\Delta q_{\|}$. As is shown also in Table 6.2, the dimensions are around 13–23 nm, values significantly larger than those reported in [71] which were in the range from 8 to 10 nm for similar films. We attribute this difference to the lower deposition rate used in the present study.

$q_{\parallel}$ (Å^{-1})	$d_{\parallel}$ (Å)	$\Delta q_{\parallel}$ (Å^{-1})	$\Delta D_{\parallel}$ (Å)	I_n
1.1537	5.45	0.0272	231	28
1.4735	4.26	0.0354	177	100
1.7204	3.65	0.0346	182	60
2.3793	2.64	0.0458	137	12
3.0741	2.05	0.0410	153	2

Table 6.2: Bragg reflections found by GIXD measurements on DIP thin films on SiO_2. The positions of the peaks in $q_{parallel}$ are listed together with their corresponding lattice spacing ($d_{\parallel}$), the width of the peaks ($\Delta q_{\parallel}$), and the derived estimation of the dimensions of the crystallites ($\Delta D_{\parallel}$). The relative intensities are also given (I_n).

6.1.2 Optical properties

The optical properties of the DIP layers have been studied by spectroscopic ellipsometry. Since the layers on SiO_2 are an in-plane randomly-oriented polycrystalline film, it is expected that they display isotropic properties in the plane of the layer. Thus, as occurred for F_{16}CuPc on SiO_2, an effective dielectric constant ε_{ISO} can be derived from the ellipsometric measurements using an isotropic model. However, the fact that the symmetry of the DIP molecule is lower than that of the phthalocyanines may lead to additional optical anisotropies in these thin films not detected for F_{16}CuPc. As we have seen, the molecules stand with their long axis approximately perpendicular to the substrate surface. Under such circumstances the dielectric tensor may present a remarkably different component along the normal to the substrate surface related with the long molecular axis. Ellipsometric measurements performed at different angles of incidence φ can be used to probe anisotropies in the direction normal to the surface. As we already discussed in Section 4.3, the weight of this component in the measurement is usually low, but is different for different values of the angle of incidence. The contribution of the perpendicular component is higher for higher values of φ. The dependence of the ellipsometric measurements on φ is due to the change of the light path length and to the anisotropy of the layer.

In Figure 6.5 ellipsometric spectra acquired at incident angles φ between 75° and 50° at step intervals of 5° are plotted. Since the ellipsometric parameters

$\tan\Psi$ and $\cos\Delta$ in the isotropic case depend on the angle of incidence (through a geometrical factor, see Section 4.3), we plot the spectra as their pseudodielectric constant, in which case the geometrical dependence has been already taken into account, and any difference between the spectra can be attributed solely to anisotropies of the layer. This pseudodielectric constant is calculated by using a two phase isotropic model, and consequently its values are not a physical property of the material but rather an approximation to the dielectric tensor of a bulk-like material. In spite of that, this function is very useful to easily detect any anisotropy that the material may present, since, in an anisotropic media, it will take different values depending on the configuration of the measurement or on the orientation of the measured sample (see Section 4.3). As can be observed, remarkable differences are found between the spectra shown in Figure 6.5. As we discussed in the previous chapter, equivalent measurements on the layers on F_{16}CuPc did not show significant differences between different incident angles, from which we deduced that $\varepsilon_Z \simeq \varepsilon_X = \varepsilon_Y$ for films on SiO_2 (see Sections 5.1.2 and 5.3.2). In the DIP case this is not valid due to the observed differences between spectra. Now the component ε_Z takes considerably different values than the in-plane components ε_X and ε_Y. We can, however, write $\varepsilon_X = \varepsilon_Y$ since this is still satisfied due to the azimuthal dispersion of the crystallites, and corroborated by the fact that measurements at different azimuthal orientations of the sample (at fixed angle of incidence) are completely equal. Thus, we must treat these layers as a uniaxial media with the ordinary components in the plane of the layer and the extraordinary component pointing along the normal to the surface.

By considering a model with a uniaxial layer on an isotropic substrate (composed of the SiO_2 layer and the crystalline Si substrate) in an isotropic ambient, and fitting all six curves taken at different angles of incidence we can obtain the two components of the effective dielectric tensor of the DIP films on SiO_2. In Figure 6.6 the real and imaginary parts of the effective dielectric tensor are plotted, with the ordinary component being $\varepsilon_X = \varepsilon_Y$ and extraordinary component ε_Z. We should note that the component ε_Z takes higher values than the in-plane components. This is in accordance with having the long axis of the molecule parallel, or nearly parallel with the z-axis, since the existence of a larger oscillator strength along this direction would increase the values of the dielectric function. In addition, since the crystallites are randomly oriented, the in-plane component is an average

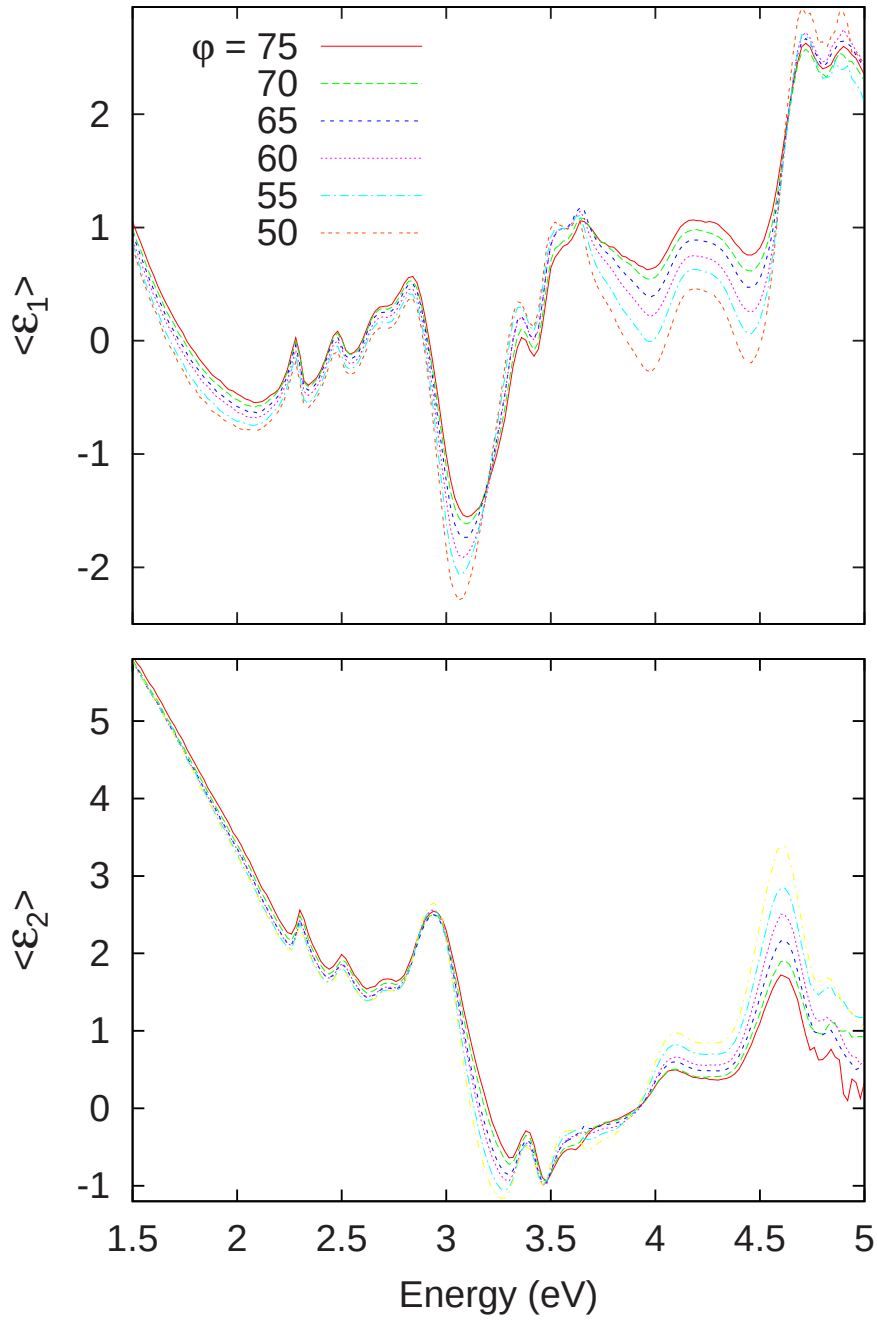

Figure 6.5: Pseudodielectric function of a 50 nm thick DIP film on SiO_2 calculated from ellipsometric measurements taken at different incident angles φ.

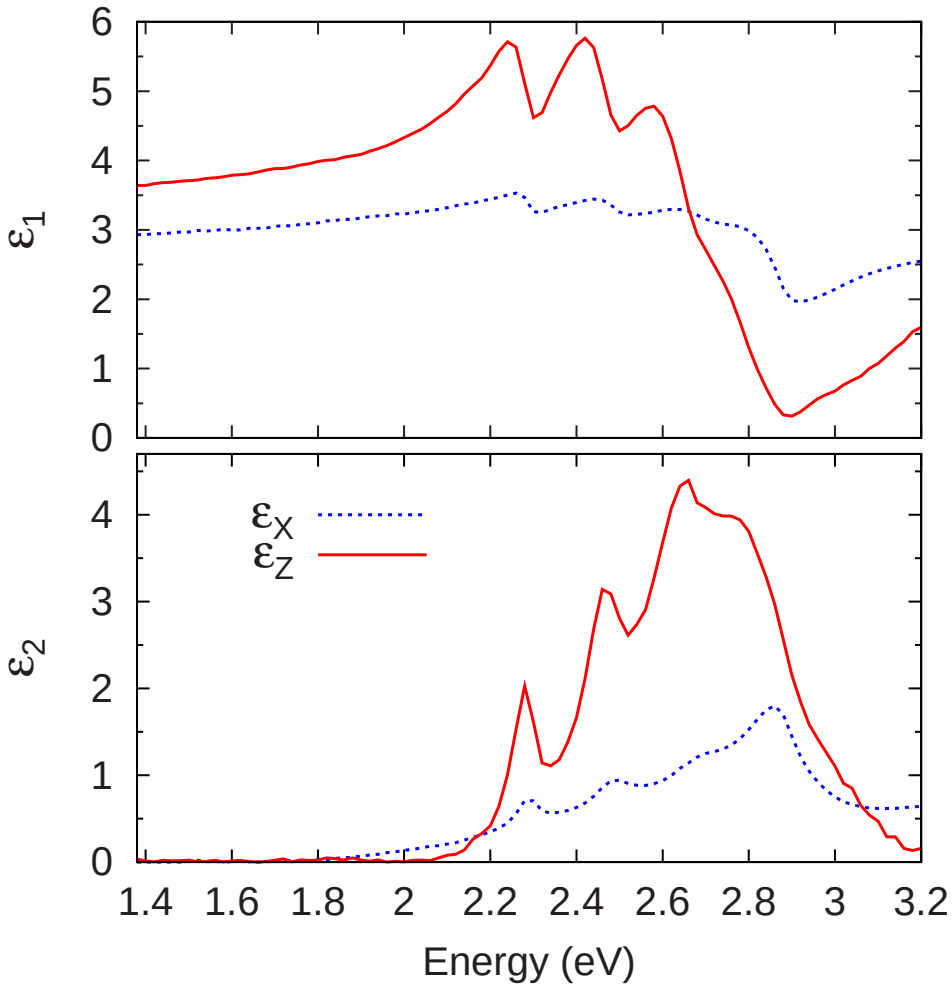

Figure 6.6: Dielectric tensor of a 50 nm DIP layer on SiO_2, obtained from a uniaxial model with ordinary component $\varepsilon_X = \varepsilon_Y$ in the plane of the film, and extraordinary component ε_Z along the normal to the surface.

of the two other principal components of the crystal/molecule, which will reduce its values further.

From the obtained dielectric function several transitions can be located. The plotted band shows a typical spectrum for compounds containing the perylene chromophore, with the lowest excitonic transition in this case around 2.3 eV and a vibronic progression with a frequency close to 0.2 eV.

6.2 DIP thin films on Al_2O_3

We shall discuss now the properties of the layers of DIP on Al_2O_3. As we have seen in the previous section the films on SiO_2 presented high structural order in the direction perpendicular to the film plane. Here, in addition and as occurred already in the films of $F_{16}CuPc$, the organic films exhibit also in-plane order. As we show, the organic layers crystallize forming regularly shaped grains, which present a preferred azimuthal orientation, as observed by AFM. The dimensions of the crystallites are considerably larger than for films on SiO_2, and can even exceed 1.5 μm. In this section we also present high resolution AFM images measured in contact mode from which two in-plane periodicities of the organic crystallites can be extracted. These periodicities determine the in-plane unit cell of the molecular material, and allow to relate the in-plane orientation of the film with that of the substrate. The in-plane structure of the layers is also investigated by x-ray diffraction, a technique that allows a quantification of the degree of in-plane order and a precise determination of the orientation of the organic layers relative to the substrate. Their optical properties display now in-plane anisotropies in addition to the out-of plane anisotropy of the films on SiO_2. Moreover, spiral growth is observed under certain growth conditions and at particular points determined by the morphology of the stepped substrate surface.

The fact that DIP films on stepped Al_2O_3 also show in-plane order, demonstrates that this is not a special characteristic of the system $F_{16}CuPc/Al_2O_3$, but the approach [116] can be applied to obtain highly oriented films of other molecular compounds. Thus, Al_2O_3 is a very interesting substrate for the growth of organic thin films with high structural definition, and even for the achievement of single-crystalline organic layers.

6.2.1 Morphology

In the preceding section we have seen that DIP films on SiO_2 present a morphology characterized by planar terraces that extend several hundreds of nanometers. Those terraces appeared separated by monomolecular steps of approximately 1.6 nm height, approximately the size of a molecule standing upright. While no regular shape of the crystallites was identified, edges defining an angle about 120° were often observed [71]. In the present study, the DIP films on Al_2O_3 also present large planar terraces separated by monomolecular steps as is shown in the AFM

images of Figures 6.7 and 6.8. In the images displayed in this last figure, two line-scan profiles over a crystallite evidence the monomolecular steps formed and allow to determine a step height around 1.6 nm as for the films on SiO_2. Such scenario is consistent with the lattice spacing in the direction perpendicular to the film plane obtained by x-ray diffraction, where the DIP molecules would stand essentially upright.

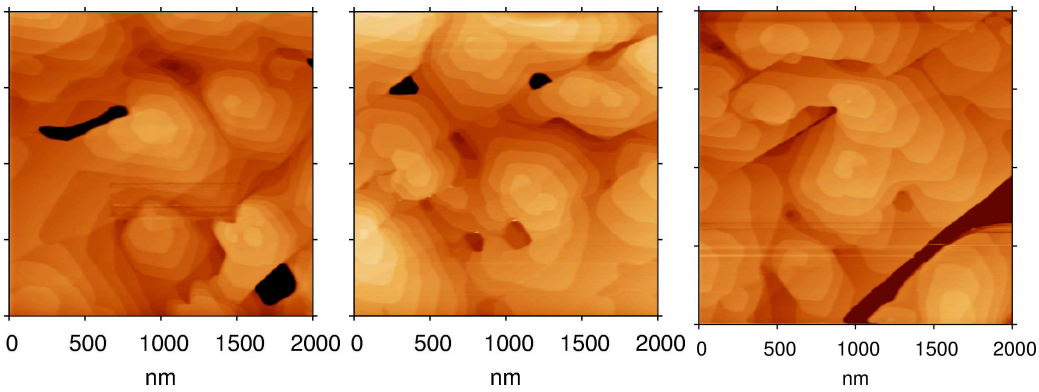

Figure 6.7: 2×2 μm AFM images of a 25 nm thick DIP film on Al_2O_3 at three different spots. The in-plane orientation of the film is evidenced by the orientation of the regular shaped crystallites. The steps of the substrate are still visible on the morphology of the film, what allows to determine the orientation of the organic grains relative to the substrate. The Al_2O_3 c-axis is approximately vertically aligned in the images.

However, in contrast to the observed morphology of films on SiO_2, the DIP crystallites on Al_2O_3 show a regular, almost hexagonal, shape (see Figures 6.7 and 6.8), whose edges define an angle around 120°. This angle is also observed in the periodicity resolved by AFM (see Section 6.2.4), and therefore we may infer that the shape of the crystallites formed is induced by the crystalline structure adopted by the organic molecules in the film. This would also explain the observation of crystallite edges defining 120° in films on SiO_2 [71]. Moreover, the crystallites appear all oriented in one azimuthal direction, suggesting an in-plane alignment of the organic layer, as was observed before for the phthalocyanine films on Al_2O_3. In Figures 6.7 and 6.8 we can observe that the stepped Al_2O_3 surface can still be traced from the AFM data, which allows a direct comparison of the orientation of the crystallites with the substrate. It is observed that one of the edges of the crystallites is nearly perpendicular to the step edges of the substrate. The c-axis

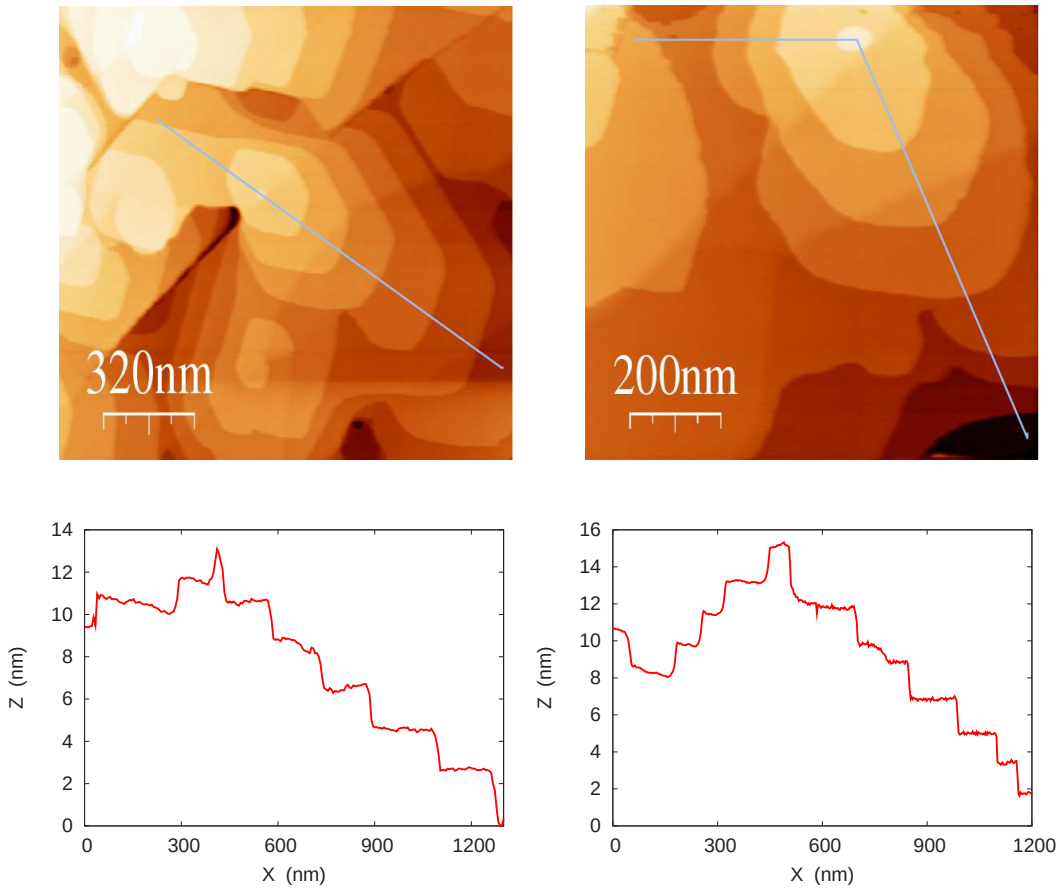

Figure 6.8: AFM images and line profiles across crystallites of a 25 nm thick DIP layer on Al_2O_3. Those films present large planar terraces separated by monomolecular steps of around 1.6 nm height. This height corresponds approximately to the lattice spacing $a_\perp$ obtained by x-ray diffraction. The average terrace width is around 100 nm.

of the Al_2O_3 substrate runs approximately vertical in the images of Figures 6.7 and 6.8, and therefore it runs along the vertical bisectrix of the hexagonal organic crystallites.

The observed roughness of these films is higher than that of $F_{16}CuPc$ films. As can be seen in Figure 6.7 deep valleys appear on the surface at several spots. In general, however, closed films are obtained.

6.2.2 X-ray Diffraction

The crystalline structure along the normal to the surface of the layers of DIP on Al_2O_3 is very similar to that of the films on SiO_2. An x-ray diffraction scan recorded under specular reflection conditions of a DIP thin film on Al_2O_3 is shown in Figure 6.9(a). At the low angle part of the spectrum appears the region with total external reflection, followed by the decrease of intensity characteristic of the Fresnel reflectivity. In this region intensity oscillations appear due to the interference of the radiation reflected on the surface of the film with the radiation reflected at the interface film-substrate (Kiessig fringes). At $q_z = 0.378$ Å^{-1}, we find the first order Bragg reflection of the organic layer. The small satellites surrounding the Bragg reflection (Laue satellites) are due to the finite thickness of the layer, and, thus, can be related to the number of monolayers that form the organic film. The position of the Bragg reflection indicates that the lattice constant of the film in the direction perpendicular to the surface is $a_{\perp,DIP} = 16.6$ Å. This lattice constant agrees with the step height found by AFM and with the structure found in the films on SiO_2. As it is found for those films, also the mosaicity of the layers on Al_2O_3 is extremely small. In Figure 6.9(b) a rocking scan over the Bragg reflection is shown. The FWHM of that peak is 0.004°, a mosaicity even lower than that found in films on SiO_2. This can be attributed to the atomically flat terraces of the Al_2O_3 substrates.

We should point out here that the rocking width of 0.004° is the narrowest found in this layer, since it depends on the azimuthal orientation of the sample, or more precisely the orientation of the step edges of the substrate relative to the x-ray beam. Thus, the stepped morphology of the substrate influences the crystalline structure of the organic layer. The film nucleates on the atomically planar terraces with $(11\bar{2}0)$ orientation of the Al_2O_3 substrate, and therefore its crystallographic planes will develop relative to that surface. However, since the physical surface is misaligned with the $(11\bar{2}0)$ plane, the overgrown film will evolve propagating this misalignment, and therefore it will present an *induced miscut* of the same magnitude as the substrate miscut. The presence of this misorientation in the organic layer is reflected in the x-ray measurements, which will now depend on the azimuthal orientation of the sample, or more precisely on the angle between the projection of the x-ray beam on the sample surface, and the direction of the step edges of the substrate. We denote this angle as ϕ, which can be related to

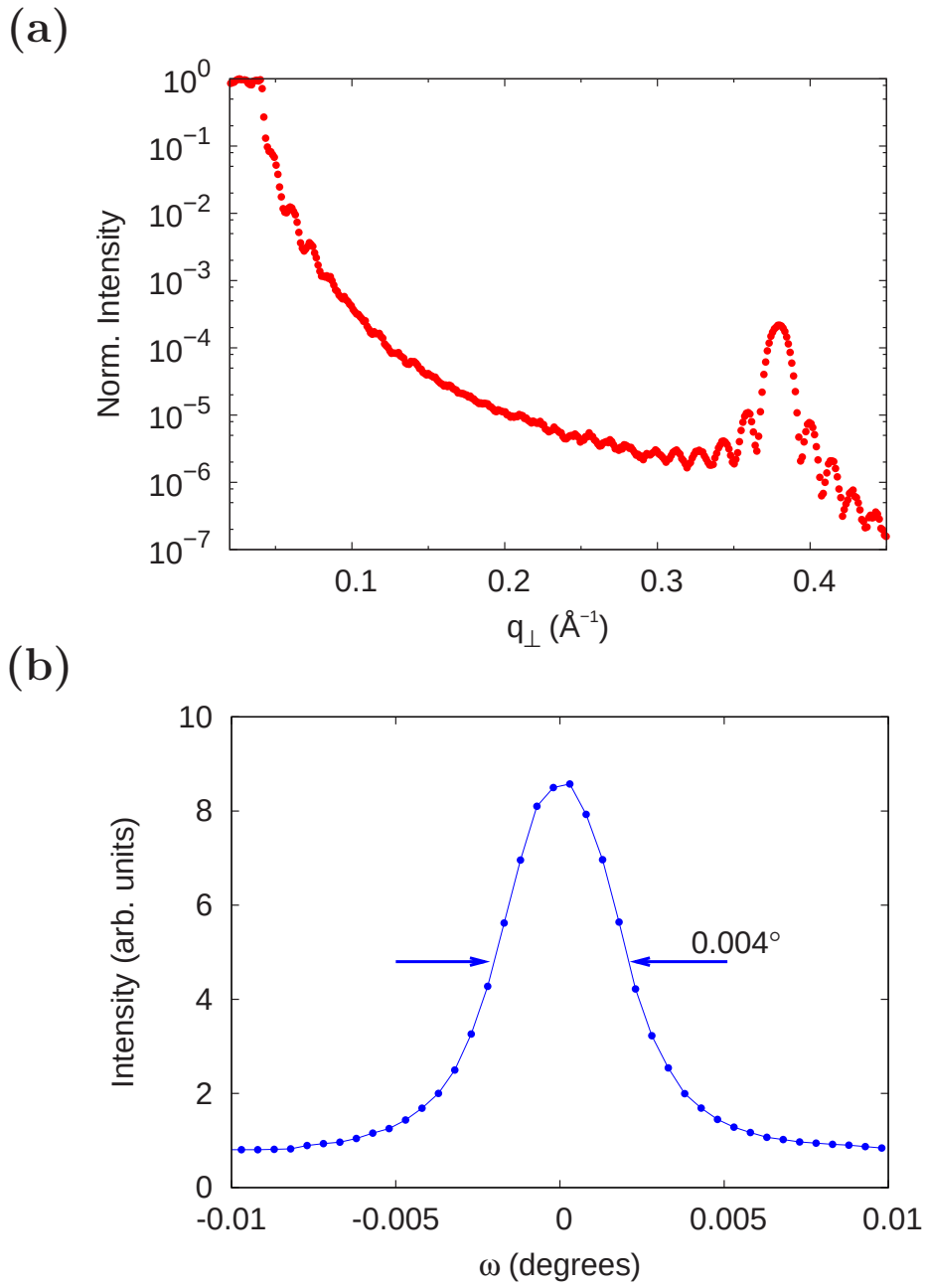

Figure 6.9: (a) Specular x-ray diffraction of a 47 nm DIP film on Al_2O_3. The first order Bragg peak gives a $a_\perp = 16.6$ Å. (b) Rocking scan over the Bragg peak at $\phi = 135°$ (see Figure 6.10), the FWHM is 0.004°.

the angle β used to describe the azimuthal orientation of the sample relative to the c-axis of the substrate. In Figure 6.10 we have plotted several rocking curves (where the x-axis is given by $\omega = 2\theta/2 - \theta$) over the Bragg peak at several values of ϕ. The schematic views drawn also in this figure illustrate the orientation of the x-ray beam relative to the step edges. We can observe two phenomena occurring as the sample is rotated, first, a shift $\Delta\omega$ of the peak maximum location from the centered position; and secondly a change of the width together with a decrease of the maximum intensity.

The shift of the peak is a direct consequence of the induced misorientation or miscut on the overgrown layer. The maximum shift will determine the miscut magnitude while the value of ϕ at which this occurs will determine its orientation. A plot of $\Delta\omega$ against ϕ would reveal a sinusoidal dependence. As we can see in Figure 6.10, the rocking peak is at $\omega = 0°$ for $\phi = 0°$ which means when the x-ray beam projection is parallel to the step edges, while the maximum shifts are found at ϕ = 90 and -90° with a shift of $\Delta\omega \simeq 0.27$. A more precise determination of the miscut is performed following the procedure described in Appendix A. The miscut presented by the organic layer has 0.27° of magnitude.

We can also observe, that, while the integrated intensity of the rocking curve is approximately the same in all the curves of Figure 6.10, the width and maximum intensity of the peaks change depending on the orientation of the sample ϕ, meaning that the mosaicity of the layers is not the same in all orientations. The mosaicity is the distribution of the of the crystallite orientation in a given direction, in this case along the normal to the surface. This distribution is found to be broader in the direction perpendicular to the step edges. This higher mosaicity in this direction is due to the presence of defects at the step edges, where crystallites with slightly different orientation develop.

Thus, the stepped morphology of the substrate induces a miscut in the overgrown layer, or in other words, the miscut of the substrate is propagated through the organic film. This has been also observed in the $F_{16}CuPc$ films on Al_2O_3 as we mentioned in Section 5.3.1. The mosaicity of the layer is also increased by the presence of the steps, where organic crystallites with slightly different out-of-plane orientations develop. Consequently, the measured mosaicity of the layers depend on their azimuthal orientation, with a minimum of 0.004°.

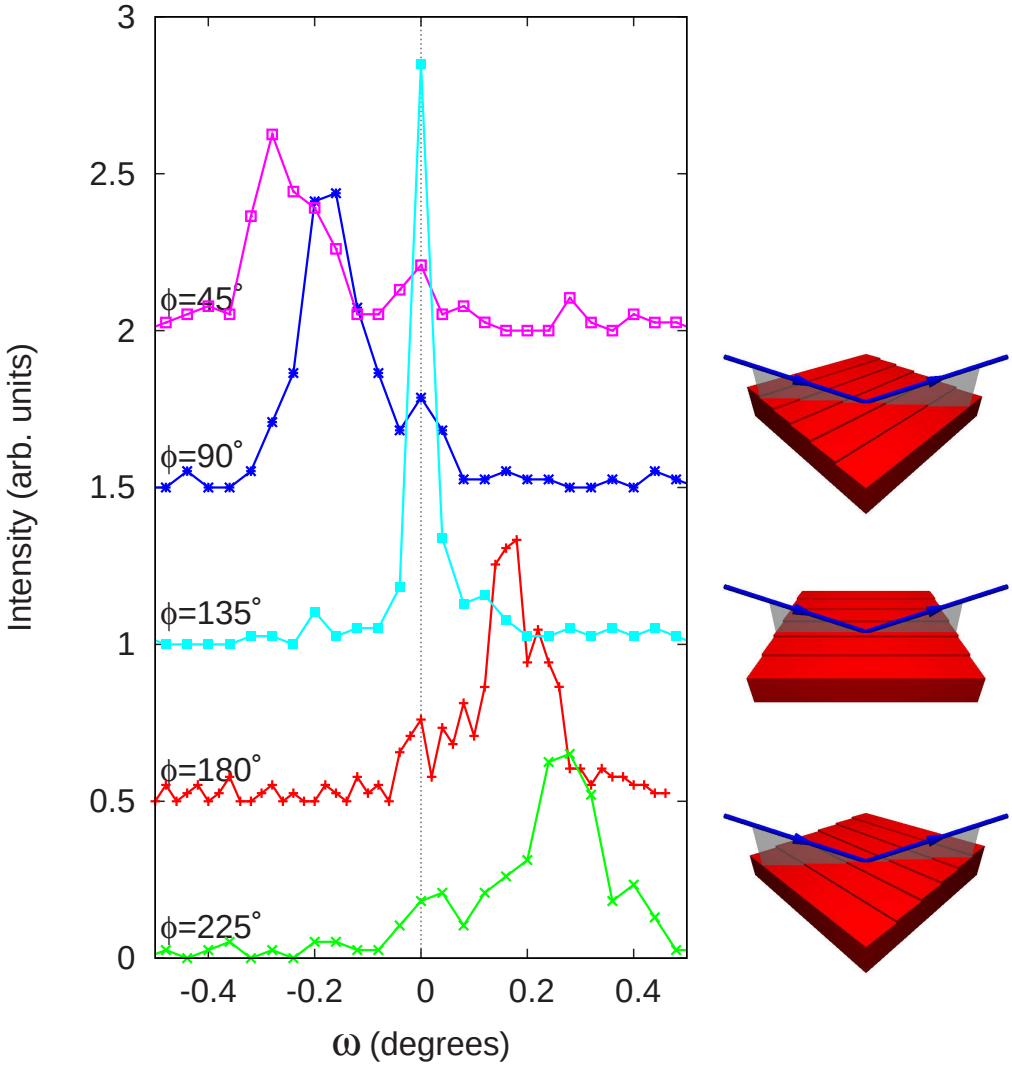

Figure 6.10: Rocking scans over the DIP Bragg peak at different azimuthal orientations of the sample. It can be seen how the position of the Bragg peak changes as the sample is rotated, following the miscut of the substrate, and therefore, showing that the film lattice planes are parallel to the terraces. The width of the peak also changes with the orientation of the sample, with the minimum at $\omega = 0°$.

6.2.3 Growth

In order to study the properties of the DIP layers on Al_2O_3 at different growth stages, several films of different thicknesses in the range from 6 to 100 nm have been deposited at the fixed substrate temperature of $T_g = 150°C$. In Figure 6.11 several AFM images of films with thicknesses of $D = 6$, 25, 50, and 100 nm are shown. Note that the area of the images is 1000×1000 nm^2 for images (a), (b), and (c), but, with the aim of clarity, in image (d) a larger area (2000×2000 nm^2) is shown.

At the early stages of growth it is not possible to observe the formation of well-defined crystallites, as can be seen in Figure 6.11(a), where the morphology of a 6 nm thick film (about 4 ML) is shown. In this case the surface is very smooth, and several wetting monolayers are observed. At some locations (i.e. bottom of the image) it is possible to observe nucleation centers at the step edges, where new monolayers are emerging. This suggests that the growth of the organic layer is controlled by a step-flow process, where the organic layer nucleates at the substrate step edge, and evolves propagating the step. When the layer thickness is increased to 25 nm (Figure 6.11(b)), the formation of islands is already visible. Crystallites with the common regular shape are formed, with edges forming approximately 120°, and terraces separated by monomolecular steps of $\sim$ 1.6 nm height. In this image one step edge of the substrate is visible in the upper-left corner. The crystallites formed expand already over the step edge to the neighboring terraces and have and average lateral size of 200-300 nm. As the thickness increases, the average diameter of the organic crystallites also increases while the shape of the grains keep the approximate hexagonal symmetry. At a film thickness of 50 nm, diameters around 1 μm are found. For the thickest film of 100 nm (image shown in Figure 6.11(d)) the crystallite size can exceed 1.5 μm. The island size is extremely large compared to the size obtained for DIP layers on SiO_2, thus, the Al_2O_3 stepped surface not only induces a preferred orientation, but also contributes to the formation of larger crystallites. This is clearly seen in Figure 6.12, where the average crystallite size of films on SiO_2 and films on Al_2O_3 is plotted against film thickness. We can see that the crystallite size determined from the AFM data of films on Al_2O_3 can increase in one order of magnitude relative to the films on SiO_2. This crystallite size is also extremely high compared to other organic films grown on other substrates.

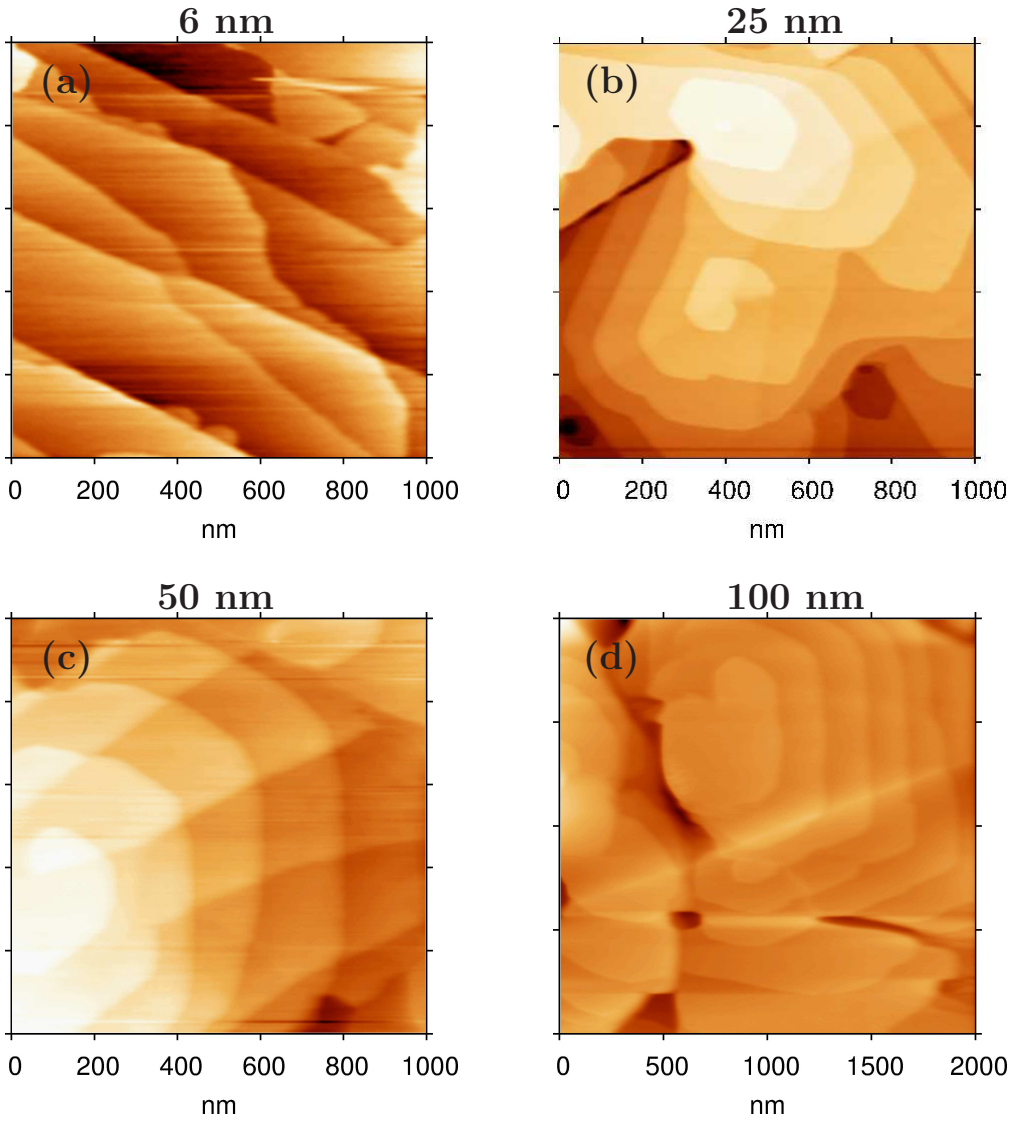

Figure 6.11: AFM images of several samples with different thicknesses from 6 to 100 nm. At the thickness of 6 nm (a) there is no well defined crystallite yet. When the thickness is 25 nm (b), the formation of regularly-shaped crystallites on the terraces can already be observed, the diameter of the grains is around 20 nm. As the thickness increases the crystallites keep growing in size, at 50 nm (c), their diameter is about 1 μm extending over several terraces. When the thickness is 100 nm (d) , extremely large crystallites are observed with diameters above 1.5 μm. Moreover, the crystallites are all oriented in one azimuthal direction. The c-axis of the substrate is aligned approximately vertically in the images.

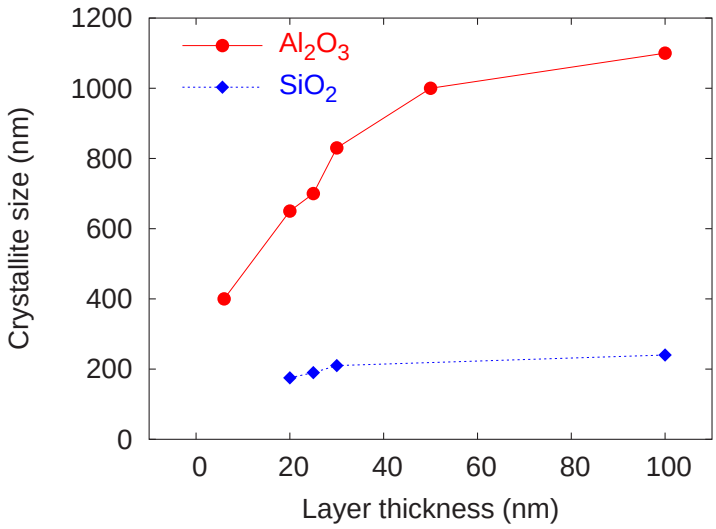

Figure 6.12: Dependence of the lateral crystallite size determined by AFM as function of film thickness for films on Al_2O_3 (circles) and films on SiO_2 (squares). The crystallite size of the films on Al_2O_3 is nearly one order of magnitude larger that of the films on SiO_2.

6.2.4 In-plane structure

The crystalline structure of the layers within the plane has been studied by AFM and GIXD experiments. While high-resolution AFM images allow to depict the in-plane 2D unit cell of the films in the real space, GIXD measurement supply information in the reciprocal space with a higher precision and probing a larger area of the film.

In Figure 6.13 several high resolution AFM images of a DIP layer are shown. Two periodicities are clearly observed in the images, forming an angle that differs substantially from 90°. We denote the periodicities as d_1 and d_2 and the angle they form as δ, as shown in Figure 6.13(c). The values determined are $d_1 = 6.7 \pm 1$ Å, $d_2 = 9.8 \pm 1$ Å, and $\delta = 120 \pm 10°$. In all the images shown in Figure 6.13 the Al_2O_3 c-axis is aligned approximately vertically. For comparison, the unit cell of the substrate is also shown in image (c) of this figure. However, we should point out that the Al_2O_3 unit cell has been depicted on the AFM image only to illustrate its dimensions compared to the organic unit cell and its approximate orientation, but should not be taken as an exact picture of the substrate lattice, since its relative lateral location can not be determined from the AFM data. Also, its orientation is approximate, since misalignment of the

substrate on the holder may lead to variations of about ±10°. Images taken at different points on a crystallite show the same orientation of the stripes, which indicates that the crystallites observed by AFM are single domain. Moreover, one of the stripes orientation is always parallel to one of the faces of the crystallites, which indicates that the nearly-hexagonal shape adopted by the crystallites is related to the organic lattice.

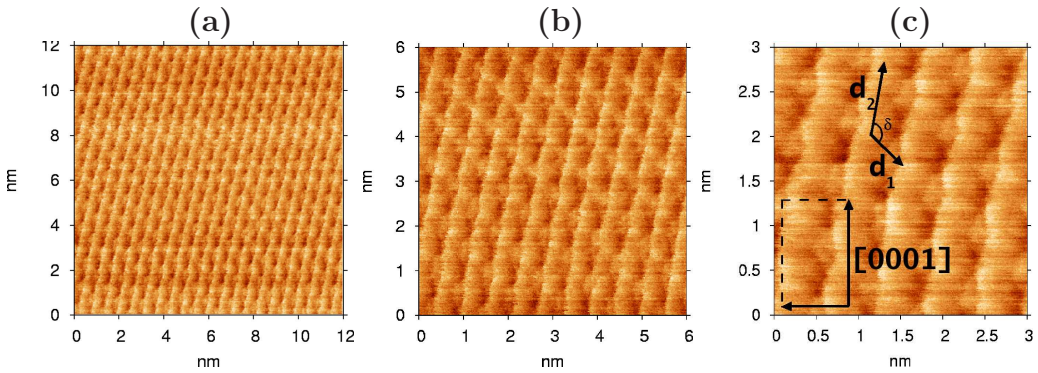

Figure 6.13: High resolution AFM images allow to determine the in-plane 2D unit cell of the organic layer. We define d_1, d_2, and δ as shown in image (c). For comparison also the unit cell of the substrate is plotted in image (c). As is showed, the c-axis of the substrate runs approximately vertically in all the images. However, misalignment of the substrate could lead to variations of about 10°.

Although AFM data provide a direct characterization of the 2D in-plane unit cell, the precision of the data is not high enough for a complete and accurate determination of the lattice parameters of the organic layer. X-ray diffraction in GIXD geometry allows the precise determination of the in-plane lattice periodicities that give rise to Bragg reflections. The reflections found in the films on SiO_2 reported in Section 6.1.1, have been also located in the films on Al_2O_3. Azimuthal scans have been performed while the detector has been kept fixed at the $q_{||}$ of each reflection to determine the azimuthal distribution of these peaks. The in-plane reflections that could be scanned are $q_{||} = 1.1537$, 1.4735, and 2.3793 $Å^{-1}$. The located peaks are shown in Figure 6.14 as circles, while their symmetry-related reflections have been added to this plot as squares. The c-axis of the substrate points in the 0° direction, and thus forms a symmetry axis. However, due to the geometry of the measurement and experimental limitations only a limited azimuthal range could be accessed. This azimuthal range is shown by the solid line in Figure 6.14.

Comparing the x-ray data with the AFM measurements discussed above, it can be stated that the in-plane periodicity defined as d_2 can be identified with the reflection $q_{\|} = 1.1537$ Å^{-1}. The lattice spacing measured with AFM is in accordance with the spacing derived from this reflection, having $d_{xr} = 5.45$ Å $\simeq d_2/2$. The angle between this reflection and the c-axis of the substrate determined from the x-ray measurements is 10.7°, which is also in agreement with the angle derived from the AFM data. The azimuthal spread of the crystallites in the plane can be also determined from the x-ray scans, which show that all the in-plane peaks located have FWHM of 2-3°, and therefore show a high degree of in-plane alignment of the crystallites. The second AFM periodicity d_1 can be associated to the Bragg reflection found in films on SiO_2 at $q_{\|} = 1.7204$ Å^{-1} which, due to experimental limitations, could not be found within the experimental range scanned. However, the fact that this peak is not in the scanned azimuthal range

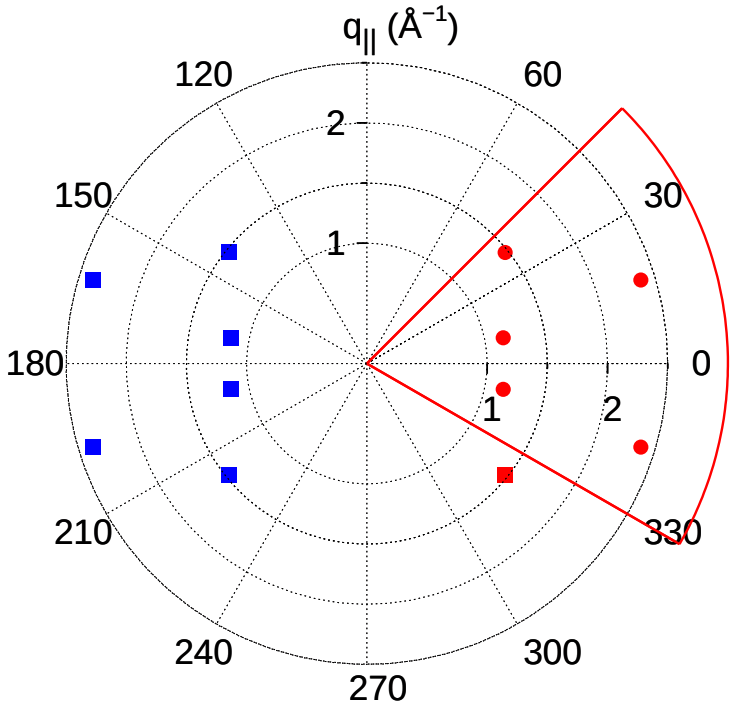

Figure 6.14: Azimuthal distribution of the in-plane Bragg reflections of a DIP layer on Al_2O_3. The azimuthal range that could be accessed is delimited by the solid line. The c-axis of sapphire is located at 0°.

is also consistent with the AFM data.

Since the DIP bulk structure is not yet well-established, it is not possible to make an assignment of the reflections found here. However, they can be compared to several proposed crystalline structures of bulk DIP and also of thin films. All these proposed structures are listed in Table 6.3. While Pflaum *et al.*determined a triclinic unit cell by x-ray diffraction on DIP single crystals [69], different crystalline structures have been reported for DIP thin films on several substrates. Hoshino *et al.* reported monoclinic structures determined by TEM measurements [70] of thin films on NaCl and perylene. An in-plane rectangular unit cell has been also proposed for films on SiO_2 based on x-ray measurements [75].

Frey and Karl Single crystal		Hoshino *et al.* DIP/NaCl	Hoshino *et al.* DIP/Perylene	Düerr *et al.*[75] DIP/SiO_2
	Triclinic	Monoclinic	Monoclinic	2D rectangular
$Z =$	4	2	2	2
$a =$	11.59	8.67	11.0	8.55
$b =$	12.97	6.96	10.6	7.09
$c =$	14.88	18.55	17.5	-
$\alpha =$	98.11	90.0	90.0	-
$\beta =$	98.10	93.5	106.0	-
$\gamma =$	114.53	90.0	90.0	90.0

Table 6.3: Triclinic DIP bulk structure determined by Frey and Karl, with four molecules per unit cell and $P\bar{1}$ symmetry [69]. Different crystal structures are reported by Hoshino with monoclinic symmetry for films on various substrates [70]. An in-plane rectangular unit cell has also been proposed [73].

6.2.5 Optical constants

The optical properties of in-plane oriented layers are expected to have in-plane anisotropies, as occurred in the case of $F_{16}CuPc$ on Al_2O_3. To determine the orientation of the principal axes of the layers, β-scan measurements (see Section 4.3) have been performed by acquiring the ellipsometric parameters $\tan\Psi$ and $\cos\Delta$[95] at different azimuthal orientations of the sample and at different settings of the fixed analyzer. From these scans, shown in Figure 6.15, it is possible to determine whether there is an optical axis of the layer on the film plane,

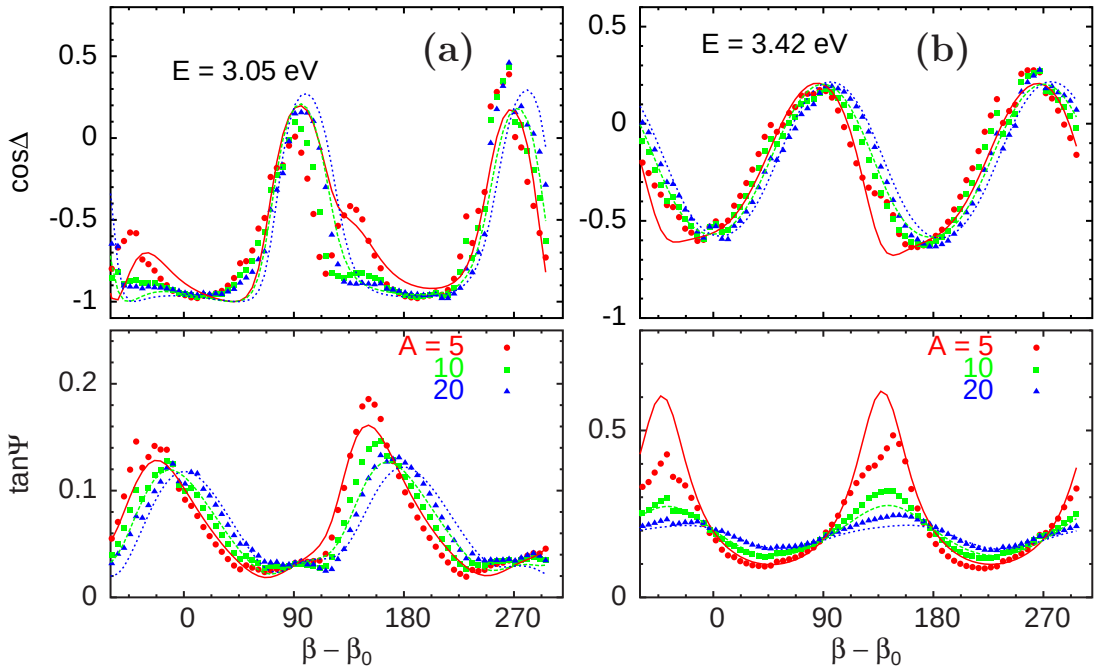

Figure 6.15: Two β-scans at the energies of 3.05 and 3.42 eV for different settings of the analyzer angle A. The red curve has been measured at A=5°, the green curve at A=10°, and the blue curve at A=20°. The thickness of the film is 1000 Å and the growth temperature 150°C.

and if this is the case its orientation can be determined. The curves in Figure 6.15 are recorded on a 50 nm thick film grown at $T_g = 150$°C. The analyzer angles are $A = 5$,10, and 20°, and they are taken at the energies of 3.05 eV (Figure 6.15(a)) and 3.42 eV (Figure 6.15(b)). As we see, the curves in each plot cross

In Figure 6.16 the *effective dielectric function* of the layer is plotted. The two recorded spectra have been measured at the azimuthal angles of $\beta = 56$ and 146°, where the lines of the β-scans shown in Figure 6.15 cross. As we see the anisotropy of those layers is considerably strong, although they are not so strongly polarized as in the case of F_{16}CuPc on Al_2O_3.[82, 116] As we have seen, in the isotropic films grown on SiO_2 there is no azimuthal dependence of the dielectric tensor, due to the fact that the crystallites forming the layer are randomly oriented in the plane. However, the out-of-plane component was different from that in the plane. In the present case, the layers have three different components of the dielectric tensor, that is $\varepsilon_X \neq \varepsilon_Y \neq \varepsilon_Z$. The information derived from the films on SiO_2

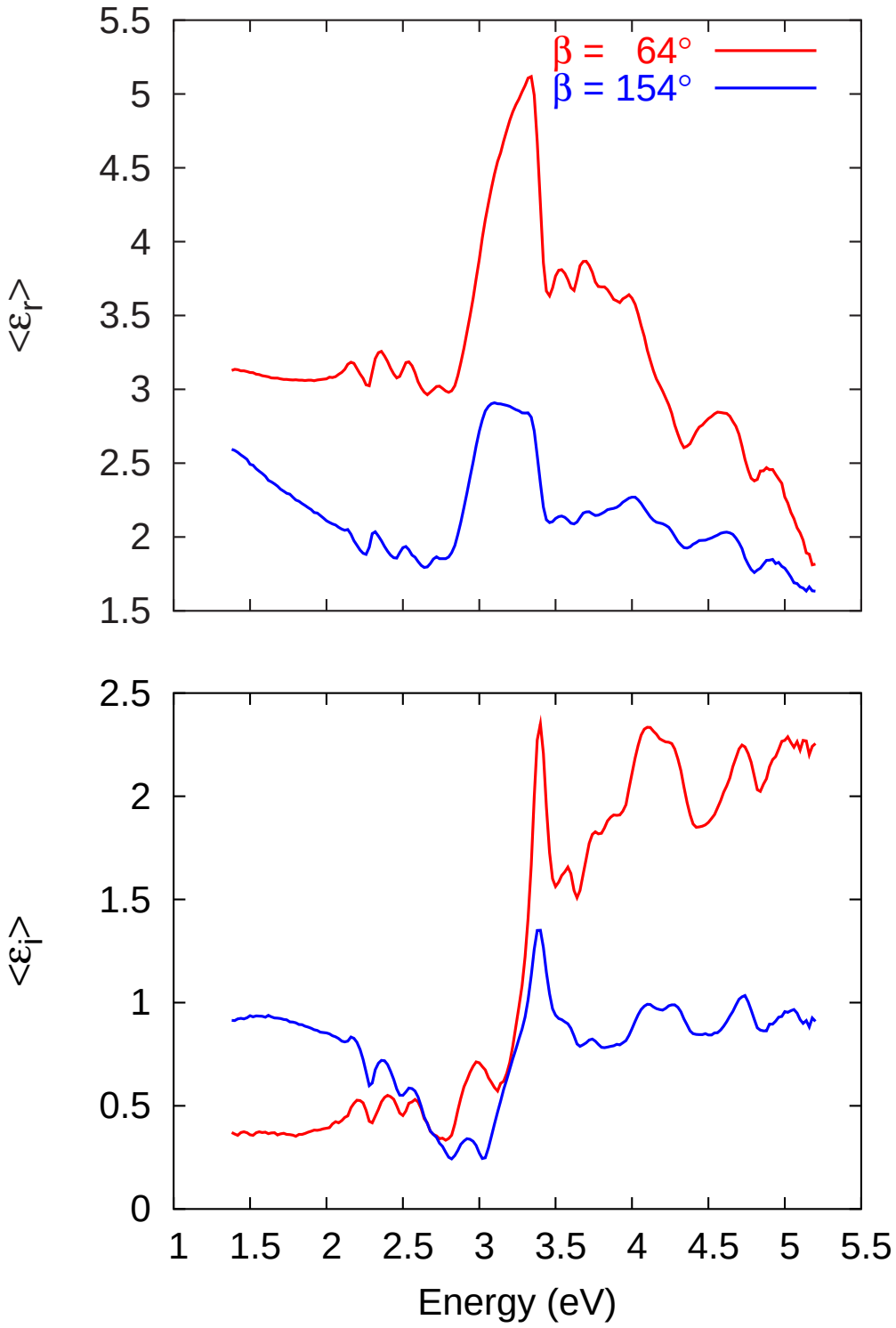

Figure 6.16: Effective dielectric function of a 50 nm thick film on Al_2O_3 measured at two different azimuthal orientations of the sample.

can be used here to fix the value of the out-of-plane component ε_Z to determine the two in-plane functions.

Thus, the layers on Al_2O_3 allow the study of the optical and electronic properties of those materials, single crystals of which are very difficult to obtain or have too small dimensions.

6.2.6 Low temperature deposition

A complete study of the properties of DIP films on SiO_2 as a function of the substrate deposition temperature can be found in references [71, 72], where it was determined that at $T_g = 150°C$ the best structural properties are obtained. In the present study we have deposited the layers at this fixed substrate temperature T_g, however, layers at lower values of T_g have been used to compare their properties, especially for the films on Al_2O_3, where at high temperatures the films are in-plane oriented.

In Figure 6.17 an AFM image of a 25 nm thick film deposited at $T_g = -50°C$ is shown. It can be seen that the grain density is higher than the films grown at higher T_g. The grains have, thus, smaller dimensions, and interestingly they do not show the regular shape observed on other films (see e.g. Figure 6.7). The roughness of the layer is higher, and the crystalline quality lower. The terraces separated by monomolecular steps are no longer visible. Moreover, the optical

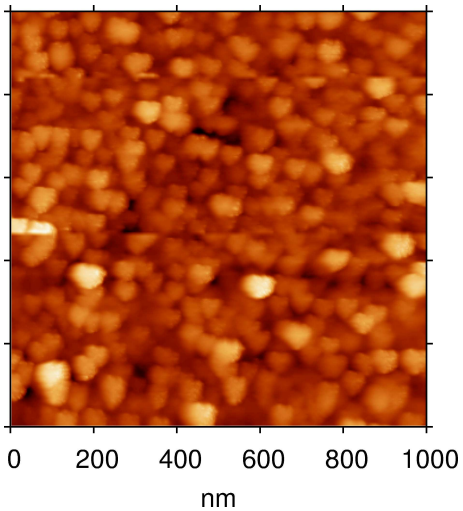

Figure 6.17: DIP thin film on Al_2O_3 deposited at $T_g = -50°C$. The thickness of the layer is 25 nm.

properties of this layer determined by spectroscopic ellipsometry measurements, show no in-plane anisotropy, from what follows that the layers have no preferred in-plane orientation.

6.2.7 Spiral Growth

We have seen that the surface of the Al_2O_3 substrate before growth presents atomically flat terraces separated by steps of around 2 nm. At several points, however, the facet steps of two adjacent terraces merge into a single step edge. At this position, therefore, one of the terrace disappears, and thus the surface presents n terraces (or $n-1$ step edges) at one side of this point and $n+1$ terraces (or n step edges) at the other side. The inverse situation also takes place, i.e. a step edge is divided into to and a new terrace appears. Such a situation can be observed in detail in the 3D representation of the AFM image of Figure 6.18(a). At these positions, a particularly interesting growth behavior is observed. As can be seen in Figure 6.18(b) the organic layer develops forming a *spiral* or *screw dislocation*. The center of the spiral is exactly the point where the step edges of the substrate merge, as is illustrated in the AFM images of Figure 6.18. The image on the left (a) shows the bare substrate, while the image on the right shows

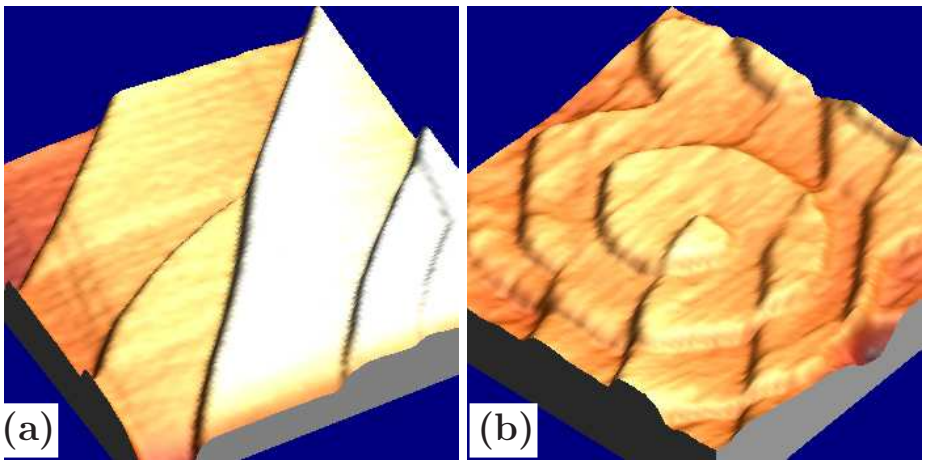

Figure 6.18: AFM images in 3D representation (a) of the Al_2O_3 substrate before the growth at a position where two step edges merge; and (b) of a 25 nm DIP layer on an equivalent location.

25 nm thick film evaporated at $T_g = 150°C$. Obviously the images are not taken at exactly the same position, but it can be stated that they are equivalent positions since the steps of the substrate can still be outlined on the AFM image of the film (Figure 6.18(b)).

Both spiral orientations are observed, depending in which direction the steps join, since the substrate presents both orientations, the layer also shows spirals growing both right-handed and left-handed orientations. This can be seen in Figure 6.19, where images (a) and (c) show right-handed spirals whereas image (b) shows two left-handed spirals. It should be pointed out that the spirally growing crystallites preserve the nearly-hexagonal shape characteristic of the DIP films on Al_2O_3. The step height of the organic crystallites is also around 1.6 nm, as was determined in Section 6.2.1.

The evolution of the spirally growing crystallites is shown in Figure 6.19, where AFM images of DIP thin films of thicknesses of 6 (image (a)), 25 (b), and 50 nm (c) are shown. As can be seen, the growth in spiral is already found in the 6 nm film (about 4 monolayers). Finally, in the 50 nm film, we see that the spiral expands over more than 500 nm in diameter. The dimensions of the spirals are comparable to the other crystallites observed in the film discussed in Section 6.2.3.

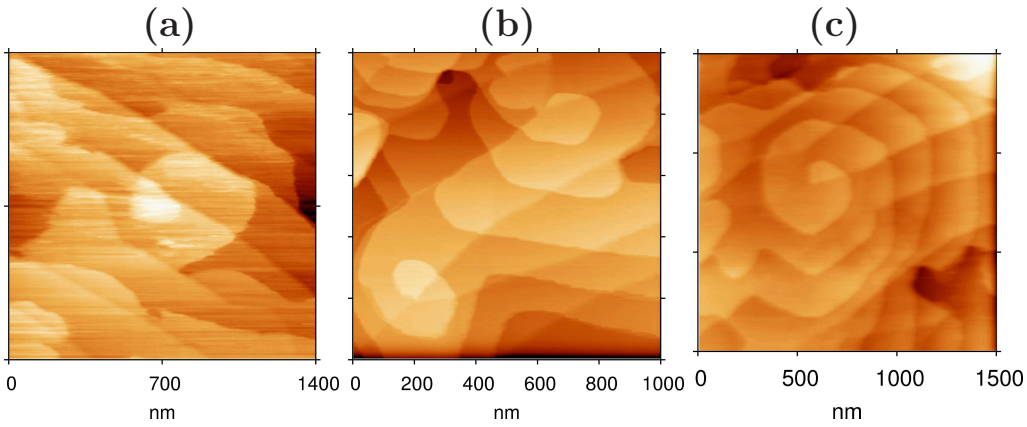

Figure 6.19: AFM images of spirally growing crystallites at different deposited thickness D values, 6 nm (a), 25 (b), and 50 nm (c). It can be seen also that spirals growing in both orientations are obtained.

High resolution AFM images on the spirals show the same stripe periodicity found in Section 6.2.4. In addition images at different locations of a single crystallite show the same stripe orientation, as is shown in Figure 6.20

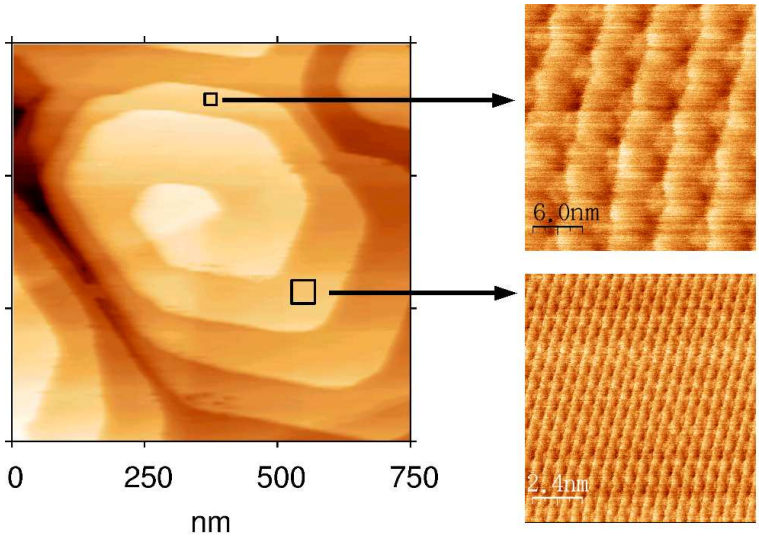

Figure 6.20: Molecular resolution images taken at different spots on a spiral show the same orientation of the resolved periodicities.

6.3 Conclusions

DIP thin films on SiO_2 and Al_2O_3 have been grown at $T_g = 150°C$ at various thicknesses from 6 to 100 nm. The degree of order in the direction perpendicular to the film plane is similar on both substrates. The molecules stand nearly perpendicular to the substrate surface and low roughnesses are obtained within the studied thickness range. Although the films present the same crystalline structure independently of the substrate used, the degree of order is different in each case. While an in-plane random distribution of domain orientation is found in films on SiO_2, films on Al_2O_3 exhibit a preferred orientation. The shape of the organic crystallites, observed by AFM, is also different on both substrates. While rounded grains are observed on SiO_2, regularly shaped, almost hexagonal crystallites are found in films on Al_2O_3. This regular shape can be related to the in-plane unit cell determined by high-resolution AFM data which is in accordance with the x-ray Bragg reflections located by GIXD. The dimensions of the crystallites as a function of film thickness has been studied by AFM. Films on Al_2O_3show a larger grain size than films on SiO_2, and micrometer-seized grains can be obtained. The large crystallite size and their in-plane preferred orientation of films on Al_2O_3 are very promising results, which can be considered as a step towards the achievement of single-crystalline organic thin films. The high degree of order is observed in the

anisotropic optical properties of the layers, studied by spectroscopic ellipsometry. Several electronic transitions can be located, which the lowest excitonic transition around 2.3 eV. It has also been shown that the morphology of the substrate can promote dislocations in the organic layer which evolve in a spiral growth.

Chapter 7

Organic heterostructures

The use of more complex structures than just an organic thin film on a substrate is needed in electronic applications of organic materials. Many organic devices consist of a sequence of several layers on a substrate. First of all, wiring and metal contacts must exist to provide a path of charge injection in the organic active layer. An insulating layer is also required in many devices, as in OFETs, where it is used as the dielectric between the gate and the organic layer. Finally, several organic layers of different materials are used in applications as OLEDs or solar cells, where basically a *pn*-junction allows the effective transport of electrons and holes towards or away from the organic-organic interface. Moreover, additional organic layers, which serve as electron or hole blocking layers, are often used to improve the performance of these devices. The construction of more complex heterostructures as organic quantum wells or organic supperlattices involves many organic-organic interfaces. Thus, the study of all those interfaces is of interest in the technology of organic electronic devices.

Although the electronic structure at the organic-metal and organic-organic interfaces has been focus of several studies during the last years [135], the structural properties of these interfaces has not been taken into account in their interpretation. Fundamental issues as interdiffusion, organic on organic epitaxy, or structural changes induced by these interfaces need to be addressed before the electronic properties of the interfaces can be fully understood. Recently, the metal-organic interface of DIP/Au has been studied relating their structural properties with their electronic properties derived from UPS measurements [75]. The insulator-organic interface has been also recently studied [76] and has been shown that the

stability of the organic material can be improved by the insulating capping layer. The organic-organic interface holds probably the most intriguing properties due to the complexity of both materials which can lead to very different scenarios.

In this chapter we discuss the interface between the two organic compounds used in this work, i.e., F_{16}CuPc and DIP. In the preceding chapters we have presented the properties of each individual layer deposited on several substrates, and we have determined the optimum growth conditions in each case. Now we focus in the interfaces of DIP/F_{16}CuPc and F_{16}CuPc/DIP of organic bilayers. We have deposited DIP on previously grown F_{16}CuPc layers, and F_{16}CuPc on DIP films to characterize the interface in the two cases. The deposition of the first organic layer has been performed under the growth parameters determined as optimal in the previous chapters. After the growth of the first layer, the films have been characterized in the in-situ AFM. The usual morphology has been observed and the samples have been transferred again to the growth stage, where the second organic layer has been grown. The second evaporation has been performed in both cases at three different depositions temperatures $T_g = -150°C$, room temperature (RT), 150°C. The substrates used were SiO_2 and Al_2O_3. MgO has not been used since the overgrown layer presented lower structural definition and high roughness, as discussed in Chapter 5. This chapter is focused in the structural properties of these interfaces, and especially in the differences found at the interface DIP-F_{16}CuPc as a function of the deposition parameters. As we show strong differences appear depending on the order in which the two organic materials are evaporated. Thus, the DIP on F_{16}CuPc interface exhibit different properties than the F_{16}CuPc on DIP interface.

7.1 DIP on F_{16}CuPc films

Films of DIP deposited on F_{16}CuPc layers show very promising properties since their structure is well-ordered across the two organic layers. It is found that the organic-organic interface is well-defined with low interdiffusion. This is seen in Figure 7.1(a), where the x-ray reflectivity curve is shown. As we can see, the Kiessig oscillations do not exhibit a constant spacing between two consecutive minima as observed in single layers (see, e.g., Figures 5.2 and 6.1). This is due to interferences between x-rays reflected at the ambient-organic layer, organic-organic, and organic-substrate interfaces.

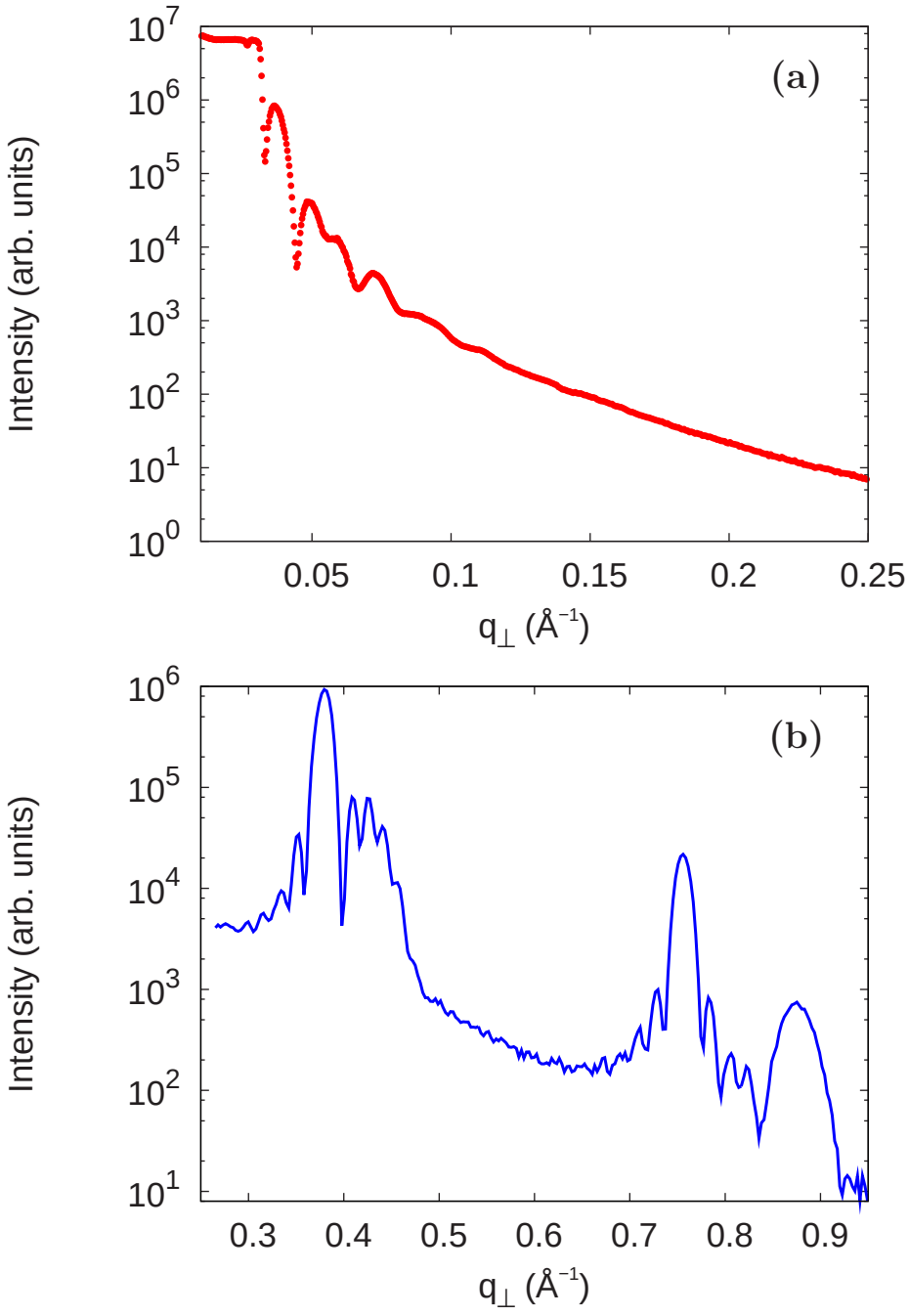

Figure 7.1: (a) X-ray reflectivity curve of a DIP layer evaporated on F_{16}CuPc/SiO_2. (b) First and second order Bragg reflections of DIP and F_{16}CuPc.

At higher values of the scattering vector, the Bragg reflections of both organic layers appear, as is shown in Figure 7.1(b). The peak at the low scattering vector values is the first order out-of-plane reflection of the DIP layer. This reflection presents very well-defined Laue oscillations on the left side of the peak. On the right side, we can see that the Laue oscillations are also present but superimposed to the F_{16}CuPc Bragg reflection. The similarity of the lattice constants of both organic layers give rise, thus, to such an interesting pattern. In Figure 7.1(b) we can also see the second order Bragg reflections of DIP and F_{16}CuPc, at the scattering vector values of 0.756 and 0.867 Å^{-1} respectively.

A rocking scan performed between the position of the DIP and F_{16}CuPc first order Bragg reflections (at $q_z = 0.40$ Å^{-1}) is shown in Figure 7.2. As we can see, it is evident that two peaks are superimposed in this curve, a higher in intensity

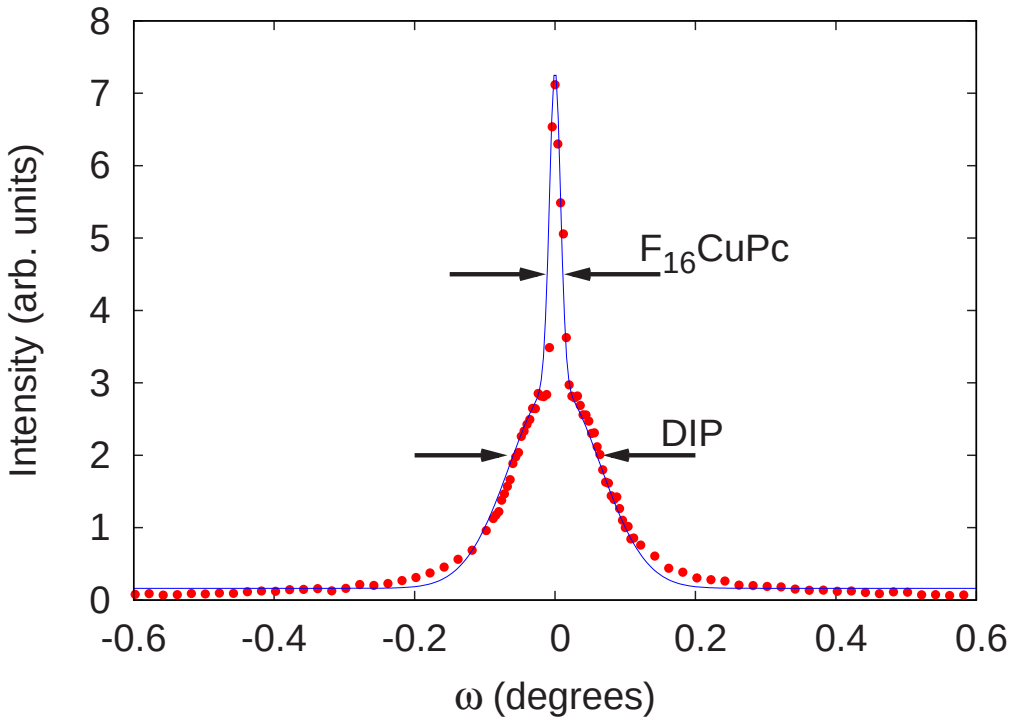

Figure 7.2: Rocking scan performed at $q_z = 0.40$ Å^{-1} (position between the first order Bragg reflections of the two organic layers). The curve can be fitted with two Gaussian functions. The FWHM value of each function accounts for the mosaicity of each organic layer.

and narrower peak, and a second peak lower in intensity and broader. Both peaks are centered at $\omega = 2\theta/2 - \theta = 0$, and therefore on the specular path. They can be attributed to each single organic layer. Since the Bragg peaks of both materials are very close in q_z, the contributions of both Bragg peaks are present in the rocking curves. This curve can be fitted with two Gaussian functions, as shown in the figure. From the fit the FWHM values of 0.017° and 0.16° are derived. The broadest peak arises from the mosaicity of the DIP layer while the narrowest peak accounts for the mosaicity F_{16}CuPc layer. Thus, the low mosaicity of the firstly deposited layer (0.017°) is similar to that found in single films (Chapter 5) and is not modified by the deposition of the second layer. On the other hand, the mosaicity of the second layer (0.16°) is one order of magnitude higher, however, this is still a relatively low mosaicity.

The two organic layers have different electron densities and consequently their critical angles also differ. This is clearly seen in Figure 7.1(a), where two decays of the intensity are observed. This is also observed if a sufficiently broad rocking scan is performed on the reflectivity regime, as is shown in Figure 7.3. This rocking scan performed at $q_z = 0.066$ Å^{-1} ($2\theta = 0.5°$at the radiation energy of 15 keV). In the plotted curve we can see that the intensity increases considerably at both sides of the narrow rocking peak. These peaks are the so called *Yoneda wings* and appear when the incident, α_i, or final angle, α_f, are equal to the critical angle [136]. The wing labelled with a "1" arise from the DIP layer, while the weaker peaks labelled with a "2" correspond to the F_{16}CuPc layer.

7.2 F_{16}CuPc on DIP films

A very different situation is found when the films are evaporated in the opposite order, that is, when F_{16}CuPc is evaporated on DIP films. In this case the F_{16}CuPc layers exhibit a different crystalline structure than that found in single films. The interfaces are not well-defined. This can be seen in the x-ray reflectivity curves plotted in Figure 7.4. As can be observed a very low definition of the interfaces is found when the F_{16}CuPc layer is evaporated at $T_g = 150$°C (red, solid line). The reflectivity curve presents very week Kiessig oscillations and a strong damping of the intensity. This is an evidence of high roughness and low definition of the interfaces. The film deposited at $T_g = -150$°C, shows a better defined interface as is derived from the better definition of the Kiessig fringes of the reflectivity

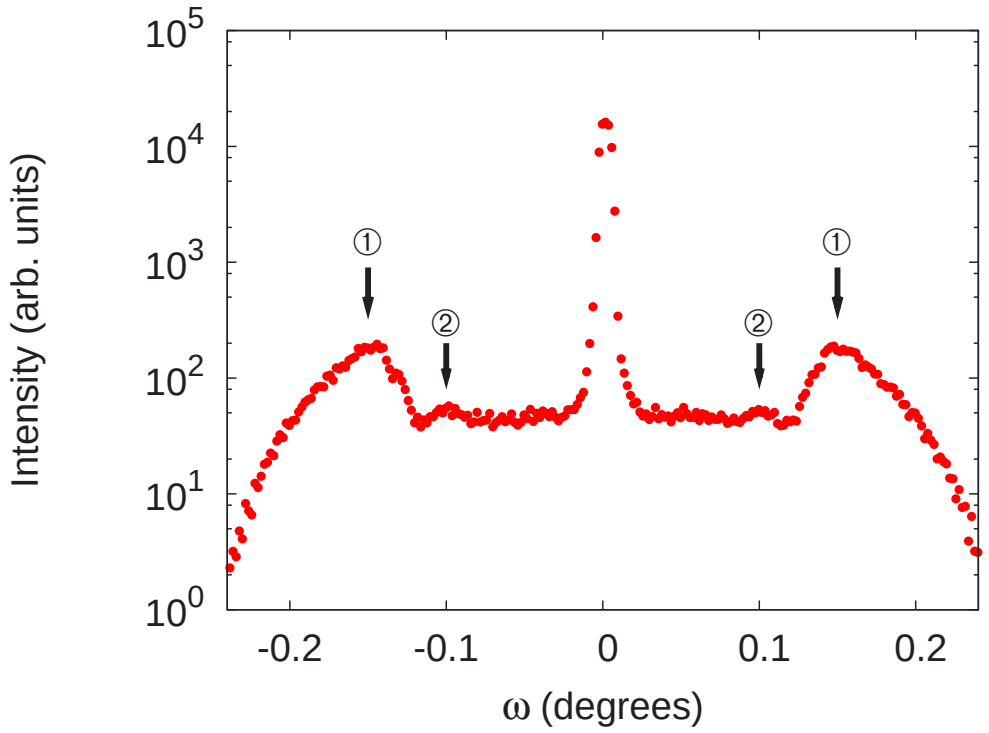

Figure 7.3: Rocking curve measured at $q_z = 0.066$ Å^{-1} ($2\theta = 0.5°$ at the radiation energy of 15 keV). Yoneda wings [136] arising from the two organic layers are observed.

curve, which is also plotted in Figure 7.4 (blue, dashed line). The best situation is found when the F_{16}CuPc layer is evaporated at room temperature. This is shown in Figure 7.5, where we can observe that many Kiessig oscillations are found along the reflectivity regime.

However a different molecular orientation is found in these films. While the firstly deposited DIP layer shows the usual structural properties studied in Chapter 6, the F_{16}CuPc layer exhibits very different properties. As we can see in Figure 7.4 there is a Bragg reflection at $q_z \simeq 0.378$ Å^{-1} which corresponds to the DIP layer. In the film deposited at $T_g = 150°$C, this reflection presents no Laue oscillations, which can be due to interdiffusion of F_{16}CuPc in the DIP film. In the film deposited at $T_g = -150°$C on the other hand, the Bragg peak presents several Laue oscillations. This can be attributed to a lower interdiffusion due to the low temperature of the substrate during deposition of the second layer, which limits

the mobility of the incoming F_{16}CuPc molecules. An important finding is that the usual peak from the F_{16}CuPc layer at $q_z \simeq 0.42$ Å^{-1} is not present in these scans. As we can see, for the layer deposited at high temperature, there is no evidence of this peak, while in the layer deposited at low temperature the asymmetry of the DIP Bragg reflection could point to a broad F_{16}CuPc peak. However, in both cases there is a Bragg reflection at $q_z = 1.98$ Å^{-1}, which corresponds to a lattice spacing around 3.2 Å. This reflection has been found at the same position where an in-plane peak was found in the F_{16}CuPc single-layers (see Sections 5.1 and 5.3). Therefore, the fact that this peak appears now out-of-plane suggests that the F_{16}CuPc molecules crystallize on the DIP surface lying approximately flat.

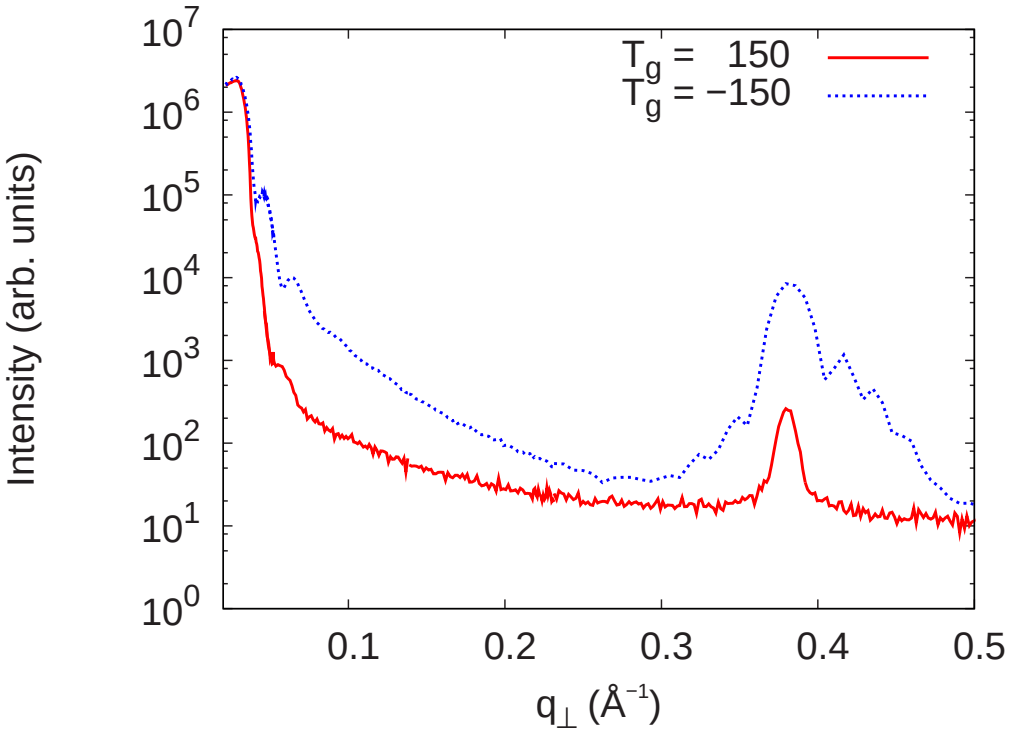

Figure 7.4: Reflectivity curves of two F_{16}CuPc on DIP bilayers. The second layer (F_{16}CuPc) has been deposited maintaining the substrate at 150°C (red, solid line) and at −150°C (blue, dashed line). The DIP first order Bragg reflection is also visible in both curves. These scans have been performed at a rotating-anode station with Mo-K_α radiation (0.71069 Å).

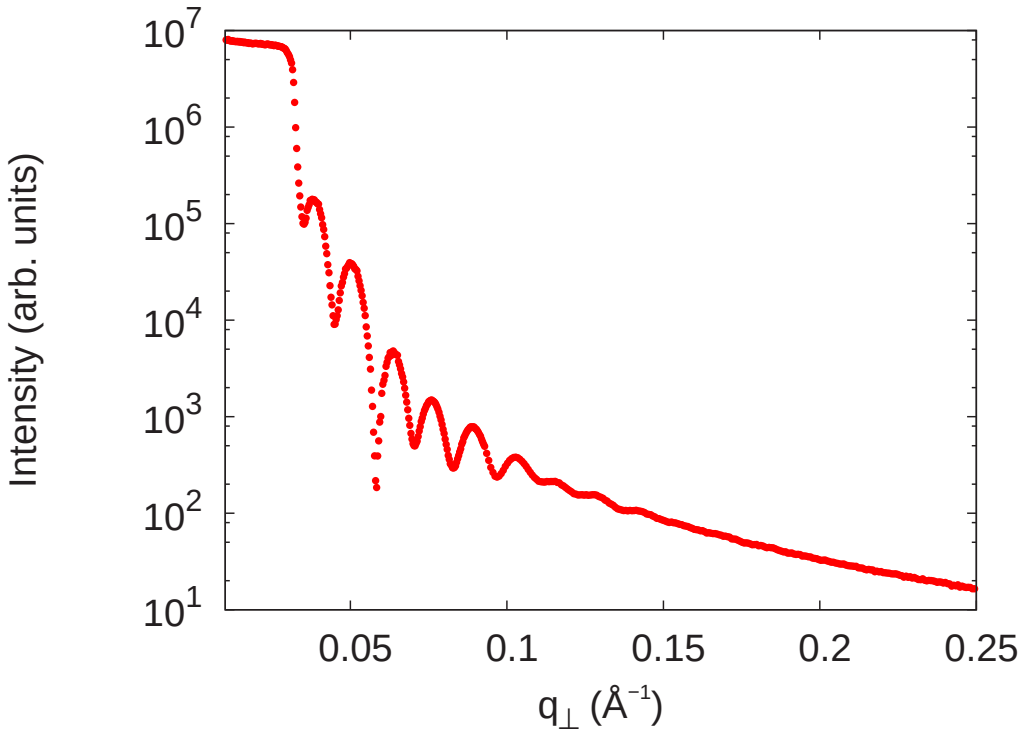

Figure 7.5: X-ray reflectivity curve of a bilayer of F_{16}CuPc on DIP on SiO_2. The F_{16}CuPc layer has been deposited at RT.

7.3 Conclusions

We have shown in this chapter the deposition of organic heterostructures may involve complex processes which lead to more different scenarios than in the single layers. In addition, the deposition conditions drastically influence the organic-organic interface. Thus, a complete structural characterization is needed before the electronic structure of the interfaces can be addressed. Interestingly, the DIP-F_{16}CuPc interface is asymmetric in that films of DIP on F_{16}CuPc show very different properties than the F_{16}CuPc films evaporated on DIP. In the first case the interface is very well defined, and the structural properties of the second layer are similar to the single layers (although a higher mosaicity is obtained). In the second case the F_{16}CuPc layer evaporated on DIP show a completely different ordering behavior, and the organic-organic interface presents high diffusion.

Chapter 8

Summary

Thin films of F_{16}CuPc and DIP have been deposited on SiO_2, Al_2O_3, and MgO substrates and have been characterized by AFM, x-ray diffraction, Raman scattering and SE. The thin film growth has been performed at different substrates temperatures T_g, and with various film thicknesses below 100 nm. The influence that the growth conditions and the substrates used have on the properties of the layers are studied. The use of the different techniques allow to relate the optical properties of the films with their crystalline structure and degree of order. As has been shown, the optoelectronic properties of the layers are closely related to the degree of structural order they exhibit.

Organic heterostructures (bilayers) have been also studied. A first organic layer has been deposited under optimal evaporation conditions (previously determined), while the second layer has been grown at different substrate temperatures. The structural properties of the organic-organic interface, studied by x-ray diffraction, have been shortly discussed.

8.1 Thin films on SiO_2 and MgO

Deposition on oxidized silicon wafers results in films with a well-defined out-of-plane stacking of molecular lattice planes, and narrow rocking widths when evaporated at substrate temperatures near desorption. Rocking widths of 0.017° are obtained for F_{16}CuPc films grown at $T_g = 250$°C, and 0.009° for DIP films deposited at $T_g = 150$°C. The films are coherently ordered across the entire thickness, and surfaces with low roughness are obtained. In-plane cristallinity has been observed by GIXD, but on these flat amorphous substrates there is no overall azimuthal

order, rather, in-plane randomly oriented crystallites are formed.

AFM measurements on F_{16}CuPc layers exhibit a characteristic morphology with elongated features. At higher resolution, a needle-like substructure of the terraces becomes apparent. These features are related to the inherently strong anisotropy of the F_{16}CuPc crystallites in structure and shape. However, the optical properties determined by SE are isotropic, due to the in-plane random orientation of the crystallites. Several electronic transitions in the Q-band could be identified by SE at the energies of 1.57, 1.76, 1.90, and 2.00 eV.

The properties of the F_{16}CuPc layers have been investigated as a function of the substrate temperature and films thickness. It has been found that the lattice constant of the organic layer, $a_\perp$, depends on the growth temperature T_g. Upon increasing T_g, a monotonic increase of $a_\perp$ from 14.5 Å for samples grown at room temperature to 15.3 Å for samples grown at 250°C is found. For films grown at −150°C a broadened Bragg reflection revealed a lower out-of-plane coherence length, and a larger mosaicity (0.1°), while the lattice constant is 15.2 Å. The surface roughness is considerably increased at low temperatures.

Films of DIP on SiO_2 exhibit a higher roughness than F_{16}CuPc films, however it remains in moderate values and closed films are formed. The morphology exhibits rounded terraces with well-defined step edges of ∼15 Å height. Several in-plane reflections of the organic layer have been identified by GIXD. The optical properties of these layers present a uniaxial symmetry as determined from SE measurements at different incident angles. While the in-plane random distribution of the crystallites originates the two ordinary components of the effective dielectric tensor, the out-of-plane component exhibits higher values. This is in agreement in having the molecules standing with their long axis approximately perpendicular to the substrate surface. The lowest excitonic transition has been found at 2.3 eV.

F_{16}CuPc thin films on MgO substrates present a lower crystalline definition, with mosaicities around 0.15° for films deposited at T_g = 250°C. In addition, the morphology exhibits a high roughness, which can be due to the irregular surface of the substrate.

8.2 Thin films on Al_2O_3

Films on stepped Al_2O_3 exhibit the most attractive properties. The degree of structural order of the films in the out-of-plane direction is similar to that of films on SiO_2, and even lower roughnesses are obtained. However, the in-plane structural properties of the layers are importantly improved by the use of this substrate and the convenient growth conditions. First of all, and in contrast to the "in-plane powder" films on SiO_2, the organic crystallites on Al_2O_3 exhibit a preferred in-plane orientation. Secondly, the in-plane dimensions of the observed crystallites are one order of magnitude larger in films on Al_2O_3. These two structural differences of films on Al_2O_3, together with the smoother surfaces obtained, change substantially the properties of the thin films on Al_2O_3, which will now display strong anisotropies.

The preferred azimuthal alignment of the layers on Al_2O_3 is independently observed from all the experimental techniques used. AFM measurements evidence that the F_{16}CuPc needles or the hexagonal DIP crystallites are all aligned azimuthally. High resolution AFM images allow to draw the in-plane unit cell of the organic materials. X-ray diffraction measurements in GIXD geometry allow a more precise determination of the azimuthal alignment as well as the orientation of the organic layer relative to the substrate. The Bragg reflections located in films on SiO_2 are as well present in films on Al_2O_3, indicating that the same crystalline structure is formed on both substrates. By analyzing the azimuthal dependence of the Raman scattering spectra, a quantitative analysis of the degree of order as well as of the molecular orientation of the layers can be performed. Finally, SE evidences the high optical anisotropies derived from the high degree of in-plane order of the layers. F_{16}CuPc films behave as optically biaxial media, with two principal axes in the surface of the sample, essentially coinciding with the substrate *c*-axis direction and the perpendicular to it.

The Al_2O_3 induced alignment is only found in films deposited at high temperatures. When the growth temperature is decreased higher azimuthal disorder and rougher morphologies are obtained. Also, growth on different types of sapphire substrates, i.e., with different step pattern due to different miscuts and annealing conditions, lead to different types of ordering. Consequently, the step edges play an important role in the final structural properties. However, the organic

layers are aligned (or nearly) aligned with the crystallographic *c*-axis axis of the substrate. This would point to a epitaxial or quasiepitaxial structure of the organic layers on the Al_2O_3 surface, with a well-defined orientational relationship between the film and the substrate lattice interaction. The step facets would favor the anisotropic growth in a given azimuthal orientation and serve as nucleation centers of the organic crystallites. Thus, it is possibly the complex interplay of various factors (epitaxy and step facets) which leads to such a well-oriented layers on Al_2O_3. A more detailed study of this alignment mechanism would require a systematic study of the early stages of the growth process, starting at the submonolayer regime, which is not in the scope of this study.

8.3 Organic heterostructures

The structure at the organic-organic interface of F_{16}CuPc and DIP has been studied as a function of the deposition order (DIP on F_{16}CuPc vs. F_{16}CuPc on DIP) and at different substrate temperatures. It has been found that the substrate temperature influences especially the interdiffusion at the organic-organic interface and the crystalline structure of the top layer. At high T_g interdiffusion at the organic-organic interface is favored, while at low T_g the structure of the second organic layer is not well-defined, and a high roughness is obtained. The best structural properties are found when the top layer is evaporated at ambient temperature. Strong changes are found depending on the order of deposition. Thin films of DIP on F_{16}CuPc exhibit very well defined interfaces and good crystallinity of both layers with narrow mosaicities. The same Bragg reflections found in single layers are observed, indicating that a similar packing and orientation takes place. On the other side, F_{16}CuPc films on DIP exhibit important differences. The interaction at the organic-organic interface induces the growth of the second layer (F_{16}CuPc) in a completely different crystalline orientation. The Bragg reflection usually found in the plane of the layer in single F_{16}CuPc films is now found in the out-of-plane direction, indicating that the molecules are lying nearly flat on the firstly-deposited DIP layer.

Structural changes induced by the organic on organic deposition will obviously change the properties of the layers. Therefore, a full structural characterization is needed before an attempt to interpret the electronic properties at the organic-organic interface is made.

Appendix A

Al_2O_3 substrates

Crystalline aluminium oxide (Al_2O_3) in its purest form is known as *corundum* or sapphire. The red variety of Al_2O_3 is known as ruby, and the term sapphire is used to refer to other colors, and scientifically it is used to refer to the crystal. It is the second hardest natural mineral known (9 in Mohs' scale, after diamond). Al_2O_3 has a broad transmission band spanning the UV, visible, and IR bands. These excellent mechanical and optical properties makes sapphire an excellent material for applications in optics, high pressure or even high temperature (sapphire has a melting point of 2053°C).

Sapphire belongs to the space group $R\bar{3}c$ (D_3^6d) and therefor it is rhombohedral. However, it is commonly described in terms of the hexagonal four-dimensional Miller-Bravais indices [88]. The hexagonal structural unit cell is described by the parameters

$$\begin{aligned} a &= 4.748 \text{ Å} \\ c &= 12.991 \text{ Å} \\ U &= 254.792 \text{ Å}^3 \end{aligned}$$

which is formed by 30 atoms, 12 Al^{3+} and 18 O^{2-}.

The most common orientations of Al_2O_3 are shown in Figure A.1. The (0001) or *c*-plane is the basal plane containing the hexagonal lattice. The orientation of the substrates used in this work is $(11\bar{2}0)$ plane (A-plane). This plane contains the *c*-axis and therefore is a two-fold symmetry plane.

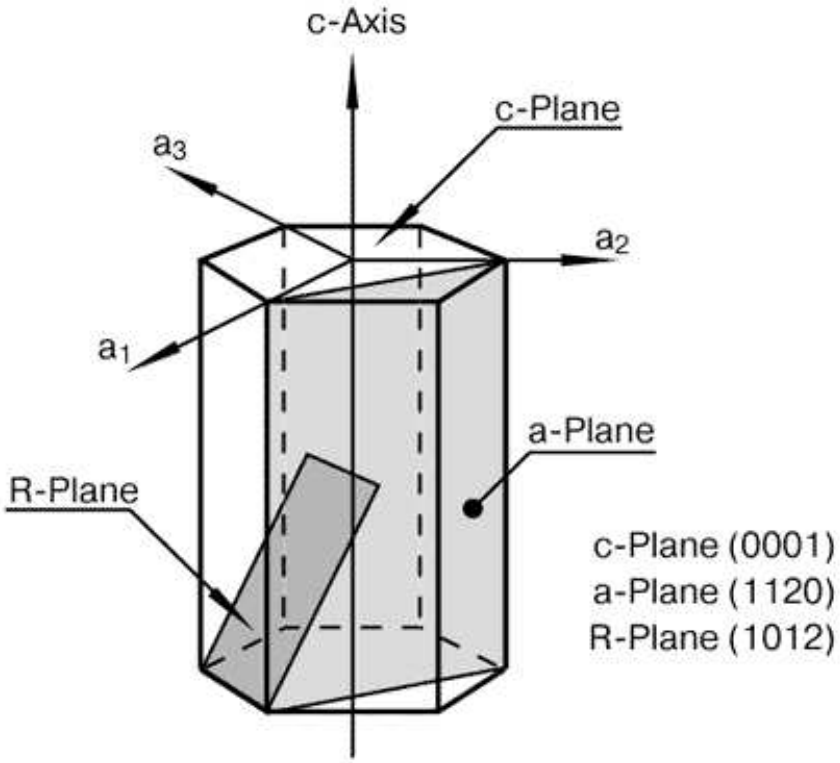

Figure A.1: Definition of the most common orientations of Al_2O_3. The surface used in this work is the $(11\bar{2}0)$ plane or A-plane.

The Al_2O_3 substrates are usually chemo-mechanically polished when purchased. An atomically flat surface can be obtained by annealing the substrates at temperatures higher than 1000°C. After this annealing process the surface is reorganized. However, the physical surface is usually not perfectly aligned with the crystallographic $(11\bar{2}0)$ plane, and a small misorientation is present (*miscut*). Misorientations between 0.1 and 2° are common. The $(11\bar{2}0)$ surface is an energetically preferred low-index plane, and therefore the reorganized surface of the substrate after annealing presents atomically flat terraces, which are exactly aligned with the $(11\bar{2}0)$ plane, separated by steps. This situation is illustrated in Figure A.2.

The misorientation of the physical surface relative to the crystallographic planes is the miscut magnitude. The orientation of the miscut is the angle between the projection of the surface normal on the $(11\bar{2}0)$ plane and the [0001] direction (c-axis). These two angles, together with the annealing temperature and time will determine the morphology of the Al_2O_3 surface.

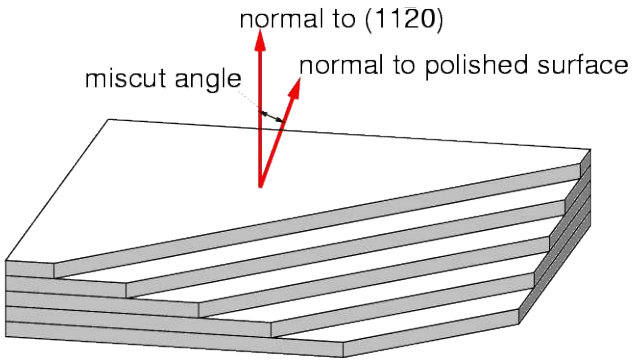

Figure A.2: Schematic illustration of the misorientation between the physical surface of the substrate and the normal to the (11$\bar{2}$0) plane.

In Figure A.3 AFM images of four sapphire substrates (labeled I to IV) with different morphologies are shown. The substrates have different miscut and have been treated with different annealing processes, all these parameters are listed in Table A.1. We can see that very different surfaces are obtained. In substrate (I), the step edges are not very well defined due to the relatively short time and low temperature (see Table A.1) of the annealing process. In substrate (II) the fact that the orientation of the miscut is nearly perpendicular to the c-axis is reflected in the parallel step edges obtained, also the high magnitude of the miscut increases the density of step edges. In the opposite case (III), due the low magnitude of the miscut, very broad terraces are obtained. Finally, in substrate (IV) the step edges are not completely parallel due to the orientation of the miscut.

	Miscut		Annealing treatment	
Al_2O_3	magnitude	orientation	Temperature	Duration
(I)	0.63°	40°	1300°C	20 hours
(II)	1.80°	87°	1500°C	48 hours
(III)	0.15°	27°	1500°C	30 hours
(IV)	0.26°	49°	1400°C	15 hours

Table A.1: Miscut magnitude and orientation (relative to the $c-axis$) and temperature and duration of the annealing process of the Al_2O_3 substrates shown in Figure A.3.

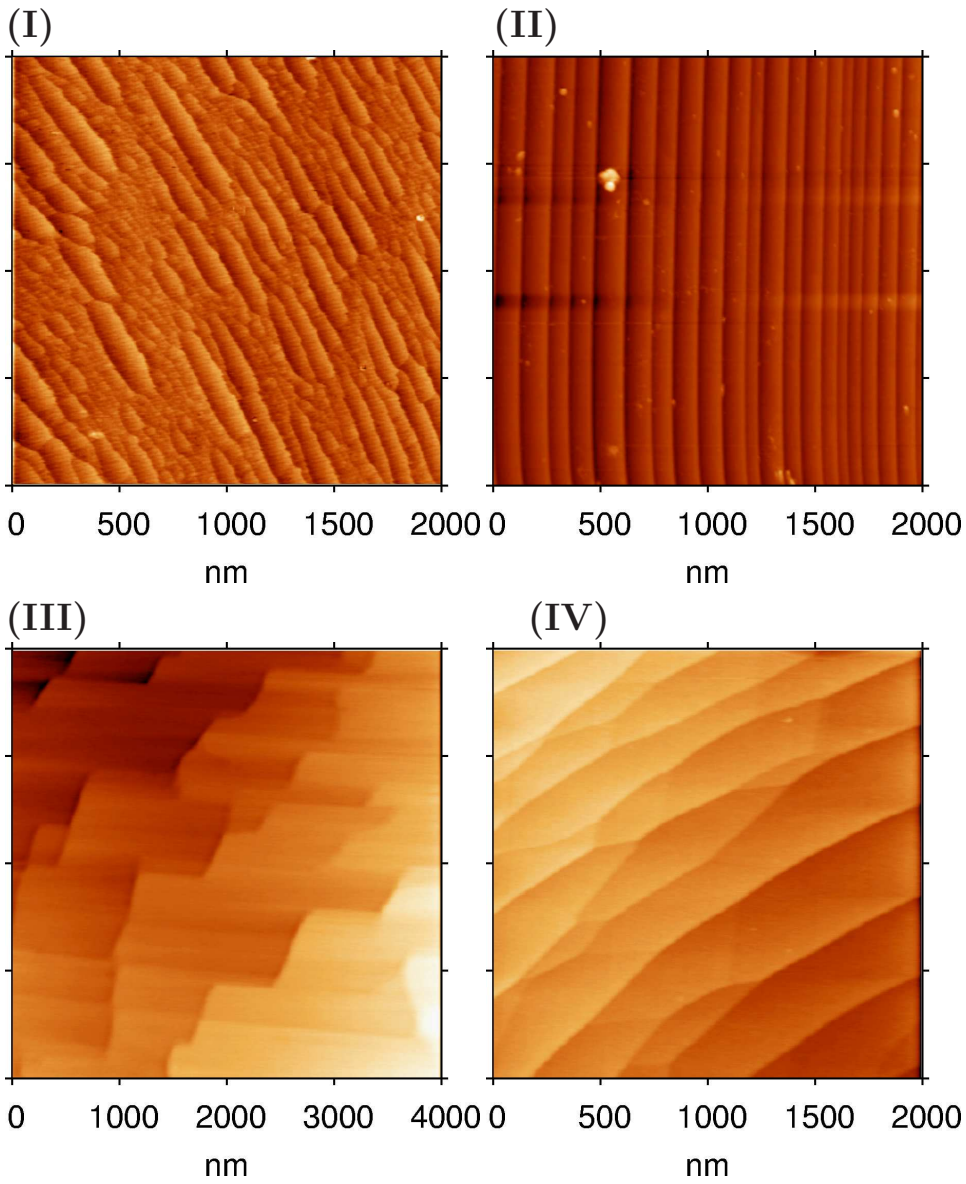

Figure A.3: Morphology of four sapphire substrates with different miscuts and annealed at different conditions. The miscut parameters and annealing conditions are listed in Table A.1

L

Appendix B

Unit cell determination of F_{16}CuPc by powder diffraction

The crystal structure of F_{16}CuPc does not appear in the literature. However, the crystalline structure of several phthalocyanines derivatives have been reported. Robertson [46] determined monoclinic structures with the space group $P2_1/a$ for the metal-free, nickel-, copper- and platinum derivatives, with two molecules per unit cell in all cases. The results on the metal-free compound were confirmed recently by Matsumoto [57] and the more accurate data collection allowed to determine that the molecule is distorted in the crystal, leading to a molecular symmetry of C_i as opposed to D_{2h}. The results for H_2Pc and CuPc are summarized in Table B.1.

	H_2Pc [46]	H_2 Pc [57]	β-CuPc [46]	β-CuPc [58]	F_{16}CuPc [62]
M	514.55	514.55	575.67	575.67	863.9
Space group	$P2_1/a$	$P2_1/a$	$P2_1/a$	$P2_1/a$	$P2_1/a$
a (Å)	19.85	19.870	19.6	19.407	20.018
b (Å)	4.72	4.731	4.79	4.79	5.106
c (Å)	14.8	14.813	14.6	14.628	15.326
β	122.25°	121.98°	120.60°	120.56°	111.83°
U (Å^3)	1173	1181	1180	1166	1454
Z	2	2	2	2	2

Table B.1: Cell parameters reported for metal-free and copper-phthalocyanine by Robertson [46], Brown [58], and Matsumoto [57]. Last column shows the unit cell parameters of the compound F_{16}CuPc determined.

We have determined the unit cell parameters of bulk F_{16}CuPc from powder diffraction measurements. F_{16}CuPc powder was purified twice by gradient sublimation and introduced in a Knudsen cell in the UHV system. The material was outgassed at sublimation temperature ($> 500°$C) and after this procedure it was formed by small and elongated crystallites, which where used to acquire powder spectra. The powder diagram was taken in a powder x-ray diffractometer using Cu-Kα_1 radiation (1.5405 Å). The spectrum recorded is shown in Figure B.1. The intensity is normalized to the maximum peak intensity, corresponding to the first peak found (at 2θ=2.63°). Table B.1 shows a list with the most prominent lines that could be found in the diagram (46 lines) together with their relative intensities. Due to the elongated shape of the crystallites which form the powder, a preferred orientation is expected in the powder sample. The line intensities recorded will reflect this preferred orientation, and therefore they do not correspond to an ideal powder pattern. However, the peak positions can be used for pattern indexing.

The 20 most prominent lines from the spectrum were taken as input for the automatic indexing using the program DICVOL91 [137]. The boundary conditions of the program (minimum and maximum values of the unit cell parameters) were chosen in accordance to the structures reported for other phthalocyanines derivatives (as those listed in Table B.1) and were as follows

$$\begin{aligned} a_{max} &= 30 \text{ Å} \\ b_{max} &= 6 \text{ Å} \\ c_{max} &= 18 \text{ Å} \\ \beta_{min} &= 90° \\ \beta_{max} &= 130° \\ U_{min} &= 800 \text{ Å}^3 \\ U_{max} &= 2500 \text{ Å}^3 \end{aligned}$$

this is justified due to the similarity between the powder pattern of the compound under study with those reported for H_2Pc and CuPc. From the automatic indexation, two possible solutions, with monoclinic symmetry were obtained. However, those do not include information on the space group. The structures of H_2Pc and of CuPc shown in table Table B.1 have all the space group $P2_1/a$. The Friedel's law for P2 establish that:

$$|F_{hkl}| = |F_{\bar{h}k\bar{l}}| = |F_{\bar{h}\,\bar{k}l}| = |F_{h\bar{k}l}| \tag{B.1}$$

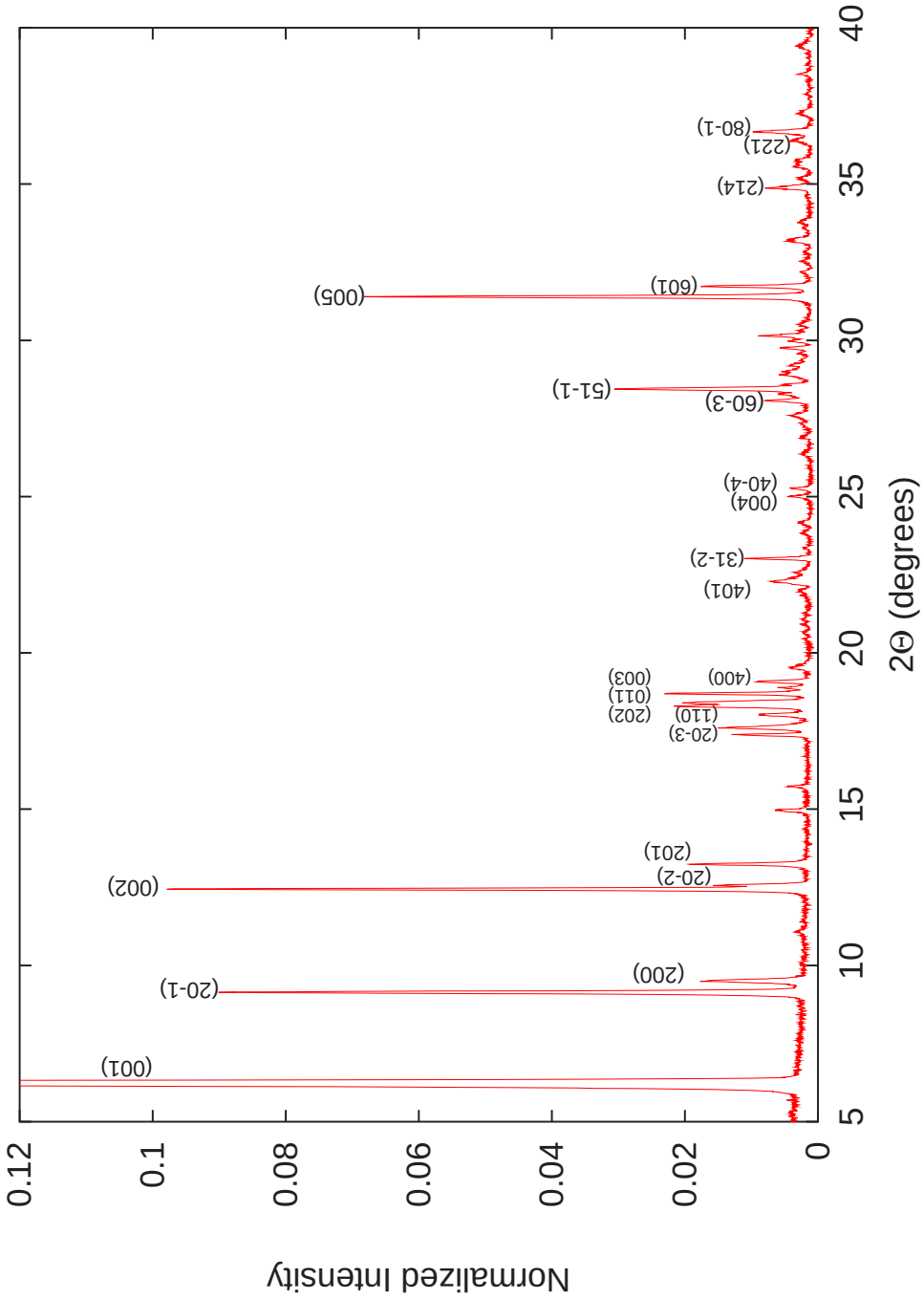

Figure B.1: Powder diffraction pattern of F_{16}CuPc using Cu-Kα1 radiation. The most prominent lines are indexed according to the parameters listed in Table B.1

and for $P2_1/a$, there are systematic absences for:

$$\begin{array}{rcl} (0k0) \text{ for } k & = & \text{odd} \\ (h0l) \text{ for } h & = & \text{odd} \end{array} \tag{B.2}$$

$P2_1/a$ (or $P2_1/c$) is the only space group of the monoclinic structures that can be uniquely determined from the symmetry diffraction pattern and from the systematic absences. This is in agreement with one of the solutions obtained, the parameters of which are listed in the last column of Table B.1.

The indexation of the 26 remaining lines of the pattern is in very good agreement with the predicted reflections of this solution. In Table B.2 the Miller indexes of the 46 reflections are listed, with the experimental spacings (or diffraction angles) and their corresponding calculated value. The maximum deviation of the calculated spacings is 0.05 Å, while the mean deviation is only 0.007 Å. Thus, a very good agreement is found.

H	K	L	2θ-obs	2θ-calc	$\Delta 2\theta$	d-obs	d-calc	Δd	Norm. Int.
0	0	1	6.230	6.207	0.023	14.1746	14.2276	0.05303	1.000
2	0	-1	9.186	9.224	-0.0385	9.6194	9.5797	0.03969	0.090
2	0	0	9.511	9.511	-0.0002	9.2911	9.2912	0.00017	0.018
0	0	2	12.448	12.433	0.015	7.1046	7.1134	0.00881	0.099
2	0	-2	12.579	12.536	0.0428	7.0310	7.0552	0.02418	0.016
2	0	1	13.171	13.166	0.005	6.7162	6.7190	0.00280	0.019
2	0	-3	17.580	17.537	0.043	5.0405	5.0529	0.01246	0.015
1	1	0	18.036	17.998	0.0381	4.9140	4.9245	0.01051	0.009
2	0	2	18.310	18.295	0.0151	4.8411	4.8452	0.00415	0.022
0	1	1	18.427	18.443	-0.0157	4.8106	4.8067	0.00387	0.020
0	0	3	18.704	18.695	0.0089	4.7400	4.7425	0.00242	0.023
4	0	0	19.088	19.088	0.0003	4.6454	4.6457	0.00025	0.009
1	1	1	19.535	19.633	-0.0985	4.5403	4.5179	0.02238	0.004
4	0	1	22.289	22.210	0.0794	3.9850	3.9992	0.01422	0.007
3	1	0	22.581	22.546	0.0354	3.9341	3.9404	0.00625	0.003
3	1	-2	23.025	23.051	-0.0257	3.8593	3.8552	0.00409	0.011
2	0	-4	23.354	23.196	0.1575	3.8058	3.8314	0.02563	0.002
0	0	4	25.010	25.015	-0.0053	3.5574	3.5568	0.00060	0.004

(continued)

H	K	L	2θ-obs	2θ-calc	Δ2θ	d-obs	d-calc	Δd	Norm. Int.
4	0	-4	25.268	25.226	0.0422	3.5216	3.5275	0.00593	0.004
4	1	-3	27.604	27.524	0.08	3.2286	3.2380	0.00933	0.004
6	0	-3	28.073	27.917	0.1563	3.1757	3.1933	0.01755	0.007
5	1	-1	28.451	28.427	0.0241	3.1344	3.1371	0.00272	0.031
2	1	3	29.754	29.777	-0.0228	3.0000	2.9979	0.00213	0.005
4	0	-5	30.151	30.091	0.0598	2.9615	2.9673	0.00586	0.009
0	0	5	31.407	31.412	-0.0054	2.8459	2.8455	0.00037	0.068
6	0	1	31.743	31.745	-0.0022	2.8165	2.8164	0.00008	0.018
6	1	-3	33.203	33.057	0.1459	2.6959	2.7076	0.01167	0.004
6	1	0	33.787	33.820	-0.0333	2.6506	2.6482	0.00243	0.003
2	1	4	34.887	34.890	-0.0035	2.5695	2.5694	0.00015	0.007
6	1	-4	35.202	35.203	-0.0006	2.5472	2.5473	0.00006	0.003
4	0	-6	35.558	35.502	0.0564	2.5225	2.5265	0.00398	0.003
6	0	2	35.661	35.631	0.0296	2.5155	2.5176	0.00212	0.003
5	1	2	35.770	35.732	0.0378	2.5081	2.5108	0.00266	0.003
6	1	1	36.408	36.399	0.0088	2.4656	2.4663	0.00067	0.004
8	0	-1	36.677	36.782	-0.105	2.4481	2.4415	0.00665	0.010
0	2	2	37.278	37.387	-0.1088	2.4100	2.4033	0.00667	0.003
3	2	-2	38.525	38.403	0.1219	2.3348	2.3420	0.00722	0.003
8	1	-4	41.602	41.616	-0.0143	2.1690	2.1684	0.00063	0.004
5	2	-3	43.159	43.163	-0.0039	2.0943	2.0942	0.00010	0.040
3	1	5	43.326	43.370	-0.0444	2.0866	2.0846	0.00195	0.002
6	1	3	44.117	44.115	0.0023	2.0510	2.0511	0.00018	0.005
4	2	2	44.510	44.531	-0.0209	2.0338	2.0329	0.00083	0.005
8	0	2	45.331	45.315	0.0161	1.9988	1.9996	0.00075	0.005
2	1	6	46.411	46.398	0.0131	1.9548	1.9554	0.00060	0.012
10	1	-4	49.410	49.412	-0.0019	1.8429	1.8429	0.00001	0.009
8	2	-3	51.300	51.285	0.0147	1.7794	1.7799	0.00054	0.004

Table B.2: Reflections observed in the powder spectra with their corresponding Miller indexes according to the determined structre.

The dimensions of the determined unit cell would imply that it is formed by two molecules. The cell parameters found are similar to those reported for H_2Pc

and CuPc. An expansion of the lattice constants is found (Δa=0.8 Å, Δb=0.3 Å, Δc=0.7 Å, and $\Delta\beta$= -8.8° relative to the CuPc parameters) as could be expected from the fact that the H surrounding the molecule have been substituted by F (the characteristic bond length for C-H is 1.08 Å, while for C-F is 1.38 Å).

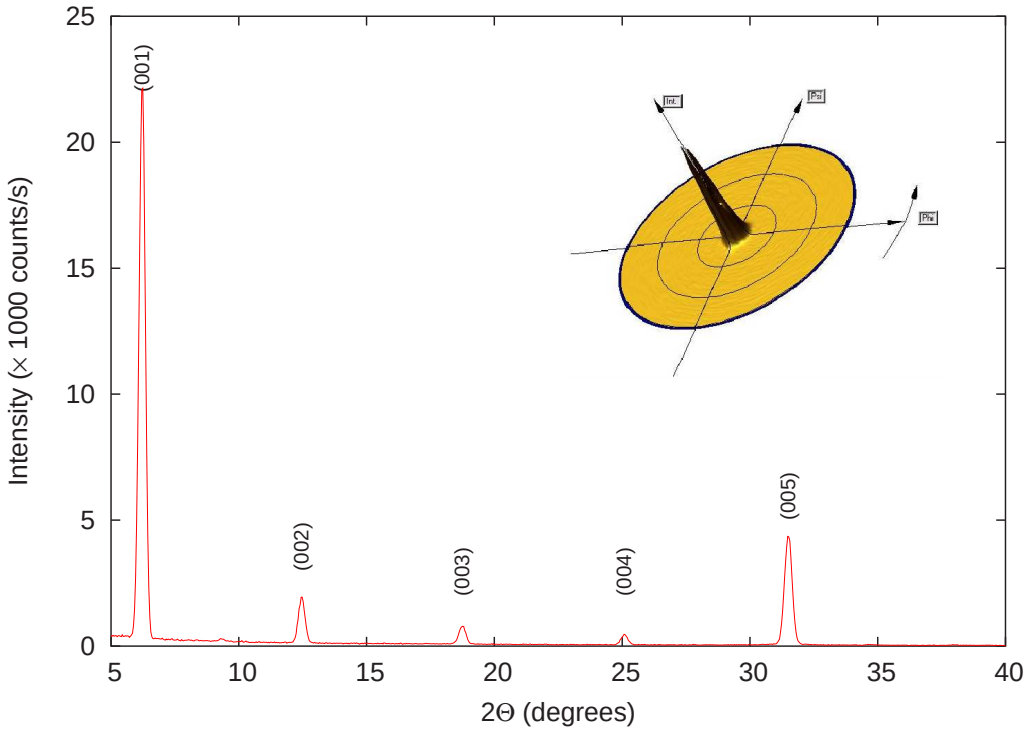

Figure B.2: $\theta/2\theta$ scan on the largest plane of the F_{16}CuPc crystals. Up to the 5th order of the (001) reflection are observed. The position and also the relative intensities match perfectly well with those found in the powder pattern (see Figure B.1). The inset shows the pole figure of the first order reflection, where $-90° \leq \psi \leq 90°$ (30° grid step) and $0° \leq \phi < 360°$.

Recently, single crystals of F_{16}CuPc became available.The small size of the crystals, with needle-like shape, makes difficult their study, and a full characterization with x-ray diffraction has not been possible yet. In a powder diffraction pattern the orientation of the reflections in the reciprocal space is lost due to the random orientation of the crystallites. This information, however, can be obtained from x-ray measurements on single crystals. The inter-planar distance of plane (hkl), d_{hkl}, and the angle between the planes $(h_1k_1l_1)$ and $(h_2k_2l_2)$, ρ, in monoclinic

systems can be written as

$$\begin{aligned} \frac{1}{d_{hkl}^2} &= \frac{1}{\sin^2\beta}\left(\frac{h^2}{a^2}+\frac{k^2\sin^2\beta}{b^2}+\frac{l^2}{c^2}-\frac{2hl\cos\beta}{ac}\right) \\ \cos\rho &= \frac{d_1 d_2}{\sin^2\beta}\left[\frac{h_1h_2}{a^2}+\frac{k_1k_2\sin^2\beta}{b^2}+\frac{l_1l_2}{c^2}+\frac{(l_1h_2+l_2h_1)\cos\beta}{ac}\right] \end{aligned} \tag{B.3}$$

these equations can be used to locate the desired reflections in the single crystals.

F_{16}CuPc single crystals were mounted on a Si(510) holder which do not contribute to scattering, and measured with a Cu-$K\alpha$ (1.5418 Å) four-circle diffractometer (Philips X'pert 45 kV/40 mA). The largest face of the needle-shaped crystals was parallel to the holder plane. A first $\theta/2\theta$ scan on this plane is shown in Figure B.2. Up to the 5th order reflection of the plane (001) are present. Thus the largest face of the single crystals corresponds to the (001) plane, as is found also for other phthalocyanines single crystals [46]. The relative intensities and the positions of those peaks are equivalent to the lines found in the powder spectrum. This orientations was used for alignment of the sample. In the inset of Figure B.2 the *pole figure* [1] of the (001) reflection is shown, it is centered in the diagram, as should be expected. Besides the (001) reflection and its higher orders, five other reflections have been located and the pole figures of each of them recorded. These are (201), (20$\overline{2}$), (202), (20$\overline{3}$), and (200). Their corresponding inter-planar distance and angles verify in all cases the structure determined from the powder data following Equations B.4.

[1] A pole figure represents the orientation distribution of a given Bragg reflection.

Appendix C

Angular dependence of Raman intensities

The angular dependence of Raman intensities for a monoclinic crystal with A_g and B_g symmetry, and for molecular modes with A_{1g}, B_{1g}, B_{2g}, and E_g are listed in Table C.1. $x'y'z'$ are the laboratory axes defined in Figure 5.14, with z' normal to the plane of the film and x' parallel to the polarization of the incoming laser light. P- and C-configurations are, respectively $\bar{z}'(x'x')z'$ and $\bar{z}'(x'y')z'$. Axes XYZ are the axes of the molecule (crystal) (see Chapter 5.4 and Figure 5.14) with Z along the C_4 (C_2) symmetry axis. Angles α and $\phi = \beta - \beta_0$ are, respectively, those between z' and Z and x' and X. We assume that X is contained in the plane of the film ($x'y'$).

(a) Monoclinic crystal

mode	$I(x'x')$	$I(x'y')$
A_g	$(A\cos^2\phi + B - D\sin 2\phi)^2$	$\left(\frac{A}{2}\sin 2\phi + D\cos 2\phi\right)^2$
B_g	$4E^2\sin^2\phi\sin^2\alpha$	$F^2\sin^2\alpha$

$A = a - B$

$B = b\cos^2\alpha + c\sin^2\alpha$

$D = d\cos\alpha$

$E = e\cos\phi - f\cos\alpha\sin\phi$

$F = e\cos 2\phi - f\cos\alpha\sin 2\phi$

(b) Molecular modes

mode	$I(x'x')$	$I(x'y')$
A_{1g}	$(A\cos^2 hi + B)^2$	$\frac{A^2}{4}\sin^2 2\phi$
B_{1g}	$(C\cos^2\phi - c_0\cos^2\alpha)^2$	$\frac{C^2}{4}\sin^2 2\phi$
B_{2g}	$d_0^2\cos^2\alpha\sin^2 2\phi$	$d_0^2\cos^2\alpha\cos^2 2\phi$
E_g	$4e_0^2\sin^2\alpha\sin^2\phi\,(\sin^2\alpha\cos^2\phi + \cos^2\alpha)$	$e_0^2\sin^2\alpha\,(\sin^2\alpha\cos^2 2\phi + \cos^2\alpha)$

$A = (a_0 - b_0)\sin^2\alpha$

$B = a_0\cos^2\alpha + b_0\sin^2\alpha$

$C = c_0\,(1 + \cos^2\alpha)$

Table C.1: Angular dependence of Raman intensities for the monoclinic crystal (a) and the molecular modes (b).

List of Figures

List of Tables

List of Symbols

M	molecular weight	11
U	unit cell volume	14
Z	molecules per unit cell	14
$a, b, c,$		
α, β, γ	unit cell parameters	14
$\mathrm{T_g}$	substrate temperature during growth	20
a	acommodation coefficient	23
F_i	molecular flux of the consituent i	23
s	sticking coefficient	23
s_{o-i}	organic on inorganic sticking coefficient	23
s_{o-o}	organic on organic sticking coefficient	23
T_e	temperature of the desorbed molecules	23
T_i	source temperature of the constituent i	23
N_{ad}	number of adsorbed molecules	23
N_{tot}	number of molecules arriving on the substrate surface	23
σ_{rms}	root mean square roughness	28
n	refractive index	37
$\delta,\ \beta$	dispersive and dissipative parts of the refractive index	37
ρ_e	electron density of the medium	37
μ	lineal absorption coefficient of the medium	37
λ	wavelenght of the radiation	37
r_e	classical radius of the electron	37
c	speed of light	37
$\alpha_i, \alpha_t, \alpha_f$	incident, refracted, and diffracted angles of the x-ray beam	37
α_c	x-ray critical angle of the material	37
$\vec{q}$	momentum transfer of the scattering process	38
$\vec{k}_i,\ \vec{k}_f$	wave vectors of the incident and diffracted wave	38

$r,\ t$	Fresnel coefficients	38
D_j	average thickness of a layer	39
X_j	ratio between the reflected and transmitted wave-amplitudes	39
E_t	transmitted x-ray wave	40
Λ	penetration depth of the evanescent x-ray wave	40
φ	angle of incidence in an ellipsometer	42
$\chi_i,\ \chi_r$	incident and reflected polarization states	42
$\Psi,\ \Delta$	ellipsometric angles	42
ρ	complex reflectance ratio	43
$E_p,\ E_s$	parallel and perpendicular components of the electric field	44
$E_i,\ E_r$	incident and reflected Jones vectors	44
$\vec{E}^i,\ \vec{E}^r$	incident and reflected Jones matrix	44
$R_{pp}, R_{ss},$ R_{ps}, R_{sp}	reflection matric components	44
I, I_0	Intensity and average intensity measured at the detector	44
α, β	first order Fourier coefficients of the signal at the detector	44
ω	angular frequency of the rotating element of an ellipsometer	44
A	analyzer angle of an ellipsometer	45
$\vec{E}$	applied electric field	45
$\vec{D}$	induced electric displacement	45
ε	dielectric tensor	45
$\varepsilon_1, \varepsilon_2$	real and imaginary parts of the dielectric tensor	45
$<\rho>$	pseudoreflectance ratio	47
β	azimuthal orientation of the sample	47
ω, ω'	incident and scattered frequency of the light in a Raman process	48
Ω	frequency shift in a Raman process	48
$\vec{k}, \vec{k}'$	wavevector of the incident and scattered light in a Raman process	48
$\vec{Q}$	momentum tranfer in a Raman process	48
2θ	x-ray scattering angle	54
$a_\perp$	lattice spacing of the organic layer in the normal to the surface	54
n_c	number of repetitions of the lattice constant in the layer	54
$\widehat{\rho}_e$	average electron density of the organic layer	56
A	amplitude of the oscillations of the electron density	56
ϕ	phase of the sinusoidal wave that describes the electron density	56
$\alpha_\circ$	angle between the molecular plane and the substrate surface	57

$n,\ k$	real and imaginary parts of the complex refractive index	59
X, Y, Z	principal axes of the dielectric tensor of the organic layer	68
x, y, z	laboratory axis in ellipsometric measurements	68
$\beta_\circ$	angle between the c-axis of the substrate and the Y axis	68
x', y', z'	laboratory axis in Raman measurements	73
X, Y, Z	symmetry axis of the molecule/crystal in Raman measurements	73
X', Y', Z'	coordinate system relative to the substrate in Raman measurements	74
$I(x', x')$	intensity of a Raman peak in parallel configuration	74
$I(x', y')$	intensity of a Raman peak in crossed configuration	74
b_s	amplitude parameter of the intensity of Raman lines	74
$\delta_\circ$	angle between the $F_{16}CuPc$ planes in the monoclinic unit cell	74
Γ	vibrational modes of the $F_{16}CuPc$ molecule/crystal.	76
A, A'	amplitude parameters of Raman lines in P and C polarizations	84
C, C'	constant background of Raman lines in P and C polarizations	84
s_e	normalized effective sticking coefficient	92
D_{ev}	expected thickness from the amount of evaporated material	92
$\Delta\beta_\circ$	azimuthal distribution of the in-plane Bragg reflection at $q_{\|\|} = 1.982$ Å^{-1} in $F_{16}CuPc$ layers	97
$\mathcal{R}$	dichroic ratio	97
ν	Raman order parameter	97
ϕ	azimuthal orientation of the sample in the x-ray diffractometer	115
$\Delta\omega$	shift from the centered position of a rocking curve	117
d_1, d_2, δ	in-plane periodicites and angle between them in DIP thin films	121

List of Acronyms

AFM atomic force microscopy
AM amplitude modulation (non-contact AFM)
BSM $\beta-$scan method
CCD charge-coupled device
DIP diindenoperylene
F_{16}CuPc Copper hexadecafluorophthalocyanine, ($C_{32}N_8CuF_{16}$)
FM frequency modulation (non-contact AFM)
FWHM full-width at half maximum
GE generalized ellipsometry
GIXD grazing incidence x-ray diffraction
HOMO highest ocuppied molecular orbital
HOPG highly-oriented pyrolitic graphite
KKR Kramers-Kronig relations
LEED low-energy electron diffraction
LUMO lowest unocuppied molecular orbital
MBE molecular beam epitaxy
MFM magnetic force microscope
ML monolayer
OFET organic field-effect transistor
OLED organic light-emitting device
OMBD organic molecular beam deposition
OMBE organic molecular beam epitaxy
POI plane of incidence
PSPD position sensitive photodetector
QCM quartz crystal monitor
QMS quadrupole mass spectrometer
RAE rotating analyzer ellipsometer

RGA residual gas analyzer
RHEED reflection high-energy electron diffraction
RPE rotating polarizer ellipsometer
SE spectroscopic ellipsometry
SNOM scanning near-field optical microscope
SPM scanning probe microscope
STM scanning tunneling microscope
TEM transmission electron microscopy
UHV ultra-high vacuum

Bibliography

[1] C. D. Dimitrakopoulos and P. R. L. Malenfant. Organic thin film transistors for large area electronics. *Adv. Mater.*, 14:99–117, 2002. http://www3.interscience.wiley.com/cgi-bin/abstract/89015263/.

[2] H. Y. Choi, S. H. Kim, and J. Jang. Self-organized organic thin-film transistors on plastic. *Adv. Mater.*, 16:732–736, 2004. http://www3.interscience.wiley.com/cgi-bin/abstract/108561169/.

[3] T. Tsutsui and K. Fujita. The shift from "hard" to "soft" electronics. *Adv. Mater.*, 14:949–952, 2002. http://www3.interscience.wiley.com/cgi-bin/abstract/95515409/.

[4] R. Farchioni and G. Grosso, editors. *Organic Electronic Materials*. Springer-Verlag, Berlin, 2001.

[5] W. E. Howard and O. F. Prache. Microdisplays based upon organic light-emitting diodes. *IBM J. Res. & Dev.*, 45(1):115–127, 2001. http://www.research.ibm.com/journal/rd/451/howaraut.html.

[6] H. E. A. Huitema, G. H. Gelinck, J. B. P. H. van der Putten, K. E. kuijk, C. M. Hart, E. Cantatore, P. T. Herwig, A. J. J. M. van Breemen, and D. M. de Leeuw. Plastic transistors in active-matrix display. *Nature*, 414: 599, 2001. http://dx.doi.org/10.1038/414599a.

[7] D. Wöhrle and D. Meissner. Organic solar cells. *Adv. Mater.*, 3(1):129–138, 1991.

[8] C. J. Brabec, A. Cravino, D. Meissner, N. S. Sariciftci, T. Fromherz, M. T. Rispens, L. Sanchez, and J. C. Hummelen. Origin of the open circuit voltage

of plastic solar cells. *Adv. Funct. Mat.*, 11(5):374–380, 2001. http://www3.interscience.wiley.com/cgi-bin/abstract/85514175/.

[9] Martin Pope and Charles E. Swenberg. *Electronic Processes in Organic Crystals*. Oxford University Press, 1982.

[10] Jean-Pierre Farges. *Organic Conductors: Fundamentals and Applications*. Applied Physics. Marcel Dekker, 1994.

[11] F. Schreiber. Organic molecular beam deposition: Growth studies beyond the first monolayer. *Phys. Stat. Sol. (a)*, 201:1037–1054, 2004. http://www3.interscience.wiley.com/cgi-bin/abstract/108562902/.

[12] J. Fraxedas. Perspectives on thin molecular organic films. *Adv. Mater.*, 14: 1603–1614, 2002. http://www3.interscience.wiley.com/cgi-bin/abstract/101020011/.

[13] S. R. Forrest. Ultrathin organic films grown by organic molecular beam deposition and related techniques. *Chem. Rev.*, 97:1793–1896, 1997. http://dx.doi.org/10.1021/cr941014o.

[14] W. Kowalsky, T. Benstem, A. Böhler, S. Dirr, H.-H. Johannes, D. Metzdorf, H. Neuner, J. Schöbel, and P. Urbach. Organic molecular beam deposition: technology and applications in electronics and photonics. *Phys. Chem. Chem. Phys.*, 1:1719–1725, 1999. hppt://dx.doi.org/10.1039/a809431d.

[15] E. Umbach, M. Sokolowski, and R. Fink. Substrate-interaction, long-range order, and epitaxy of large organic adsorbates. *Appl. Phys.*, A63:565–576, 1996.

[16] D. E. Hooks, T. Fritz, and M. D. Ward. Epitaxy and molecular organization on solid substrates. *Adv. Mater.*, 13:227–241, 2001. http://www3.interscience.wiley.com/cgi-bin/abstract/77004430/.

[17] B. Krause, A. C. Dürr, K. Ritley, F. Schreiber, H. Dosch, and D. Smilgies. Structure and growth morphology of an archetypal system for organic epitaxy: PTCDA on Ag(111). *Phys. Rev. B*, 66:235404, 2002. http://link.aps.org/abstract/PRB/v66/e235404.

[18] Bärbel Krause. *Growth and Structure of the Organic Molecule PTCDA on Ag(111)*. PhD thesis, Max-Planck-Institut für Metallforschung - Institut für Theoretische und Angewandte Physik der Universität Stuttgart, Stuttgart, May 2002.
http://elib.uni-stuttgart.de/opus/volltexte/2003/1280/.

[19] N. Karl and J. Marktanner. Structural order and photoelectric properties of organic thin films. *Mol. Cryst. Liq. Cryst.*, 315:163–168, 1998.

[20] Zhenan Bao. Materials and fabrication needs for low-cost organic transistor circuits. *Adv. Mater.*, 12:227–230, 2000.
http://www3.interscience.wiley.com/cgi-bin/abstract/69501069/.

[21] D.M. de Leeuw, M. M. J. Simenon, A. R. Brown, and R. E. F. Einerhand. Stability of n-type doped conducting polymers and consequences for polymeric microelectronic devices. *Synth. Met.*, 87:53–59, 1997.
http://dx.doi.org/10.1016/S0379-6779(97)80097-5.

[22] A. Dodabalapur, J. Laquindanum, H. E. Katz, and Z. Bao. Complementary circuits with organic transistors. *Appl. Phys. Lett.*, 69(27):4227–4229, 1996.
http://dx.doi.org/10.1063/1.116953.

[23] A. Dodabalapur, J. Baumbach, K. Baldwin, and H. E. Katz. Hybrid organic/inorganic complementary circuits. *Appl. Phys. Lett.*, 68(16):2246–2248, 1996.
http://dx.doi.org/10.1063/1.115873.

[24] L. Torsi, A. Dodabalapur, L. J. Rothberg, A. W. P. Fung, and H. E. Katz. Intrinsic transport properties and performance limits of organic field-effect transistors. *Science*, 272:1462–1464, 1996.
http://www.sciencemag.org/cgi/content/abstract/272/5267/1462.

[25] I. D. W. Samuel and A. Beeby. Sidestepping the selection rules. *Nature*, 403:710–711, 2000.
http://dx.doi.org/10.1038/35001688.

[26] M. A. Baldo, M. E. Thompson, and S. R. Forrest. High-efficiency fluorescent organic light-emitting devices using a phosphorescent sensitizer. *Nature*, 403: 750–753, 2000.
http://dx.doi.org/10.1038/35001541.

[27] Ching W. Tang and N. Y. Rochester. Multilayer organic phthovoltaic elements. United States Patent 4,281,053, 1981.

[28] A. Pochettino. *Atti Acad. Lincei Rend.*, page (1) 355; (2) 171, 1906.

[29] A. Szent-Györgi. *Science*, 93:609, 1941.

[30] D. D. Eley. *Nature*, 162:819, 1948.

[31] H. Akamatu, H. Inokutchi, and Y. Matsunaga. *Nature*, 173:168, 1954.

[32] Y. Okamoto and W. Brenner. *Organic Semiconductors*. Reinhold, New York, 1964.

[33] Felix Gutmann and Lawrence E. Lyons. *Organic Semiconductors*. John Wiley & Sons, New York, 1967.

[34] A. Rembaum and R. F. Landel. Electrical properties of polymers. *J. Polym. Sci. C*, 17, 1967.

[35] J. A. Rogers, Z. Bao, A. Dodabalapur, and A. Makhija. Organic smart pixels and complementary inverter circuits formed on plastic substrates by casting and rubber stamping. *IEEE Electron. Dev. Lett.*, 21(3):100–103, 2000. http://ieeexplore.ieee.org/xpl/abs_free.jsp?arNumber=823569.

[36] J. A. Rogers, Z. Bao, K. Baldwin, A. Dodabalapur, B. Crone, V. R. Raju, V. Kuck, H. Katz, K. Amundson, J. Ewing, and P. Drzaic. Paper-like electronic displays: large-area rubber-stamped plastic sheets of electronics and microencapsulated electrophoretic inks. *Proc. Natl. Acad. Sci.*, 98(9):4835–4840, 2001. http://dx.doi.org/10.1073/pnas.091588098.

[37] N. Karl. *Charge-Carrier Mobility in Organic Crystals*, chapter 8, pages 283–326. Springer, 2001.

[38] Claus Hamann. *Organische Festkörper und Organische Dünne Schichten*. Akademische Verlagsgesellschaft Geest & Portig K.-G., Leipzig, 1978.

[39] G. Gu, G. Parthasarathy, P. E. Burrows, P. Tian, I. G. Hill, A. Kahn, and S. R. Forrest. Transparent stacked organic light emitting devices. I. Design

principles and transparent compound electrodes. *J. Appl. Phys.*, 86(8):4067–4075, 1999.
http://dx.doi.org/10.1063/1.371331.

[40] G. Gu, G. Parthasarathy, P. Tian, P. E. Burrows, and S. R. Forrest. Transparent stacked organic light emitting devices. II. Device performance and applications to displays. *J. Appl. Phys.*, 86(8):4076–4084, 1999.
http://dx.doi.org/10.1063/1.371428.

[41] Gilles Horowitz. Organic field-effect transistors. *Adv. Mater.*, 10(5):365–377, 1998.
http://www3.interscience.wiley.com/cgi-bin/abstract/30001455/.

[42] J. Simon and J.-J. André. *Molecular Semiconductors: Photoelectrical Properties and Solar Cells*. Springer-Verlag, Berlin Heidelberg, 1985.

[43] N. Karl and Ch. Günther. Structure and ordering principles of ultrathin organic molecular films on surfaces of layered semiconductors organic-on-inorganic MBE. *Cryst. Res. Technol.*, 34:243–254, 1999.

[44] A. Braun and J. Tcherniac. *Ber. Deutsch. Chem. Ges.*, 40:2709, 1907.

[45] R. P. Linstead and A. R. Lowe. *J. Chem. Soc.*, page 1022, 1934.

[46] J. M. Robertson. An x-ray study of the structure of the phthalocyanines. part I. the metal free, nickel, copper, and platinum compounds. *J. Chem. Soc.*, pages 615–621, 1935.

[47] J. M. Robertson. *J. Chem. Soc.*, page 1195, 1936.

[48] J. M. Robertson and I. Woodward. *J. Chem. Soc.*, page 219, 1937.

[49] Frank H. Moser and Arthur L. Thomas. *The Phthalocyanines*, volume 1 and 2. CRC Press, 1983.

[50] C. C. Leznoff and A. B. P. Lever. *Phthalocyanines: Properties and Applications*. VCH Publishers Inc., New York, 1989.

[51] D. Gu, Q. Chen, X. Tang, F. Gan, S. Shen, K. Liu, and H. Xu. Application of phthalocyanine thin films in optical recording. *Optics Communication*, 121:125–129, 1995.

[52] A. W. Snow and W. R. Barger. *Phthalocyanine Films in Chemical Sensors*, volume 1, chapter 5, pages 341–391. VCH, New York, 1996.

[53] Meng-Sheng Liao and Steve Scheiner. Electronic structure and bonding in metal phthalocyanines, Metal = Fe, Co, Ni, Cu, Zn, Mg. *J. Chem Phys.*, 114(22):9780–9791, 2001.
http://dx.doi.org/10.1063/1.1367374.

[54] Z. Bao, A. J. Lovinger, and J. Brown. New air-stable n-channel organic thin film transistors. *J. Am. Chem. Soc.*, 120:207–208, 1998.

[55] Y.-Y. Lin, A. Dodabalapur, R. Sarpeshkar, Z. Bao, W. Li, K. Baldwin, V. R. Raju, and H. E. Katz. Organic complementary ring oscillators. *Appl. Phys. Lett.*, 74:2714–2716, 1999.
http://dx.doi.org/10.1063/1.123946.

[56] B. Crone, A. Dodabalapur, Y.-Y. Lin, R. W. Filas, Z. Bao, A. LaDuca, R. Sarpeshkar, H. E. Katz, and W. Li. Large-scale complementary integrated circuits based on organic transistors. *Nature*, 403:521–523, 2000.
http://dx.doi.org/10.1038/35000530.

[57] S. Matsumoto, K. Matsuhama, and J. Mizuguchi. β metal-free phthalocyanine. *Acta Cryst.*, C55:131–133, 1999.
http://dx.doi.org/10.1107/S0108270198011020.

[58] C. J. Brown. Crystal structure of β-copper phthalocyanine. *J. Chem. Soc. A*, pages 2488–2493, 1968.

[59] R. D. Gould. Structure and electrical conduction properties of phthalocyanine thin films. *Coord. Chem. Rev.*, 156:237–274, 1996.
http://dx.doi.org/10.1016/S0010-8545(96)01238-6.

[60] S. M. Bayliss, S. Heutz, G. Rumbles, and T. S. Jones. Thin film properties and surface morphology of metal free phthalocyanine films grown by organic molecular beam deposition. *Phys. Chem. Chem. Phys.*, 1:3673–3676, 1999.
hppt://dx.doi.org/10.1039/a904089g.

[61] O. Berger, W.-J. Fischer, B. Adolphi, S. Tierbach, V. Melev, and J. Schreiber. Studies on phase transformations of Cu-phthalocyanine thin films. *J. Mat. Sci.: Mat. Electr.*, 11:331–346, 2000.

[62] J. O. Ossó *et al.* Space group and unit cell parameters of F_{16}CuPc determined from powder diffraction data. 2004. in preparation.

[63] M. Münch. *Strukturelle Beeinflussung der Elektrischen Transporteigenschaften dünner organische Schichten.* PhD thesis, Universität Stuttgart, 2001.
http://elib.uni-stuttgart.de/opus/volltexte/2001/959/.

[64] J. von Braun and G. Manz. *Patent Num. 595 024: Verfahren Zur Herstellung Von Kondensationsprodukten Des Fluoranthens.* Deutsches Reichspatentamt, Berlin, 1934.

[65] E. Clar. *Aromatische Kohlenwasserstoffe - Polycyclische Systeme.* Springer-Verlag, Berlin, 1952.

[66] L. J. E. Hofer and W. C: Peebles. X-ray diffraction patterns of solid aromatic hydrocarbons. *Anal. Chem.*, 23:690, 1951.

[67] L. J. E. Hofer and W. C: Peebles. X-ray diffraction patterns of 2,4,7-trinitrofluorenone derivatives of aromatic hydrocarbons. *Anal. Chem.*, 24: 822, 1952.

[68] L. J. E. Hofer, W. C. Peebles, and E. H. Bean. X-ray powder diffraction patterns of solid hydrocarbons, derivatives of hydrocarbons, phenols, and organic bases. *Bureau of Mines Bulletin*, 613:1, 1963.

[69] J. Pflaum, W. Frey, and N. Karl. in preparation.

[70] A. Hoshino, S. Isoda, and T. Kobayashi. Epitaxial growth of organic crystals on organic substrates - polynuclear aromatic hydrocarbons. *J. Cryst. Growth*, 115:826–830, 1991.

[71] Arndt C. Dürr. *Growth and structure of DIP thin-films and Au-contacts on DIP thin-films.* PhD thesis, Max-Planck-Insitut für Metallforschung - Institut für Theoretische und Angewandte Physik der Universität Stuttgart, Stuttgart, July 2002.
http://elib.uni-stuttgart.de/opus/volltexte/2002/1215/.

[72] A. C. Dürr, F. Schreiber, M. Münch, N. Karl, B. Krause, V. Kruppa, and H. Dosch. High structural order in thin films of the organic semiconductor

diindenoperylene. *Appl. Phys. Lett.*, 81(12):2276–2278, 2002. http://dx.doi.org/10.1063/1.1508436.

[73] A. C. Dürr, F. Schreiber, K. A. Ritley, V. Kruppa, J. Krug, H. Dosch, and B. Struth. Rapid roughening in thin film growth of the organic semiconductor diindenoperylene (DIP). *Phys. Rev. Lett.*, 90:016104, 2003. http://dx.doi.org/10.1103/PhysRevLett.90.016104.

[74] A. C. Dürr, F. Schreiber, M. Kelsch, H. D. Carstanjen, and H. Dosch. Morphology and thermal stability of metal contacts on crystalline organic thin films. *Adv. Mater.*, 14:961–963, 2002. http://www3.interscience.wiley.com/cgi-bin/abstract/95515411/.

[75] A. C. Dürr, N. Koch, M. Kelsch, A. Rühm, J. Ghijsen, R. L. Johnson, J.-J. Pireaux, J. Schwartz, F. Schreiber, H. Dosch, and A. Kahn. Interplay between morphology, structure, and electronic properties at diindenoperylene-gold interfaces. *Phys. Rev. B*, 68:115428, 2003. http://dx.doi.org/10.1103/PhysRevB.68.115428.

[76] S. Sellner, A. Gerlach, F. Schreiber, M. Kelsch, N. Kasper, H. Dosch, S. Meyer, J. Pflaum, M. Fischer, and B. Gompf. Strongly enhanced thermal stability of crystalline organic thin films induced by aluminium oxide capping layers. *Adv. Mater.*, 2004.

[77] Marian A. Herman and Helmut Sitter. *Molecular beam epitaxy: fundamentals and current status*. Springer, Berlin, 1996.

[78] L.L. Chang and K. Ploog. *Molecular Beam Epitaxy and Heterostructures*. Martinus Nijhoff, 1985.

[79] M. Hara, H. Sasabe, A. Yamada, and A. F. Garito. Epitaxial growth of organic thin films by organic molecular beam epitaxy. *Jpn. J. Appl. Phys.*, 28:L306–L308, 1989.

[80] A. Koma. Molecular beam epitaxial growth of organic thin films. *Prog. Crystal Growth and Charact.*, 30:129–152, 1995. http://dx.doi.org/10.1016/0960-8974(95)00009-V.

[81] G. Witte and C. Wöll. Growth of aromatic molecules on solid substrates for applications in organic electronics. *J. Mat. Res.*, 19:1899–1916, 2004. http://dx.doi.org/10.1557/JMR.2004.0251.

[82] M. I. Alonso, M. Garriga, J. O. Ossó, F. Schreiber, E. Barrena, and H. Dosch. Strong optical anisotropies of F_{16}CuPc thin films studied by spectroscopic ellipsometry. *J. Chem. Phys.*, 119:6335–6340, 2003. http://dx.doi.org/10.1063/1.1602056.

[83] M. I. Alonso, M. Garriga, N. Karl, J. O. Ossó, and F. Schreiber. Anisotropic optical properties of single crystalline PTCDA studied by spectroscopic ellipsometry. *Organic Electronics*, 3:23–31, 2002. http://dx.doi.org/10.1016/S1566-1199(01)00027-1.

[84] J. O. Ossó, F. Schreiber, M. I. Alonso, M. Garriga, E. Barrena, and H. Dosch. Structure,morphology,and optical properties of thin films of F_{16}CuPc grown on silicondioxide. *Organic Electronics*, 2004. http://dx.doi.org/10.1016/j.orgel.2004.01.006.

[85] J. A. Venables, G. D. T. Spiller, and M. Hanbücken. Nucleation and growth of thin films. *Rep. Prog. Phys.*, 47:399–459, 1984. http://stacks.iop.org/rpp/47/399.

[86] W. E. Lee and K. P. D. Lagerlof. Structural and electron diffraction data for sapphire (α-Al_2O_3). *J. Electr. Micr. Tech.*, 2:247–258, 1985.

[87] Th. Becker, A. Birkner, G. Witte, and Ch. Wöll. Microstructure of the α-Al_2O_3 $(11\bar{2}0)$ surface. *Phys. Rev. B*, 65:115401, 2002. http://dx.doi.org/10.1103/PhysRevB.65.115401.

[88] F. C. Frank. On Miller-Bravais indices and four-dimensional vectors. *Acta Cryst.*, 18:862–867, 1965.

[89] G. Binnig and H. Rohrer. The scanning tunneling microscope. *Sci. Am.*, 253:40–46, 1985.

[90] G. Binnig, C. F. Quate, and Ch. Gerber. Atomic force microscope. *Phys. Rev. B*, 56:930–933, 1986.

[91] B. E. Warren. *X-Ray Diffraction.* Addison-Wesley, New York, 1990.

[92] H. Dosch. *Critical Phenomena at Surfaces and Interfaces, Springer Tracts in Modern Physics, vol.126.* Springer, Heidelberg, 1992.

[93] Jens Als-Nielsen and Des McMorrow. *Elements of Modern X-ray Physics*. John Wiley & Sons, Ltd, 2000.

[94] E. Hecht and A. Zajac. *Optics*. Addison-Wesley, Mass., 1974.

[95] R. M. A. Azzam and N. M. Bashara. *Ellipsometry and Polarized Light*. North-Holland, Amsterdam, 1977.

[96] L. G. Parrat. Surface studies of solids by total reflection of x-rays. *Phys. Rev.*, 95:359–369, 1954.
http://dx.doi.org/10.1103/PhysRev.95.359.

[97] ID10B Troïka II, multi-purpose, high-brilliance undulator beamline, ESRF, Grenoble, France.
http://www.esrf.fr/UsersAndScience/Experiments/SCMatter/ID10B/.

[98] European synchrotron radiation facility (ESRF), Grenoble, France.
http://www.esrf.fr.

[99] Hamburger Synchrotronstrahlungslabor (HASYLAB), Hamburg, Germany.
http://www-hasylab.desy.de/.

[100] Deutsches Elektronen-Synchrotron (DESY), Hamburg, Germany.
http://www.desy.de/html/home/index.html.

[101] Angströmquelle Karlsruhe GmbH (ANKA); Institute for Synchrotron Radiation, Karlsruhe, Germany.
http://hikwww1.fzk.de/anka/.

[102] Sergi Tortosa. *Caracterització òptica de materials mitjançant el·lipsometria generalitzada i models de medi efectiu*. PhD thesis, Universitat Autònoma de Barcelona, 1998.

[103] R.M.A. Azzam and N.M. Bashara. Simplified approach to propagation of polarized-light in anisotropic media - application to liquid-crystals. *J. Opt. Soc. Am.*, 62(11):1252–1257, 1972.

[104] M. I. Alonso and M. Garriga. Optical properties of anisotropic materials: an experimental approach. *Thin Solid Films*, 455–456:124–131, 2004.
http://dx.doi.org/10.1016/j.tsf.2003.12.061.

[105] Miquel Garriga. *Ellipsometrische Untersuchungen der optischen und elektronischen Eigenschaften van AlAs/GaAs-Übergittern und Hochtemperatur-Supraleitern.* PhD thesis, Universität Stuttgart, 1990.

[106] P. Yeh. Optics of anisotropic layered media: a new 4×4 matrix algebra. *Surf. Sci.*, 96:41, 1980.

[107] D. W. Berreman. Optics in stratified and anisotropic media: 4×4 matrix formulation. *J. Opt. Soc. Am.*, 62:502, 1972.

[108] D. Schlettwein, H. Graaf, J.-P. Meyer, T. Oekermann, and N. I. Jaeger. Molecular interactions in thin films of hexadecafluorophthalocyaninatozinc (F_{16}CuPc) as compared to islands of n,n'-dimethylperylene-3,4,9,10-biscarboximide (MePTCDI). *J. Phys. Chem. B*, 103:3078–3086, 1999. http://dx.doi.org/10.1021/jp983111h.

[109] R. Resel, M. Ottmar, M. Hanack, J. Keckes, and G. Leising. Preferred orientation of copper phthalocyanine thin films evaporated on amorphous substrates. *J. Mater. Res.*, 15:934–939, 2000. http://www.mrs.org/membership/preview/apr2000jmr/016.html.

[110] C. D. Dimitrakopoulos, A. R. Brown, and A. Pomp. Molecular beam deposited thin films of pentacene for organic field effect transistor applications. *J. Appl. Phys.*, 80:2501–2508, 1996. http://jap.aip.org/jap/top.jsp?vol=80&pg=2501&x=30&y=6.

[111] J. K. Gimzewski, E. Stoll, and R. R. Schlitter. Scanning tunneling microscopy of individual molecules of copper phthalocyanine adsorbed on polycrystalline silver surfaces. *Surf. Sci.*, 181:267–277, 1987.

[112] P. H. Lippel, R. J. Wilson, M. D. Miller, Ch. Wöll, and S. Chiang. High-resolution imaging of copper-phthalocyanine by scanning-tunneling microscopy. *Phys. Rev. Lett.*, 62:171–174, 1989. http://prola.aps.org/pdf/PRL/v62/i2/p171_1.

[113] H. Peisert, T. Schwieger, J. M. Auerhammer, M. Knupfer, M. S. Golden, J. Fink, P. R. Bressler, and M. Mast. Order on disorder: Copper phthalocyanine thin films on technical substrates. *J. Appl. Phys.*, 90(1):466–469, 2001. http://link.aip.org/link/?JAP/90/466/1.

[114] D. E. Aspnes. Approximate solution of ellipsometric equations for optically biaxial crystals. *J. Opt. Soc. Am.*, 70:1275–1277, 1980.

[115] T. Miyahara and M. Shimizu. Single crystal growth of organic semiconductors using melted anthracene as a solvent: N,N'-dimethylperylene-3,4:9,10-bis (dicarboximide) and phthalocyanines. *J. Cryst. Growth*, 226:130–137, 2001.
http://dx.doi.org/10.1016/S0022-0248(01)01275-1.

[116] J. O. Ossó, F. Schreiber, V. Kruppa, H. Dosch, M. Garriga, M. I. Alonso, and F. Cerdeira. Controlled molecular alignment of phthalocyanine thin films on stepped sapphire surfaces. *Adv. Funct. Mater.*, 12:455–460, 2002.
http://www3.interscience.wiley.com/cgi-bin/abstract/94518271/.

[117] E. Barrena, J. O. Ossó, F. Schreiber, H. Dosch, M. Garriga, and M. I. Alonso. Self-organization of phthalocyanines on Al_2O_3 $(11\bar{2}0)$ in aligned and ordered films. *J. Mat. Res.*, 19:2061–2067, 2004.
http;//dx.doi.org/10.1557/JMR.2004.0258.

[118] J. Martensson and H. Arwin. Optical characterization of thin films of some phthalocyanines by spectroscopic ellipsometry. *Thin Solid Films*, 188:181–192, 1990.
http://dx.doi.org/10.1016/0040-6090(90)90204-Q.

[119] M. J. Stillman and T. Nyokong. *Phthalocyanines: properties and applications*. VCH Publishers, 1989.

[120] Emmanuel A. Lucia and Frank D. Verderame. Spectra of polycrystalline phthalocyanines in the visible region. *J. Chem. Phys.*, 48:2674–2681, 1968.

[121] M. K. Debe and D. R. Field. Variable angle spectroscopic ellipsometry studies of oriented phthalocyanine films. *J. Vac. Sci. Technol. A*, 9(3):1265–1271, 1991.

[122] M. K. Debe. Variable angle spectroscopic ellipsometry studies of oriented phthalocyanine films. II. Copper phthalocyanine. *J. Vac. Sci. Technol. A*, 10(4):2816–2820, 1992.

[123] G. H. Watson, Jr. W. B. Daniels, and C. S. Wang. Measurements of raman intensities and pressure dependence of phonon frequencies in sapphire. *J.*

Appl. Phys., 52(2):956–958, 1981.
http://link.aip.org/link/?JAP/52/956/1.

[124] C. A. Melendres and V. A. Maroni. Raman spectra and normal coordinate analysis of the planar vibrations of iron phthalocyanine. *J. Raman Spectr.*, 15:319–326, 1984.

[125] T. V. Basova and B. A. Kolesov. Raman polarization studies of the orientation of molecular thin films. *Thin Solid Films*, 325:140–144, 1998.
http://dx.doi.org/10.1016/S0040-6090(98)00511-2.

[126] C. Jennings, R. Aroca, A.M. Hor, and R. O. Loutfy. Raman spectra of solid films (3–Mg, Cu, and Zn phthalocyanine complexes). *J. Raman Spectrosc.*, 15:34–37, 1984.

[127] B. A. Kolesov, T. V. Basova, and I. K. Igumenov. Determination of the orientation of CuPc film by raman spectroscopy. *Thin Solid Films*, 304: 166–169, 1997.
http://dx.doi.org/10.1016/S0040-6090(97)00174-0.

[128] A. J. Bovill, A. A. McConnell, J. A. Nimmo, and W. E. Smith. Resonance raman spectra of α-copper phthalocyanine. *J. Phys. Chem.*, 90:596–575, 1986.

[129] M. Kuwahara, G. Mizutani, K. Sakamoto, and S. Ushioda. Absolute raman scattering cross sections of surface adsorbed Cu-phthalocyanine molecules. *Surf. Sci.*, 242:544–548, 1991.

[130] T-H Huang, K. E. Rieckhoff, and E-M Voigt. Resonance raman in platinum phthalocyanine. *Can. J. Chem.*, 56:976–984, 1978.

[131] M. J. Frisch et al. *Gaussian 98, Revision A.7.* Gaussian, Inc., Pittsburgh, PA, 1998.

[132] C. J. Brown. Crystal structure of platinium phthalocyanine: A reinvestigation. *J. Chem. Soc. A*, pages 2494–2498, 1968.

[133] D. A. Tenne, S. Park, T. U. Kampen, A. Das, R. Scholz, and D. R. T. Zahn. Single crystals of the organic semiconductor perylene tetracarboxylic

dianhydride studied by raman spectroscopy. *Phys. Rev. B*, 61(21):14564–14569, 2000.
http://dx.doi.org/10.1103/PhysRevB.61.14564.

[134] R. Scholz, A. Yu. Kobitski, T. U. Kampen, M. Schreiber, D. R. T. Zahn, G. Jungnickel, M. Elstner, M. Sternberg, and Th. Frauenheim. Resonant raman spectroscopy of 3,4,9,10-perylene-tetracarboxylic-dianhydride (PTCDA) epitaxial films. *Phys. Rev. B*, 61(20):13659–13669, 2000.
http://dx.doi.org/10.1103/PhysRevB.61.13659.

[135] D. Cahen and A. Kahn. Electron energetics at surfaces and interfaces: concepts and experiments. *Adv. Mater.*, 15:271–277, 2003.
http://dx.doi.org/10.1002/adma.200390065.

[136] Y. Yoneda. Anomalous surface reflection of x rays. *Phys. Rev.*, 131:2010–2013, 1963.
http://dx.doi.org/l10.1103/PhysRev.131.2010.

[137] A. Boultif and D. Louër. Indexing of powder diffraction patterns for low-symmetry lattices by the successive dichotomy method. *J. Appl. Cryst.*, 24: 987–993, 1991.

Acknowledgments

I would like to acknowledge the many people who have contributed to the results of this thesis. The work presented here has been realized in a collaboration between the Insitut de Ciència de Materials de Barcelona (Barcelona, Spain), and the Max-Plank-Institut für Metallforschung (Stuttgart, Germany).

I would like to thank my advisor, Dr. Miquel Garriga, who started the collaboration Barcelona-Stuttgart that gave me the possibility to start my thesis on organic semiconductors. I also appreciate his support and guidance over these years. I would like to thank Prof. Dr. Helmut Dosch for the opportunity of working under excellent scientific conditions and for his support during my stay in his institute. I also thank Prof. Jordi Pascual, for accepting to be the tutor of this thesis and for his advice.

I am enormously indebted to Dr. Isabel Alonso and Dr. Frank Schreiber, without whose support and help this thesis would not have been possible. I would like to thank Dr. Frank Schreiber, who always had his office door open to me, for his constant support and for the numerous discussions we have had over the last years. The contributions from Dr. Isabel Alonso have been essential during these years. Without her knowledge on ellipsometry and anisotropic materials part of this thesis would simply not exist. I also thank Dr. Isabel Alonso for the many hours she has spent in the laboratory and for the good advices.

I would also like to thank all the colleagues of the organic thin films group and the "Abteilung Dosch" for making the everyday work pleasant. Dr. Esther Barrena for showing me how to use the AFM and for the good friendship. Dr. Arndt Dürr for his guide tours, not only through the diffractometers in the labs but also through Hamburg and Grenoble, which make long beamtimes enjoyable. From Dr. Ken Ritley I learned many experimental skills, especially on MBE. Dr. Bärbel Krause for her knowledge on thin film growth and for many discussions. Dr. Volker Kruppa for his help in AFM measurements. Last but not least, to Stefan Sellner,

for two years sharing office, for many good times, and for his unvaluable help during beamtimes.

Prof. Dr. Fernando Cerdeira for his work and discussions on the Raman spectra of F_{16}CuPc thin films.

Thanks are due to Prof. Dr. Norbert Karl and Dr. Jens Pflaum for interesting discussions, and Stefan Hirshmann for purification of material.

Index